Modeling Atmospheric Mercury Deposition to the Great Lakes: Analysis for 2011

Dr. Mark Cohen

NOAA Air Resources Laboratory

College Park, MD, USA

December 18, 2017

Final Technical Report

for work conducted with FY2014-2015 funding from the

Great Lakes Restoration Initiative

Version History

1. December 6, 2017. Initial version.

2. December 18, 2017. Added several new maps and plots to enhance the visualization and interpretation of the results. Text describing these new graphics was also added. These new graphics included:

- maps of gridded emissions and deposition contributions from anthropogenic sources (Figure 17, Figure 25, and Figure 85 though Figure 94);
- maps of emissions and deposition contributions from large point and area sources in the U.S. and Canada (Figure 18 through Figure 24, and Figure 144 through Figure 148); and
- plots of emissions and deposition contributions as a function of distance of the source from the lake (Figure 7, and Figure 119 through Figure 129).

Contents

Acknowledgments

The following individuals, organizations, and programs are gratefully acknowledged for their important contributions to this analysis:

- Christopher Loughner, NOAA Air Resources Laboratory (ARL), for creating a parallelized version of HYSPLIT-Hg, allowing model simulations to be conducted with multiple processors;

- Richard Artz (retired) and Roland Draxler (retired), formerly of NOAA ARL, for helpful discussions about this work;

- Winston Luke, Paul Kelley, and Xinrong Ren, colleagues in the atmospheric mercury program at NOAA ARL, for insights into the fate and transport of atmospheric mercury;

- Ariel Stein, Glenn Rolph, Barbara Stunder, Christopher Loughner, Alice Crawford, Tianfeng Chai, Hyun-Cheol Kim, Fantine Ngan, and Roland Draxler (retired) of the NOAA ARL HYSPLIT modeling group;

- Rick Jiang, Chief Information Officer at the Air Resources Laboratory, and colleague Fred Shen for maintenance, troubleshooting, and development of the Linux-based computational server used to carry out the modeling in this study;

- Surya Ramaswamy and Mark Garrison, ERM, for estimating the mercury speciation profiles for each point source in the 2011 National Emissions Inventory;

- Hang Lei , NOAA, for providing global land, ocean, volcanic, and biomass-burning emission fields based on the Lei *et al*. (2013, 2014) analyses, that were adapted for use in this project;

- Frits Steenhuisen, Simon Wilson, Jozef Pacyna and colleagues for creation of the AMAP/UNEP global anthropogenic mercury emissions inventory used in this work;

- National Atmospheric Deposition Program (NADP), Illinois State Water Survey, Champaign, IL, for 2011 mercury wet deposition data at sites in the NADP's Mercury Deposition Network;

- David Gay, National Atmospheric Deposition Program (NADP), Illinois State Water Survey, Champaign, IL, for coordinating transfer of 2011 ambient mercury concentration data from the NADP Atmospheric Mercury Network (AMNet) for use in this project;

- All of the researchers, and field and laboratory personnel involved with collecting the MDN and AMNet data mentioned above;

- Environment Canada, for 2011 CAMNet ambient mercury monitoring data downloaded from the Canadian National Atmospheric Chemistry (NAtChem) Toxics Database, along with all research, laboratory, and field personnel involved with collection of these data.

Executive Summary

Mercury contamination in the Great Lakes remains a public and wildlife health concern due to neurodevelopment impacts. The primary route of exposure is consumption of fish containing methyl mercury. Fish mercury concentrations in some parts of the Great Lakes region appear to be increasing in recent years. Atmospheric deposition is the largest current loading pathway for mercury to the region, and there is strong evidence that recently deposited mercury is more bioavailable than legacy mercury in Great Lakes ecosystems. Accordingly, it is important to understand and quantify emissions of mercury to the air, transport of the mercury through the air to and/or within the Great Lakes region, and deposition of mercury to the Great Lakes and their watersheds. This report describes an analysis using the NOAA HYSPLIT-Hg model to estimate the amount and source-attribution of mercury deposition to the Great Lakes for the year 2011. This work was partially supported with FY2014 and FY2015 funding through the Great Lakes Restoration Initiative.

An earlier analysis was carried out with the HYSPLIT-Hg model for the year 2005[1] using solely a gridded ("Eulerian") modeling methodology. In this analysis for the year 2011, several different methodologies in addition to the gridded-only approach were used. The additional methodologies used here were alternative hybrid combinations of plume-based ("Lagrangian") and gridded simulation methodologies. In the hybrid Lagrangian-Eulerian approaches, priority was given to optimize the accuracy of Great Lakes deposition and source-attribution estimates in allocating computational resources.

Anthropogenic mercury emissions to the air from U.S. and Canadian sources were estimated from 2011 national inventories; anthropogenic emissions from the rest of the world were estimated using data from a global emissions inventory for the year 2010. These emissions are *direct anthropogenic* emissions sources, e.g., from power plants, waste incinerators, smelters, and other active processes. Global emissions from land/vegetation, biomass burning, geogenic sources, re-emissions, and the ocean were also included. Except for geogenic sources (e.g., volcanoes), a significant fraction of the emissions from these source categories are re-emissions of previously deposited anthropogenic emissions, and so, can be considered *indirect anthropogenic* contributions.

The modeling analysis tracked the atmospheric fate and transport of these emissions, with particular attention to the amount that each source contributed to each of the Great Lakes and their watersheds during the year 2011. The modeling approach was evaluated by comparing model predictions with available ambient measurements in the Great Lake region and elsewhere. Because the modeling analysis was optimized for estimating deposition to specific large receptors (i.e. the Great Lakes), it was not expected that modeling results would closely match measurements at specific monitoring locations.

---

[1] Cohen MD, Draxler RR, Artz RS, Blanchard P, Gustin MS, Han Y, et al. Modeling the global atmospheric transport and deposition of mercury to the Great Lakes. Elementa 2016; 4:000118.

However, modeled and measured mercury concentrations and deposition are extensively compared in the report, with attention given to both model and measurement uncertainties and limitations. In general, despite numerous uncertainties, modeling results were reasonably consistent with measurements. The best agreement between modeling results and measurements was generally found in the Great Lakes region, lending credibility to the Great Lakes source-attribution results presented.

Eulerian-only and several hybrid Lagrangian/Eulerian methodologies were used, and detailed results for all simulation methodologies are presented in the main body of the report. Results for "Run Scheme 04" (RS-04) – the most advanced and computationally intensive hybrid Lagrangian/Eulerian scheme used – are shown below in Figure 1 through Figure 6. These figures show the fractional contribution to the Great Lakes from different source categories, and it can be seen and/or inferred that:

- *Direct* anthropogenic emissions tended to have the highest impact on Lake Erie (~38-40% of total estimated deposition) and the lowest impact on Lake Superior (~23-24%), with intermediate impacts on the other lakes.
- The combined contribution of ocean, biomass burning, and terrestrial surfaces ("Land/Vegetation" and "Prompt Re-emission", but excluding "Geogenic" contributions) ranges from 54% for Lake Erie to 67% for Lake Superior of the model-estimated deposition. However, since 2/3 or more of these contributions likely represent indirect anthropogenic sources, these indirect anthropogenic contributions would represent 36% - 45% or more of the total modeled deposition to Lakes Erie and Superior, respectively.
- The total *direct* and *indirect* anthropogenic contributions to the Great Lakes is likely on the order of ~70% or more, with the following RS-04 estimates for each lake: Superior (69%), Huron (70%), Michigan (71%), Erie (75%), Ontario (72%). These estimates assume 2/3 of the emissions from oceanic and terrestrial reservoirs in 2011 were *indirect* anthropogenic emissions, but the fraction could be higher.
- The importance of US *direct* anthropogenic emissions contributions to individual lakes varied from a high of ~21% for Lake Erie to a low of ~4% for Lake Superior.
- China was generally the country with the 2nd highest *direct* anthropogenic contribution, behind the United States, contributing on the order of ~5-7% of 2011 deposition to the Great Lakes basin. The importance of Chinese anthropogenic emissions contributions to individual lakes was much more uniform than that for the U.S., as expected, given their relative distance from the Great Lakes region..
- Canada's *direct* anthropogenic sources were estimated to be most important for Lake Ontario (~7%) and least important for Lake Superior and Lake Michigan (<1%). India, Mexico, and Russia were all estimated to contribute on the order of ~0.5–1% of the total 2011 deposition.
- The total *direct* anthropogenic contribution from all "other" countries in the world during 2011 was on the order of ~7-9% of the total model-estimated deposition.

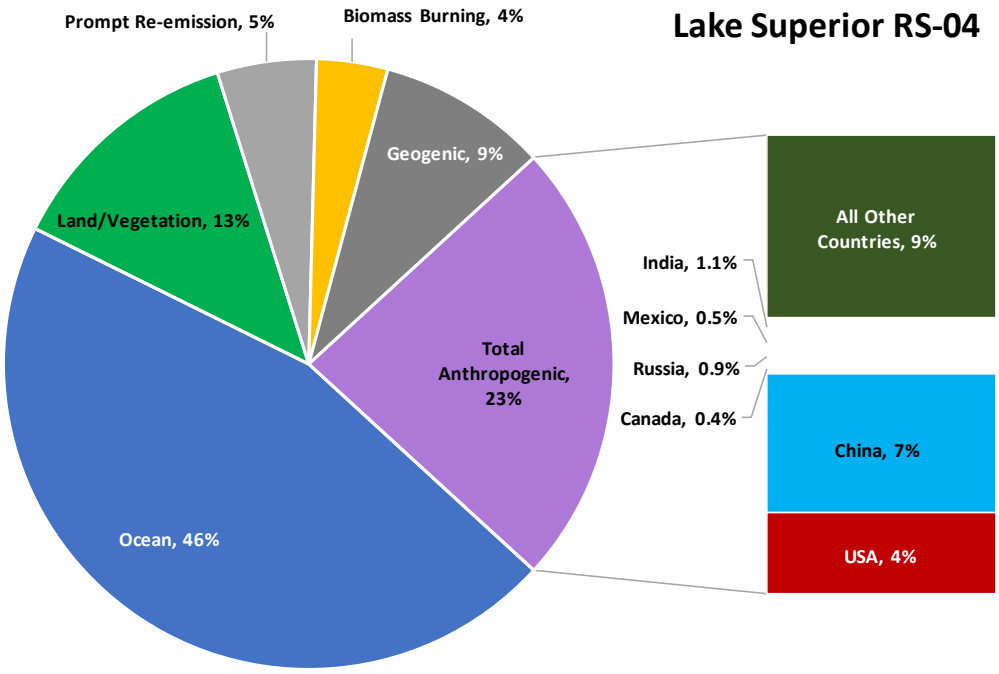

Figure 1. Fraction of total modeled mercury deposition to Lake Superior contributed by each source category

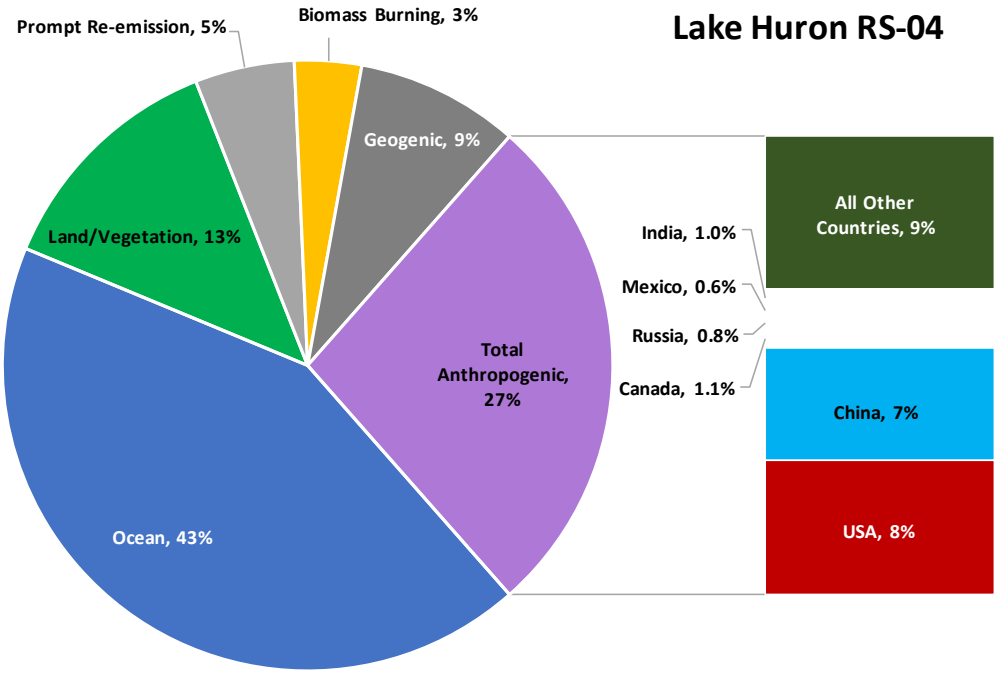

Figure 2. Fraction of total modeled mercury deposition to Lake Huron contributed by each source category

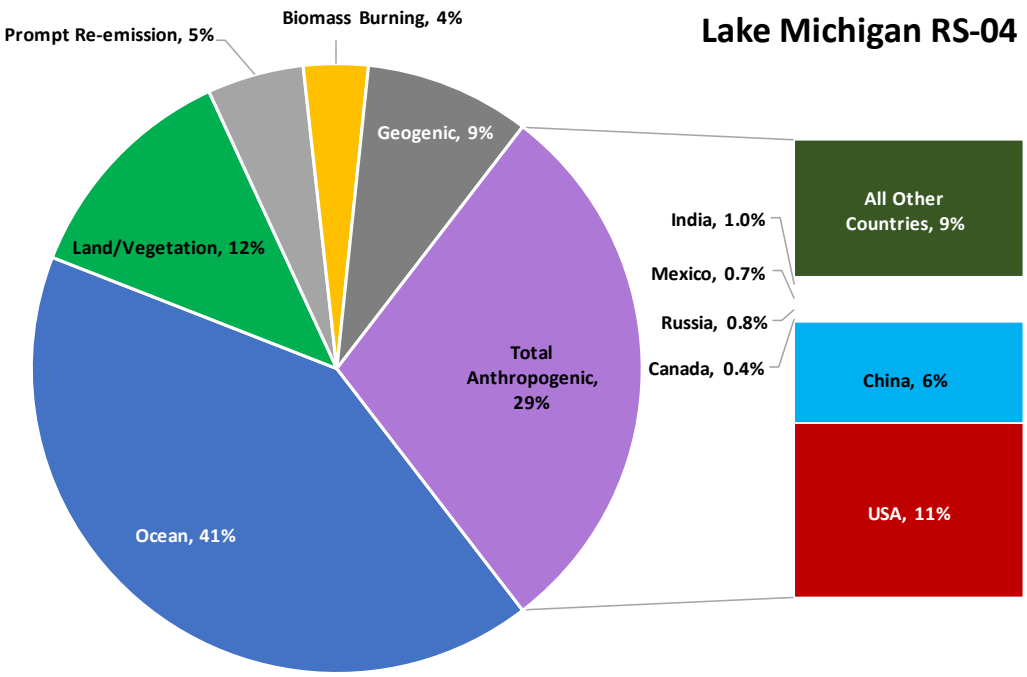

Figure 3. Fraction of total modeled mercury deposition to Lake Michigan contributed by each source category

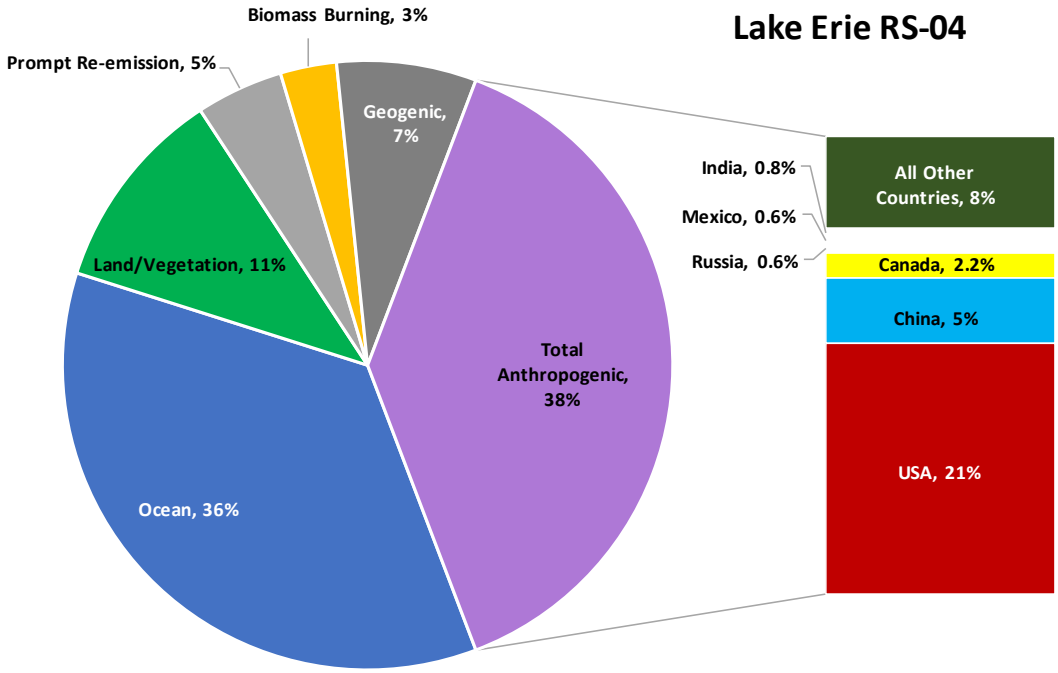

Figure 4. Fraction of total modeled mercury deposition to Lake Erie contributed by each source category

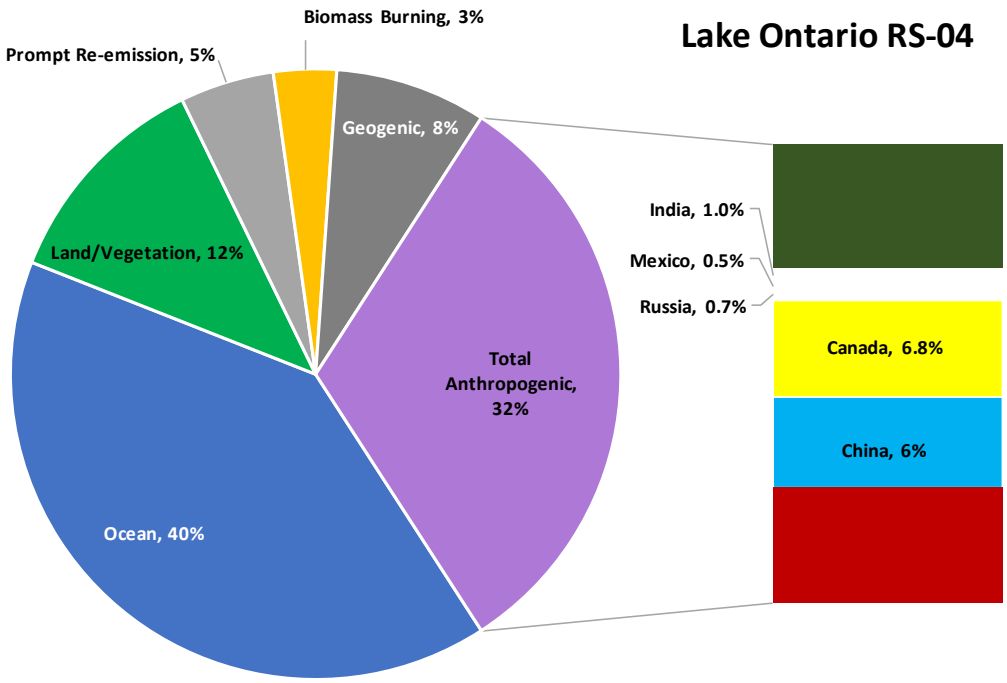

Figure 5. Fraction of total modeled mercury deposition to Lake Ontario contributed by each source category

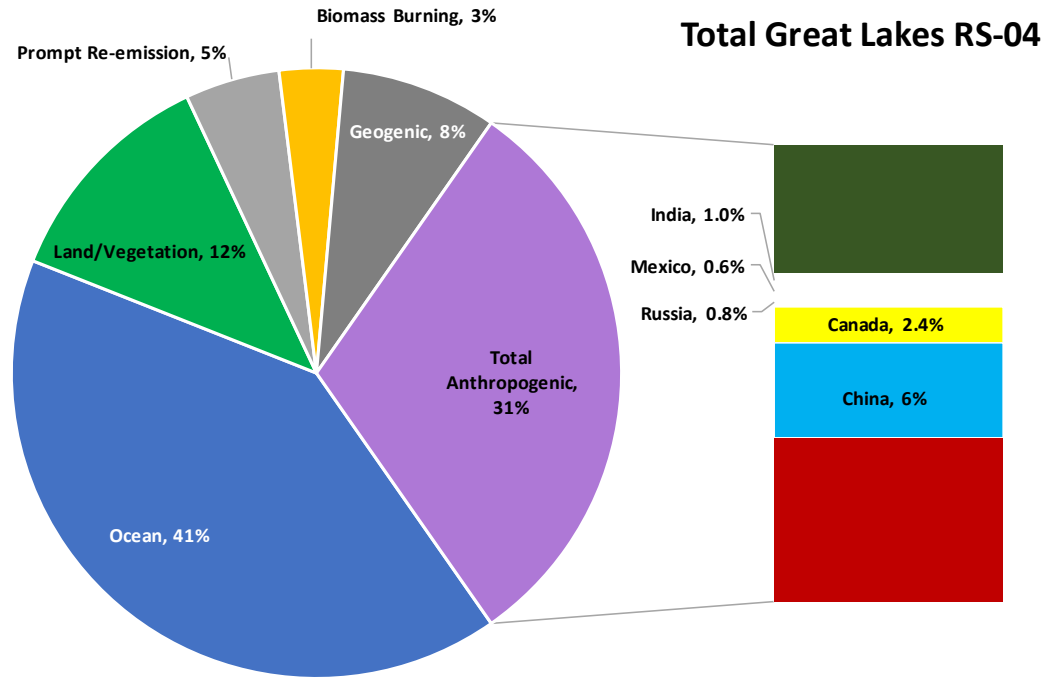

Figure 6. Fraction of total modeled mercury deposition to the Great Lakes contributed by each source category

An analysis of emissions and contributions to deposition arising from direct anthropogenic sources in different distance ranges away from each lake and watershed was conducted, and these results are summarized in Figure 7 below.

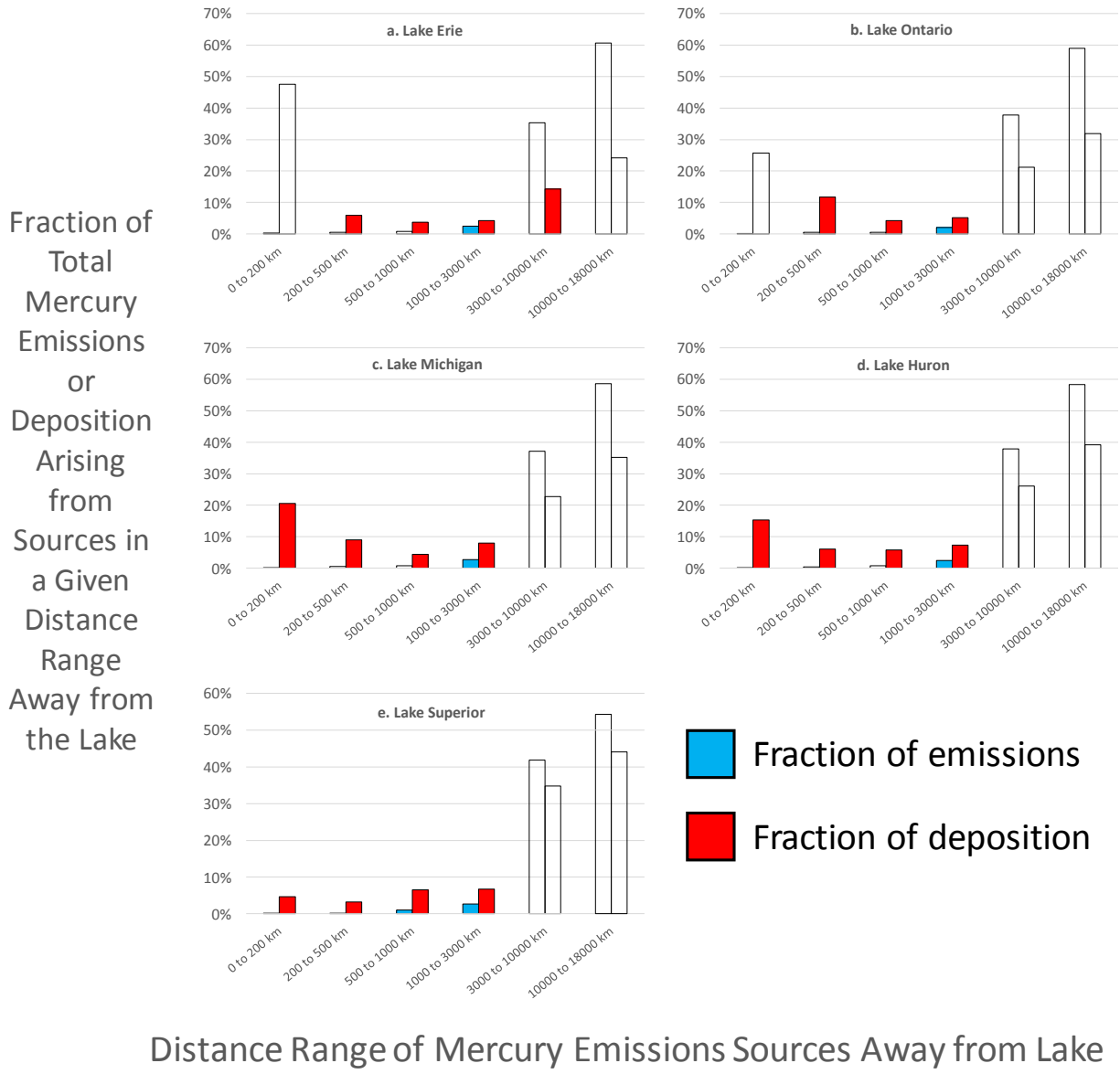

Figure 7. Mercury emissions and deposition arising from direct anthropogenic emissions in different distances ranges away from each of the Great Lakes.

This figure shows that nearly half (47.5%) of the modeled atmospheric mercury deposition to Lake Erie from direct anthropogenic emissions comes from sources within 200 km of the lake. These sources, within 200 km of the lake, represent only 0.3% of the total global direct anthropogenic emissions used in the modeling. For Lake Erie, 96% of all direct anthropogenic emissions are from sources more than 3000 km away from the lake, but these sources only contribute a little more than 38% of the corresponding deposition.

For Lake Ontario, a quarter (25.7%) of the modeled atmospheric mercury deposition from direct anthropogenic emissions comes from sources within 200 km of the lake. These nearby sources represent only 0.1% of the total global direct anthropogenic emissions used in the modeling. For Lake Ontario, 96% of all direct anthropogenic emissions are from sources more than 3000 km away from the lake, but these sources only contribute a little more than half (53%) of the deposition due to direct anthropogenic emissions.

A fifth (20.5%) of the modeled atmospheric mercury deposition to Lake Michigan from direct anthropogenic emissions comes from sources within 200 km of the lake. These nearby sources represent only 0.1% of total global direct anthropogenic emissions. For Lake Michigan, 96% of all direct anthropogenic emissions are from sources more than 3000 km away from the lake, but these sources only contribute a little more than half (58%) of the deposition due to direct anthropogenic emissions.

For Lake Huron, about 15% of the modeled atmospheric mercury deposition from direct anthropogenic emissions comes from sources within 200 km of the lake. These nearby sources represent only 0.2% of total global direct anthropogenic emissions. For Lake Huron, 96% of all direct anthropogenic emissions are from sources more than 3000 km away from the lake, and these sources contribute about 2/3 (65%) of the deposition due to direct anthropogenic emissions.

Less than 5% of the modeled atmospheric mercury deposition to Lake Superior from direct anthropogenic emissions comes from sources within 200 km of the lake. These nearby sources represent only 0.1% of total global direct anthropogenic emissions. For Lake Superior, 96% of all direct anthropogenic emissions are from sources more than 3000 km away from the lake, and these sources contribute nearly 80% of the deposition due to direct anthropogenic emissions.

The grid-based Eulerian-only (RS-00) results of this analysis for 2011 can be directly compared to the aforementioned HYSPLIT-Hg results for 2005, as the methodologies are consistent.

Figure 8 shows the model-estimated deposition flux from all emissions types to each of the Great Lakes for the 2005 and 2011 Eulerian-only analyses. For each lake, it is seen that the modeled 2011 deposition is less than the modeled 2005 deposition. Figure 9 shows these same data, but expressed as fractions of the total modeled deposition for each lake. It can be seen that the model-estimated amount and fraction due to U.S. emissions declined significantly for all of the lakes. The primary reason for this is that the emissions in the U.S. declined dramatically between 2005 and 2011, especially in the Great Lakes region, as can be seen from Figure 10, which shows the time evolution of emissions at different distances away from each Great Lakes.

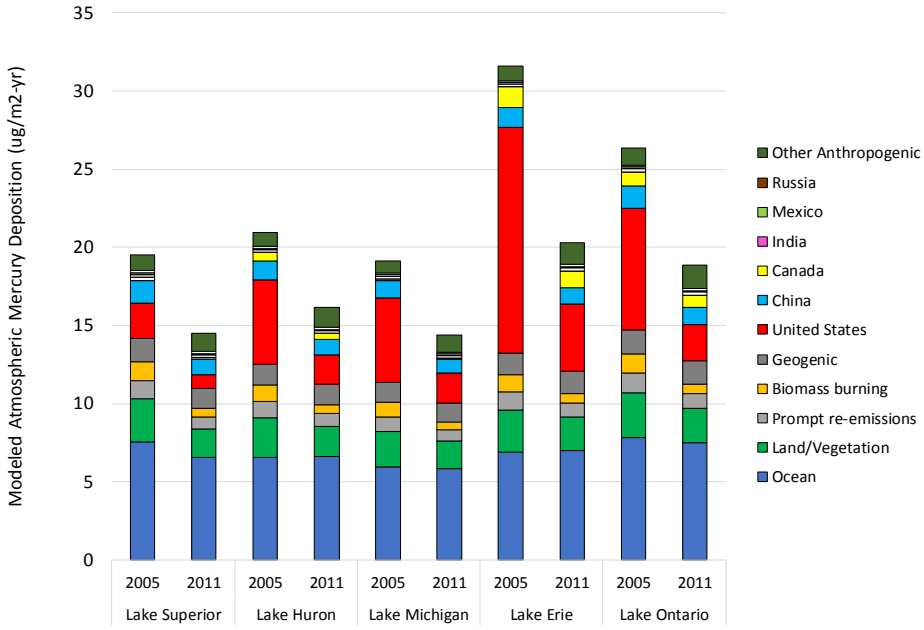

Figure 8. Comparison of Eulerian-only (RS-00) model-estimated 2005 and 2011 atmospheric mercury deposition flux contributions to the Great Lakes from each source category.

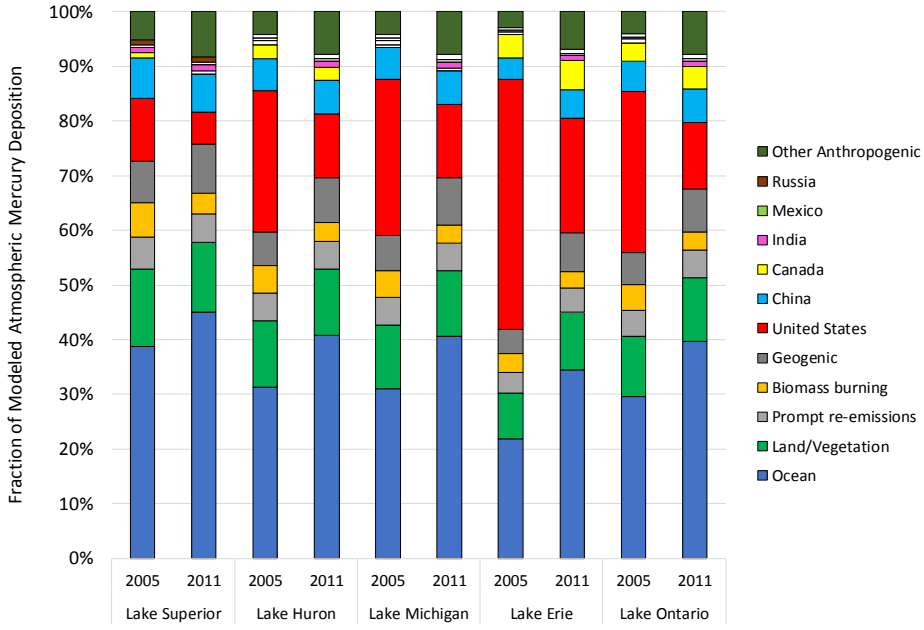

Figure 9. Comparison of Eulerian-only (RS-00) model-estimated 2005 and 2011 atmospheric mercury deposition flux to the Great Lakes, fractional contributions from each source category.

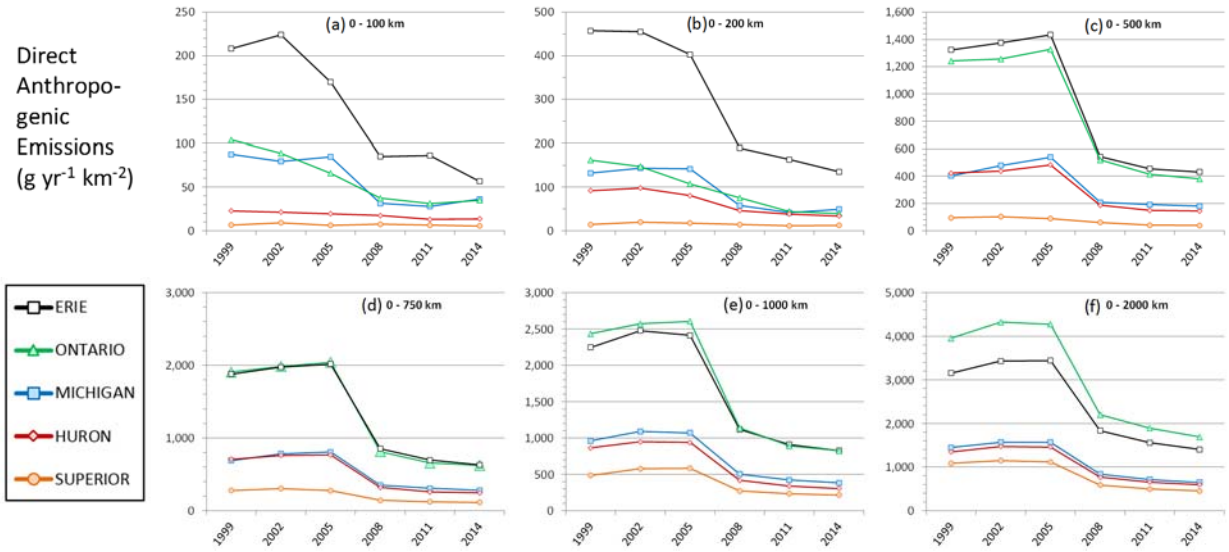

Figure 10. Total Hg point source emissions from the USEPA National Emissions Inventory and the Canadian National Pollutant Release Inventory within (a) 100 km, (b) 200 km, (c) 500 km, (d) 750 km, (e) 1000 km, and (f) 2000 km of each Great Lake. [Figure S8 from Zhou et al., 2017[2], prepared by the author)

[2] Zhou, C., M. Cohen, et al. (2017). "Mercury Temporal Trends in Top Predator Fish of the Laurentian Great Lakes from 2004 to 2015: Are Concentrations Still Decreasing?" Environmental Science & Technology **51**(13): 7386-7394.

1. Introduction

Mercury contamination is an ongoing concern in the Great Lakes region (Figure 11), with public health and wildlife toxicology ramifications (Bhavsar, Gewurtz et al. 2010, Evers, Wiener et al. 2011, Wiener, Evers et al. 2012, Gandhi, Tang et al. 2014, Visha, Gandhi et al. 2015).

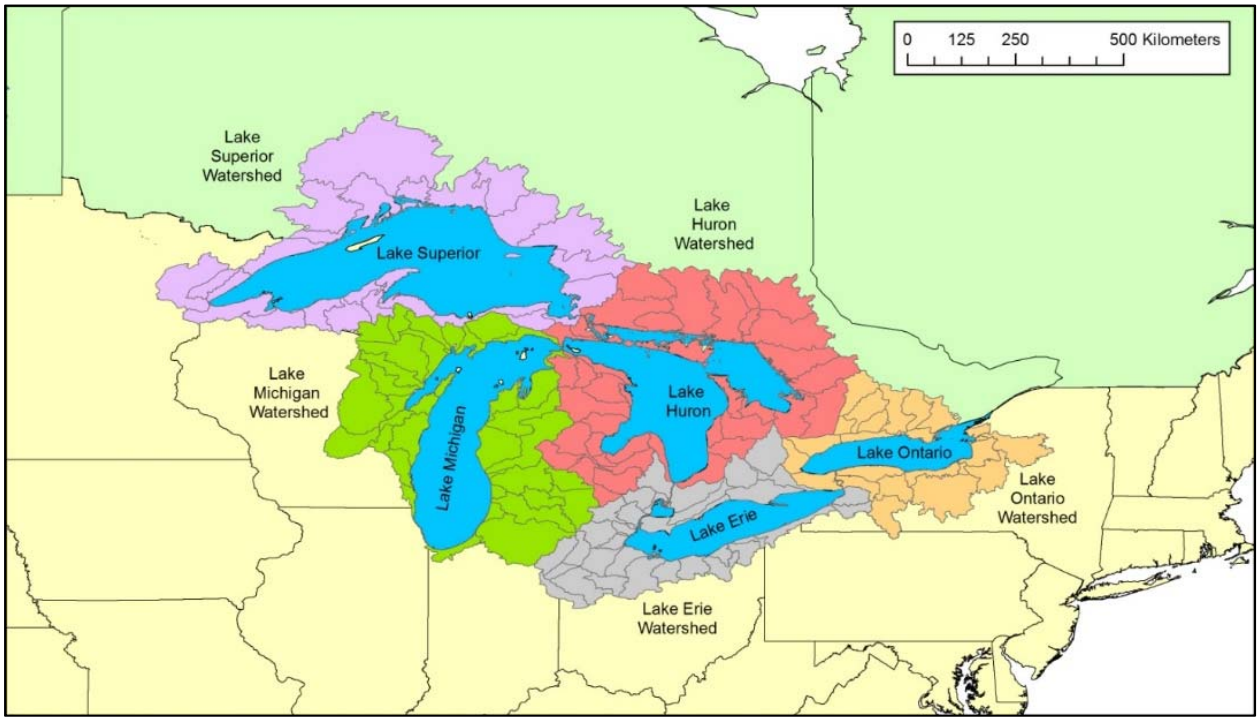

Figure 11. Great Lakes and their watersheds.

Great Lakes male anglers have been found, on average, to have significantly higher blood mercury concentrations than the general population (Christensen, Thompson et al. 2016). While the population studied ate approximately 30% more fish than the general population, their blood mercury levels averaged more than 2.5 times that of the corresponding general population (Figure 12). Approximately 25% of women anglers in the Great Lakes region of child-bearing age may be exceeding health-based fish consumption guidelines (Connelly, Lauber et al. 2017).

A recent study found that mercury often plays a significant role in the human health risks associated with eating Great Lakes fish, even in cases where PCB's were considered the "primary" reason for a given fish consumption advisory (Gandhi, Drouillard et al. 2017). Figure 13 and Figure 14 (both reproduced with permission from this publication), show that mercury appears to represent a very high fraction of the overall risk to both the general population and sensitive population (women of childbearing age) from exposure to the known suite of toxic chemicals found in Great Lakes fish.

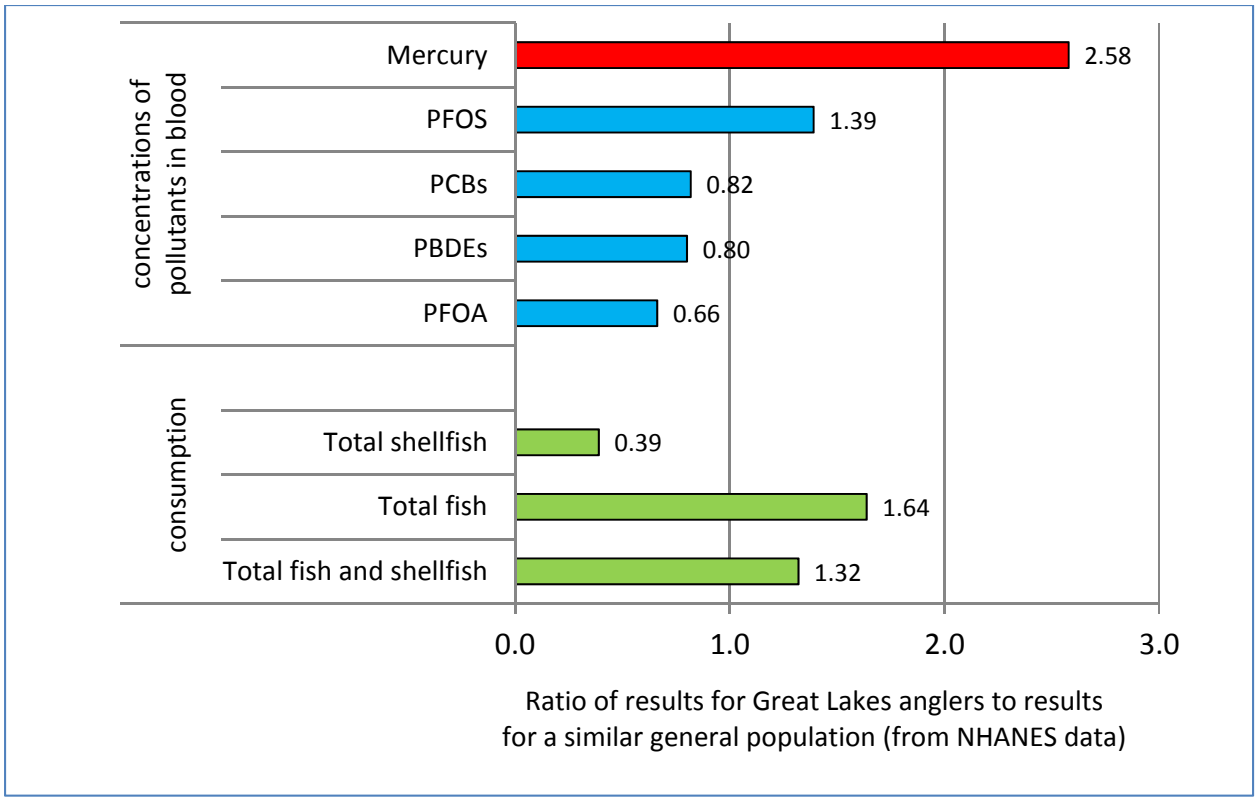

Figure 12. Mercury in the blood of Great Lakes anglers compared to the general population, based on data from Christensen, Thompson et al. (2016)).

Groth (2017)) reviewed recent epidemiological evidence and toxicological modeling of the risks and benefits of eating fish and found that current fish consumption guidelines may be based on underestimates of the toxic effects of mercury. Numerous recent epidemiological studies have found neurotoxic effects of mercury at exposure levels near the EPA's Reference Dose (RfD). The Reference Dose – 0.1 µg Hg per kg of body weight per day – was established based on the early epidemiological study of Grandjean, Weihe et al. (1997)), after applying a 10-fold reduction for safety and to account for variations in individual susceptibility to mercury toxicity. This RfD was thought to be the level at which no adverse effects would occur. However, Groth (2017)) discusses 13 recent studies that found adverse effects at/around this dose. As a result of this evidence, it appears that mercury may be at least as toxic as earlier thought, and is very likely more toxic than considered when the RfD was originally developed. In other words, the RfD may need to be reduced. Since mercury-related fish consumption advisories are often based directly or indirectly on the RfD, it is possible that current mercury-based fish advisories are not restrictive enough. One reason why the original RfD may not have accurately reflected the toxicity of mercury is that the analysis did not factor in the beneficial effects of eating fish, e.g., the beneficial effects of Omega-3 fatty acids. By not factoring in these effects, the toxicity of mercury appeared much less than it actually was.

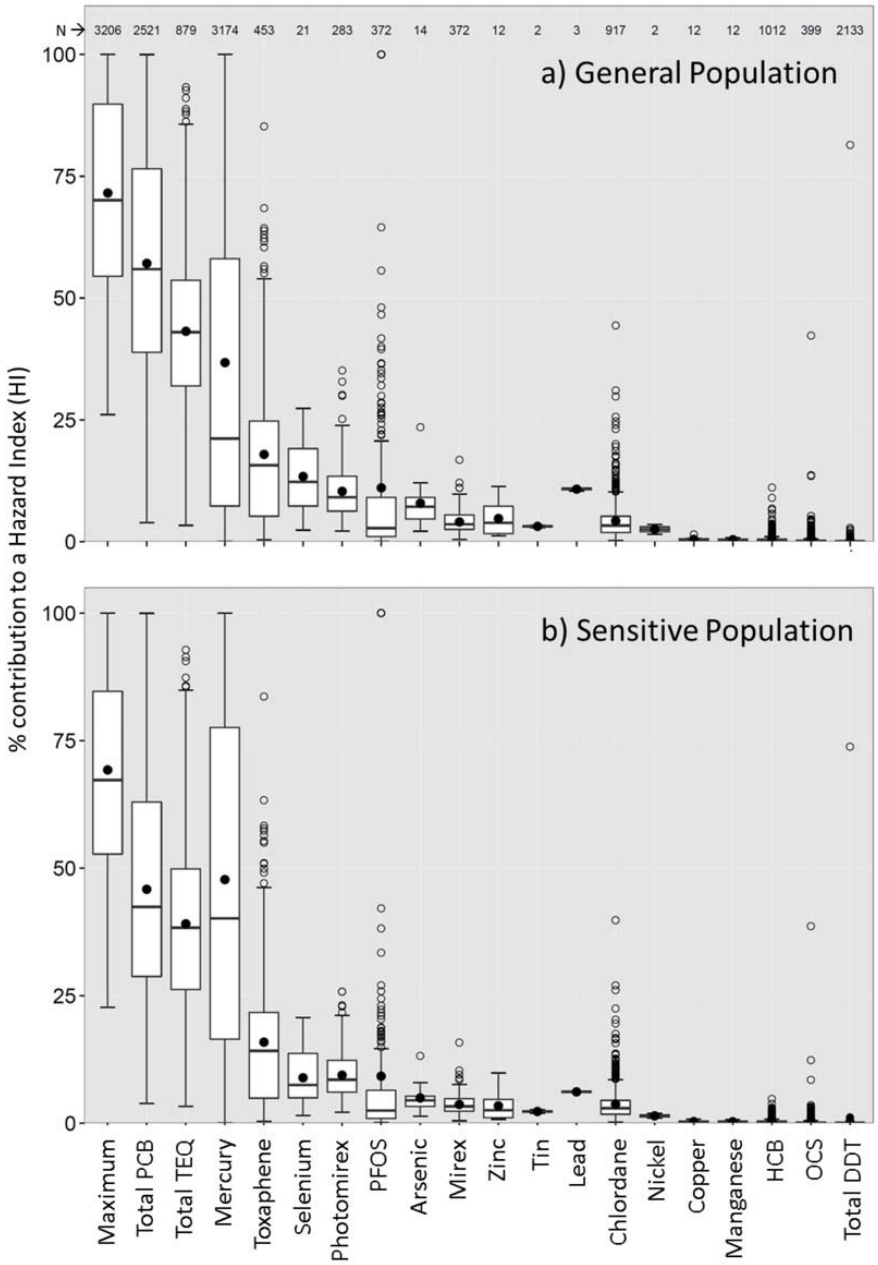

Figure 13. Percent contribution of contaminant-specific hazard quotient (HQ) to the hazard index (HI) calculated using the multi-chem advisory approach for (a) the general population and (b) the sensitive population (women of childbearing age). The maximum is the highest contribution of an HQ to an HI regardless of contaminant. The solid circle indicates the mean, the line within the box indicates the median, the box indicates the 25th and 75th percentiles, the whiskers indicate the highest and lowest values not classified as statistical outlier values < 1.5 times away from the interquartile range. Nondetect values were excluded. Similar results for a data set that included nondetects are presented in Figure S9. DDT, dichlorodiphenyltrichloroethane; HCB, hexachlorobenzene; OCS, octachlorstyrene; PCB, polychlorinated biphenyl; PFOS, perfluorooctane sulfonate; TEQ, toxic equivalent. ***Caption text and Figure reproduced with permission from Environmental Health Perspectives (Gandhi, Drouillard et al. 2017)***

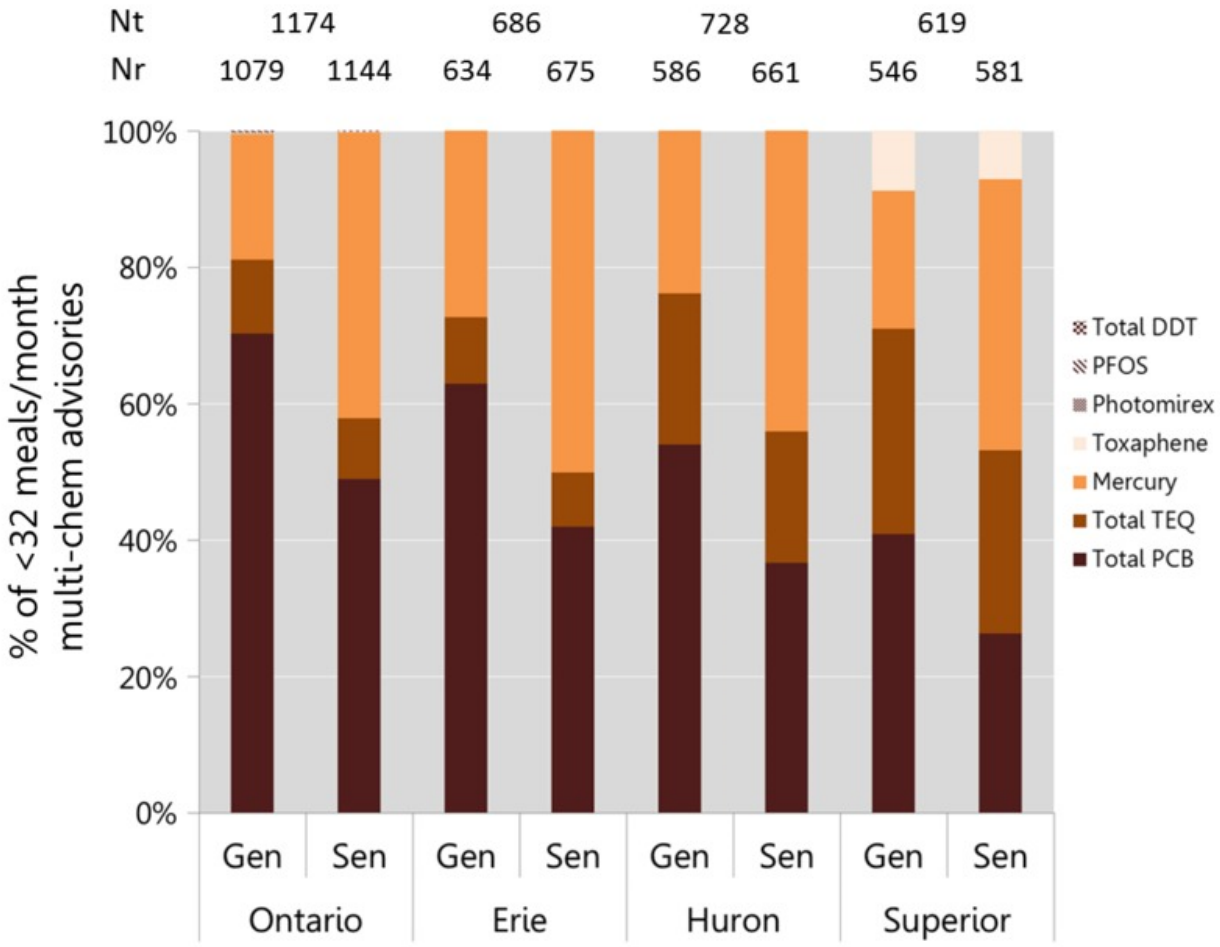

Figure 14. Percent of the multi-chem advisories for which a contaminant is the major contributor to the overall additive effect [assessed as a Hazard Index (HI)]. The contaminants not in the figure were not a major contributor to any HI. Photomirex, perfluorooctane sulfonate (PFOS) and total dichlorodiphenyltrichloroethane (DDT) were major contributors for < 1% of the multi-chem advisories for Lake Ontario only. Gen = general population; Nr = number of advisories that are < 32 meals/month; Nt = total number of advisories; PCB = polychlorinated biphenyl; Sen = sensitive populations; TEQ = Toxic Equivalent. *Caption text and Figure Reproduced with permission from Environmental Health Perspectives (Gandhi, Drouillard et al. 2017)*

A recent study by Zhou, Cohen et al. (2017)) found that mercury concentrations in top predator fish in Lakes Huron and Superior appear to still be decreasing (Figure 15). However, the study found that fish Hg concentrations in Lake Michigan appear to have leveled off, and fish Hg concentrations in Lakes Erie and Ontario have been increasing in recent years (Figure 16).

Atmospheric deposition is a highly significant contemporary loading pathway (Mason and Sullivan 1997, Sullivan and Mason 1998, Rolfhus, Sakamoto et al. 2003, Jeremiason, Kanne et al. 2009). Lepak, Yin et al. (2015)) found that fish in Lakes Michigan, Superior, and Ontario had isotopic mercury compositions

more similar to atmospheric mercury than sediment mercury, indicating the importance of atmospheric deposition to current food chain mercury bioaccumulation.

The HYSPLIT-Hg atmospheric fate and transport model has been previously used to estimate the amount and source-attribution of mercury to the Great Lakes and their watersheds arising from anthropogenic sources in the United States and Canada in 1996 (Cohen, Artz et al. 2004) and 1999 (Cohen, Artz et al. 2007). The analysis was extended to estimate 2005 deposition arising from global anthropogenic and natural sources (Cohen, Draxler et al. 2016).

This report describes work supported by FY2014 and FY2015 funding through the Great Lakes Restoration Initiative (GLRI). A brief summary of HYSPLIT-Hg analyses supported by the Great Lakes Restoration Initiative funding is provided in Table 1.

As in previous reports, we will refer to three "kinds" of atmospheric mercury: (i) elemental mercury, Hg(0), also called Gaseous Elemental Mercury or GEM; (ii) soluble oxidized mercury (Hg(II)), also referred to as reactive gaseous mercury (RGM) and gaseous oxidized mercury (GOM); and (iii) particulate mercury, or Hg(p). Except where noted, e.g., in the model evaluation section, results presented in this report are for total mercury (the sum of the three different forms), for simplicity and brevity's sake, even though the entire modeling analysis has been done with explicit treatment of the different mercury forms.

Table 1. HYSPLIT-Hg Projects Partially Supported by GLRI Funding

GLRI Funding	Brief Description of Work	Reference(s)
FY2010	A 2005 analysis of atmospheric deposition to the Great Lakes was carried out, including source-attribution for the model-estimated deposition.	(Cohen, Draxler et al. 2011)
FY2011	A detailed sensitivity analysis was carried out to examine the influences of important uncertainties in model inputs and methodologies	(Cohen, Draxler et al. 2013)
FY2012	The consequences of future emissions scenarios on atmospheric mercury deposition to the Great Lakes and their watersheds were estimated	(Cohen, Draxler et al. 2014)
FY2013	Updating and extending 2005 model results reflecting model improvements and new methodological approaches	(Cohen 2016, Cohen, Draxler et al. 2016)
FY2014	Updating baseline, global Eulerian analysis from the model year 2005 (with 2005 emissions) to the model year 2011 (with 2011 emissions)	this report
FY2015	Developing source-by-source contribution estimates for 2011 Great Lakes mercury deposition	

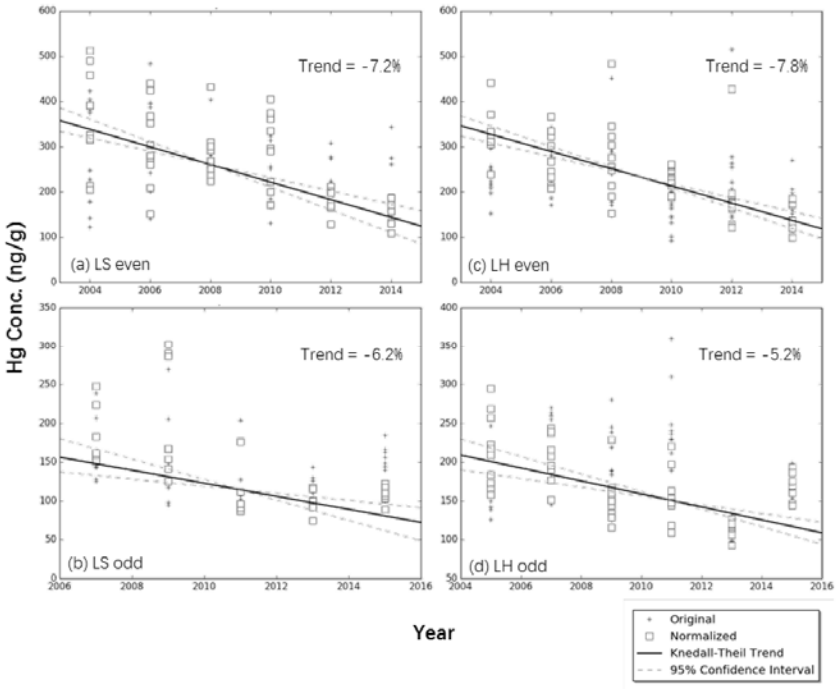

Figure 15. Total fish Hg concentration for lake trout from Lake Superior shallow (a) and deep (b) sites, and Lake Huron shallow (c) and deep (d) sites from 2004-2015 (Zhou et al. 2017).

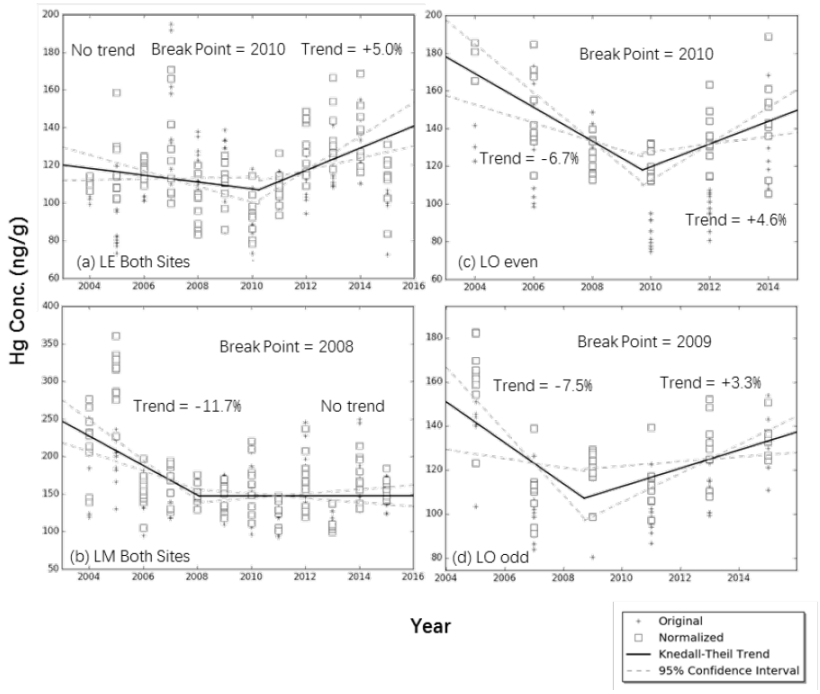

Figure 16. Total fish Hg concentration for Lake Erie walleye (a), and lake trout from Lake Michigan (b), Lake Ontario shallow (c) and deep (d) sites from 2004-2015 (Zhou et al. 2017).

2. Atmospheric Mercury Emissions

Mercury emissions used as model input included the following components: anthropogenic, biomass burning, geogenic, soil/vegetation, ocean, and prompt reemissions. The anthropogenic component was subdivided into emissions of Hg(0), Hg(II), and Hg(p), as described below. Emissions from all other components were considered as Hg(0). All inventory components were ultimately assembled on a global 2.5^{o} x 2.5^{o} grid, equivalent to the horizontal spacing of the global meteorological data used for the modeling (described in Section 3.7 below). Anthropogenic emissions in the United States and Canada were also specified as point sources, with a specific latitude and longitude, and area sources, e.g., at the county level in the United States.

Point-source anthropogenic mercury emissions for the U.S. were assembled from the USEPA 2011 National Emissions Inventory (NEI) (USEPA 2015). Speciation profiles were applied to the total mercury emissions in the point source 2011 NEI by Surya Ramaswamy and Mark Garrison, Environmental Resources Management (ERM), and were provided for use in this analysis. A similar procedure was carried out at the NOAA Air Resources Laboratory for area and mobile sources in the 2011 NEI. These U.S. sources were specified at the county level. EPA-recommended process-based "speciation" factors were utilized to estimate the emissions partitioning (USEPA 2006).

For point-source mercury emissions in Canada, Environment and Climate Change Canada's (ECCC) 2011 National Pollutant Release Inventory (NPRI) was utilized (Environment Canada 2016). For Canadian area sources, 2011 data from ECCC's Atmospheric Pollutant Emissions Inventory (APEI) system were utilized (Environment and Climate Change Canada 2016, Environment and Climate Change Canada 2017). The following methodology was used to assemble these APEI data for use in this analysis. First, the mercury air emissions data were downloaded for all source sectors and all provinces. APEI data are only available as aggregated totals at the province level. For each province, point source mercury emissions records from NPRI data were identified and subtracted from the APEI total for the matching sector for that province. The remaining sector-by-sector emissions for each province were then spatially apportioned within a given province to census subdivisions proportionally to the 2011 population of each subdivision. Each of these "area sources" was then assigned a location at the centroid of the subdivision. There were a total of 5253 census subdivisions in Canada with data reported in the Canadian 2011 census. So, for each of the 23 source categories with mercury emissions reported in this inventory (Table 2), there 5,253 separate records in the Canadian area source inventory that was created for this analysis. Thus, there were a total of 23 x 5,253 = 120,819 area source records in this Canadian area-source inventory. EPA-recommended speciation factors noted above were utilized to estimate emissions partitioning for Canadian emissions inventories.

Figure 17 show the total direct 2011 anthropogenic emissions from U.S. and Canadian sources, estimated using the data sources above, aggregated to a 1^{o} x 1^{o} grid. Figure 18 shows a map of large (defined here as greater than 10 kg/yr) point and area sources associated with coal-fired power generation. Figure 19 shows a comparable map for all large – emitting 10 or more kg/yr – point and area sources associated with all other fuel combustion. Figure 20 shows a comparable map of all large U.S.

and Canadian sources associated with waste incineration and cremation. Figure 21 is an analogous map for all large metallurgical and mining emissions sources, and Figure 22 is a map of all large manufacturing sources, and any source that did not fit into the above categories. Figure 23 shows a map of all sources except for coal-fired power generation sources, and Figure 24 shows a map of all large sources for all categories. A map showing large point sources of mercury in the U.S. and Canada is also provided in the Appendix, Section 7.1 (Figure 149, page 164). Temporal variations (e.g., monthly) variations were not available in the above data sources and so anthropogenic emissions were assumed constant throughout the year.

Table 2. Source categories with mercury emissions reported in Environment and Climate Change Canada's Air Pollutant Emissions Inventory for 2011

Asphalt Paving Industry	Commercial Cooking
Iron and Steel Industries	Construction Fuel Combustion
Mining and Rock Quarrying	Home Firewood Burning
Non-Ferrous Smelting and Refining Industry	Human
Total Electric Power Generation	Residential Fuel Combustion
Electronics	Other Miscellaneous Sources
Metal Fabrication	Crematoriums
Wood Products	Industrial and Commercial Incineration
Other Industries	Municipal Incineration
Marine Transportation	Waste
Rail Transportation	Other Incineration and Utilities
Fuel Use	

For direct anthropogenic mercury emissions in the remainder of the world, the 2010 Arctic Monitoring and Assessment Program (AMAP) global inventory of Pacyna and colleagues was used (AMAP/UNEP 2013, AMAP/UNEP 2013). The AMAP inventory is specified on a 0.5 x 0.5 degree grid (approximately 50 km x 50 km), with total emissions of Hg(0), Hg(II), and Hg(p) for each grid cell.

A map of total direct anthropogenic emissions in the U.S. and Canada, and the rest of the world, aggregated to a 2.5o x 2.5o grid is shown in Figure 25.

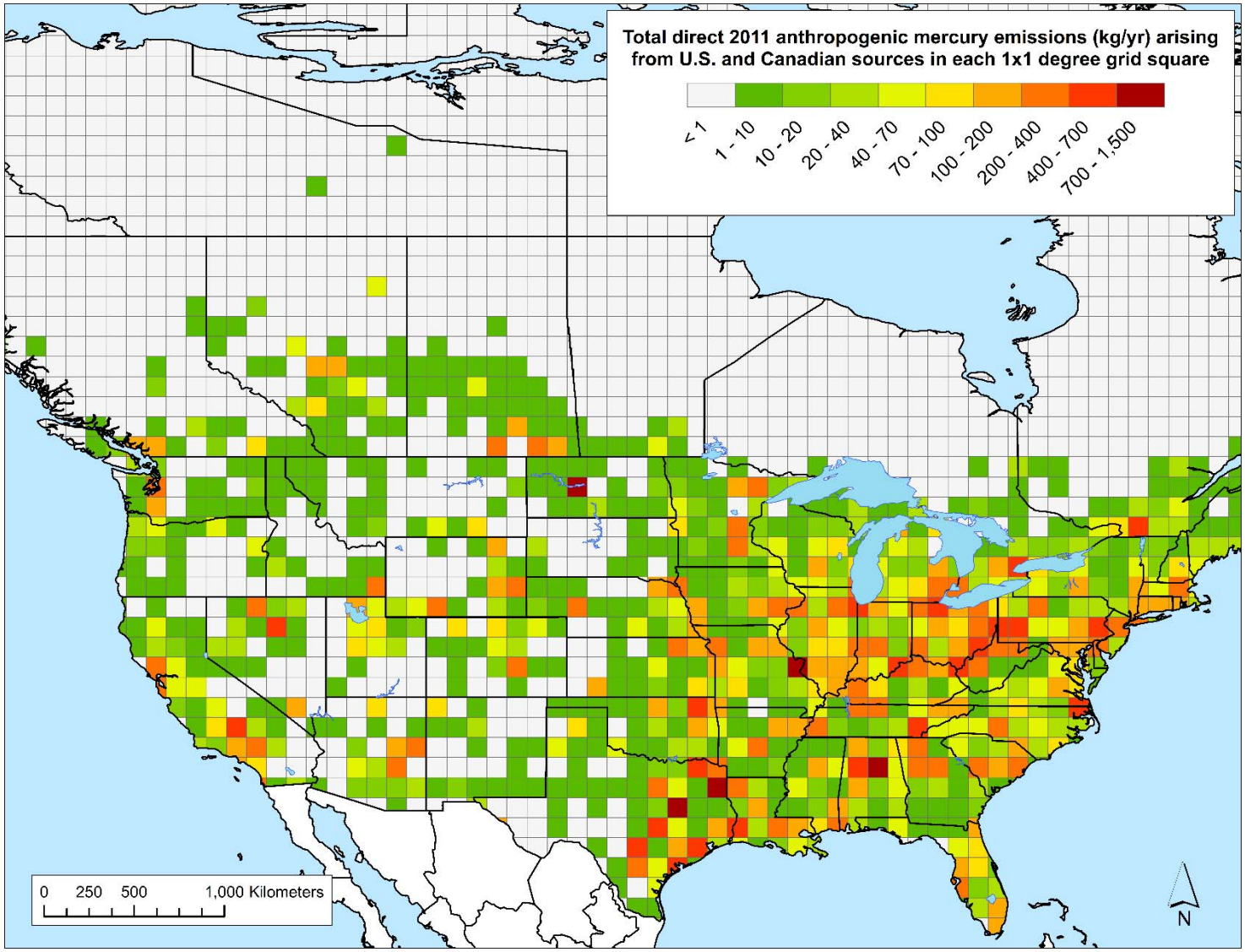

Figure 17. Direct U.S. and Canadian anthropogenic mercury emissions (2011) aggregated onto a 1 x 1 degree grid.

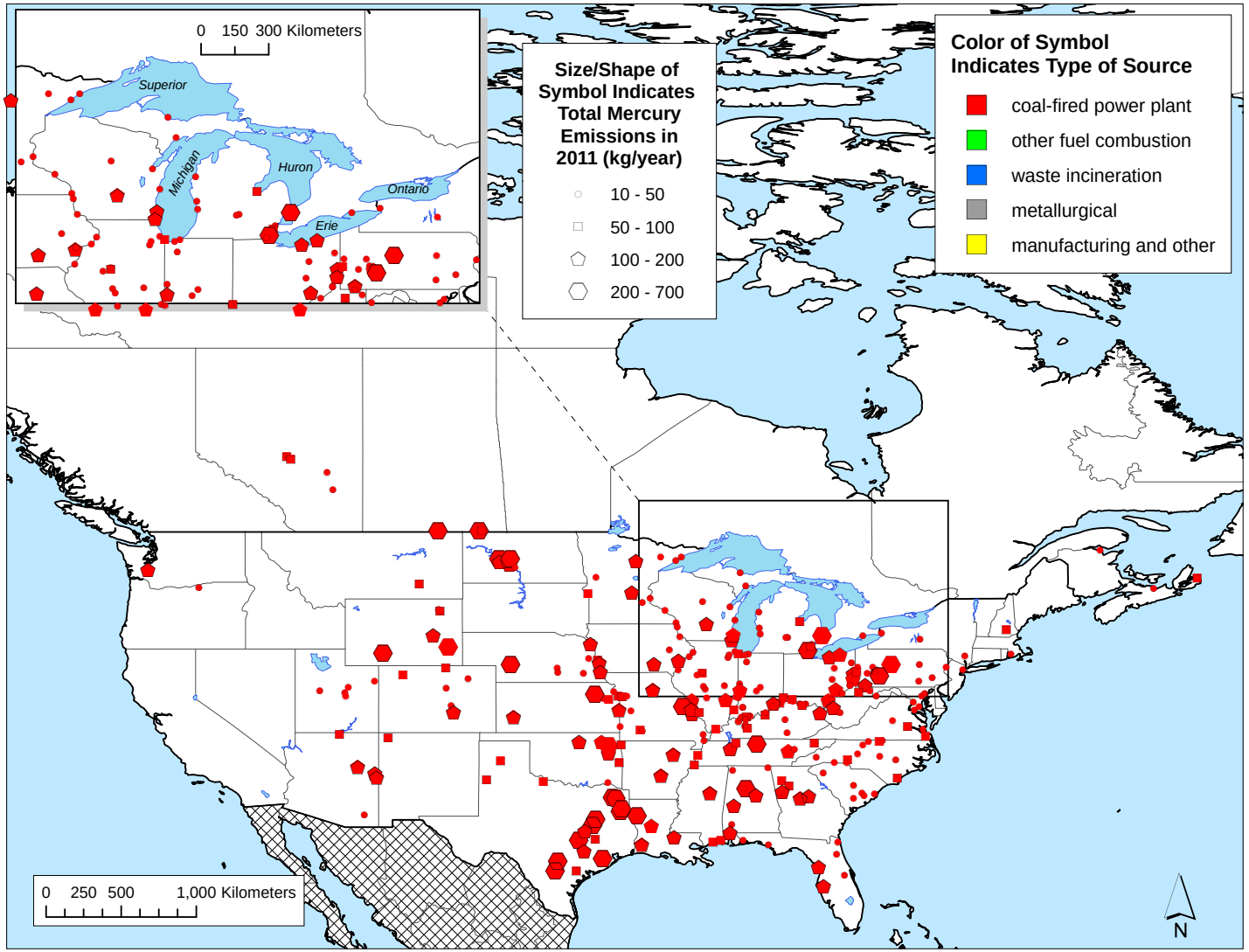

Figure 18. Direct U.S. and Canadian anthropogenic mercury emissions (2011) from large coal-fired power generation point and area sources.

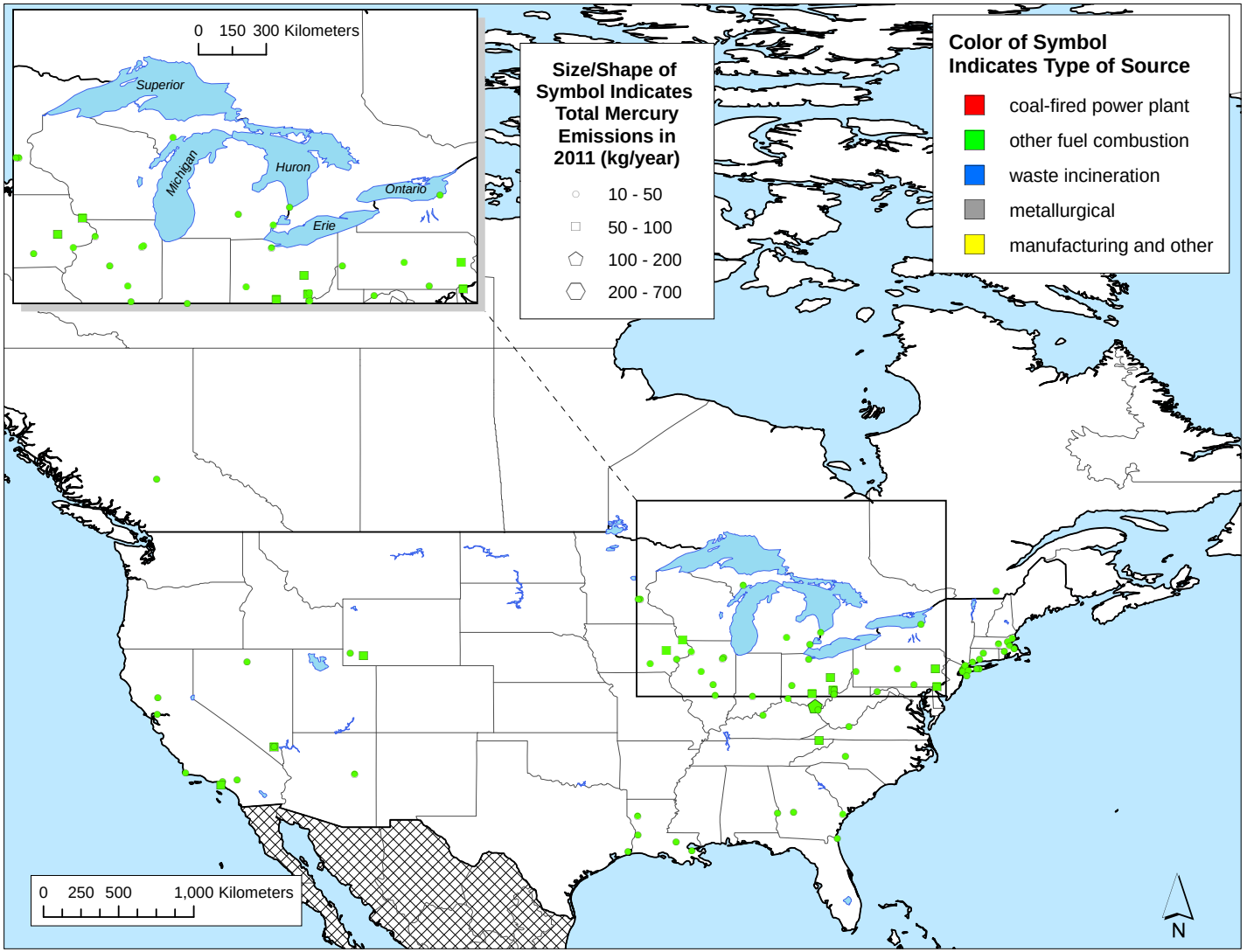

Figure 19. Direct U.S. and Canadian anthropogenic mercury emissions (2011) from large point and area sources burning fuel other than coal.

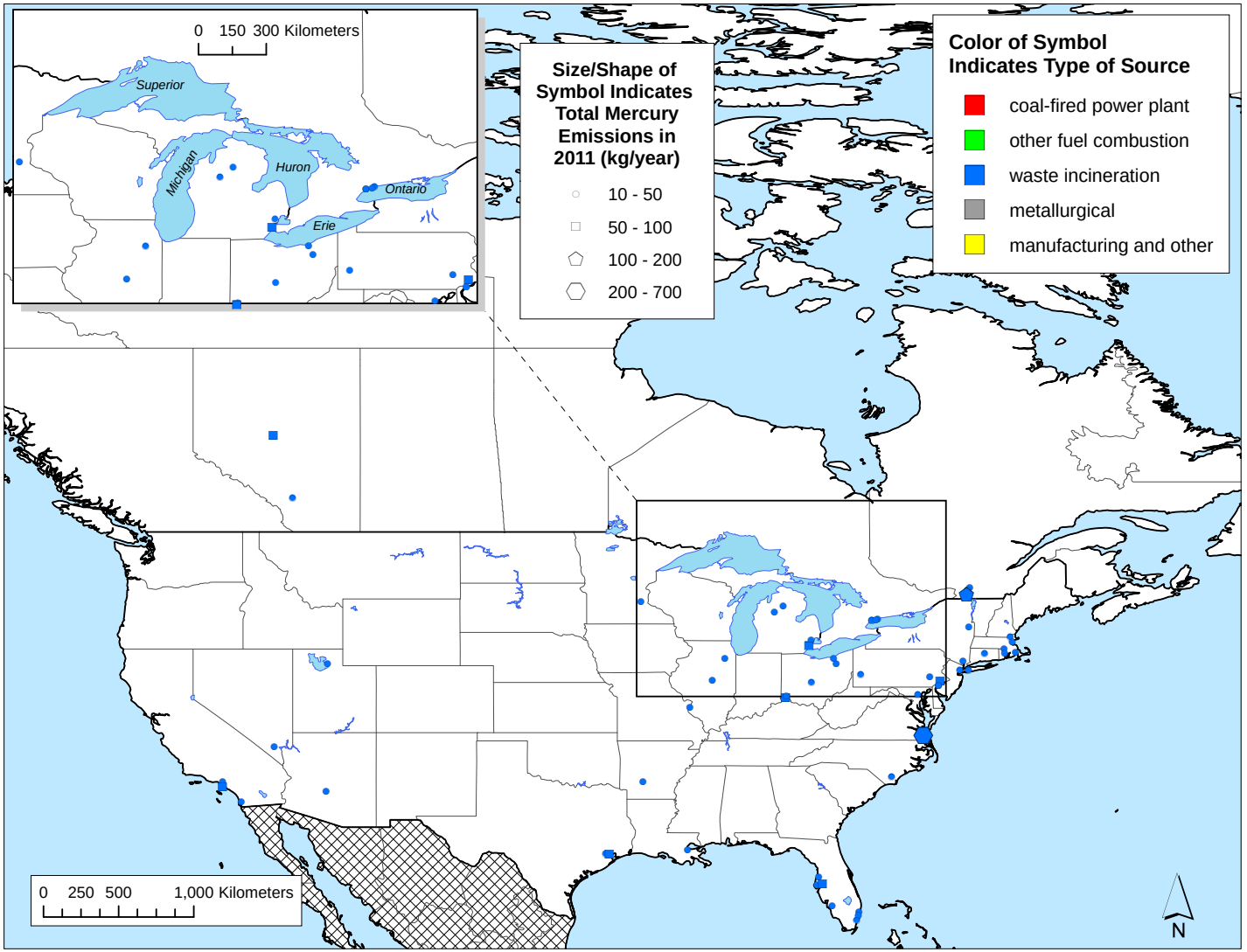

Figure 20. Direct U.S. and Canadian anthropogenic mercury emissions (2011) from large point and area sources associated with waste incineration, including incineration of municipal, hazardous, sewage sludge, and medical waste, as well as cremation.

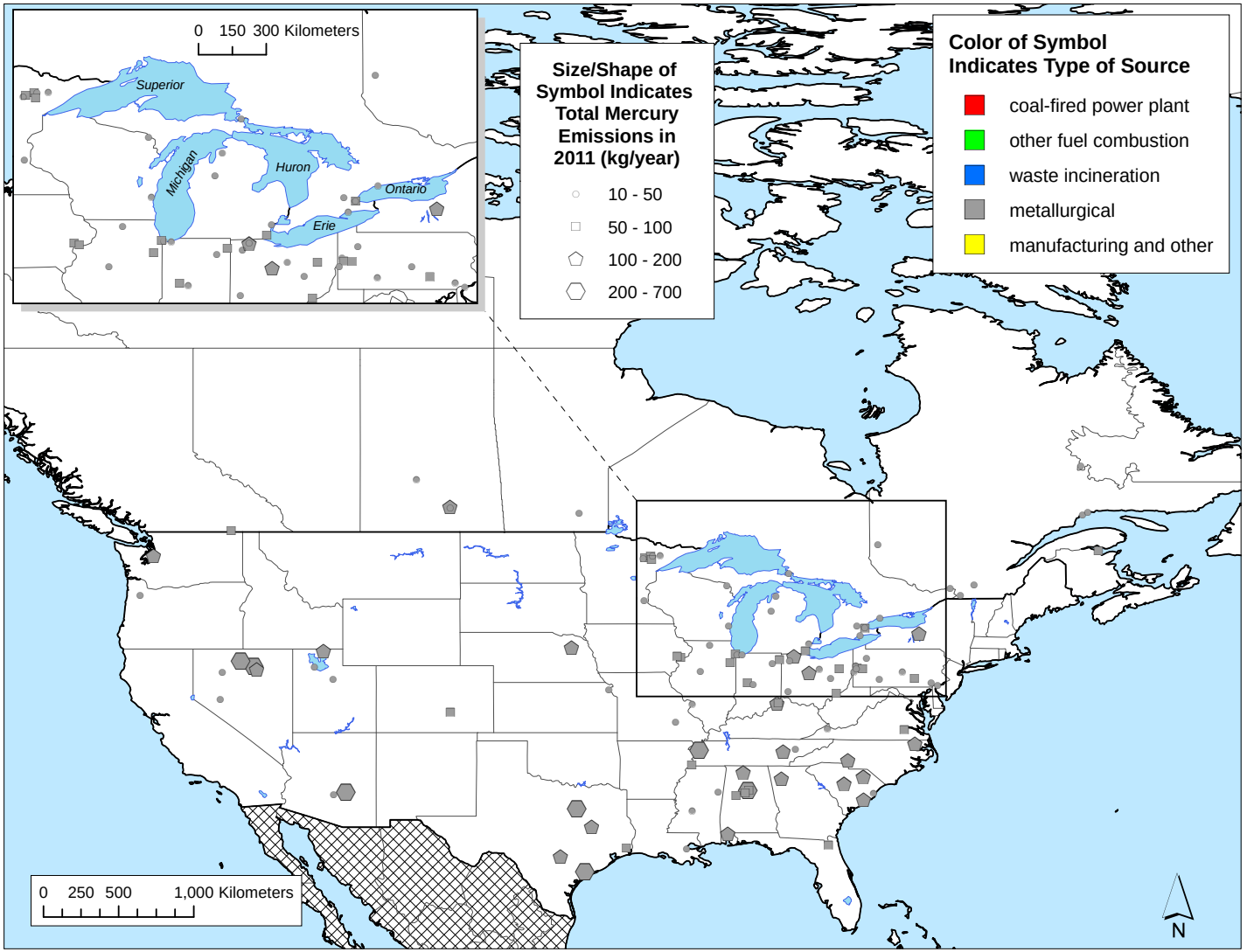

Figure 21. Direct U.S. and Canadian anthropogenic mercury emissions (2011) from point and area sources associated with mining, smelting and other metallurgical processes.

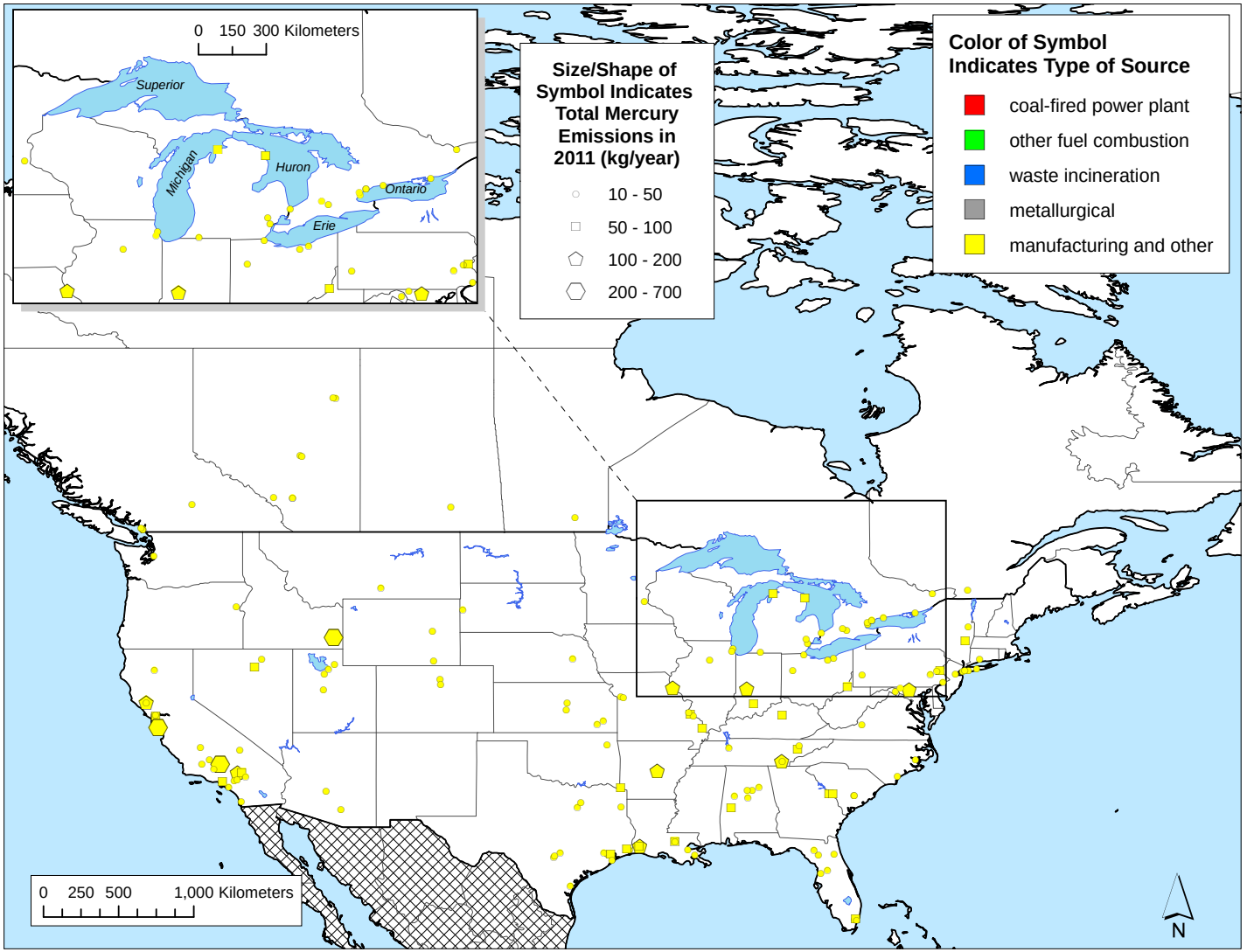

Figure 22. Direct U.S. and Canadian anthropogenic mercury emissions (2011) from large point and area sources associated with manufacturing, as well as all other source categories not included in Figure 18 through Figure 21.

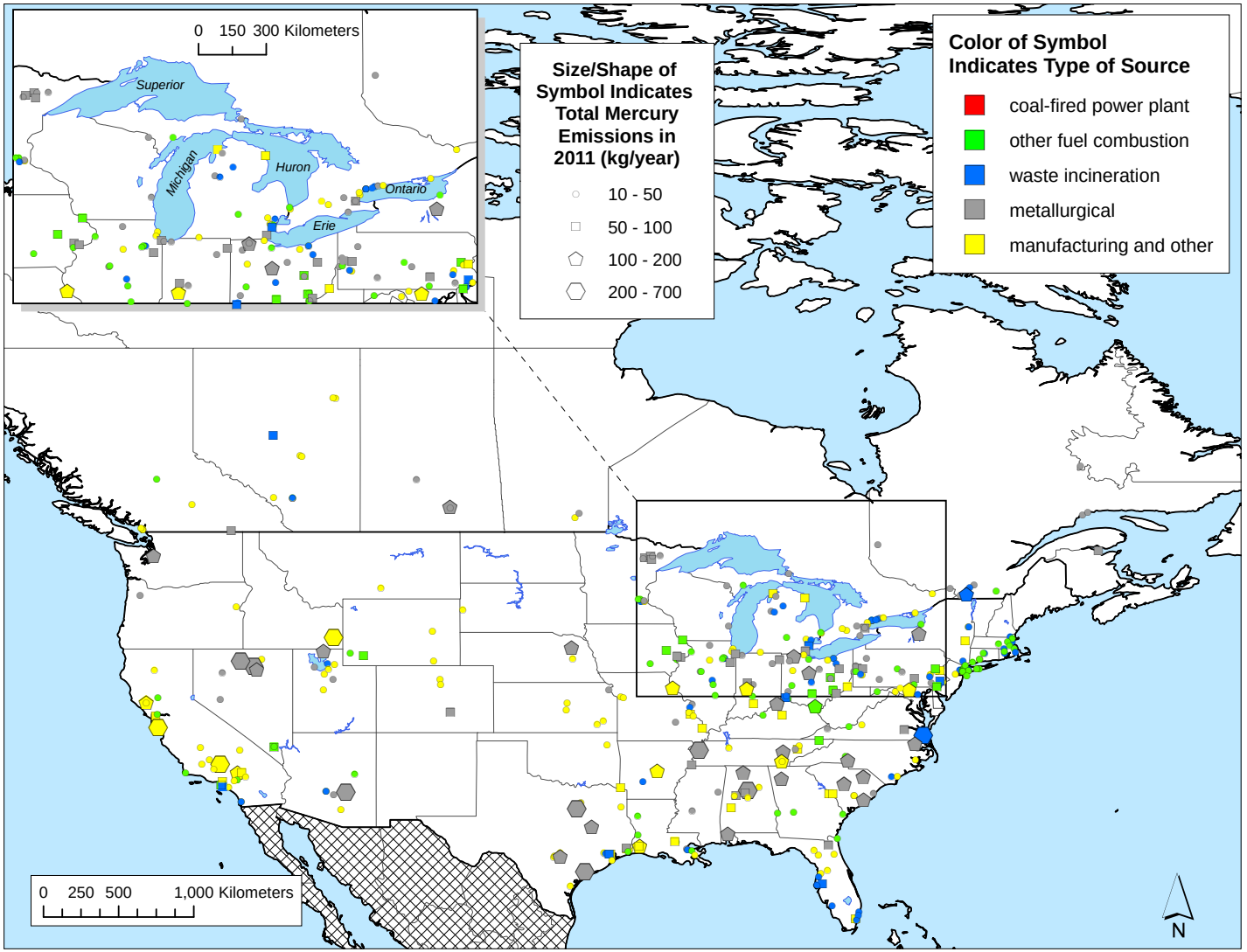

Figure 23. Direct U.S. and Canadian anthropogenic mercury emissions (2011) from all large point and area sources except for coal-fired power generation facilities.

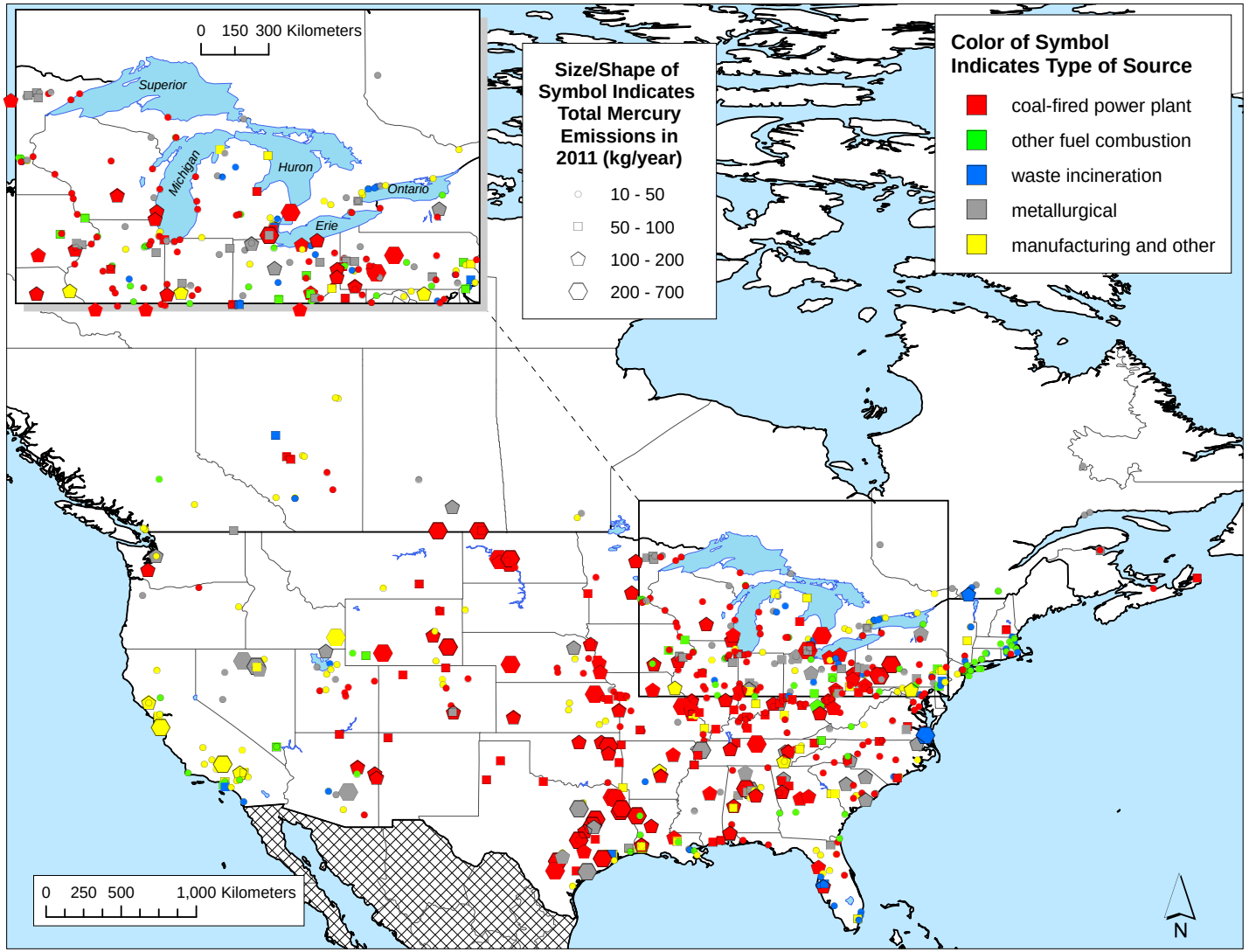

Figure 24. Direct U.S. and Canadian anthropogenic mercury emissions (2011) from all large point and area sources.

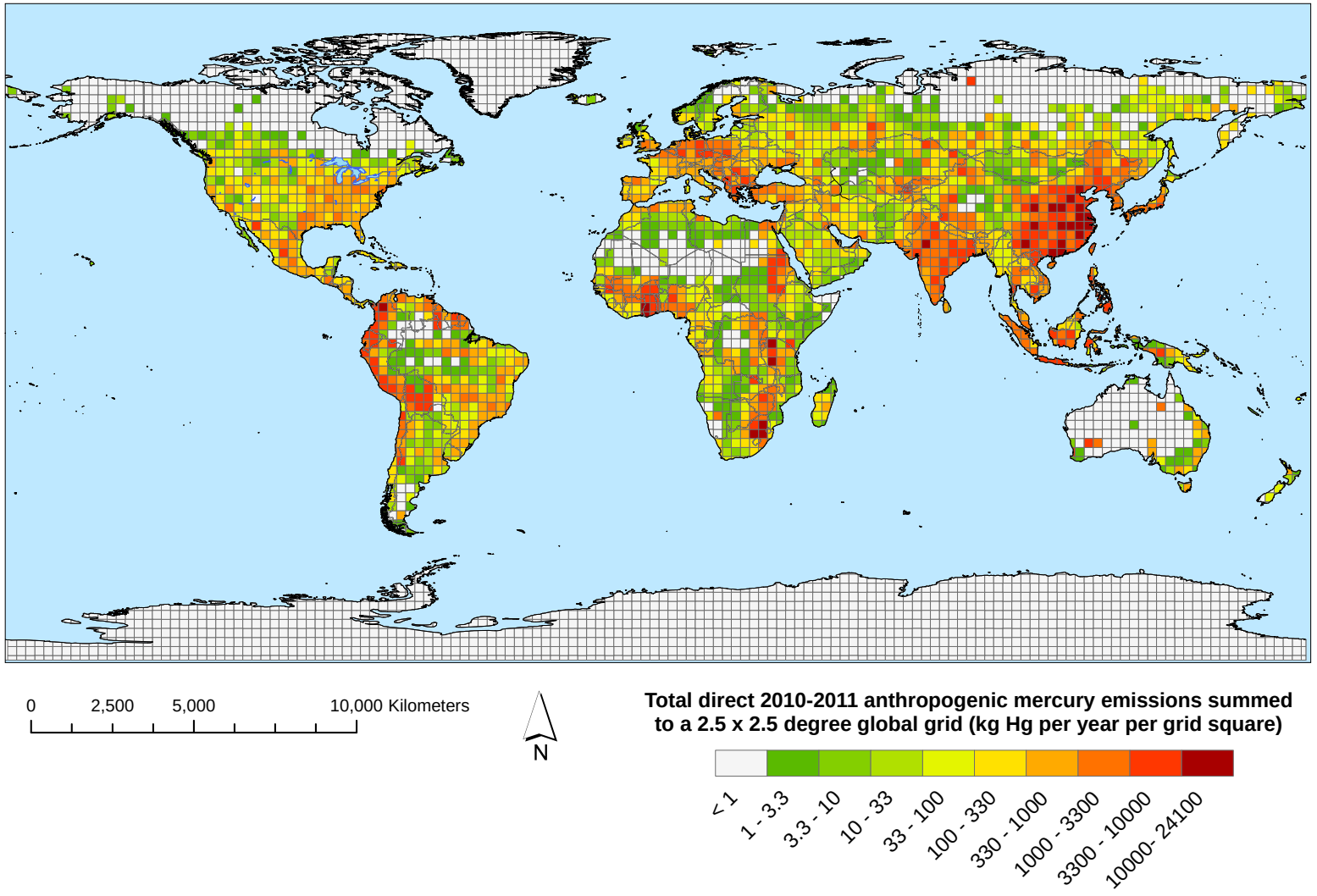

Figure 25. Direct anthropogenic mercury emissions (2010-2011) aggregated onto a 2.5 x 2.5 degree grid.

Global mercury emissions from biomass burning was assumed to be 300 Mg/yr, consistent with the200-400 Mg/yr values used in some other recent modeling analyses – e.g., (Holmes, Jacob et al. 2010, Kikuchi, Ikemoto et al. 2013, Chen, Wang et al. 2014, Song, Selin et al. 2015). Global mercury emissions from geogenic processes were assumed to be 500 Mg/yr as used by Lei et al. (2013, 2014), Kikuchi et al. (2013) , Holmes et al. (2010), and Selin et al. (2008).

Emissions from terrestrial and oceanic surfaces are comprised of re-emissions of previously deposited anthropogenic emissions and "natural" emissions. Natural emissions are those that would occur without any anthropogenic intervention. There are significant uncertainties in quantifying these processes (Agnan, Le Dantec et al. 2016, Zhu, Lin et al. 2016, Zhang, Lyman et al. 2017). For terrestrial and oceanic surfaces, the exchange of Hg(0) is bidirectional. Upward (emissions) flux is occurring at the same time as downward (deposition) flux, resulting in a net emissions or deposition, depending on the relative magnitude of the two competing processes. Studies have shown that the net direction of the transfer can change, depending on numerous factors, including, for example, meteorological parameters such as temperature, wind speed, and relative humidity (Bash and Miller 2009, Hartman, Weisberg et al. 2009, Edwards and Howard 2013, Sommar, Zhu et al. 2013, Wang, Lin et al. 2014, Wright and Zhang 2015).

As noted above, a significant fraction of the net emissions from oceanic and terrestrial surfaces are re-emissions of previously deposited mercury that initially came from anthropogenic emissions. It is difficult to quantify source-attribution information for these re-emissions, i.e., where they came from originally. However, a recent modeling analysis has estimated source-receptor relationships for previously deposited mercury contributing to oceanic and terrestrial reservoirs (Chen, Zhang et al. 2018). Results from this work suggest that North American sources have contributed the largest fraction of mercury to the global oceanic and terrestrial environment, compared to other source regions. While direct anthropogenic emissions from Asia have exceeded those from North America since the 1970's, cumulative Asian source contributions to the global ocean and terrestrial environment have not yet exceeded those from North American sources.

In HYSPLIT-Hg model simulations, emissions are specified as the *gross*, or *one-way*, upward flux, as opposed to the *net*, or bidirectional, upward flux. The *downward* component of the surface exchange is estimated as the simulation proceeds via run-time deposition modeling. Global, annual *one-way* mercury *emissions* from soil/vegetation were taken to be 900 Mg/yr, similar to many other studies: e.g., 1100 Mg/yr was used by Selin et al (2008), 890 Mg/yr was used in the base simulation of Kikuchi et al. (2013), and an optimized emissions of 860 Mg/yr was recently estimated by Song et al. (2015).

Prompt re-emissions of deposited Hg(II) were assumed to be 30% of the total Hg(II) deposition to terrestrial surfaces. In this analysis, prompt re-emissions amounted to 344 Mg/yr, consistent with the 260 – 600 Mg/yr range used in other modeling studies [e.g., (Selin, Jacob et al. 2008, Holmes, Jacob et al. 2010, Kikuchi, Ikemoto et al. 2013, Song, Selin et al. 2015)]. Taken together, the one-way Hg(0) emissions from soil/vegetation and prompt re-emissions totaled ~1250 Mg/yr. As described below in the results section, gross, one-way dry deposition flux of Hg(0) to land surfaces was modeled to be 680 Mg/yr; thus, the net Hg(0) emissions from land surfaces in the model was ~560 Mg/yr. This total is

consistent with a recent empirically-based global estimate of 607 Mg/yr, although it is noted that a large uncertainty range was associated with this recent estimate (-513 – 1653 Mg/yr) (Agnan, Le Dantec et al. 2016). The global, annual, gross (one-way) mercury emissions from the ocean were taken to be 4000 Mg/yr. As described below, the gross, one-way deposition flux of Hg(0) to the ocean's surface was estimated to be 1520 Mg/yr. Thus, the net Hg(0) emissions flux from the ocean surface in this modeling analysis was ~2500 Mg/yr, very similar to the bottom-up estimate of 2700 Mg/yr developed from flux measurements (Pirrone, Cinnirella et al. 2010), and consistent with the range of 2000 – 3600 Mg/yr used in numerous other modeling analyses (Selin, Jacob et al. 2008, Holmes, Jacob et al. 2010, Corbitt, Jacob et al. 2011, Amos, Jacob et al. 2012, Kikuchi, Ikemoto et al. 2013, Chen, Wang et al. 2014, Song, Selin et al. 2015).

The spatial and temporal (monthly) variations for the biomass-burning, geogenic processes, soil/vegetation, ocean, and prompt-reemission inventory components were adapted from the results of the Lei et al. (2014) analysis. The total emissions used in this analysis, using the net exchange of Hg(0) from surfaces, was ~5700 Mg/yr. In Figure 26, the emissions utilized in this study are compared with those used in several other analyses (Shia, Seigneur et al. 1999, Bergan and Rodhe 2001, Mason and Sheu 2002, Selin, Jacob et al. 2007, Selin, Jacob et al. 2008, Holmes, Jacob et al. 2010, Pirrone, Cinnirella et al. 2010, Corbitt, Jacob et al. 2011, Kikuchi, Ikemoto et al. 2013, Lei, Liang et al. 2013, Chen, Wang et al. 2014, Song, Selin et al. 2015). An overall map of total, global mercury emissions used in this modeling is shown in Figure 27.

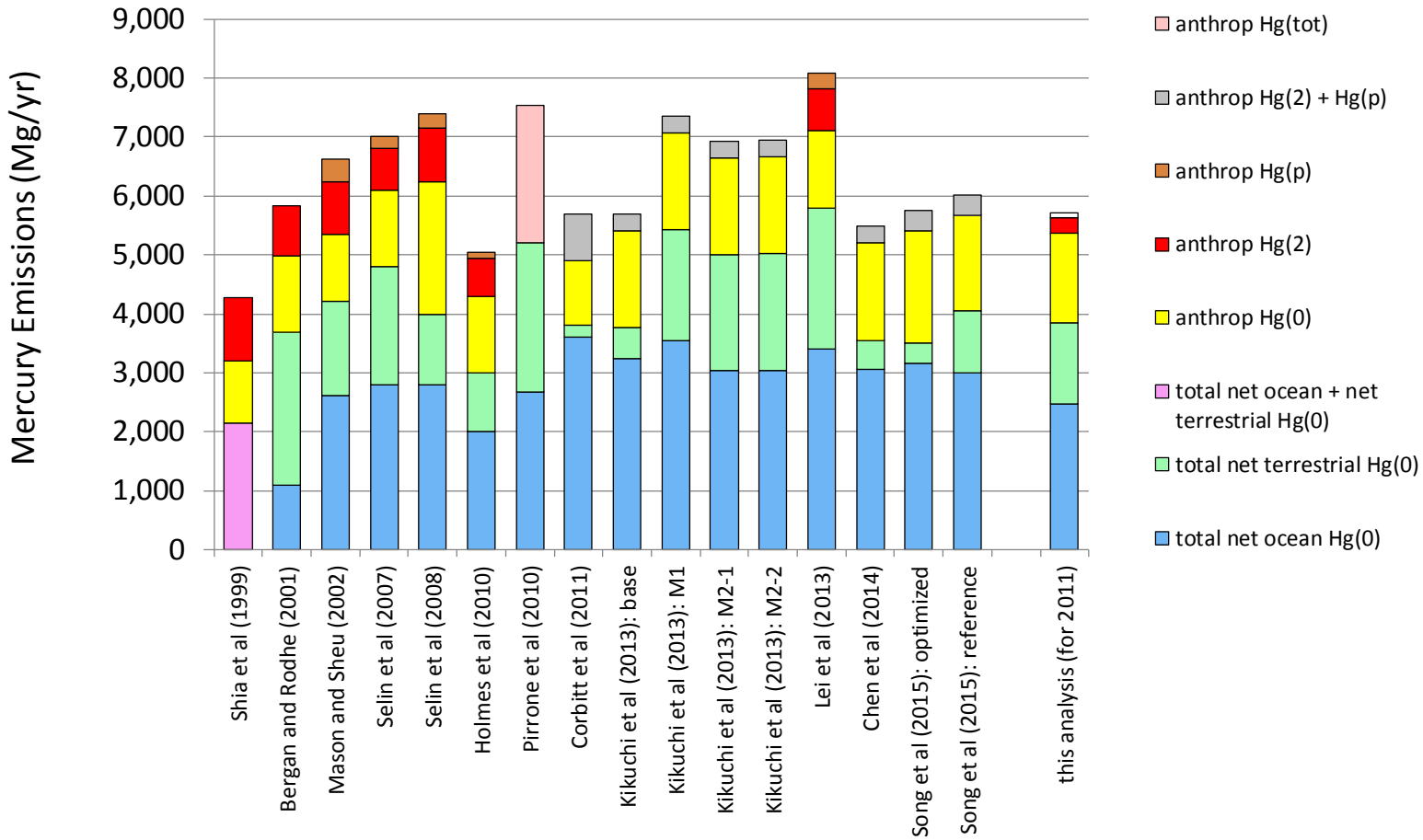

Figure 26. Comparison of mercury emissions used in this analysis with those used in other studies. For each study, the net ocean and net terrestrial emissions are combined with the antrhopogenic emissions to show the total emissions used in the analysis. In the Kikuchi et al study (2013), several variations were presented in addition to the base case: M1 (with a new soil-emissions parameterization); M2-1 (with O3 as an atmospheric oxidant); M2-2 (same as M2-1 but with a different treatment of polar emissions).

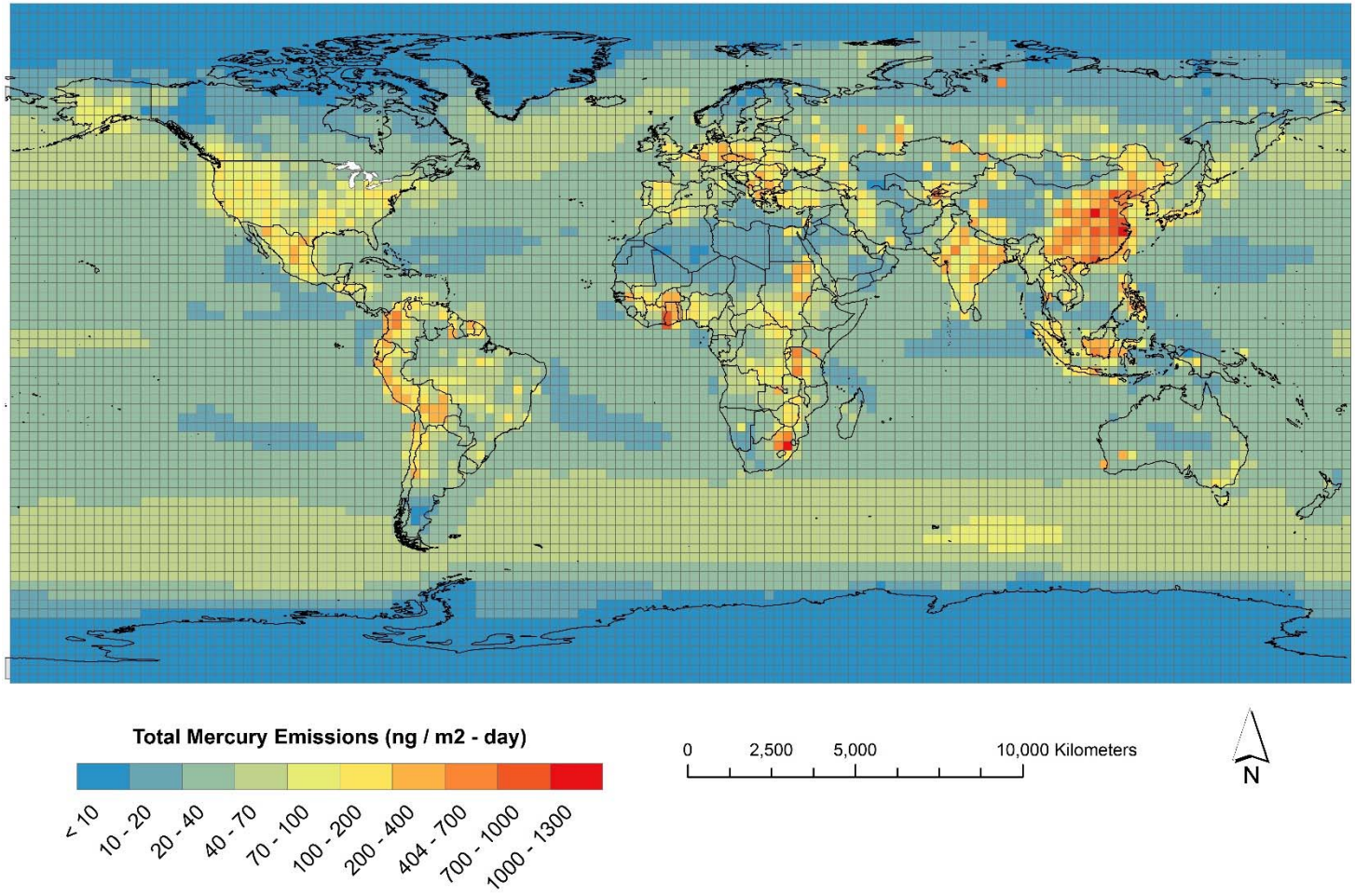

Figure 27. Atmospheric mercury emissions from all source categories. Annual total emissions of all forms of mercury (Hg(0), Hg(II), and Hg(p)) on the 2.5° x 2.5° global grid used in this modeling. Emissions shown in this map are gross "one-way" emissions used as input to the HYSPLIT-Hg model, as opposed to net emissions, and include contributions from anthropogenic, biomass burning, soil/vegetation, re-emissions, oceanic, and geogenic sources. For anthropogenic emissions, the 2010 AMAP/UNEP inventory was used for all countries other than the U.S. and Canada. For the U.S., the 2011 National Emissions Inventory was used, as described in the text. For Canada, data from Environment and Climate Change Canada were used, as described in the text.

3. Simulation Methodologies

3.1. Introduction

The sources, transport, and fate of atmospheric mercury encompass a wide array of phenomena, some of which are relatively poorly understood (Driscoll, Mason et al. 2013, Ariya, Amyot et al. 2015). In addition to HYSPLIT-Hg, there are numerous other fate and transport models that attempt to synthesize knowledge about these phenomena to create a comprehensive simulation of atmospheric mercury (Table 3).

Table 3. Atmospheric Mercury Fate and Transport Models

Model	Example References
CAM-Chem/Hg	(Lei, Liang et al. 2013, Lei, Wuebbles et al. 2014)
CMAQ	(Bullock and Brehme 2002, Holloway, Voigt et al. 2012, Lin, Shetty et al. 2012, Bash, Carlton et al. 2014, Bieser, De Simone et al. 2014, Grant, Kim et al. 2014)
CTM-Hg	(Seigneur, Vijayaraghavan et al. 2004, Lohman, Seigneur et al. 2008, Seigneur and Lohman 2008)
ECHMERIT	(Jung, Hedgecock et al. 2009, De Simone, Gencarelli et al. 2014)
GEOS-Chem	(Holmes, Jacob et al. 2010, Amos, Jacob et al. 2012, Zhang, Jaegle et al. 2012, Cheng, Zhang et al. 2013, Kikuchi, Ikemoto et al. 2013, Chen, Wang et al. 2014, Song, Selin et al. 2015)
GRAHM	(Dastoor and Larocque 2004, Durnford, Dastoor et al. 2010, Kos, Ryzhkov et al. 2013)
HYSPLIT-Hg	(Cohen, Artz et al. 2004, Cohen, Artz et al. 2007, Cohen 2016)
MSCE-Hg-Hem	(Travnikov 2005)
STEM-Hg	(Pan, Carmichael et al. 2008, Pan, Lin et al. 2010)

While there are similarities between the models, there are often differences in the emissions, atmospheric chemistry, phase partitioning, meteorological data, transport, dispersion, and deposition algorithms and parameterizations (Ryaboshapko, Bullock et al. 2007, Ryaboshapko, Bullock et al. 2007, Bullock, Atkinson et al. 2008, AMAP/UNEP 2013, Ariya, Amyot et al. 2015, Bieser, Slemr et al. 2017).

3.2. The HYSPLIT-Hg Model

The HYSPLIT atmospheric transport model has been developed since the early 1980's (Draxler and Taylor 1982) by Roland Draxler and colleagues at the NOAA Air Resources Laboratory (Draxler and Hess 1997, Draxler and Hess 1998, Stein, Draxler et al. 2015).

In this study, we have used the *HYPSLIT-Hg* model, a version of the HYSPLIT model with special features (e.g., atmospheric mercury chemistry, dynamic phase partitioning) added to simulate atmospheric mercury. Initially, HYSPLIT-Hg (and HYSPLIT) used only a Lagrangian modeling scheme and was used to estimate the atmospheric transport and deposition of mercury to the Great Lakes from anthropogenic sources in the U.S. and Canada (Cohen, Artz et al. 2004, Cohen, Artz et al. 2007) and throughout a European domain in a model intercomparison experiment (Ryaboshapko, Bullock et al. 2007, Ryaboshapko, Bullock et al. 2007). A global Eulerian capability (Draxler 2007) was recently incorporated into HYSPLIT (Draxler 2007, Stein, Draxler et al. 2015, Cohen, Draxler et al. 2016). With this addition, HYSPLIT can be run in a Lagrangian mode, an Eulerian mode, or combination of the two. In the combined mode, emitted pollutants are initially simulated in a Lagrangian fashion. After a user-specified pollutant age (i.e., time after emission), pollutants are transferred to a global Eulerian grid and simulated with an Eulerian methodology from then on. The mercury-related algorithms in HYSPLIT-Hg were subsequently incorporated into this enhanced multi-mode version of HYSPLIT to create the integrated Lagrangian-Eulerian atmospheric mercury model used in this study.

Several model improvements were implemented in this work, including the following:

- Rates of the most significant chemical reactions are now temperature dependent. These changes are described below in Section 3.5.
- The estimation of the liquid water content of the atmosphere has been improved (now, no liquid water is formed when the temperature is below freezing).
- The HYSPLIT-Hg model has been parallelized, allowing execution using more than one CPU. This will allow us to carry out simulations faster, if desired, although, fewer simulations would be able to be carried out at one time, as the total number of CPU's available to this project is constant. Nevertheless, for testing and in some other situations, it will be helpful to be able to run a complete 6 year simulation (2006-2011) faster than the ~3 weeks required if a single CPU is used.
- A new Git-based repository has been established for the HYSPLIT-Hg model to make version control and collaboration more efficient.

3.3. Dispersion Methodologies

Several different dispersion modeling approaches ("run schemes") were used in this work. These are described below and summarized in Table 4. Run-Scheme 00 represented the work carried out for the FY14-funded GLRI project, while Run-Schemes 01-04 represented work carried out for the FY15-funded GLRI project.

3.3.0. Run Scheme 00 (Eulerian Only)

Directly analogous to the approach used in Cohen et al. (2016) and the FY13-funded GLRI project (Cohen 2016) – except now for the year 2011, rather than 2005 – this approach used only a global Eulerian simulation methodology on a 2.5^o x 2.5^o grid for all emissions sectors: direct anthropogenic, biomass, land/vegetation, oceanic, prompt-reemissions, and geogenic. In this scheme, the elemental mercury emissions from global emissions from all non-anthropogenic sectors were simulated (a total of 5 simulations), and separate runs for direct anthropogenic Hg(0), Hg(II), and Hg(p) emissions were made for the U.S., Canada, Mexico, China, Russia, India, and Other (i.e., all other countries). Thus, a total of 3 x 7 = 21 anthropogenic-only simulations were carried out. And thus, a total of 5 + 21 = 26 global Eulerian simulations were carried out.

Each simulation took the equivalent of ~18 CPU-days, and so, these simulations required a total of 26 x 18 = 468 CPU-days or 1.3 CPU-years. Note that the simulations were carried out on a Linux workstation with the equivalent of 96 virtual CPU's. While all 96 CPU's were rarely used at one time – e.g., to leave computing capacity for other tasks – a significant fraction were generally used. As an illustrative example, if 75% of the virtual CPU's were used (i.e., 72 virtual CPU's), then these simulations would have required 468 / 72 = 6.5 days. This run scheme corresponded to the work associated with the FY14-funded GLRI project, i.e., to update the FY13-funded 2005 analysis to 2011.

3.3.1. Run Scheme 01

In this scheme and each of the following schemes, all of the emissions sectors except direct anthropogenic emissions, i.e., biomass, land/vegetation, re-emissions, oceanic, and geogenic, were simulated using the same global Eulerian simulation on a 2.5^o x 2.5^o grid used in Run Scheme 00 ("RS-00"). *The only differences in this scheme and the following schemes lie in the methodology used to estimate the fate/transport of the direct anthropogenic emissions*.

Here, in RS-01, direct anthropogenic emissions were simulated using a spatial and chemical interpolation procedure based on a set of unit source simulations from standard source locations (SSL's). A total of 111 SSL's were used, including 32 "global" locations (Figure 28) and 79 North American locations (Figure 29). Simulations of unit emissions of Hg(0), Hg(II), and Hg(p) were carried out for each of these 111 locations, as described below.

In this scheme – and in all the following schemes – unit-emissions simulations of Hg(0), Hg(II), and Hg(p) were carried out from each of the 32 global SSL's with a Global Eulerian Model (GEM) methodology, using 2.5^o x 2.5^o NCEP/NCAR global reanalysis meteorological data and a corresponding 2.5^o x 2.5^o Eulerian grid. A 3-year spin-up period was used for these GEM simulations, i.e., to produce results for 2011, the model run was started in 2008. A 60-minute time step was used.

In this scheme, unit-emissions simulations of Hg(0), Hg(II), and Hg(p) were carried out from each of the 79 North American locations with a Lagrangian Puff (PUF) methodology, using 2.5^o x 2.5^o NCEP/NCAR

meteorological data. In these 237 PUF simulations (3 emit species x 79 SSL's), a maximum of 20,000 PUF's were allowed at any one time, horizontal and/or vertical puff-splitting was allowed to occur once every 24 hours, and 3 grams of the appropriate mercury form were emitted once every 3 hours (equivalent to 1 g hr^{-1}).

Table 4. Summary of Simulation Methodologies Used

<table>
<tr><th></th><th>simulation of emissions from ocean, land, re-emissions, biomass, geogenic</th><th>simulation of global anthropogenic emissions, other than from the U.S. and Canada</th><th>simulation of anthropogenic emissions from the U.S. and Canada of Hg(0) and Hg(II)</th><th>simulation of anthropogenic emissions from the U.S. and Canada of Hg(p)</th><th>total number of CPU-years required for simulations</th></tr>
<tr><td>Run-Scheme 00</td><td rowspan="5">global Eulerian simulation on a 2.5°x2.5° grid using NCEP/NCAR 2.5°x2.5° meteorological data with a 5 year spin-up period

5 sectors x 18 days/run = 90 CPU-days</td><td colspan="3">global Eulerian simulation on a 2.5°x2.5° grid using NCEP/NCAR 2.5°x2.5° meteorological data with a 5 year spin-up period
3 species * 7 regions * 18 days/run = 368 CPU-days</td><td>1.3</td></tr>
<tr><td>Run-Scheme 01</td><td rowspan="4">interpolation using 32 standard sources modeled with a global Eulerian simulation on a 2.5°x2.5° grid using NCEP/NCAR 2.5°x2.5° meteorological data with a 36 month spin-up period

3 species x 32 standard sources * 12 days/run = 1152 CPU-days</td><td colspan="2">interpolation using 79 standard source locations modeled using Lagrangian Puff methodology using NCEP/NCAR 2.5°x2.5° meteorological data with a 3 month spin-up period

3 species * 79 standard sources * 0.75 day/run = 178 CPU-days</td><td>3.9</td></tr>
<tr><td>Run-Scheme 02</td><td colspan="2">interpolation using 79 standard source locations modeled using Lagrangian Puff methodology using NCEP's NARR 32km meteorological data with a 3 month spin-up period

3 species * 79 standard sources * 1 day/run = 237 CPU-days</td><td>4.1</td></tr>
<tr><td>Run-Scheme 03</td><td>interpolation using 79 standard source locations modeled using combined Lagrangian Puff and Eulerian methodology using NCEP/NCAR 2.5°x2.5° meteorological data with a 36 month spin-up period

2 species * 79 standard sources * 13.5 days/run = 2133 CPU days</td><td>interpolation using 79 standard source locations modeled using Lagrangian Puff methodology using NCEP/NCAR 2.5°x2.5° meteorological data with a 3 month spin-up period

1 species * 79 standard sources * 0.75 day/run = 59 CPU-days</td><td>9.4</td></tr>
<tr><td>Run-Scheme 04</td><td>interpolation using 79 standard source locations modeled using combined Lagrangian Puff and Eulerian methodology using NCEP's NARR 32km and NCEP/NCAR 2.5°x2.5° meteorological data with a 36 month spin-up period

2 species * 79 standard sources * 15 days/run = 2370 CPU-days</td><td>interpolation using 79 standard source locations modeled using Lagrangian Puff methodology using NCEP's NARR 32km meteorological data with a 3 month spin-up period

1 species * 79 standard sources * 1 day/run = 79 CPU-days</td><td>10.1</td></tr>
</table>

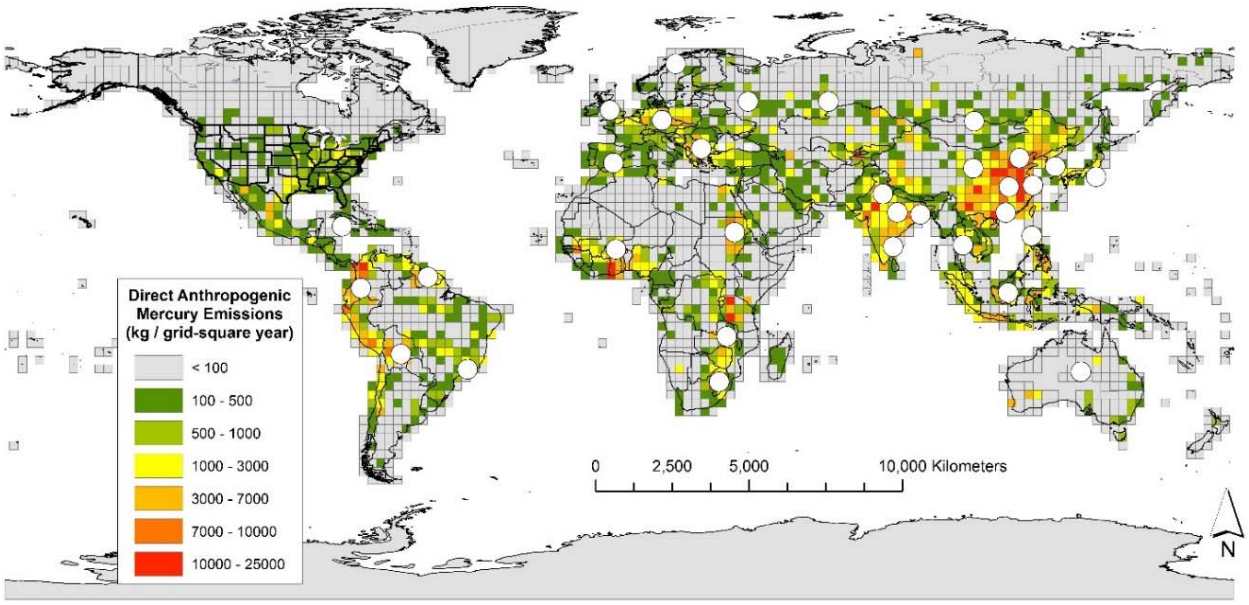

Figure 28. Global standard source locations (n=32) and direct anthropogenic emissions aggregated on a 2.5° x 2.5° grid. Emissions totals in this map are expressed in units of kg per grid square per year. Simulations from these 32 source locations were carried out with a Global Eulerian Model (GEM) methodology, as described in the text.

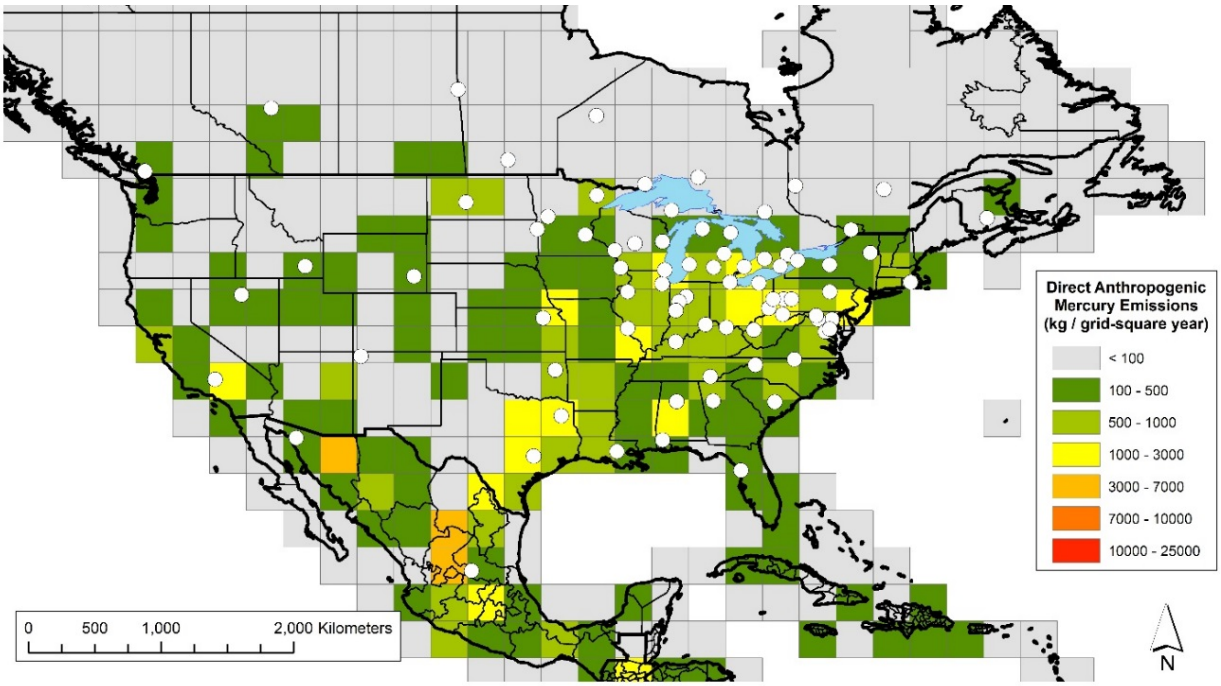

Figure 29. North American standard source locations (n=79) and direct anthropogenic emissions aggregated on a 2.5 x 2.5 grid. Emissions totals in this map are expressed in units of kg per grid square per year. Simulations from these 79 source locations were carried out with PUF and/or COM methodologies, as described in the text.

In each of the 96 GEM and 237 PUF simulations carried out for RS-01, concentrations and deposition at selected monitoring locations were tabulated – e.g., Mercury Deposition Network (MDN) and Atmospheric Mercury Network (AMNet) sites – as well as deposition to selected area receptors (e.g., each of the Great Lakes and their watersheds). In these 237 PUF SSL simulations, a spin-up period of 3 months was used, i.e., the simulations were started Oct 1, 2010 in order to produce results for 2011. A time step of 60 minutes was used.

The deposition and concentration impacts of each source in the emissions inventories used were then estimated using a spatial and chemical interpolation procedure. In the spatial interpolation process (Figure 30), a weighted average of the impacts simulated from the 3 closest Standard Source Locations (SSL's) was calculated. The weighting was done using the distance from the actual source to the respective SSL, and the relative orientation of the actual source and each SSL to the receptor. The orientation weighting was included to factor in upwind / downwind situations. For example, consider a situation where an actual source was generally upwind of a given receptor. In this case, if a particular SSL was relatively close to the actual source, but was generally downwind of the receptor, then this SSL would be given a lower weight, all things being equal, than an SSL generally upwind of the receptor.

For each of the three closest SSL's to any given actual source, a relative weight (w_i) for the results for each SSL was calculated from the following:

$$w_i = \left[\left(\frac{R_i}{R_{max}}\right)^r + \Delta\theta_i{}^a\right]^{-1} \quad (1)$$

where

R_i = the distance from SSL_i to the actual source

R_{max} = the maximum distance of the 3 closest SSL's to the actual source

r = the *distance* exponent used (default exponent = 2.0)

$\Delta\theta_i$ = the difference between the angular orientation of SSL_i to the receptor and the angular orientation of the actual source to the receptor

a = the *angular* exponent used (default exponent = 2.0)

The actual weight A_i for the source-receptor results for each of the 3 closest SSL's was then calculated from:

$$A_i = \frac{w_i}{\sum_{i=1}^{3} w_i} \quad (2)$$

In carrying out this spatial interpolation procedure, all SSL results were made available for any particular source in the emissions inventories being used. However, since the three closest SSL's to essentially any source in the U.S. and Canada were one of the 79 North American (NA) SSL's, it can be said that the U.S. and Canadian sources were simulated using these 79 NA SSL's. In the same way, essentially all of the global emissions sources were simulated using the 32 global SSL's.

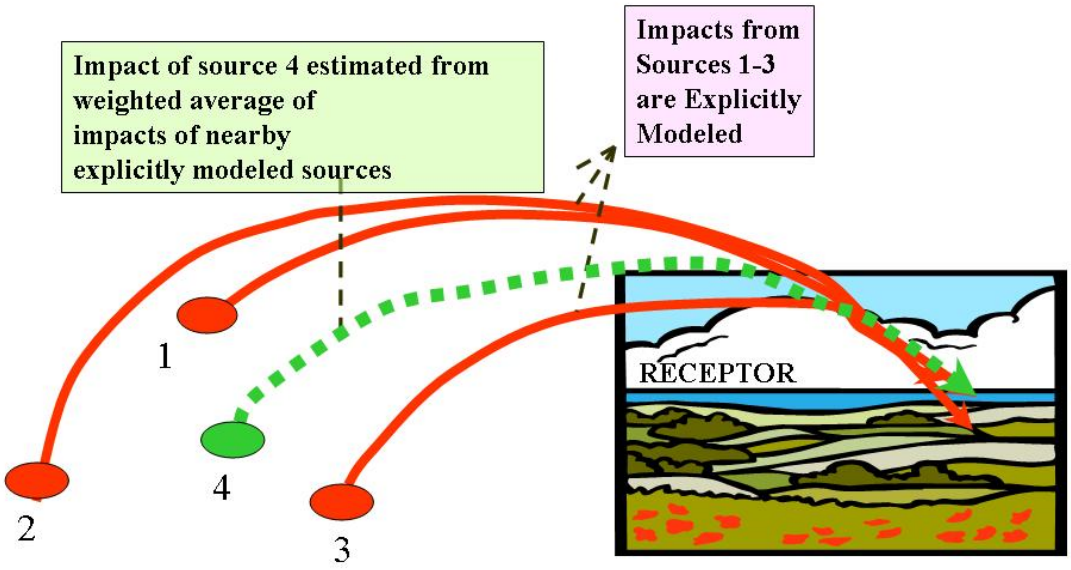

Figure 30. Conceptual diagram of the spatial interpolation procedure used.

In the chemical interpolation calculation, the unit emissions results were spatially interpolated using the approach outlined immediately above and then the single-mercury-form unit emissions results were multiplied by the actual emissions of each form of mercury from the source (illustrated in Figure 31).

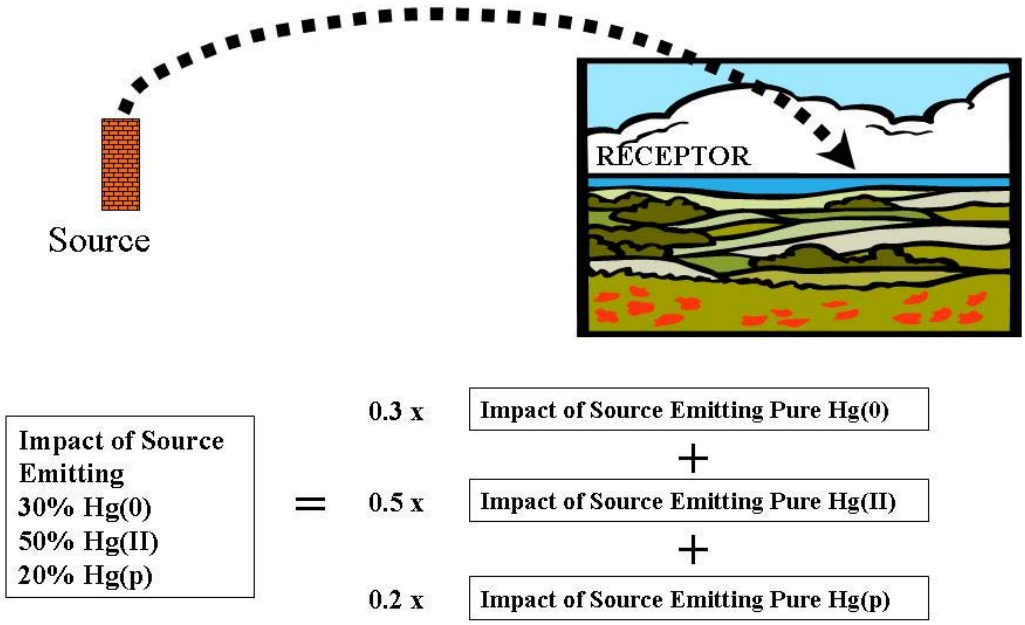

Figure 31. Conceptual diagram of the chemical interpolation procedure used, showing an illustrative example for a source emitting a particular fraction of Hg(0), Hg(II), and Hg(p).

Numerical experiments were carried out to investigate the influence of the choice of interpolation parameters used in the above equations, i.e., the number of closest SSL's used and the exponents on the distance and angular orientation weighting factors. It was found that the choice of these parameters has only a minor effect on the estimated deposition contributions of emissions sources on receptors (See Appendix, Section 7.4, page 179).

A key source of uncertainty in the interpolation-based estimates is the relative number of Standard Source Locations available for use in the calculation. However, this uncertainty has varying degrees of significance, depending on the spatial arrangement of sources, monitoring sites, and receptors.

Typically, modeling analyses are evaluated by comparing their predictions with measurements at monitoring sites. We will present such an evaluation analysis in Section 4 below. However, the primary goal of this project is to create accurate estimates of the amount and source attribution for mercury deposition to the Great Lakes – *not* to produce deposition estimates at monitoring sites in the region.

It is more difficult – and computationally intensive – to accurately predict deposition at a single monitoring site (or a set of such sites) than it is to predict deposition for large area receptors such as the Great Lakes. Consider Figure 32, a conceptual diagram in which we show a *hypothetical* situation with a receptor of interest, a monitoring site, and several (8) mercury emissions sources in the vicinity of the monitoring site. For reference, a hypothetical prevailing wind direction, distance scale, and map orientation are also shown.

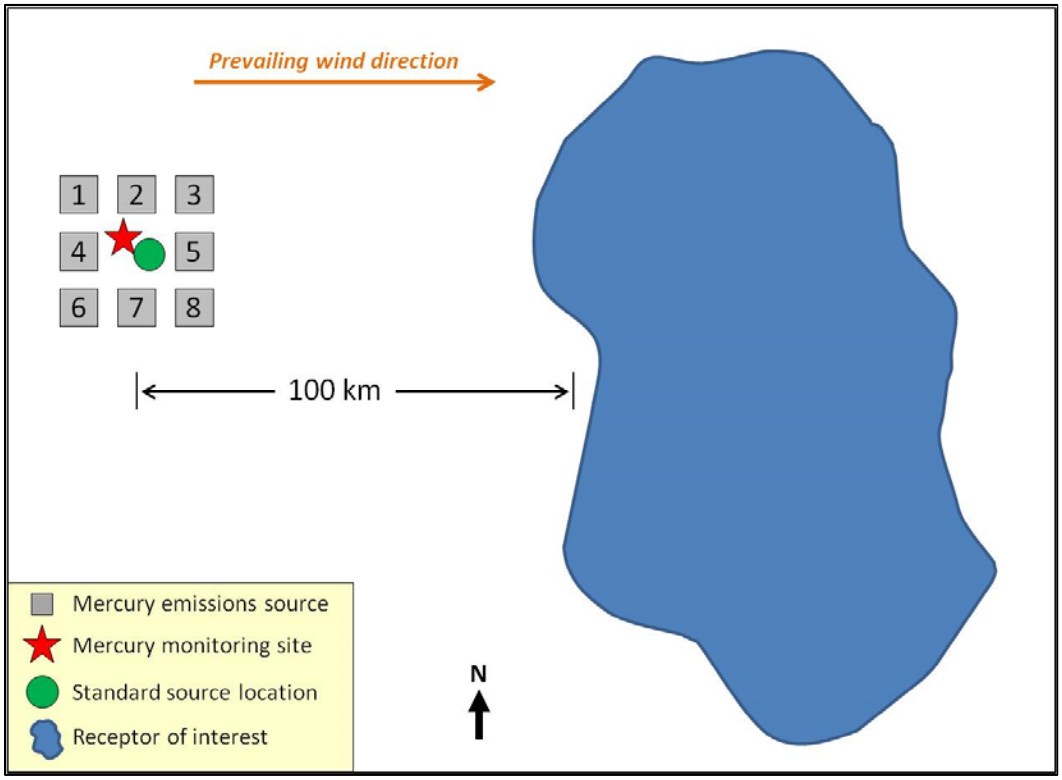

Figure 32. Conceptual Diagram of Sources, Monitoring Sites, and Receptors

Since the winds do not always blow in the "prevailing" direction, all of the sources will have some impacts on the monitoring site. However, even if each of the sources were identical, they would likely have dramatically different impacts on the monitoring site, given their different spatial orientation to the site. For example, given the prevailing wind direction, source #4 would be expected to have a relatively large impact on the site, but source #5 would be expected to have a relatively small impact on the monitoring site. The consequence is that to estimate the wet deposition or atmospheric concentrations of mercury at the monitoring site – arising simply from the sources in the vicinity of the site alone – standard sources would most likely have to be located *at each of the eight sources shown*.

However, to accurately estimate the impacts of the 8 sources on the receptor of interest, about 100 km away in this hypothetical example, a single standard source location located near the "center" of the source group would likely suffice. In other words, to estimate the concentration or deposition at the monitoring site in this simple example, 8 standard source locations would be needed – corresponding to 24 different computer simulations, one for each of the three forms of mercury emitted – whereas only 1 location (3 simulations) would be needed to estimate the deposition impact of the sources on the receptor of interest.

Because of computational resource constraints, and given the overarching goals of this project, we have prioritized the estimation of deposition to the Great Lakes – large area receptors – rather than focus on "point" monitoring sites in the region. Substantially more standard source locations than the 111 utilized would be needed to generate the same accuracy for monitoring site estimates as were generated for the Great Lakes in this analysis. Notwithstanding all of the above, as will be shown in Section 4 below, this modeling analysis produced results at monitoring sites in the Great Lakes region that were encouragingly – and perhaps even surprisingly – close to the measurements made at these sites given the sparse distribution of SSL's relative to the density of actual mercury emissions sources.

3.3.2. Run Scheme 02

The only difference between Run Scheme 02 and Run Scheme 01 (above) is that the 237 PUF simulations done for the 79 North American SSL's were carried out using the 32-km resolution North American Regional Reanalysis (NARR) meteorological data. If a particular Lagrangian puff went beyond the NARR domain, it was simulated using the 2.5^{o} x 2.5^{o} NCEP/NCAR Global Reanalysis meteorological data.

3.3.3. Run Scheme 03

The only difference between Run Scheme 03 and Run Scheme 01 (above) is that the Hg(0) and Hg(II) simulations done for the 79 North American SSL's were carried out using a combined Lagrangian-Eulerian modeling methodology. We abbreviate this combined methodology as "COM". In this COM approach, emissions from any given SSL are first modeled as Lagrangian puffs, and then, after a user-defined puff age – here, an age of 3 weeks was used – the Lagrangian puff mass was transferred to an Eulerian grid. From that point on, that mass was simulated on a global Eulerian grid. These simulations

can be thought of as starting as PUF simulations, but then transitioning to GEM approach. In RS-03, 2.5^{o} x 2.5^{o} NCEP/NCAR Global Reanalysis meteorological data were used to drive the COM simulations. The PUF-only simulation approach was kept for Hg(p), as the lifetime of particles was too short for any global circulation effects to be significant. This was tested, and it was found that there was no measurable difference between COM and PUF simulations for Hg(p) emissions.

3.3.4. Run Scheme 04

Run Scheme 04 is identical to Run Scheme 03 except in the following ways. First, the Hg(0) and Hg(II) simulations done with COM methodology were carried out using the 32-km resolution North American Regional Reanalysis (NARR) meteorological data for puffs within the NARR domain, and the 2.5^{o} x 2.5^{o} NCEP/NCAR Global Reanalysis meteorological data for puffs outside the domain. Second, the Hg(p) simulations were carried out using PUF-only methodology, using the NARR and NCEP/NCAR met data as with the Hg(0) and Hg(II) puffs.

While Run Scheme 04 can be regarded as the most "advanced" dispersion treatment, it must be noted that the number of standard source locations (SSL's) used – particularly the number of North American SSL's (79) – is a limiting factor in the accuracy of the analysis. This limited assemblage of SSL's is believed to be able to provide a reasonable estimate of source-receptor relationships for the Great Lakes, in part because of the increased density of SSL's within the Great Lakes region (e.g., see Figure 29). However, it is unlikely that this limited number of SSL's will be able to accurately capture the source-receptor relationships at each atmospheric monitoring location used for model evaluation. The model results are compared with measurements in this analysis (see Section 4, beginning on page 60), but a close match between model estimates and measurements is not expected. Note also that individual deposition contribution estimates are made in RS-01 through RS-04, but are not made in the Eulerian-only approach (RS-00).

3.4. Mercury Forms Considered in the Model

As described in previous publications (Cohen, Draxler et al. 2011, Cohen, Draxler et al. 2013, Cohen, Draxler et al. 2014, Cohen 2016, Cohen, Draxler et al. 2016), the transport, fate, and intra-conversion of four mercury forms are simulated in HYSPLIT-Hg: elemental mercury [Hg(0)], oxidized, soluble mercury [Hg(II)], particulate-phase insoluble mercury [Hg(p)], and oxidized, soluble mercury reversibly adsorbed to soot [Hg2s]. Partitioning between the vapor and droplet phases is simulated for atmospheric Hg(0) using Henry's Law. For Hg(II), vapor-droplet partitioning is simulated using Henry's Law along with a droplet-phase equilibrium calculation that estimates the ionic and molecular concentrations of relevant mercury-containing species in solution, as described below. Partitioning between dissolved Hg(II) and soot-adsorbed Hg(II) (Hg2s) is estimated using the equilibrium and rate parameters utilized by Bullock and Brehm (2002) based on the measurements of Seigneur *et al*. (1998). Particulate mercury – emitted by sources or formed as the product of chemical reactions – does not partition between phases in the model. However, particulate mercury can be enveloped as part of the insoluble core of deliquesced aerosol particles or rain droplets.

We use the differentiation among non-Hg(0) mercury forms as described above – Hg(II), Hg2s, and Hg(p) – as opposed to the more commonly used classification (GOM (Gaseous Oxidized Mercury) and Hg(p)). The rationale for this choice is that we consider Hg(II) in both the gas, aqueous, and particulate phases (as Hg2s) rather than solely in the gas phase as GOM.

3.5. Chemical Transformations

Gas-phase Hg(0) is converted to Hg(II) and Hg(p) by reaction with O_3, OH•, H_2O_2, HCl, and Cl_2. As summarized by Ariya et al (2015), the product partitioning of Hg(0) oxidation among Hg(II) and Hg(p) forms varies from 0% - 100% among atmospheric Hg models. In the absence of quantitative experimental measurement information, it was assumed in the base-case of this work that 10% of the product of the gas-phase oxidation by O_3, OH•, H_2O_2 is Hg(p) and 90% is Hg(II), while 100% of product of the HCl and Cl_2 oxidation reactions is Hg(II). In the aqueous-phase, Hg(0) is oxidized to Hg(II) by reaction with O_3, OH•, HOCl, and OCl^{-1}, while Hg(II) is reduced to Hg(0) by photolysis of $Hg(OH)_2$ and by transformation of $HgSO_3^{-1}$. The rate and equilibrium parameters used in the base-case model configuration are identical to those used in recent HYSPLIT-Hg analyses (Cohen 2016, Cohen, Draxler et al. 2016) and are summarized in Table 1 and Table 2.

Concentrations of gas-phase and aqueous-phase reactants were estimated with a variety of procedures. For O_3, SO_2, and soot, estimates of atmospheric concentrations from a global simulation using the Mozart2 model were used (Horowitz, Walters et al. 2003, Ryaboshapko, Bullock et al. 2007). For OH•, global model results from Lu and Khalil (1991) were interpolated to create estimated concentrations dependent on latitude, elevation, month, and time of day. For total H_2O_2 and HCl concentrations, a constant typical value equivalent to a gas phase mixing ratio of 1 ppb was used (Graedel and Keene 1995, Finlayson-Pitts and Pitts 2000). For total reactive chlorine, a constant value equivalent to a gas-phase mixing of 100 ppt was used for the lowest 100 m in the atmosphere over the ocean at night, following the approach of Bullock and Brehme (2002), consistent with the findings of Graedel and Keene (1995).

During each model time step within each grid cell, the liquid water content of the atmosphere was estimated based on the local relative humidity, elevation, and temperature. If no liquid water existed, then only gas-phase reactions were utilized (reactions 1-5 in Table 1). If liquid water was present, then a more complex treatment was utilized. First, the gas-liquid and aqueous phase ionic equilibrium conditions were estimated satisfying the relationships shown in Table 2 and mass/ion balances using an iterative Newton-Raphson-based approach. In calculating these equilibrium conditions, a constant pH of 4.5 and a constant Cl^{-1} aqueous phase concentration of 2.5 mg/liter was utilized in the simulation, following the approach of Ryaboshapko et al. (2007).Then, the gas-phase and aqueous-phase reactions and transformation described in Table 1 were carried out.

In earlier analyses with the HYSPLIT-Hg model (Cohen 2016, Cohen, Draxler et al. 2016) it was found that the lifetime of Hg(0) was unrealistically short (~0.3 years) and atmospheric concentrations of Hg(0) were unrealistically low if nominal literature values of the gas-phase Hg(0) oxidation reactions with OH• and

O_3 were used. It was further found that when the oxidation rate constants for these two reactions were provisionally reduced by a factor of 5, realistic atmospheric concentrations of Hg(0) were obtained. We note that in the chemical mechanism used here, the primary oxidants were found to be OH• and O3 in the gas phase; other gas-phase oxidation reactions and aqueous-phase oxidation reactions were much less important. The rates of the OH• and O3 gas-phase reactions are highly uncertain. It has been argued that the rates may be dramatically less than experimentally determined (Calvert and Lindberg 2005, Subir, Ariya et al. 2011, Ariya, Amyot et al. 2015). Therefore, we believe that the 1/5 scaling of these reaction rates used in this and previous work is within the range of uncertainty in the reaction rates for these two reactions.

There is considerable uncertainty in the rates and mechanisms of key oxidation and reduction reactions associated with atmospheric mercury (e.g., Zhang, Lyman et al. 2017). One key area of uncertainty is the relative importance of O_3, OH•, and Br in oxidizing elemental mercury in the atmosphere. With Br-mediated mechanisms, a key area of uncertainty is the concentration of Br in the atmosphere. It has been found that both O_3/OH• and Br chemical oxidation schemes can be relatively successful in reproducing observed atmospheric mercury concentrations. In one example, the GEOS-Chem model was used to investigate speciated atmospheric observations at four high-elevation sites in the Western U.S. (and one in Taiwan) (Weiss-Penzias, Amos et al. 2015). In these case studies, reactive mercury (GOM + PBM) in free-tropospheric air masses appeared to be present primarily from the photo-oxidation of GEM. It was also found that simulation results using an O_3/OH• oxidation scheme were more consistent with observations than results using a Br-based oxidation scheme.

Similar uncertainties exist with the rates and mechanisms of the reduction of oxidized mercury to elemental mercury in the atmosphere. In a recent study, CMAQ was used with a new aqueous-phase oxidized mercury reduction chemical mechanism (involving dicarboxylic acids) and GEOS-Chem boundary conditions, to simulate mercury fate and transport in the U.S. during 2001-2002 (Bash, Carlton et al. 2014). Results for wet deposition with the new chemical mechanism were found to be more consistent with observations than earlier mechanisms used in CMAQ. A new oxidized mercury reduction mechanism was also recently proposed for the GEOS-Chem model (Horowitz, Jacob et al. 2017).

Table 1. Chemical reactions and rate parameters

#	Reaction	Rate	Notes	Units
Gas-phase reactions				
1	$Hg(0) + OH\bullet \rightarrow 0.1\ Hg(p) + 0.9\ Hg(II)$	$3.55E\text{-}14 * e^{(294/T)}$	a,b,c	cm^3/molec-sec
2	$Hg(0) + O_3 \rightarrow 0.1\ Hg(p) + 0.9\ Hg(II)$	$2.1E\text{-}18 * e^{(-1203/T)}$	a,b,d	cm^3/molec-sec
3	$Hg(0) + H_2O_2 \rightarrow 0.1\ Hg(p) + 0.9\ Hg(II)$	8.5E-19	a,e	cm^3/molec-sec
4	$Hg(0) + HCl \rightarrow HgCl_2$	1.0E-19	f	cm^3/molec-sec
5	$Hg(0) + Cl_2 \rightarrow HgCl_2$	4.0E-18	a,g	cm^3/molec-sec
Aqueous-phase reactions and transformations				
6	$Hg(0) + OH\bullet \rightarrow Hg^{+2}$	2.0E+09	h	$(molar\text{-}sec)^{-1}$
7	$Hg(0) + O_3 \rightarrow Hg^{+2}$	4.7E+07	i	$(molar\text{-}sec)^{-1}$
8	$Hg(0) + HOCl \rightarrow Hg^{+2}$	2.09E+06	j	$(molar\text{-}sec)^{-1}$
9	$Hg(0) + OCl^{-1} \rightarrow Hg^{+2}$	1.99E+06	j	$(molar\text{-}sec)^{-1}$
10	$Hg(II) \leftrightarrow Hg2s$	9.00E+02	k	(g Hg2s/g soot)/ g dissolved Hg(II)/liter of water)
11	$HgSO_3^{-1} \rightarrow Hg(0)$	$T * e^{((31.971*T)-12595.0)/T)}$	l	sec^{-1}
12	$Hg(OH)_2 + hv \rightarrow Hg(0)$	6.00E-07	m	sec^{-1}

[a] In the base case, 10% of the product of this reaction assumed to be Hg(p) and 90% Hg(II).

[b] The Hg(0) oxidation rate shown in this table for the base case has been scaled to 20% of its nominal literature value.

[c] (Pal and Ariya 2004)

[d] (Hall 1995)

[e] (Tokos, Hall et al. 1998) (upper limit for rate)

[f] (Seigneur, Wrobel et al. 1994)

[g] (Calhoun and Prestbo 2001), as cited by Bullock and Brehme (2002)

[h] (Lin and Pehkonen 1997)

[i] (Munthe 1992)

[j] (Lin and Pehkonen 1998)

[k] Hg2s is Hg(II) adsorbed to soot, as described in the text. Equilibrium ratio shown coupled with 1st-order time constant (60 minutes) for rate of approach to equilibrium. Follows the approach of Bullock and Brehme (2002), based on experimental results from Seigneur et al. (1998)

[l] (Van Loon, Mader et al. 2000) (temperature T in degrees K)

[m] (Xiao, Munthe et al. 1994, Bullock and Brehme 2002) Rate shown in maximum at peak insolation. Actual rate is scaled according to local ratio of insolation to peak insolation.

Table 2. Gas-liquid partitioning and aqueous phase equilibrium relationships

#	Equilibrium	Equilibrium Constant	Units
Gas-liquid partitioning			
1	$O_3^{(aq)} \leftrightarrow O_3^{(gas)}$	0.0113[a]	molar/atm
2	$H_2O_2^{(aq)} \leftrightarrow H_2O_2^{(gas)}$	7.4E+04[a]	molar/atm
3	$Hg(0)^{(aq)} \leftrightarrow Hg(0)^{(gas)}$	0.11[b]	molar/atm
4	$Cl_2^{(aq)} \leftrightarrow Cl_2^{(gas)}$	0.076	molar/atm
5	$OH\bullet^{(aq)} \leftrightarrow OH\bullet^{(gas)}$	25.0[a]	molar/atm
6	$SO_2^{(aq)} \leftrightarrow SO_2^{(gas)}$	1.23[a]	molar/atm
7	$HgCl_2^{(aq)} \leftrightarrow HgCl_2^{(gas)}$	1.4E+06[c]	molar/atm
8	$Hg(OH)_2^{(aq)} \leftrightarrow Hg(OH)_2^{(gas)}$	1.2E+04[c]	molar/atm
Aqueous-phase equilibrium relationships			
9	$SO2 \leftrightarrow HSO_3^{-1} + H^+$	0.013[a]	molar
10	$HSO_3^{-1} \leftrightarrow SO_3^{-2} + H^+$	6.6E-08[a]	molar
11	$HgCl_2 \leftrightarrow Hg^{+2} + 2\ Cl^-$	1.0E-14	$molar^2$
12	$Hg(OH)_2 \leftrightarrow Hg^{+2} + 2\ OH^-$	1.0E-22	$molar^2$
13	$Hg^{+2} + SO_3^{-2} \leftrightarrow HgSO_3$	5.0E+12	1/molar
14	$HgSO_3 + SO_3^{-2} \leftrightarrow Hg(SO_3)_2^{-2}$	2.5E+11	1/molar

a (Seinfeld and Pandis 1998)

b (Clever, Johnson et al. 1985)

c (Lindqvist and Rodhe 1985)

3.6. Dry and Wet Deposition

Dry deposition of different mercury forms from the first-layer cells to terrestrial surfaces is estimated using a parameterized resistance-based approach (Wesely and Hicks 1977, Wesely 1989). For water surfaces, the approach of Slinn and Slinn (1980) is utilized. Dry deposition of gas-phase and particle/droplet phase mercury is considered.

The overall atmospheric particulate concentration was estimated from the following formula:

$$P = P_0 e^{(-z/k)} \quad (3)$$

where

P = the atmospheric particulate concentration (g m^{-3})

P_0 = base concentration (g m^{-3}) = 39 µg m^{-3}

z = elevation above mean sea level (meters)

k = elevation scale factor = 1000 meters

As a first approximation, a constant back-ground atmospheric particulate surface area of 3.5E-06 cm^2/cm^3 is utilized equal to the "background + local sources" value estimated by Whitby (1978). A typical particle size distribution was chosen based on Whitby (1975), as cited by Prospero et al (1983). The assumed distribution is divided into 14 particle size bins, whose mid-point particle-size diameter ranges from 0.001 – 20 microns. The details of the distribution are summarized in Figure 33. To estimate the mass and mass fraction in each bin, based on the assumed surface area distribution, it was assumed that the particles were spherical with a density of 2 g/cm3. With these assumptions, the mass loading of the entire distribution corresponds to 39 ug/m3 near the surface. Approximately 90% of the mass in the assumed distribution has a diameter of less than 10 um; thus, the PM-10 concentration associated with the assumed distribution is on the order of 35 ug/m3.

When no liquid water was present – i.e., the particles were dry – Hg(0) and Hg(II) were assumed to be entirely in the gas phase, while Hg(p) and Hg2s were assumed to be entirely in the particle phase. In this case, Hg(p) and Hg2s were apportioned to the different particle size bins based on the fraction of the total surface area in each size bin. When liquid water was present, the condensed-phase concentrations of Hg(0), Hg(II), and Hg2s were estimated via thermodynamic calculations as described above. For Hg(0) and Hg(II), the total droplet phase mass was apportioned among the different size ranges based on the estimated volume fraction in each size range. With or without the presence of liquid water, Hg(p) and Hg2s were apportioned among the different size ranges based on the fraction of the total aerosol surface area in each size range.

Wet deposition was estimated based on the vertical location of a given cell relative to the cloud layer during precipitation events. If the cell was above the cloud layer, no wet deposition occurred. If the cell was within the cloud layer, the particle-phase pollutants Hg(p) and Hg2s were wet deposited at a rate governed by an estimated volume-based scavenging ratio *WETR* (grams Hg per m3 of precipitation /

grams Hg per m3 of air). As summarized by Gatz (1976), scavenging ratios for particle-phase pollutants associated with relatively small particle sizes – like Hg(p) – are relative small, with typical values (in these units) less than 100,000. A WETR value of 60,000 was used, identical to that used for particle-phase pollutants in earlier, related HYSPLIT modeling (Cohen, Draxler et al. 2016). In-cloud wet deposition of Hg(0) and Hg(II) was estimated using the precipitation rate and the thermodynamically estimated aqueous-phase concentrations. For cells below a precipitating cloud layer, different approaches were used, depending on the relative humidity and the mercury form. Particle and droplet phase mercury was scavenged using a size-dependent scavenging coefficient estimated for falling drops in the range of 0.04 – 0.4 mm (Seinfeld and Pandis 1986). For each size range, the geometric mean value of the scavenging coefficient estimated for collectors of 0.04 mm and 0.4 mm was used. Gas-phase mercury was scavenged assuming thermodynamic partitioning between the gas-phase and falling droplets.

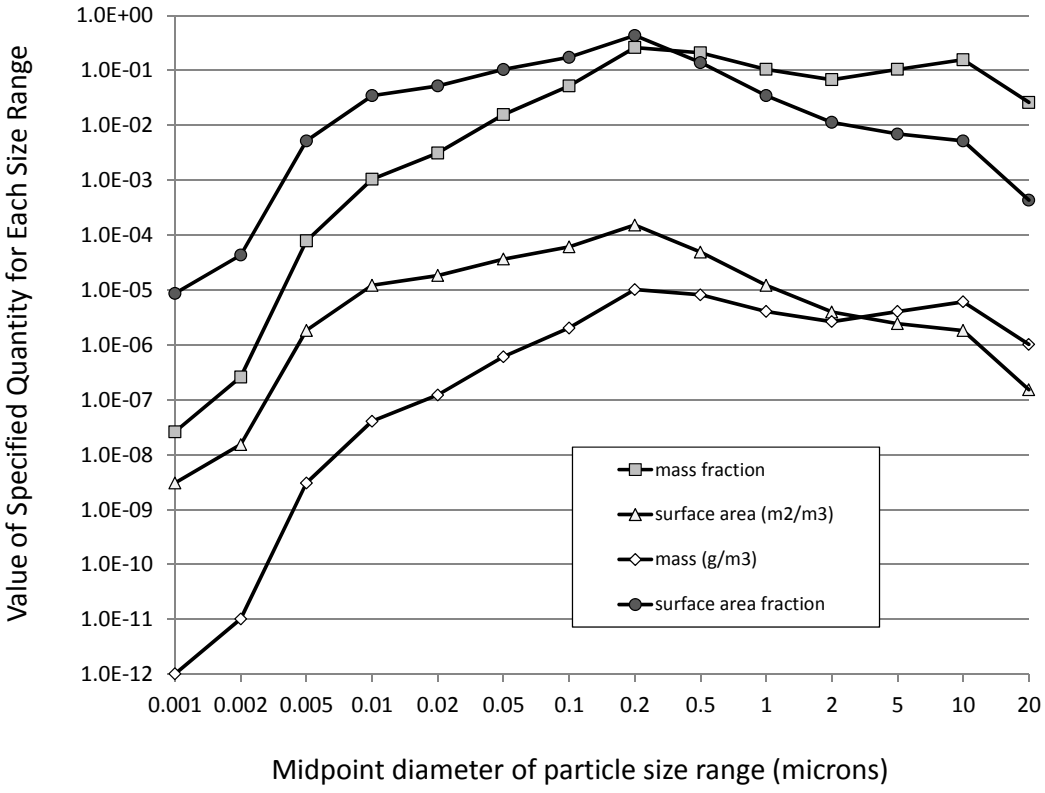

Figure 33. Particle size distribution used in this analysis.

3.7. Meteorological Data

Two different meteorological data sets were used to drive the HYSPLIT-Hg simulations, as described in Section 3.3 above.

- The NCEP/NCAR Global Reanalysis (NCAR/NWS, 1994…; NOAA ARL, 2003…). These data are specified on a 2.5^{o} x 2.5^{o} grid, with a surface layer and 17 vertical levels above the surface, up to a height of ~30 km (10 hPa). The data are specified on the 3-D grid every 6 hours.
- The North American Regional Reanalysis (NARR) (National Centers for Environmental Prediction 2017, NOAA Air Resources Laboratory 2017). These data have been converted to HYSPLIT format and are archived at the NOAA Air Resources Laboratory. The NARR-HYSPLIT data are specified on a 32km grid covering North America and surrounding oceanic regions (see Figure 34) every 3 hours, at the surface and 23 vertical levels up to ~16,000 meters. Scientists at ARL discovered that, unfortunately, the friction velocities specified in the NARR data have been incorrectly set to a minimum, constant, default value. Therefore, to use the NARR data with HYSPLIT (and HYSPLIT-Hg), we removed all of the friction velocity data and let the model estimate dry deposition and other fluxes in alternative ways that did not require friction velocity values. This was deemed preferable to using faulty friction velocity data.

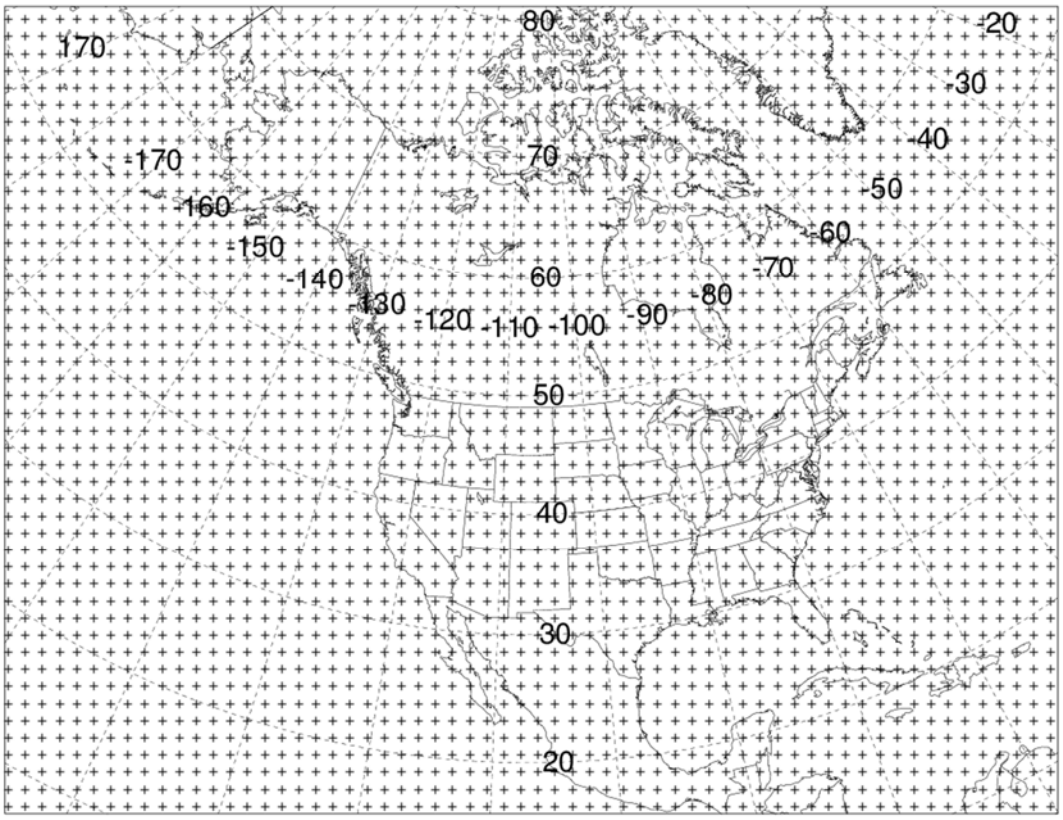

Figure 34. Domain of the North American Regional Reanalysis meteorological data archived in HYSPLIT format at the Air Resources Laboratory. Every 5th grid point is shown.

Precipitation is a key component of the meteorological data, given its importance to wet deposition processes and the importance of mercury wet deposition in the model evaluation process. As discussed below, modeled wet mercury deposition is compared measured deposition at NADP's Mercury Deposition Network (MDN) sites with data for 2011. Therefore, it is obviously important to compare the measured precipitation at these MDN sites with the precipitation in the meteorological data used to drive the HYSPLIT-Hg model.

In carrying out this comparison, it is first noted that there is some uncertainty in the "measured" precipitation at the MDN sites. The precipitation at the sites is generally measured via a rain gauge at the site. However, in some cases, the rain gauge data are not available, and in those cases, the precipitation associated with any sample is estimated based on the sample volume. The annual totals for 2011 for each of the MDN sites with complete 2011 data are compared in Figure 35. It can be seen that for some sites, the total factoring in sample volume (y-axis) is significantly higher than the total using only the available rain gauge data (x-axis), which means that there was a significant amount of missing rain gauge data.

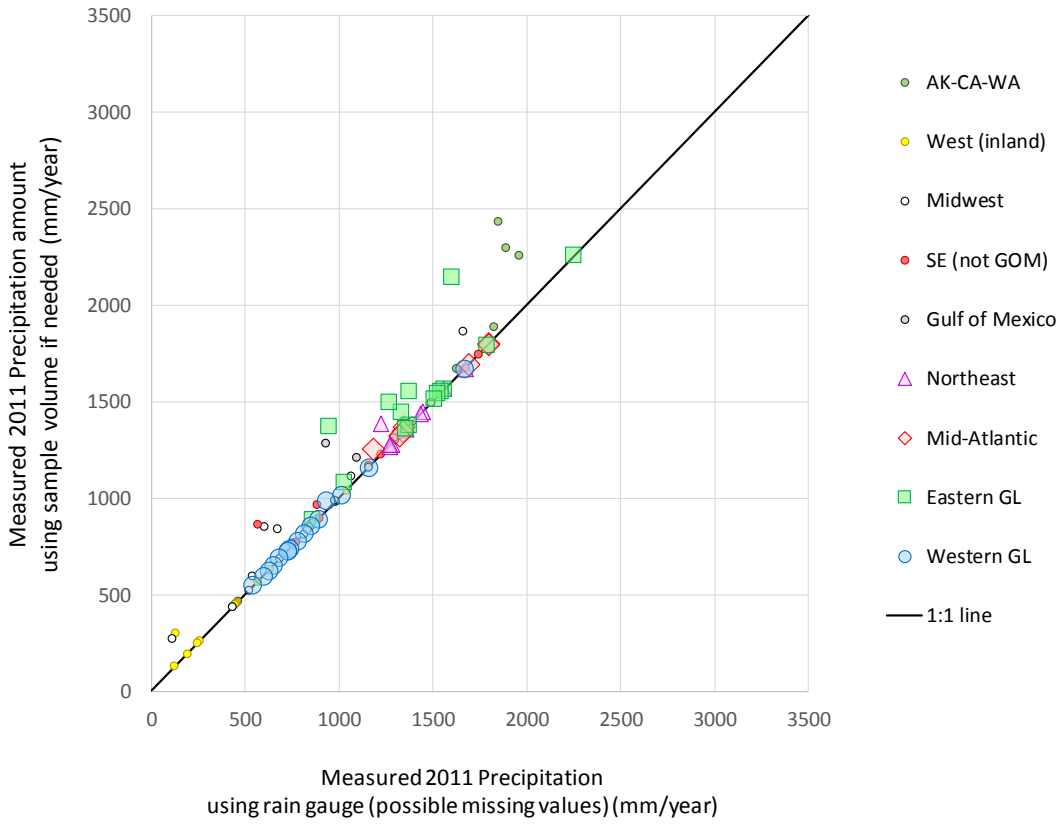

Figure 35. Comparison of 2011 precipitation measured at MDN sites with the site rain gauge (which for some samples was not available) with precipitation estimated with the rain gauge plus precipitation estimated with the sample volume when the rain gauge data were not available.

An overall comparison of NCEP/NCAR Global Reanalysis and North American Regional Reanalysis (NARR) precipitation totals for 2011 with measured precipitation at MDN sites is shown in Figure 36. Additional details of the comparison are shown for MDN sites in the western Great Lakes region is shown in Figure 37, and an analogous plot showing additional comparison details for MDN sites in the eastern Great Lakes region is shown in Figure 38. A variety of linear regressions of the different precipitation datasets are also shown in each of the these plots. It can be seen from these figures that there are differences between the models, and between the models and the measured precipitation amounts of varying degrees at these MDN sites in the Great Lakes region. In general, the NARR data may be slightly closer to the measurements than the Global Reanalysis data [e.g., correlation coefficient r^2 of 0.71 for NARR vs. 0.43 for the Global Reanalysis ("gbl2p5")], but this is not true for all sites. Given the relatively coarse grid of the global data (2.5 degrees, or roughly 250 km), and even the NARR data (32 km), it would not be expected that the modeled and measured precipitation would match perfectly, even if the models were perfect. Therefore, the limited degree of consistency found is not unexpected. Analogous plots for all other MDN sites used in the model evaluation analysis are provided in the Appendix, Section 7.2 (starting on page 166) in Figure 152 through Figure 163.

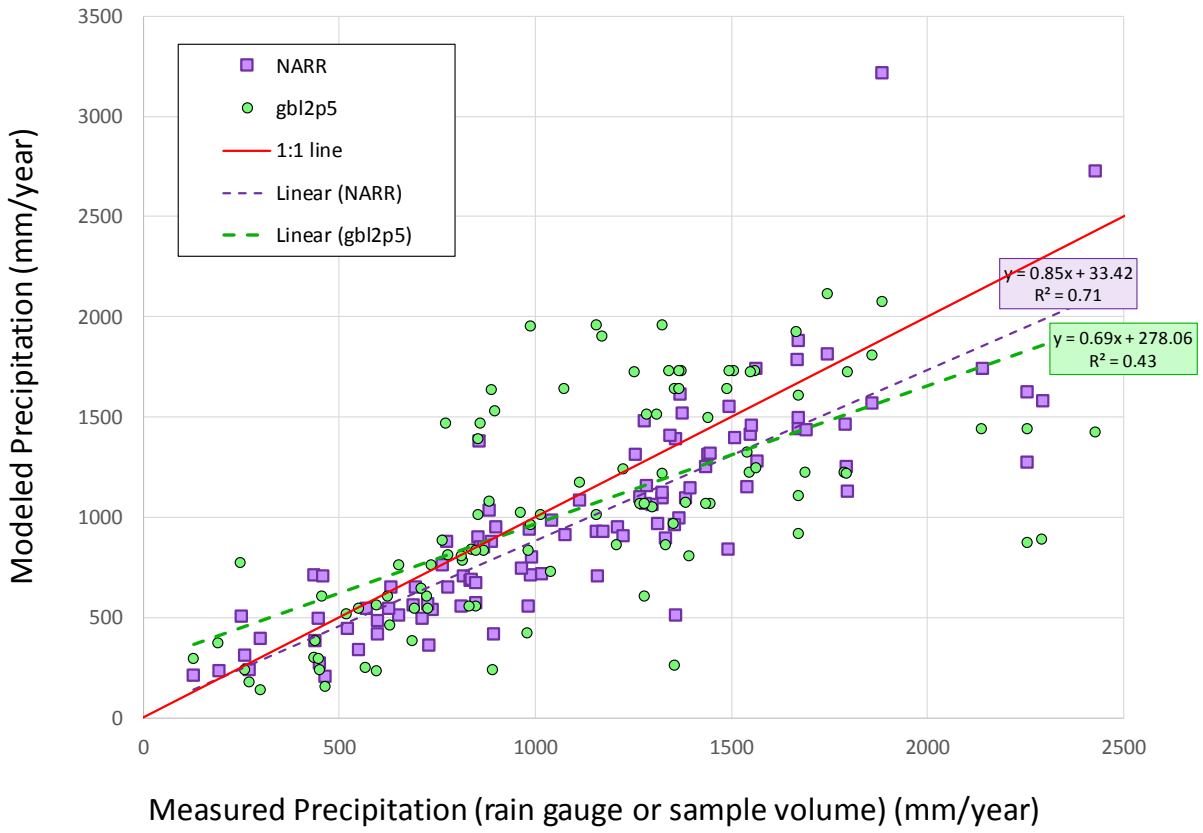

Figure 36. Overall comparison of modeled precipitation with measured precipitation at MDN sites with complete 2011 data.

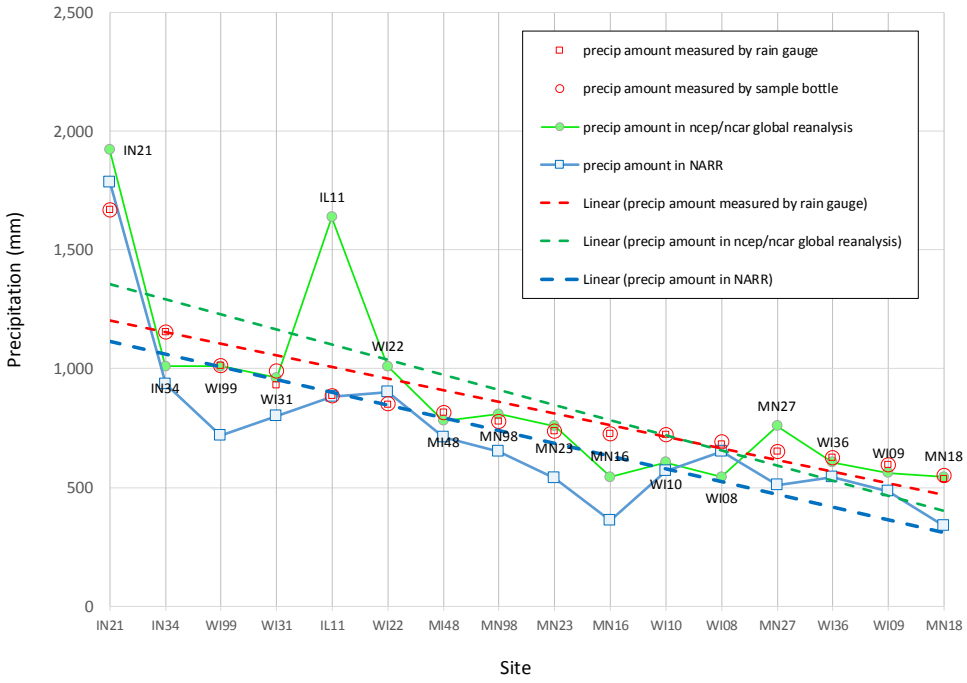

Figure 37. Comparison of NCEP/NCAR Global Reanalysis and North American Regional Reanalysis (NARR) precipitation totals for 2011 with measured precipitation at MDN sites in the western Great Lakes region.

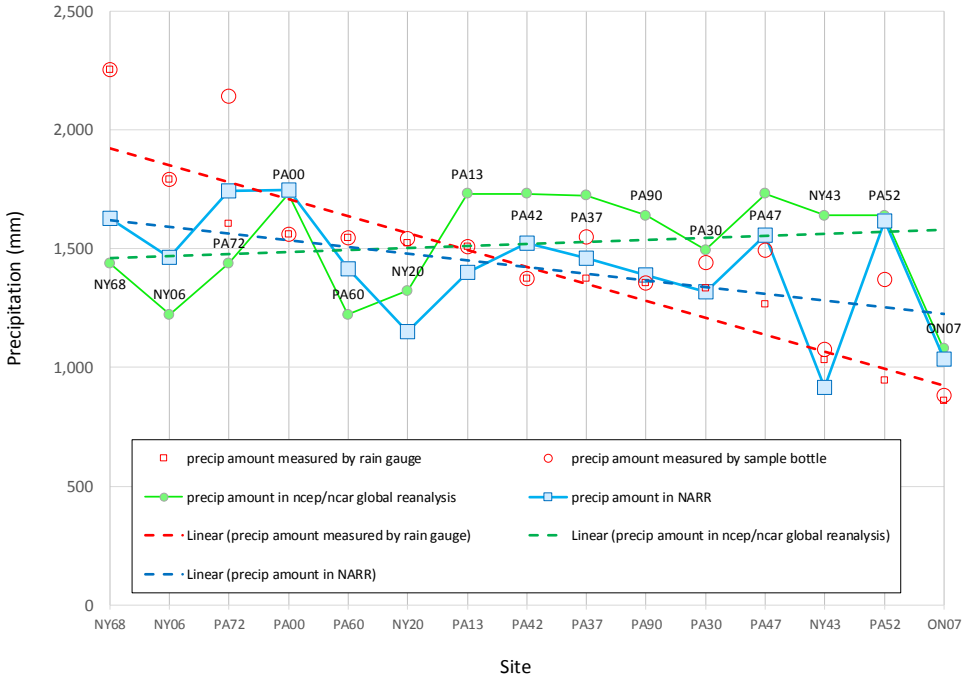

Figure 38. Comparison of NCEP/NCAR Global Reanalysis and North American Regional Reanalysis (NARR) precipitation totals for 2011 with measured precipitation at MDN sites in the eastern Great Lakes region.

3.8. Model Spin-up

Model "spin-up" refers to the length of time the model is run before the "model year" (in this case, 2011, for which results are desired) in order to remove any effects of model initialization from the results. In these HYSPLIT-Hg simulations, no atmospheric mercury initialization was used, i.e., all starting concentrations of mercury in the atmosphere were zero. Therefore, in the spin-up period, the model "fills up" with mercury until there is a relatively steady state.

As discussed in Section 3.3, three different simulation types were used in this analysis: PUF, GEM, and COM. PUF simulations used only Lagrangian puffs; GEM simulations used only a Global Eulerian Model (GEM); and COM simulations used a combination of the two, starting out with Lagrangian puffs and then transferring mass to a Eulerian grid.

For PUF simulations, a spin-up period of just 3 months was used, as a global circulation representation was not being attempted. In reality, a much shorter spin-up period could have been used, but 3 months was chose to be conservatively safe.

For GEM and COM simulations, global circulation is being considered, and much longer spin-up periods are required. At the same time, the computational resources required to carry out the simulations is directly related to the length of the spin-up period, and so one must be careful not to use overly long periods.

First, because the atmospheric lifetime of Hg(p) is on the order of weeks to at most months, a much shorter spin-up time is required for simulations emitting only Hg(p). In this context, it is useful to remember that there are no conversions of Hg(p) to other forms of mercury in the model – e.g., to Hg(0) – which would cause a wider area of impact. Therefore, for Hg(p) GEM and COM simulations, a spin-up time of just 3 months was used.

However, the lifetime of Hg(0) is much longer, and since Hg(II) can be transformed to Hg(0) in the model, emissions of Hg(II) can have a much wider impact than one might think, considering only the limited atmospheric lifetime of Hg(II). To examine this issue, a series of tests were done using 24, 36, 48, and 60 month spin-up periods, for emissions of Hg(II) and Hg(0), from two test locations: Standard Source Location #11 (in northeast Texas, latitude 32.65, longitude -94.88), and Standard Source Location #53 (in China, latitude 30.75, longitude 114.25). For SSL #11 (Texas), COM simulations were carried out. For SSL #53 (China), GEM simulations were carried out. COM simulations were not used for global SSL's as there were no specially-tracked receptors (e.g., like the Great Lakes) being considered outside North America. The results of these simulations are summarized in Figure 39 through Figure 44 below.

It can be seen from Figure 39 that using a 36-month spin-up yields a result within 1% of the 60-month spin-up value for GEM simulations of Hg(0) from the Standard Source Location in China (#53) used for this test.

It can be seen from Figure 40 that using a 24-month spin-up yields a result within 1% of the 60-month spin-up value for GEM simulations of Hg(II) from the Standard Source Location in China (#53) used for this test. A 36-month spin-up yields results within 0.5% of the 60-month value.

It can be seen from Figure 41 that there appears to be more variance in the COM simulations than the GEM simulations. This has been observed before in HYSPLIT-Hg simulations and is caused primarily by the effects of puff splitting. In this process, when puffs grow to a certain size relative to the horizontal and/or vertical spacing of meteorological data grid being used, the puffs split horizontally or vertically. However, if the puff array has already reached the maximum allowable number (in these simulations, 20,000) then puff splitting is suppressed. This introduces a small but what appears to be "random" variation in the modeling results. Nevertheless, it can be seen that there is no apparent advantage of the 48-month vs. 36-month spin-up results; i.e., the 36-month spin-up results are very similar to the 48-month spin-up results for COM simulations of Hg(0) from the Standard Source Location in Texas (#11) used for this test.

A comparable variability can be seen in Figure 42 for results of COM simulations of Hg(II) from the Standard Source Location in Texas (#11). In examining the results, the 36-month spin-up results appear, on average, to be at least as close to the 60-month spin-up results as the 24-month or 48-month tests. In general, the 36-month spin-up results are within 1-2% of the 60-month spin-up results.

Based on all of the above, a 36-month spin-up period was used for all GEM and COM simulations of Hg(0) and Hg(II). For Global Eulerian simulations of oceanic, land/vegetation, biomass, re-emissions, and geogenic sources, a 60-month spin-up was used to be consistent with earlier analyses that carried out analogous simulations for 2005.

For perspective, it can be seen from Figure 43 and Figure 44 that there is really very little difference between the results for any given receptor – e.g., Lake Superior or Lake Erie, in these example figures – when different spin-up values are used. In light of all of the above, the choice of length of spin-up periods used in this analysis appear to be contributing little to the overall uncertainty in the analysis.

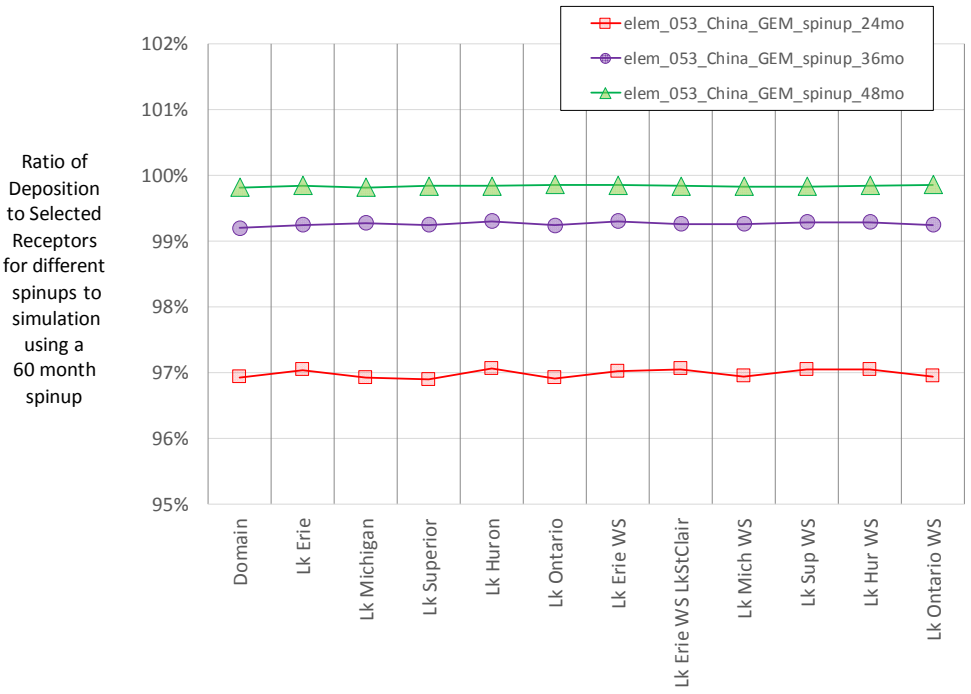

Figure 39. Spin-up test results for Global Eulerian Model (GEM) simulations of Hg(0) emissions from a standard source location in China (#53).

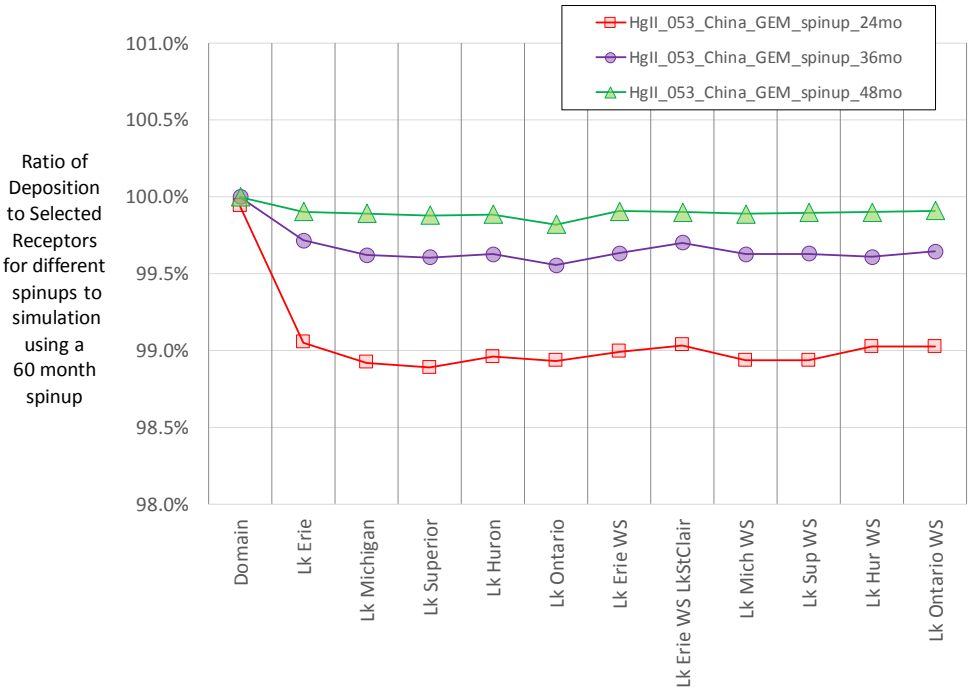

Figure 40. Spin-up test results for Global Eulerian Model (GEM) simulations of Hg(II) emissions from a standard source location in China (#53).

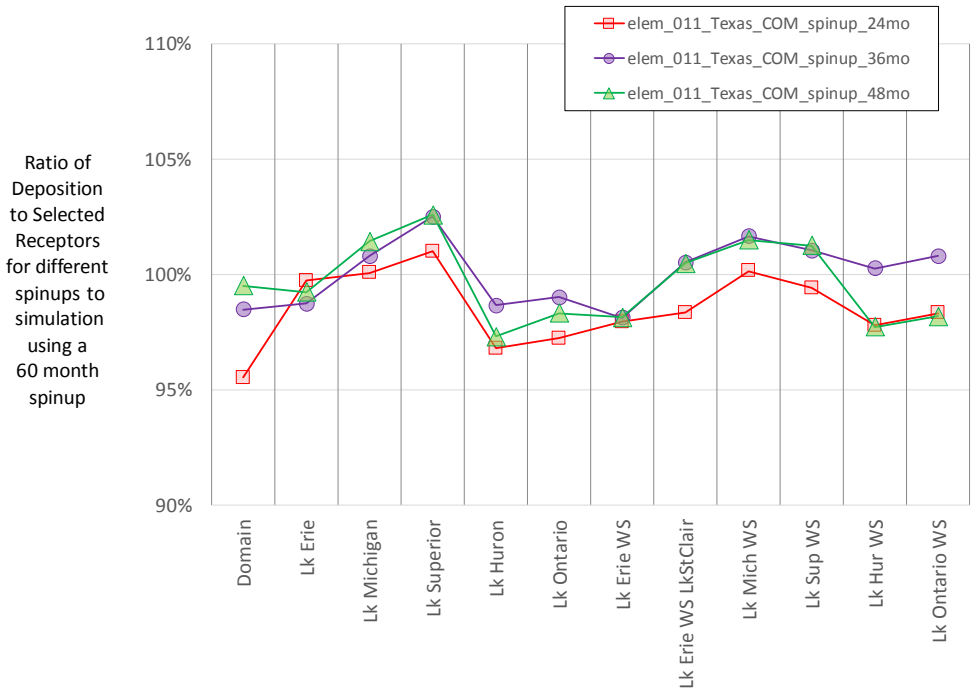

Figure 41. Spin-up test results for COM simulations of Hg(0) emissions from a standard source location in Texas (#11).

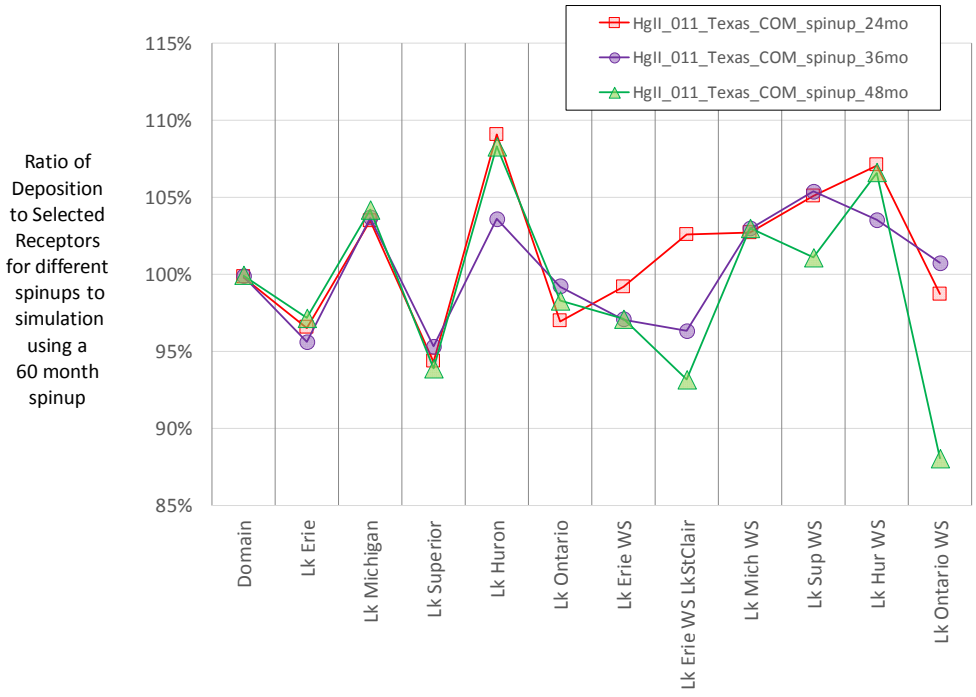

Figure 42. Spin-up test results for COM simulations of Hg(II) emissions from a standard source location in Texas (#11).

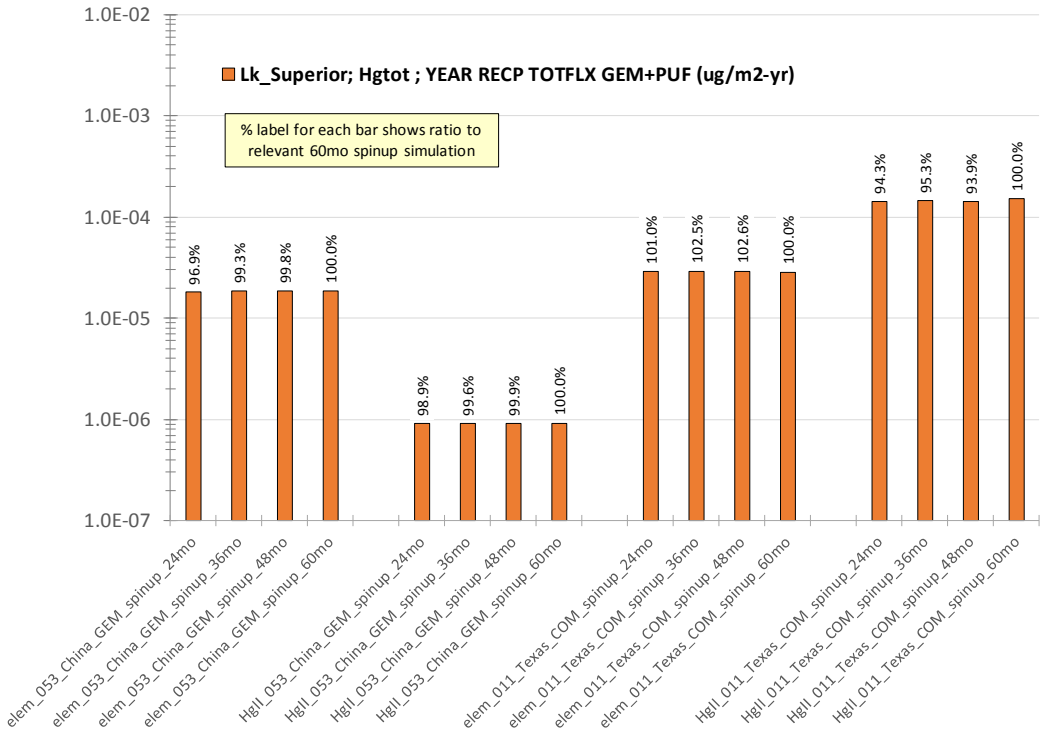

Figure 43. Comparison of all GEM and COM spin-up tests for deposition to Lake Superior.

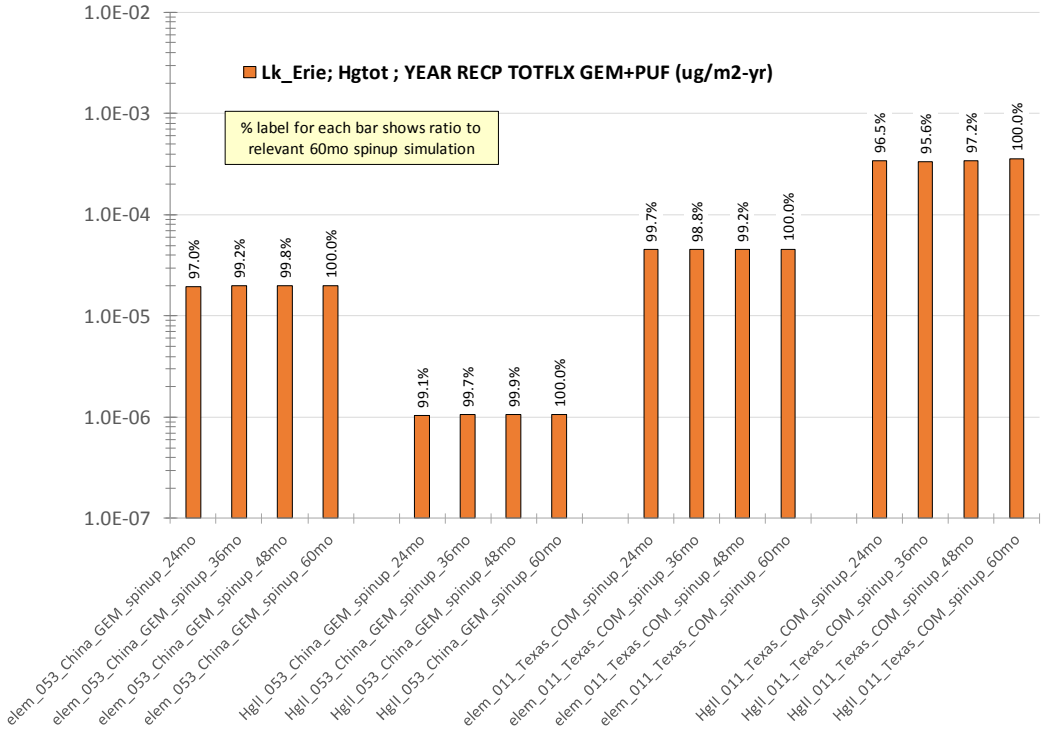

Figure 44. Comparison of all GEM and COM spin-up tests for deposition to Lake Erie.

4. Model Evaluation

4.1. Introduction

The primary way in which atmospheric mercury models are evaluated is by comparison against ambient measurements of concentrations and wet deposition. While results are sometimes encouragingly consistent with measurements, inconsistencies are evidence of the uncertainties in the models (Lin, Pongprueksa et al. 2006, Lin, Pongprueksa et al. 2007, Pongprueksa, Lin et al. 2008, Subir, Ariya et al. 2011, Subir, Ariya et al. 2012, Zhang, Blanchard et al. 2012, Kos, Ryzhkov et al. 2013, Bieser, De Simone et al. 2014, Weiss-Penzias, Amos et al. 2015) and the measurements themselves (Jaffe, Lyman et al. 2014, Gustin 2015, Lyman, Jones et al. 2016, Ren, Luke et al. 2016). A limited number of model intercomparison exercises have been carried out (e.g., (Ryaboshapko, Bullock et al. 2002, Ryaboshapko, Bullock et al. 2007, Ryaboshapko, Bullock et al. 2007, Bullock, Atkinson et al. 2008, Bullock, Atkinson et al. 2009, Zhang, Blanchard et al. 2012, AMAP/UNEP 2013, Bieser, Slemr et al. 2017, Gencarelli, Bieser et al. 2017, Travnikov, Angot et al. 2017) and it is often found that there can be significant differences in mercury concentrations and deposition estimated by different models.

Given the relatively sparse collection of standard source locations used, and in some aspects of the analysis, the relatively coarse computational grid used (2.5^o x 2.5^o), it is not expected that the model results will perfectly match the measurements at any given location, even if the model, emissions, and meteorological data used were “perfect”. This is the normal case with essentially any comparable modeling study. The impact of sub-grid-scale phenomena such as the impacts of “local” sources on a given site will not be captured by the sparse assortment of standard source locations or the coarse Eulerian computational grid. These limitations can be appreciated by examining Figure 45 through Figure 50, and Figure 79 and Figure 80. With this important limitation, we will nevertheless carry out detailed comparisons of measurements with model results in the sections below.

4.2. Atmospheric mercury concentration measurements used for model evaluation

Atmospheric mercury measurement data for 2011 was utilized to evaluate the model results. Atmospheric mercury concentration measurements used for model evaluation are summarized in Table 5 and shown in Figure 45 through Figure 50.

Table 5. Ambient Air Concentration Data Sites and Measurements used for Model Evaluation.

Group	Site Name	NADP site code	2-letter abbreviation	3-letter abbreviation	Country or region, including state or province for sites in the United States and Canada	Latitude	Longitude	Elevation (meters above mean sea level)	Average 2011 Hg(0) concentration (pg/m3)	Average 2011 Hg(2) concentration (pg/m3)	Average 2011 Hg(p) concentration (pg/m3)	Data source (see list below)
AMNet (relatively non-urban)	Beltsville	MD99	BV	BVL	USA (MD)	39.028	-76.817	46	1485	3.0	6.4	1
	Grand Bay NERR	MS12	GB	GBY	USA (MS)	30.429	-88.428	2	1445	6.2	5.7	1
	Mauna Loa	HI00	ML	MLO	USA (HI)	19.539	-155.579	3,399	1452	142.0	90.1	1
	Pensacola	FL96	PE	OLF	USA (FL)	30.550	-87.375	45	1376	1.4	3.2	1
	Piney Reservoir	MD08	PR	PNY	USA (MD)	39.705	-79.012	769	1432	7.1	3.7	1
	Stilwell	OK99	ST	STL	USA (OK)	35.751	-94.670	299	1360	2.9	4.7	1
	Underhill	VT99	UH	UND	USA (VT)	44.528	-72.868	399	1464	1.4	4.5	1
	Athens	OH02	AT	ATH	USA (OH)	39.308	-82.118	275	1395	7.5	6.9	1
	Huntington Wildlife	NY20	HW	HWL	USA (NY)	43.973	-74.223	500	1228	1.0	4.9	1
	Kejimkujik	NS01	KE	KEJ	Canada (NS)	44.433	-65.206	155	1413	0.4	3.6	1
	Thompson Farm	NH06	TF	TMF	USA (NH)	43.110	-70.950	24	1364	1.9	4.1	1
AMNet (urban)	Salt Lake City	UT97	SL	SLC	USA (UT)	40.712	-111.961	1,297	1802	16.9	13.0	1
	Rochester	NY43	RC	RCH	USA (NY)	43.146	-77.548	136	1326	3.8	10.1	1
	Yorkville	GA40	YK	YRK	USA (GA)	33.928	-85.045	395	1405	4.0	7.5	1
	Birmingham	AL19	BI	BIR	USA (AL)	33.553	-86.815	200	2225	19.6	9.6	1
	Bronx	NY06	BX	BRO	USA (NY)	40.868	-73.878	68	1511	6.2	8.7	1
Southern Hemisphere	Manaus			MAN	Brazil	-2.890	-59.970	110	1100			2
	Cape Point			CPT	South Africa	-34.350	18.483	230	905			3
	Amsterdam Island			AMS	Indian Ocean	-37.800	77.550	70	1050			2
	Bariloche			BAR	Argentina	-41.130	-71.420	801	850			2
	Dome Concordia			DMC	Antarctica	-75.100	123.350	3,220	850			2
Europe	Longobucco			LON	Italy	39.390	16.610	1,379	1400			2
	Mace Head			MHE	Ireland	53.333	-9.900	8	1450			2
	Rao			RAO	Sweden	57.394	11.914	5	1400	0.23	2.21	2,10
	Pallas Matorova			PAL	Finland	68.000	24.240	340	1450			2
Asia	Changbai Mtn			MCH	China	42.400	128.467	741	1700	1.8	40.4	4,7
	Mt Ailao			MAL	China	24.540	101.030	2,503	2090	2.2	31.3	5,8
	Mt Waliguan			MWA	China	36.290	100.900	3,816	1980	7.4	19.4	6,9
	EV-K2			EVK	Nepal	27.960	86.810	5,050	1150			2
Other	Nieuw Nickerie			NIK	Suriname	5.960	-57.040	1	1150			2
	Kodaikanal			KOD	India	10.230	77.470	2,333	1550			2
	Sisal Yucatan			SIS	Mexico	21.160	-90.050	7	1200			2
	Listvyanka			LIS	Russia	51.850	104.890	670	1250			2
	Station Nord			VRS	Greenland	81.580	-16.610	30	1550			2

1. NADP Atmospheric Mercury Network data provided by David Gay, NADP, Aug 31, 2017. A formal request for data was made, and all Principal Investigators at all AMNet sites agreed that their 2011 data could be transmitted and used in this analysis.

2. Average Hg(0) concentration for 2013, estimated from graphed data in Sprovieri, Pirrone et al. (2016)).

3. Average Hg(0) concentration for 2011, estimated from graphed data in Martin, Labuschagne et al. (2017)).

4. Average Hg(0) concentration for 2011, from Fu, Zhang et al. (2015)).

5. Average Hg(0) concentration from May 2011 to May 2011 from Fu, Zhang et al. (2015)).

6. Average Hg(0) concentration from September 2007 to September 2008 from Fu, Zhang et al. (2015)).

7. Average Hg(2) (aka GOM) and Hg(p) concentration for 2013, reported in Sprovieri, Pirrone et al. (2016)).

8. Average Hg(2) (aka GOM) and Hg(p) concentration for May 2011 to May 2012, reported in Fu, Zhang et al. (2015)).

9. Average Hg(2) (aka GOM) concentration for Sept 2007 to Sept 2008, reported in Fu, Zhang et al. (2015)).

10. Average Hg(2) and Hg(p) concentrations for 2012-2015, reported in Wangberg, Mastromonaco et al. (2016)).

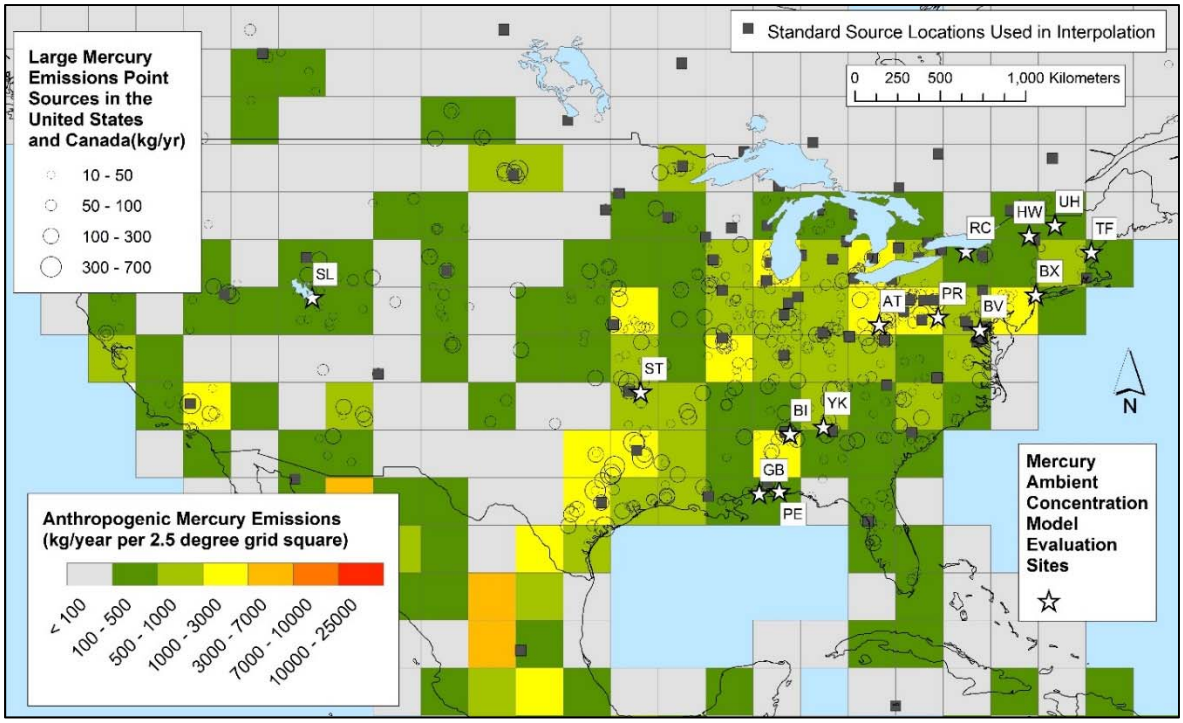

Figure 45. Ambient concentration model evaluation sites in the U.S. Standard source locations used in the analysis and large mercury point sources are also shown, along with gridded anthropogenic mercury emissions.

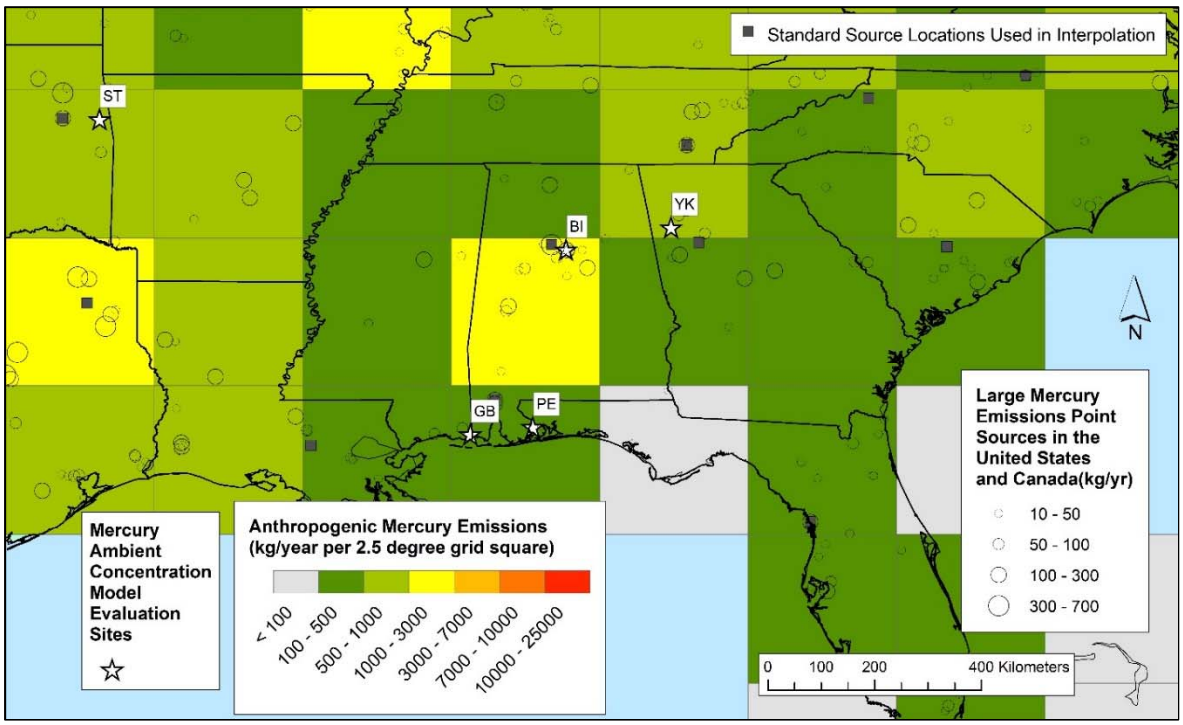

Figure 46. Ambient concentration model evaluation sites in the southern U.S. Standard source locations used in the analysis and large mercury point sources are also shown, along with gridded anthropogenic Hg emissions.

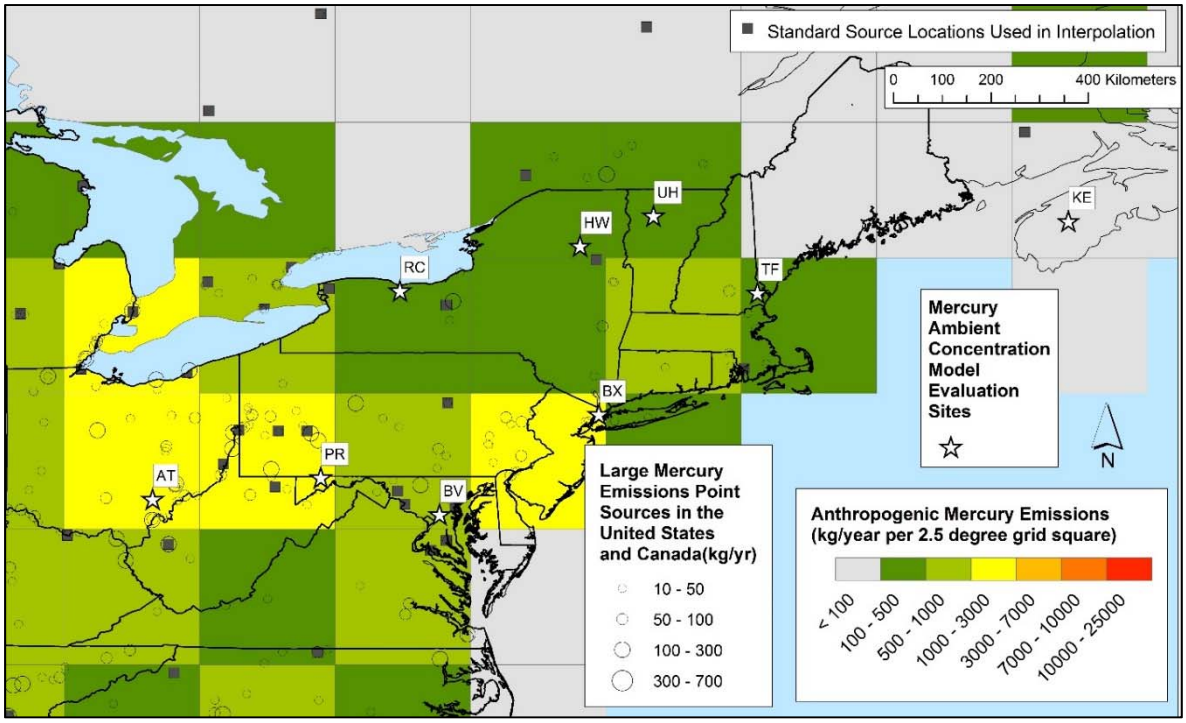

Figure 47. Ambient concentration model evaluation sites in the Mid-Atllantic and Northeastern U.S. Standard source locations used in the analysis and large mercury point sources are also shown, along with gridded anthropogenic Hg emissions.

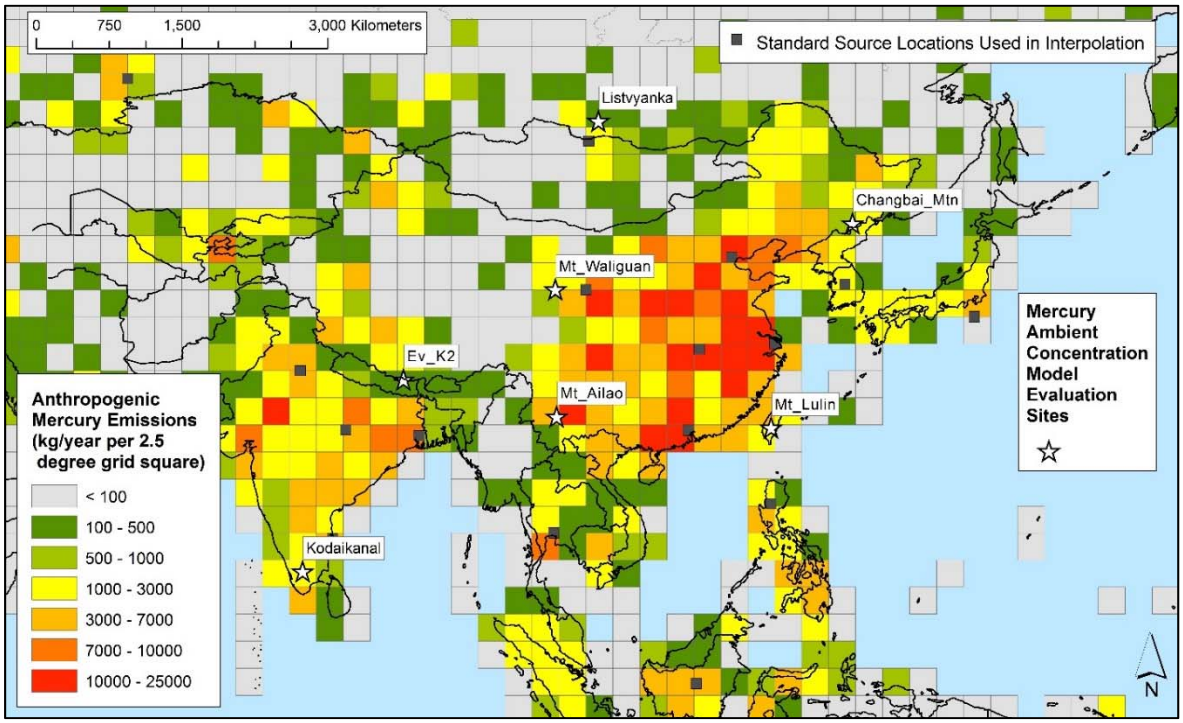

Figure 48. Ambient concentration model evaluation sites in China, India, and surrounding region. Standard source locations used in the analysis and gridded anthropogenic Hg emissions are also shown.

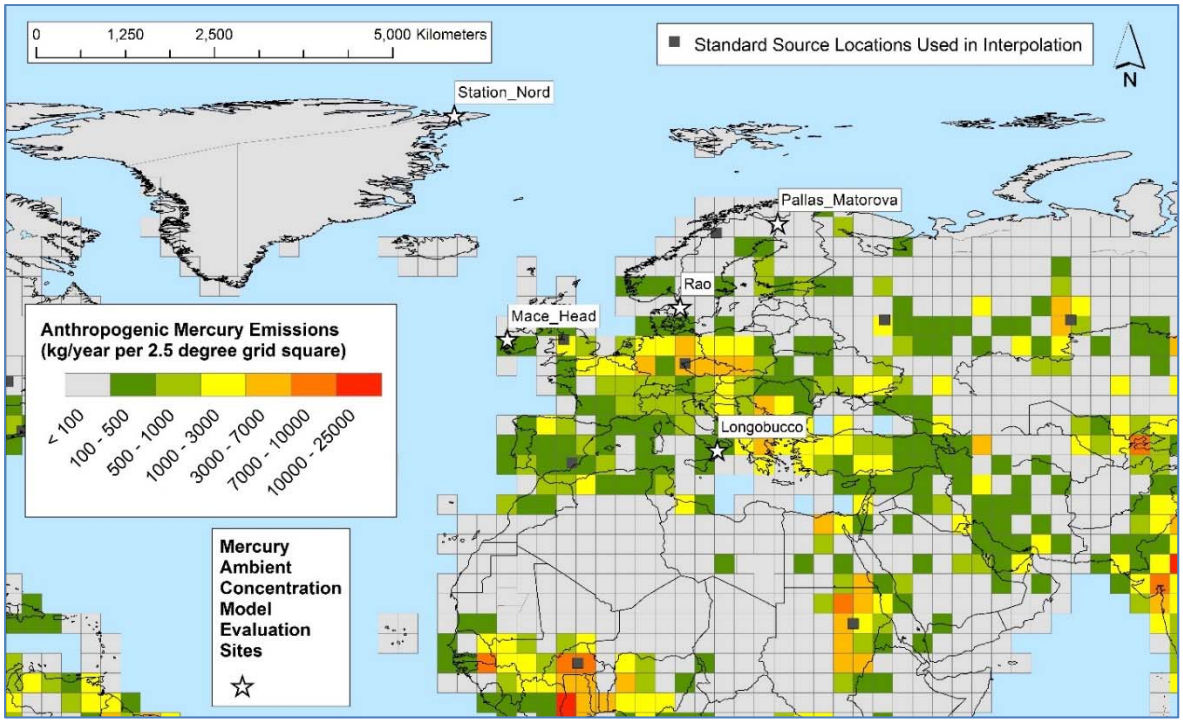

Figure 49. Ambient concentration model evaluation sites in Europe. Standard source locations used in the analysis and gridded anthropogenic Hg emissions are also shown.

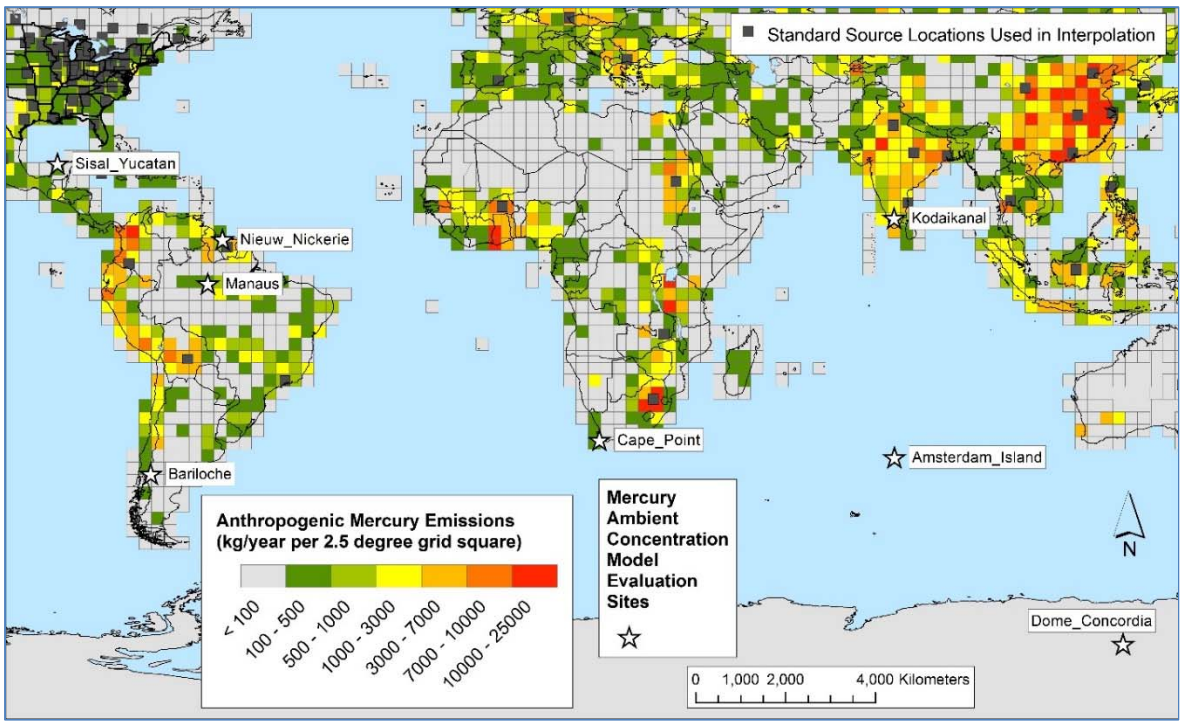

Figure 50. Ambient concentration model evaluation sites in the Southern Hemisphere. Standard source locations used in the analysis and gridded anthropogenic Hg emissions are also shown.

4.3. Comparison of model predictions against atmospheric mercury concentration measurement data

4.3.0. Introduction and Overall Comparisons

As an approximation, we have simply compared annual average concentrations, for both model and measurement results, without regard to periods when measurements were not made. For the AMNet measurement sites, we had access to the datasets including individual measurements, and so, it would be possible to align the model results with the exact hours that measurements were reported. If resources allow, this will be attempted in future work. For measurements at other sites, we did not have access to the underlying datasets, but simply were able to obtain reported annual values reported in the literature. In some cases, as can be seen in the notes for Table 5, the data were not even for 2011, but were for a different year.

The measurements at the AMNet sites were made using speciated mercury measurement instrument suites from the Tekran Instruments Corporation, as were most if not all of the measurements made at other sites around the world for which data could be obtained. Generally, in these measurements, either a 2-hour or 3-hour measurement cycle is used.

With a 2-hour measurement cycle, the reported values refer to the first hour of the 2-hour cycle, as the 2nd hour is used solely to analyze mercury collected in the first hour. So, if the instrument suite operated continuously throughout the year, the maximum percentage of the hours in the year represented by measurements would be 50%. If a site had two instrument suites running asynchronously, each using 2-hour measurement periods – this was the case at two AMNet sites (Beltsville and Grand Bay), then 100% of the hours could be measured in a year, if the instruments operating continuously.

With a 3-hour measurement cycle, the reported values refer to the first 2 hours of the 3-hour cycle, as the 3rd hour is used solely to analyze mercury collected in the first two hour. So, if the instrument suite operated continuously throughout the year, the maximum percentage of the hours in the year represented by measurements would be ~66%.

In practice, due to routine and non-routine instrument maintenance and calibration activities, as well as outages due to extreme weather events, as well as other potential issues, a site cannot reach the maximum fraction of hours in a given year. The percentage of hours in 2011 represented by measurements at AMNet sites used for model evaluation are summarized in Table 6. It can be seen that for most of the sites, the percentage is about 40-50% for GEM, GOM, and PBM. For the sites with two instrument suites, the percentage is much higher, on the order of 80%. For a few of the sites, the percentage is much lower, e.g., data from Birmingham and Salt Lake City represent only about ~20% of the hours in 2011. Since there can be significant variability in the concentrations of Hg_0, Hg_2, and Hg_p (see examples for the Beltsville site in Figure 51 through Figure 56), and The limited number of hours measured in 2011, as well as the use of simple annual averages instead of explicitly comparing model

and measurement results for the exact, specific hours of measurement in 2011 represents a limitation in this model evaluation exercise.

In all of the comparisons shown, we have compared Hg(II) model output concentrations with the "Reactive Gaseous Mercury" (RGM) or "Gaseous Oxidized Mercury" (GOM) measurements reported. We have not included the model-output Hg2s concentrations in these Hg(II) comparisons, as it is unclear *where* in the measurement system Hg2s would register. Likewise, for Hg(p) comparisons, we have used the model output Hg(p) – including material on all particle sizes – to compare against the measured Hg(p) values. The measurements of Hg(p) are usually for relatively small particles only, i.e., particles ~2.5 microns and smaller. We have not included the modeled Hg2s concentrations in the Hg(p) comparisons.

As measurements are routinely reported at Standard Temperature and Pressure (STP) (0 deg C, and 1 atm), the modeling results were converted to the same STP so that the comparisons could be made.

An overall comparison of model vs. measurement concentrations of Hg_0, Hg_2, and Hg_p is shown in Figure 57 and Figure 58. In these figures, we have shown all of the data on the same scale. It can be seen that the concentrations of the non-Hg(0) mercury forms are generally much smaller than Hg(0). In these initial figures, results are shown only for the *Eulerian-only* simulation methodology (Run Scheme 00) and the most "advanced" interpolation-based Eulerian-Lagrangian hybrid methodology (Run Scheme 04). It can be seen that for many of the comparisons, the model estimates for the two different schemes are remarkably similar. However, in a few cases, there are significant differences. Such differences are expected and will be discussed in more detail below.

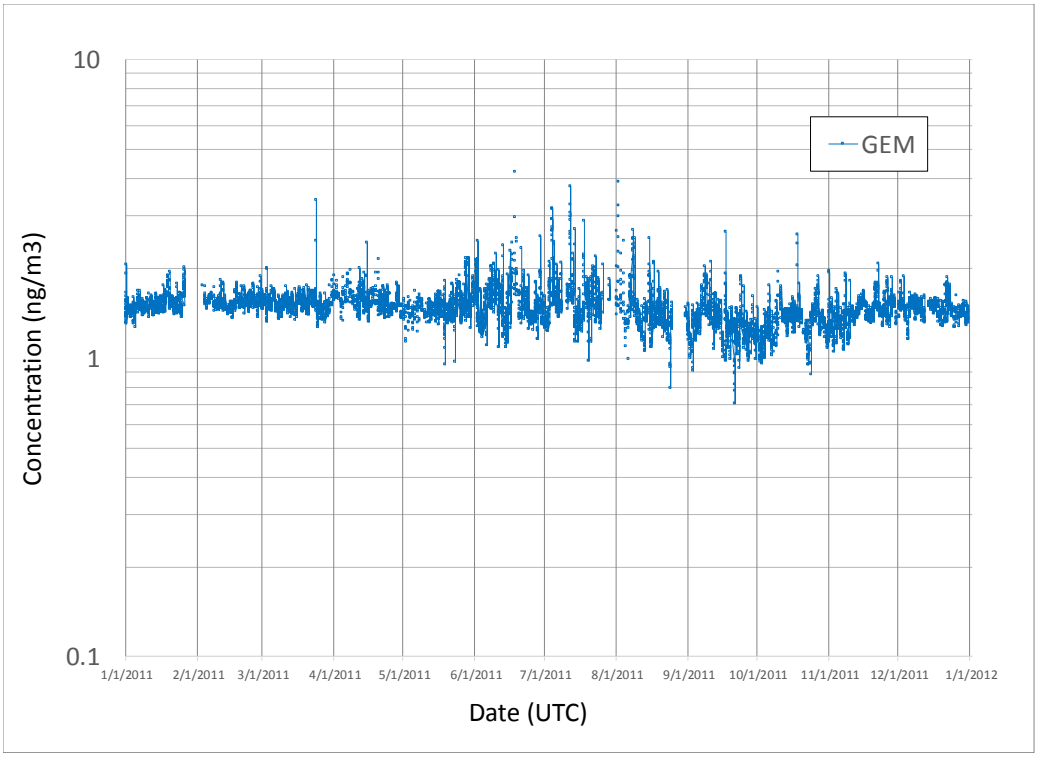

Figure 51. Gaseous Elemental Mercury (aka GEM, Hg_0) measured at Beltsville, MD (2011). Logarithmic scale.

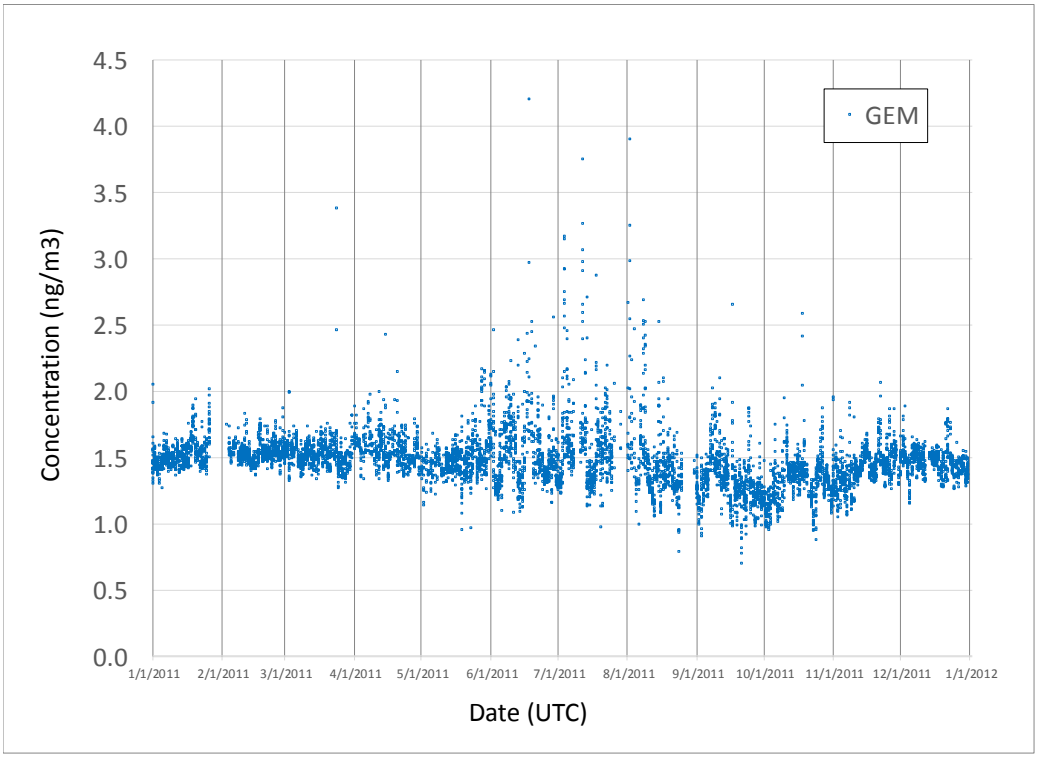

Figure 52. Gaseous Elemental Mercury (aka GEM, Hg_0) measured at Beltsville, MD (2011). Linear scale.

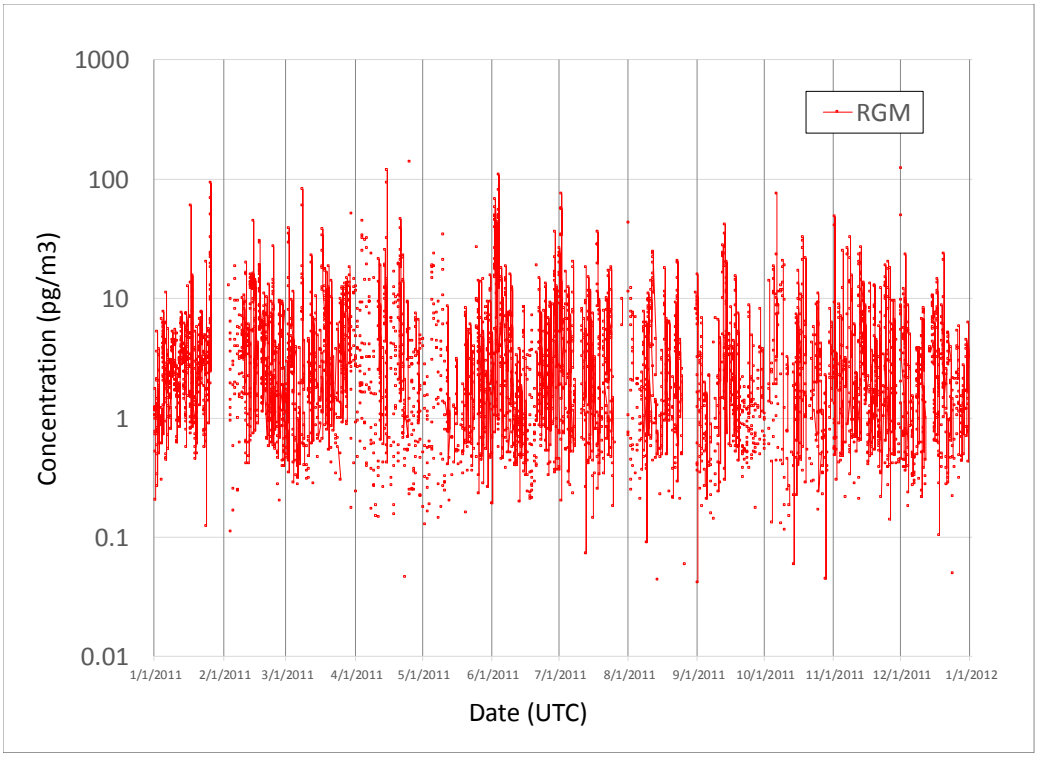

Figure 53. Reactive Gaseous Mercury (aka GOM, Hg_2) measured at Beltsville, MD (2011). Logarithmic scale.

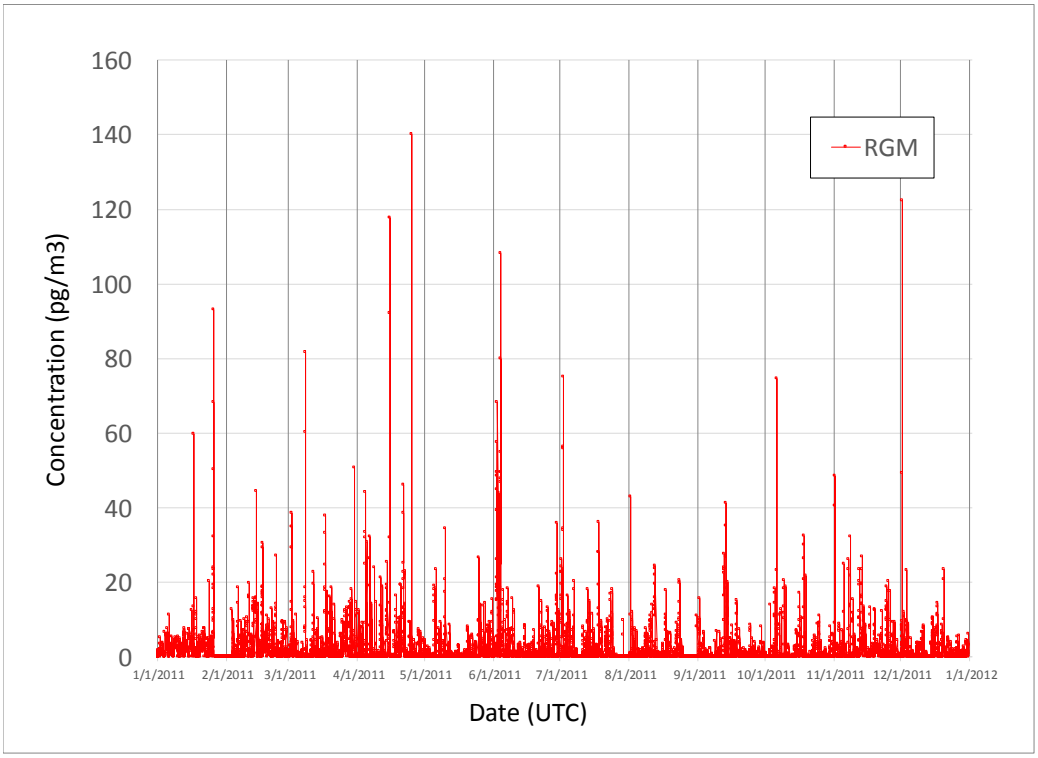

Figure 54. Reactive Gaseous Mercury (aka GOM, Hg_2) measured at Beltsville, MD (2011). Linear scale.

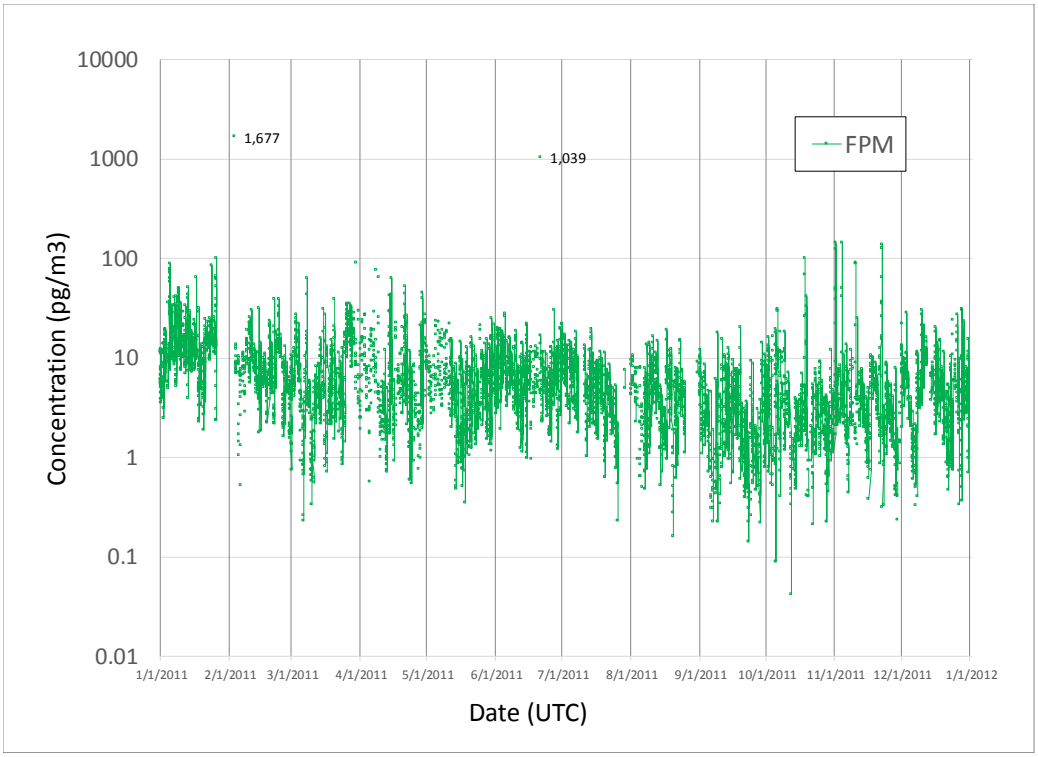

Figure 55. Fine Particulate Mercury (aka FPM, PBM, Hg_p) measured at Beltsville, MD (2011). Logarithmic scale.

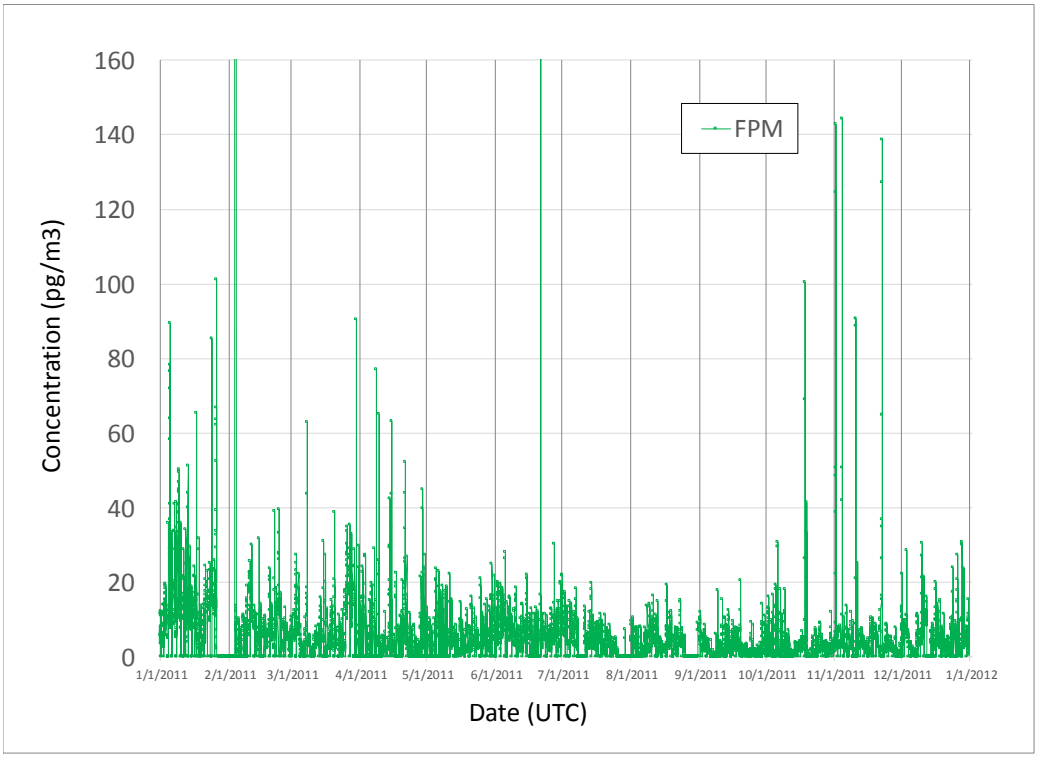

Figure 56. Fine Particulate Mercury (aka FPM, PBM, Hg_p) measured at Beltsville, MD (2011). Linear scale.

Table 6. Percentage of hours in 2011 represented by measurements at AMNet sites used for model evaluation.

Group	Site Name	NADP site code	Measurement Period (hrs) (see text for additional explanation)	Percentage of hours in 2011 with measurements			
				maximum possible	GEM	GOM	PBM
AMNet (relatively non-urban)	Beltsville	MD99	1*	100	83	79	79
	Grand Bay NERR	MS12	1*	100	87	83	80
	Mauna Loa	HI00	2	50	44	43	42
	Pensacola	FL96	2	50	43	38	37
	Piney Reservoir	MD08	3	66	57	54	54
	Stilwell	OK99	3	66	49	45	46
	Underhill	VT99	3	66	62	60	59
	Athens	OH02	3	66	53	53	53
	Huntington Wildlife	NY20	3	66	52	48	49
	Kejimkujik	NS01	3	66	61	60	61
	Thompson Farm	NH06	3	66	58	53	52
AMNet (urban)	Salt Lake City	UT97	2	50	23	20	20
	Rochester	NY43	3	66	49	42	42
	Yorkville	GA40	2	50	40	38	38
	Birmingham	AL19	2	50	23	19	19
	Bronx	NY06	3	66	58	55	56

* This site has two instruments suites operating asynchronously, each with 2-hr periods, so the effective measurement period is 1 hour.

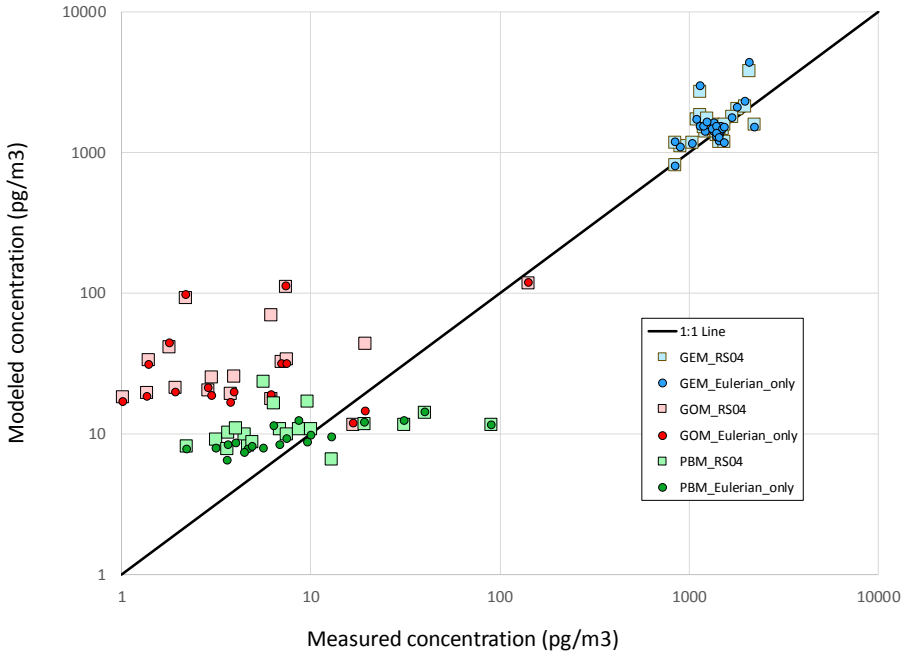

Figure 57. Modeled vs. Measured Concentrations of GEM (Hg_0), GOM (Hg_2) and PBM (Hg_p) (logarithmic scale).

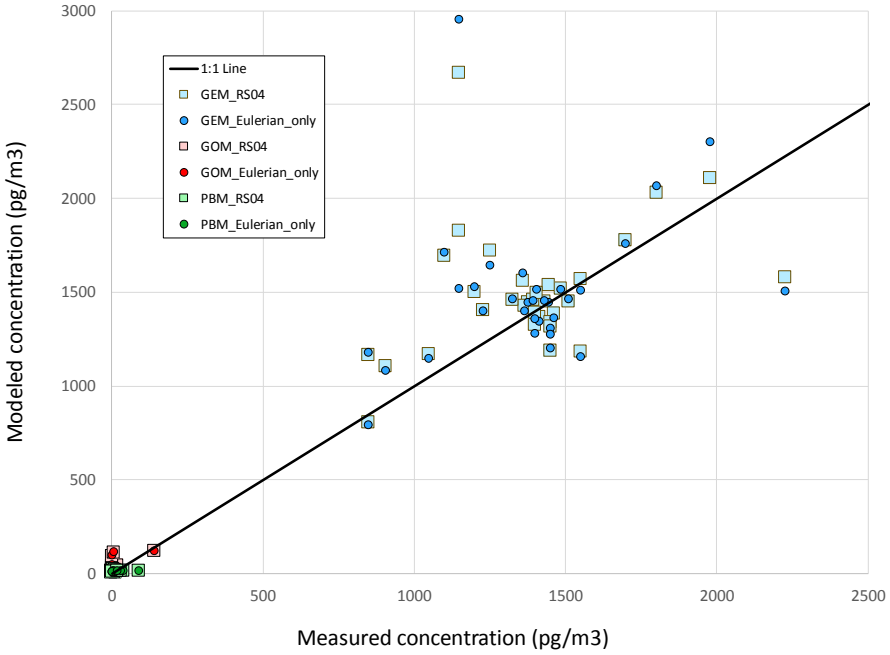

Figure 58. Modeled vs. Measured Concentrations of GEM (Hg0), GOM (Hg2) and PBM (Hgp) (linear scale).

4.3.1. Comparison of Modeled vs. Measured Elemental Mercury

Figure 62 shows a comparison of modeled vs. measured gaseous elemental mercury (GEM) (aka Hg_0) annual average concentrations for 2011 – subject to caveats discussed above Sections 4.2 and 4.3.0 – for all sites with available data. This figure just shows results for the Eulerian-only methodology (RS-00), and two Lagrangian-Eulerian hybrid methodologies (RS-02 and RS-04). It can be seen that most of the comparisons fall reasonably close to the 1:1 line, and all fall within 25%, aside from two outliers: EV-K2 (Nepal) and Mt. Ailao (China). Figure 63 shows just the data within the boxed region of Figure 62. Figure 64 and Figure 65 are analogous figures to the above two figures, but data for RS-01 and RS-03 are added, so that data for all run-schemes are now shown.

The probable reason for the discrepancy between modeled and measured Hg_0 concentrations at Mt. Ailao can be seen by examining Figure 59 (identical to Figure 48 above, page 63, reproduced here for the reader's convenience) and Figure 60, below. It can be seen that the Mt. Ailao site is relatively close to region of high emissions (Figure 59). However, it is in a pristine area relatively remote from anthropogenic influences (Zhang, Fu et al. 2016). The site is near the top of a ridge, with deep canyons on both sides (Figure 60). According to a detailed source-receptor analysis for mercury (Zhang, Fu et al. 2016), the site is relatively "disconnected" from regional mercury sources, in terms of atmospheric transport. However, the coarse Eulerian model grid may have artificially smoothed the source-receptor relationships in the region. Further, it can be seen that the nearest standard source locations (Figure 59) are quite far away (~1000 km or more), and so, any interpolation-based procedure based on only these standard source locations could be subject to large errors. Additionally, it is noted that 2013 data were used for measurements (see Table 5, above), and measurements at this site were only made for approximately 5 months of the year during 2013 (Sprovieri, Pirrone et al. 2016).

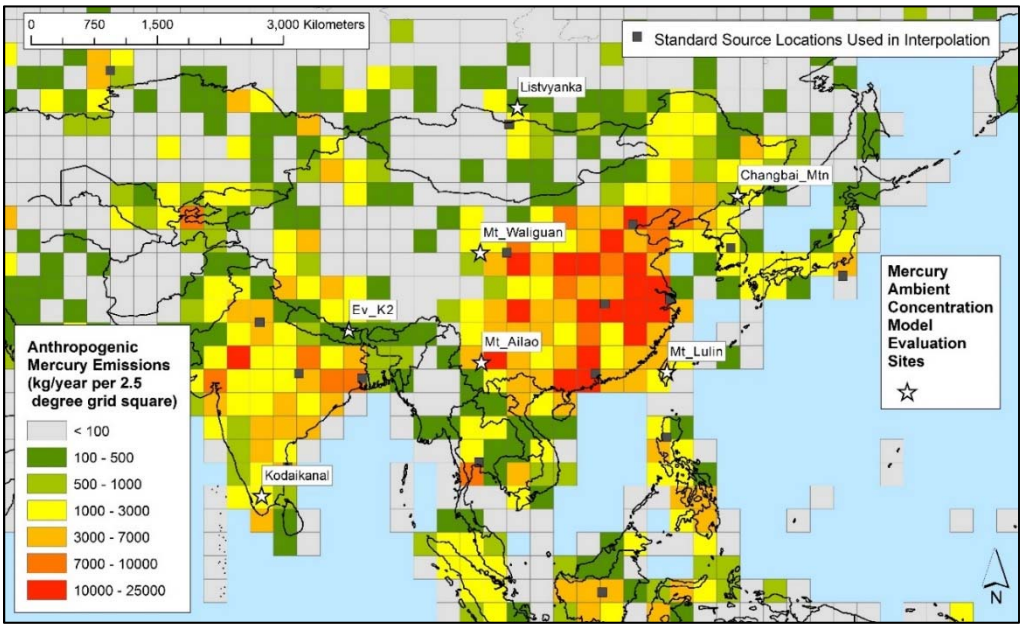

Figure 59. Ambient concentration model evaluation sites in China, India, and surrounding region.

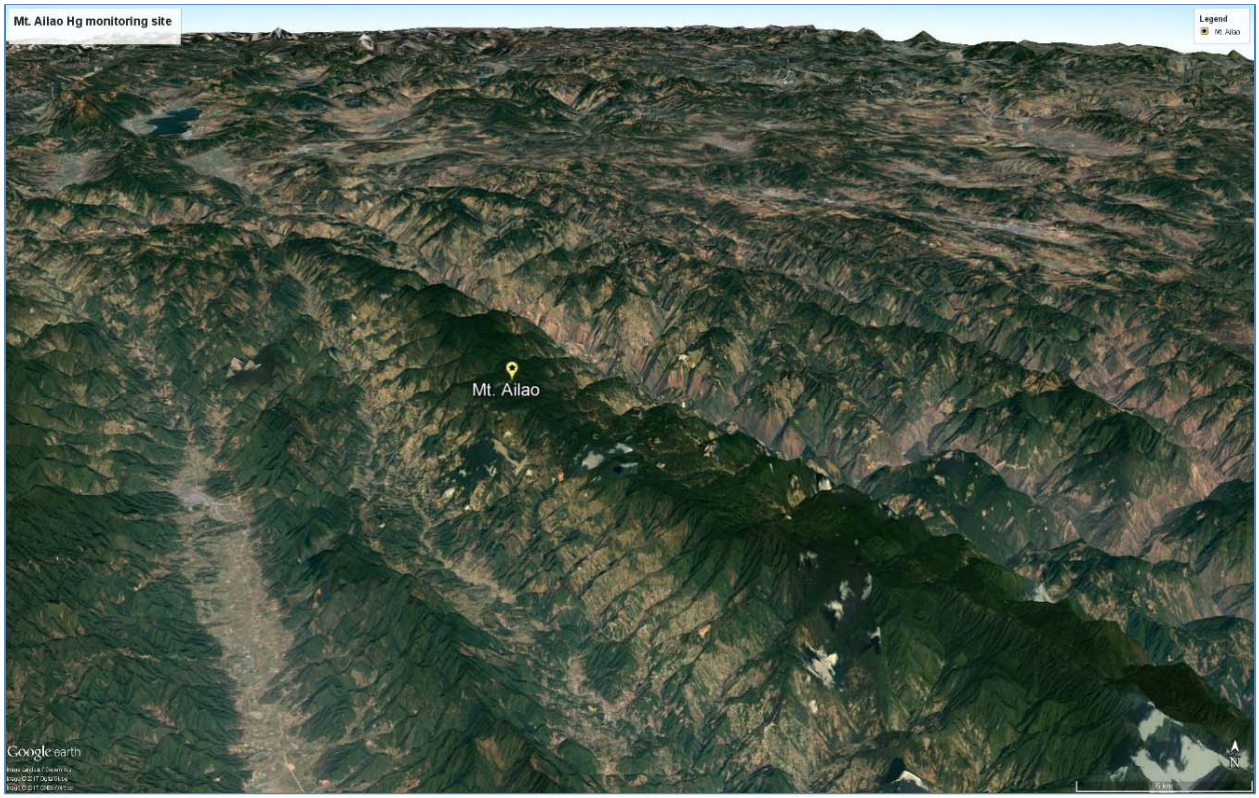

Figure 60. Google Earth view of Mt. Ailao site and surrounding region.

A similar, challenging source-receptor situation most likely exists for the high elevation EV-K2 site (5050 m) (Figure 61), exposing the limitations of the methodologies used. Measurements were only made for a little more than ½ of the year at the site (Sprovieri, Pirrone et al. 2016). In the EV-K2 case, while the site is at high elevation, it is actually in a relatively low-lying area in the region. The terrain around this site is highly complex.

The primary goal of this work was to estimate deposition to the Great Lakes, and consequently, expenditure of the computational resources required to provide realistic estimates of specific sites in China (and elsewhere outside of the Great Lakes region) was not within the scope of this work. Nevertheless, the model estimated concentrations are generally within a factor of ~2 of the measured concentration at the Mt. Ailao and EV-K2 sites.

The results for almost all sites show relatively consistent results between the different run schemes. However, Birmingham (BIR) modeling results are more variable. For this site, the RS-00 results (Eulerian only), and RS-02 and RS-04 results – using the 32km NARR meteorological data for the Lagrangian puff components of the simulation –are similar, and underestimate the measured Hg0 concentration by ~25%. The RS-01 and RS-03 results – using NCEP/NCAR 2.5 degree meteorological data for the Lagrangian puff components of the simulation – are similar to each other, but overestimate the measured Hg0 concentration by a factor of ~2. The large difference in meteorological grid resolution and the relatively urban location of the site (with a number of large regional mercury sources), along

with the sparse assembly of standard source locations used (see Figure 46) is the most likely cause of these differences.

Figure 66 and Figure 67 show results just for the relatively non-urban AMNet Hg0 concentration measurement sites. It can be seen that all of the model estimates are within 25% of the measured concentrations, and most are within 10% of the measured concentrations.

Figure 68 shows results just for the five Hg0 model evaluation sites in the Southern Hemisphere. All model results within ~50% of the measured concentrations and for two of the five sites, the modeled concentrations are within 10% of the measured value.

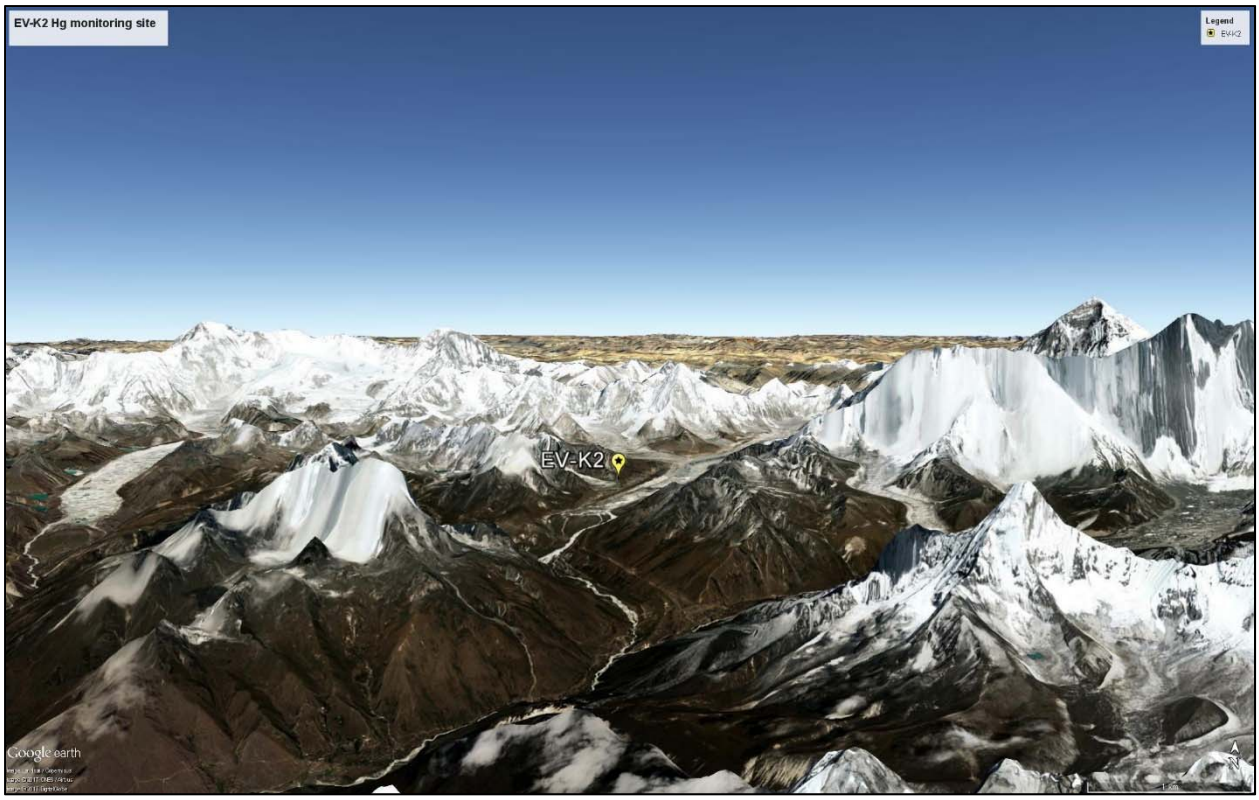

Figure 61. Google Earth view of EV-K2 site and surrounding region.

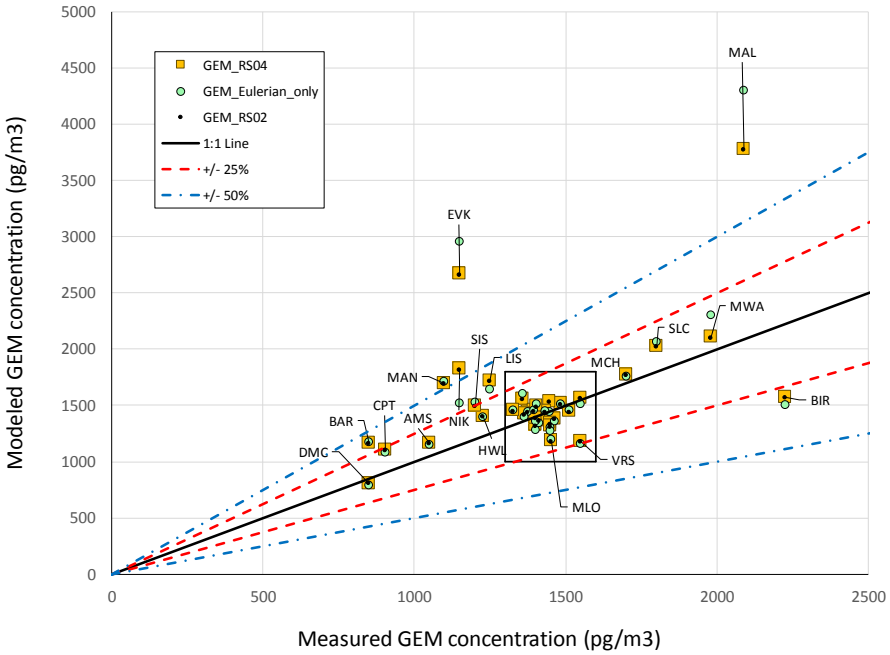

Figure 62. Modeled vs. Measured Hg0 Concentrations, all sites. Results for the Eulerian-only analysis (RS-00), the most advanced Lagrangian-Eulerian Hybrid methodology (RS-04), and RS-02 are shown. A zoomed-in view of the points within the box is shown in the next figure.

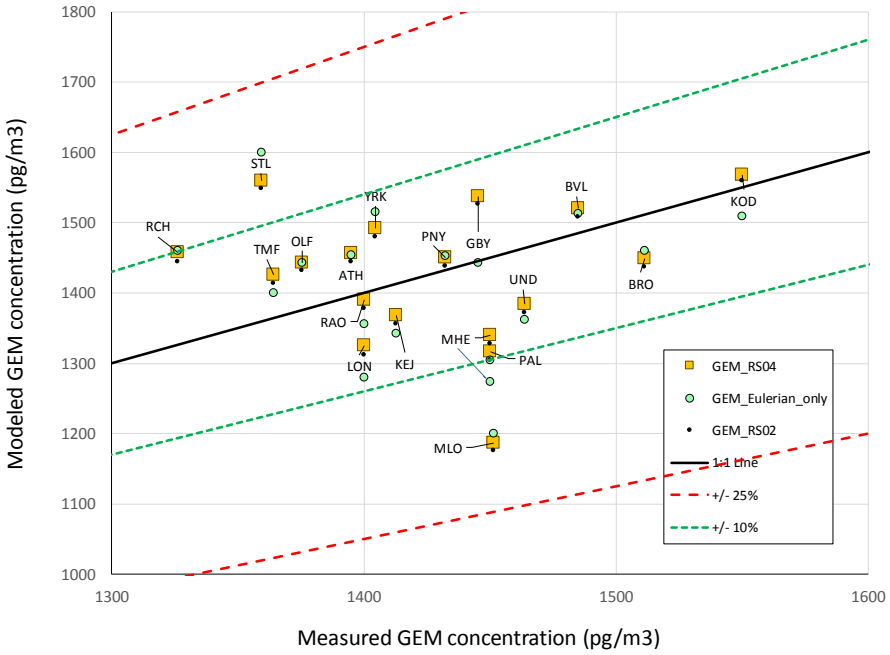

Figure 63. Modeled vs. Measured Hg0 Concentrations, all sites. In addition to the Eulerian-only results (RS-00) and the most advanced Lagrangian-Eulerian Hybrid methodology (RS-04), results for RS-02 are also shown (zoomed-in view of points within the box in the previous figure).

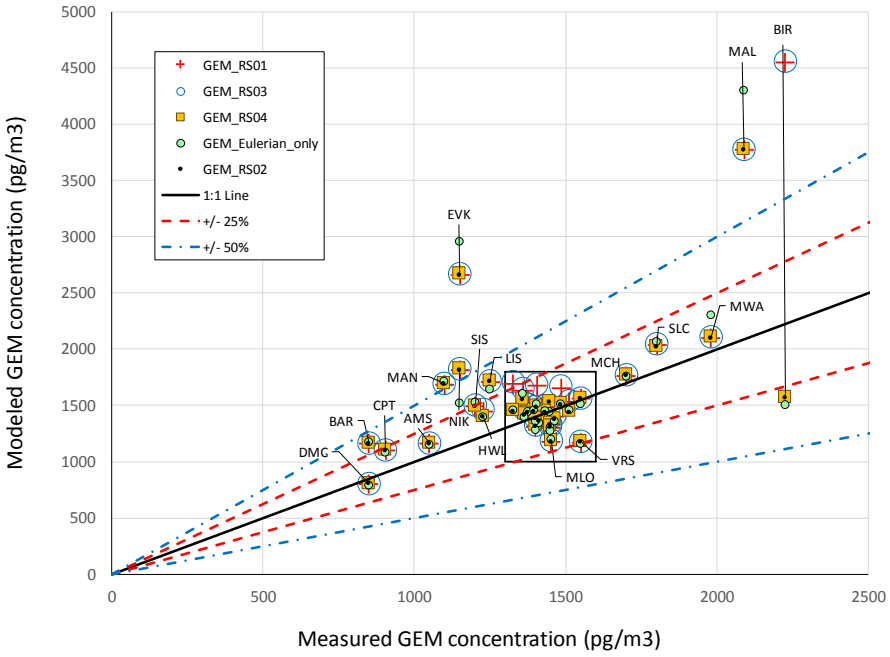

Figure 64. Modeled vs. Measured Hg0 Concentrations, all sites. In addition to the Eulerian-only results (RS-00) and the most advanced Lagrangian-Eulerian Hybrid methodology (RS-04), results for other run-schemes are also shown. A zoomed-in view of the points within the box is shown in the next figure.

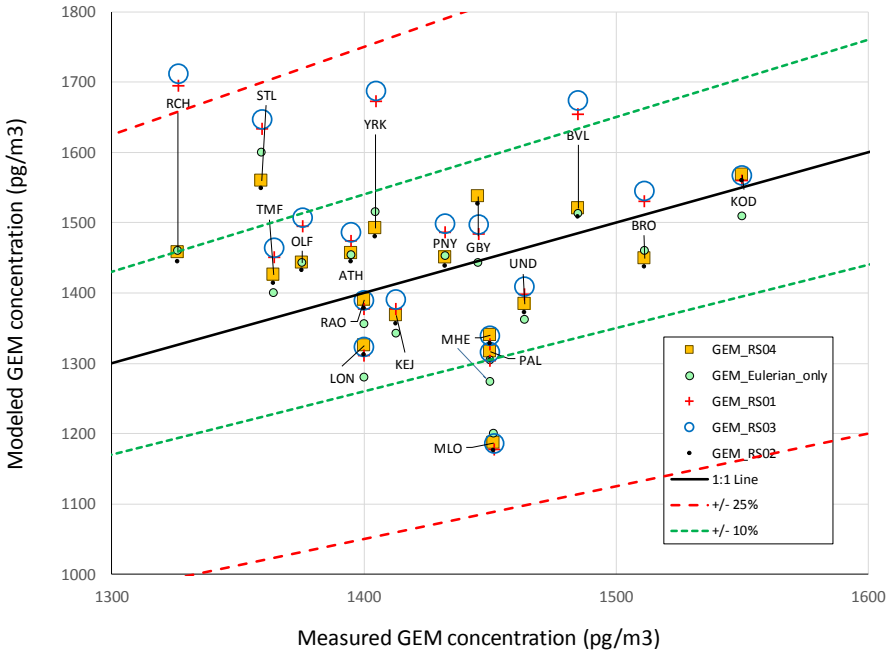

Figure 65. Modeled vs. Measured Hg0 Concentrations, all sites. In addition to the Eulerian-only results (RS-00) and the most advanced Lagrangian-Eulerian Hybrid methodology (RS-04), results for other run-schemes are also shown (zoomed-in view of the points within the box in the previous figure).

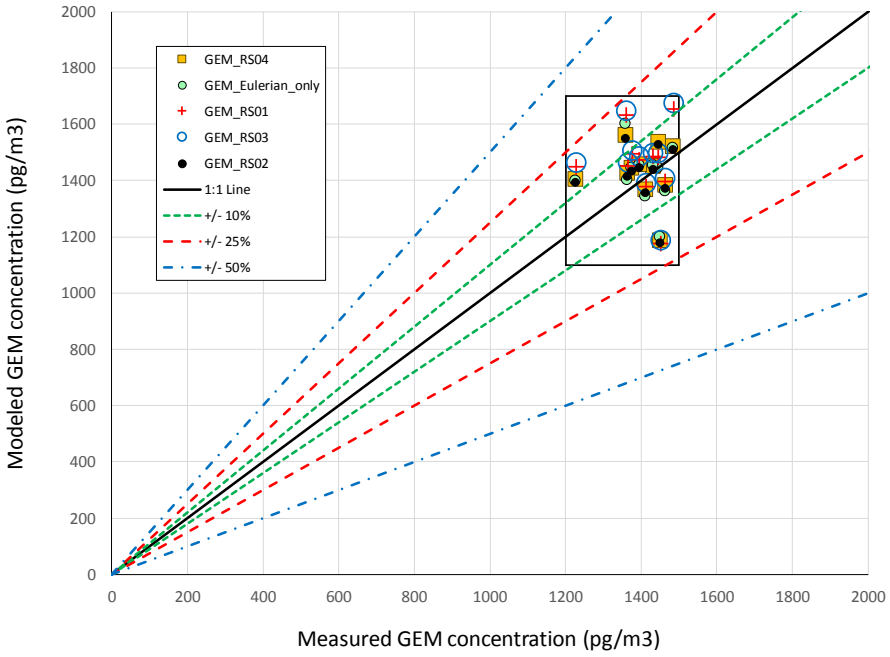

Figure 66. Modeled vs. Measured Hg0 Concentrations (AMNet Non-Urban Sites). A zoomed-in view of the points within the box is shown in the next figure.

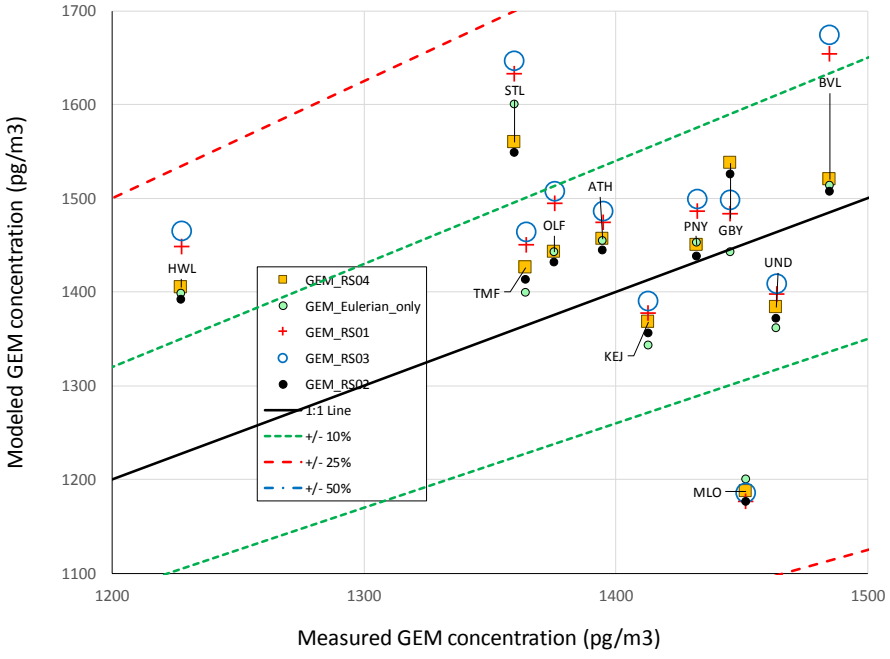

Figure 67. Modeled vs. Measured Hg0 Concentrations (AMNet Non-Urban Sites, zoomed-in view of points within the box in the previous figure).

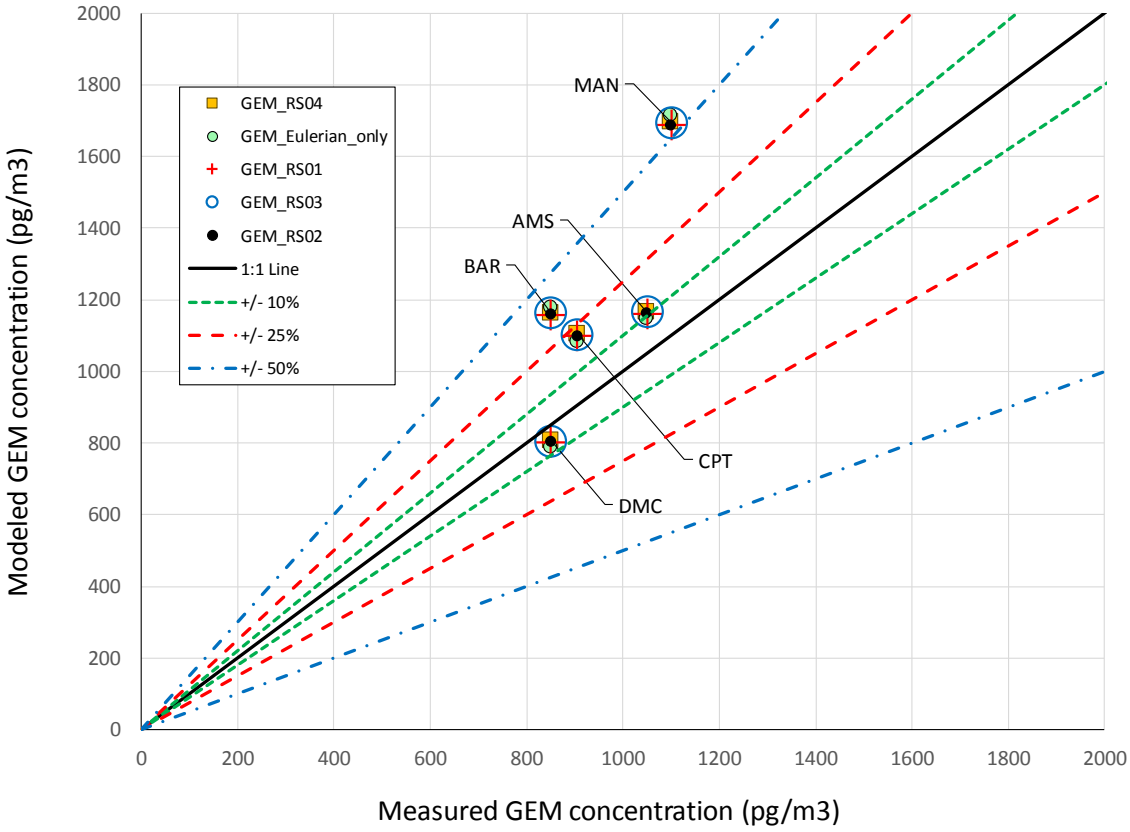

Figure 68. Modeled vs. Measured Hg0 Concentrations (Southern Hemisphere).

4.3.2. Comparison of Modeled vs. Measured Gaseous Oxidized Mercury

Figure 69 shows a comparison of modeled vs. measured reactive gaseous mercury (RGM) (aka Hg(II), Hg_2, GOM) at all measurement sites for which model evaluation data could be assembled. As described in Table 5, most data were for 2011, but in a few cases, data for other years were used as data for 2011 were not available. Concentrations of RGM are very low compared to gaseous elemental mercury, and the model successfully reproduced this overall tendency (e.g., see Figure 58, page 71), but, the model-estimated concentrations are generally higher than measured concentrations.

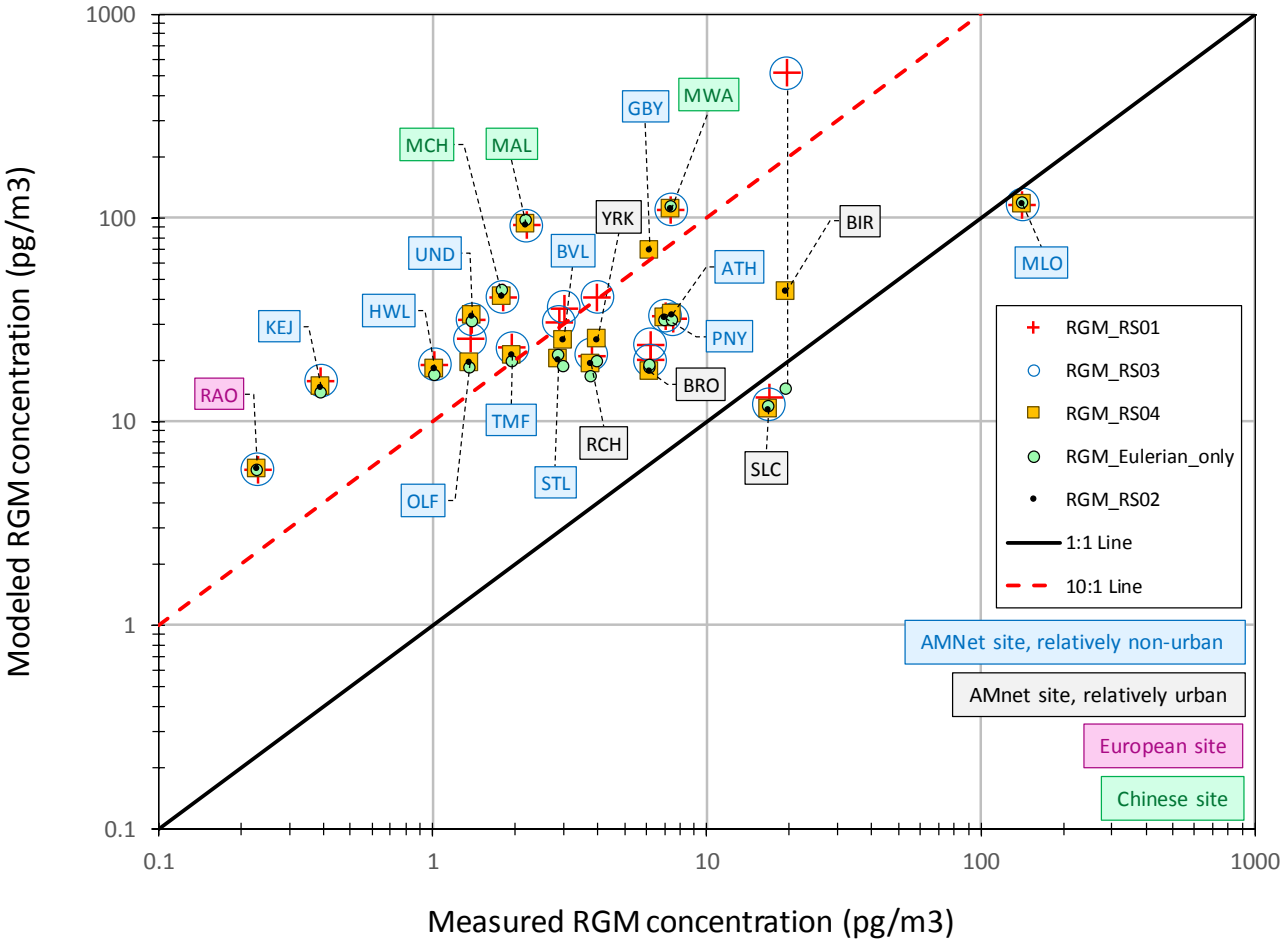

Figure 69. Modeled vs. Measured Hg2 (aka RGM or GOM) Concentrations, all sites.

The tendency for models to yield concentrations of RGM greater than RGM measurements has been found in many cases, including earlier work with the HYSPLIT-Hg model (Cohen, Draxler et al. 2016). Zhang et al. (2012) found that a nested-grid version of the GEOS-Chem model overestimated Hg(II) and Hg(p) by a factor of 4 and 2, respectively, unless it was assumed that a significant fraction (~75%) of Hg(II) emitted by coal-fired power plants was immediately reduced to Hg(0) in the downwind plume.

With the assumed plume reduction of emitted Hg(II), the model overestimated Hg(II) and Hg(p) by ~40%. In another example, "reactive mercury", defined as the sum of Hg(II) and Hg(p), was overestimated by a factor of 2.5 relative to measurements (Weiss-Penzias, Amos et al. 2015). A summary of model vs. measured concentrations of Hg(II) and Hg(p) in the Great Lakes region showed that models generally overestimated measurements by a factor of 2 to 10 (Zhang, Blanchard et al. 2012). In a related study, large model overestimates of Hg(II) and Hg(p) were also found (Kos, Ryzhkov et al. 2013). There are a number of possible reasons for the tendency of the model-estimated concentrations to be greater than the reported measurements.

One argument that has been made to attempt to explain this discrepancy is that the emissions of RGM from anthropogenic sources have been overestimated. In previous work with the HYSPLIT-Hg model, this hypothesis has been examined, by considering that a portion of the RGM emissions were rapidly reduced to Hg_0 after emissions (Cohen, Draxler et al. 2016). A similar approach has been taken in some other modeling analyses (Zhang, Jaegle et al. 2012, Kos, Ryzhkov et al. 2013, Bieser, De Simone et al. 2014, Bieser, Slemr et al. 2017, Travnikov, Angot et al. 2017).

Another possible reason for the discrepancy is that the modeled oxidation of Hg_0 is too fast and/or the reduction of Hg(II) in the atmosphere is too slow. Considering the substantial uncertainties in the rates and mechanisms of the oxidation and reduction reactions (Ariya, Amyot et al. 2015), this possible reason cannot be discounted.

A third possible cause of the discrepancy could be that the measured concentrations of Hg(II) are biased low. Essentially all measurements of Hg(II) are made with an automated denuder technique, and the tendency of this technique to underestimate the actual Hg(II) concentrations has been extensively documented (Lyman, Jaffe et al. 2010, Gustin, Huang et al. 2013, Jaffe, Lyman et al. 2014, Lyman, Jones et al. 2016).

For Hg(II), new experimental evidence is emerging that suggests that the commonly used measurements of "Gaseous Oxidized Mercury" (GOM) [also sometimes called "Reactive Gaseous Mercury" (RGM)] using coated denuders may be underestimates of the true concentration in the atmosphere. For example, Lyman et al. (2010) found that atmospheric ozone reduced the efficiency and retention of GOM capture on KCl-coated denuders. Denuders exposed to ozone lost from 29-55% of loaded $HgCl_2$ and $HgBr_2$. Collection efficiency of denuders decreased by 12-30% for denuders exposed to 50 ppb of O_3. There are other examples and hypothesized explanations of this potential measurement bias (Kos, Ryzhkov et al. 2013, Jaffe, Lyman et al. 2014, Ariya, Amyot et al. 2015, Gustin 2015, Weiss-Penzias, Amos et al. 2015).

Given the uncertainties in emissions, atmospheric chemistry and measurements, and the scarcity of measurements, it is difficult to determine the relative importance of the above possible factors – or if there are other factors – causing the model vs. measurement discrepancy for Hg(II). Further work to improve understanding of these phenomena will be needed to reduce uncertainties and to explain and reduce these discrepancies.

4.3.3. Comparison of Modeled vs. Measured Particulate Mercury

Figure 70 shows a comparison of modeled vs. measured particulate mercury, for all sites for which model evaluation data could be assembled. Like Hg(II), the concentrations of Hg(p) are dramatically smaller than Hg(0) (e.g., see Figure 58, page 71), and the modeling results generally reproduce this tendency. However, like with Hg(II) above, there are differences between the modeled and measured Hg(p) concentrations. For most of the sites, the model overpredicts the measured Hg(p) concentrations, but for a few sites, the model underestimates the measured concentrations.

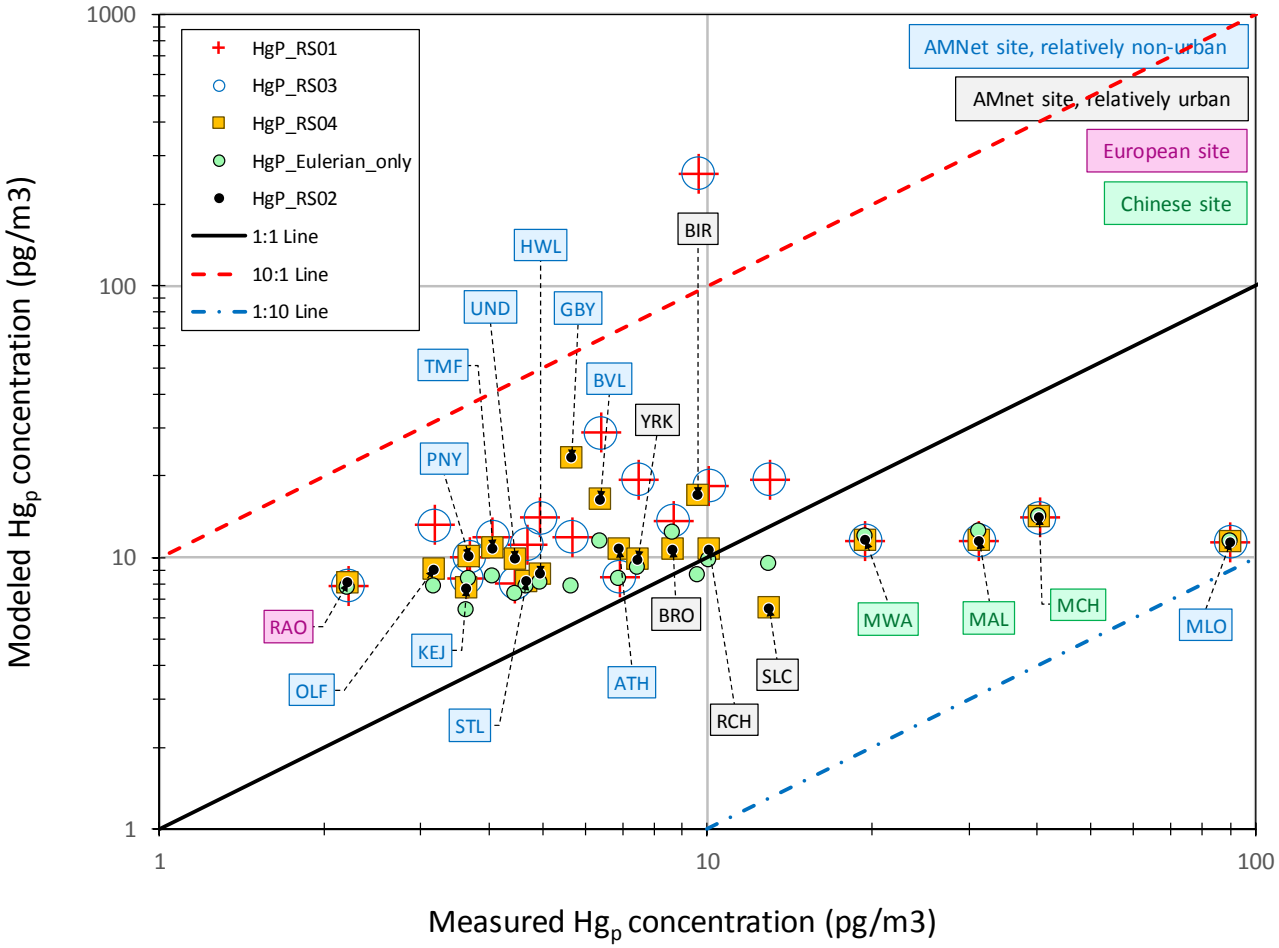

Figure 70. Modeled vs. Measured HgP (aka PBM or FPM) Concentrations.

As discussed in Section 3.4 (above, page 44), the HYSPLIT-Hg model includes and additional "form" of mercury. This additional form – Hg2s – is Hg(II) reversibly absorbed onto soot in the atmosphere. In Figure 71 (logarithmic scale) and Figure 72 (linear scale) below, the modeled concentration of Hg2s and Hg(p) have been added together and their sum compared against the measured Hg(p) concentrations at each site. It can be seen that the added Hg2s increases the modeled total for all sites.

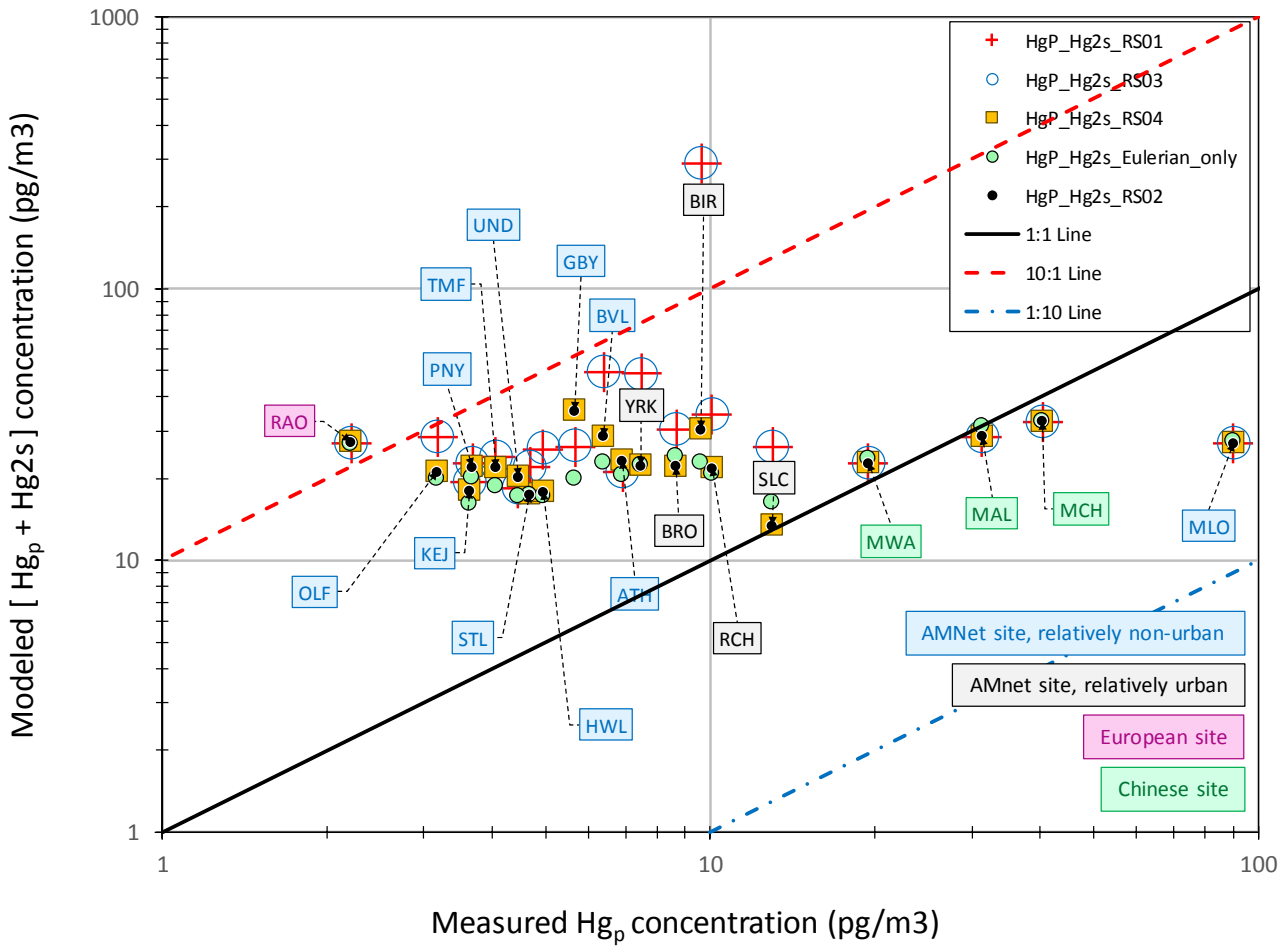

Figure 71. Modeled [HgP + Hg2s] vs. Measured HgP (aka PBM or FPM) Concentrations, Logarithmic scale.

Based on the measurement protocols used, the measurements of Hg(p) generally represent mercury on atmospheric particles less than approximately 2.5 µm in aerodynamic diameter. Mercury on larger particles are not generally measured with the prevailing measurement methodologies, by design. Thus, the measurements are more accurately called "Fine Particulate Mercury" (aka FPM), and are understood to be only a fraction of the total particulate mercury in the atmosphere. There are very limited data on the size distribution of Hg(p). In a related study investigating aerosol mercury at a marine and a coastal site, significant mercury was often found in coarse aerosol size fractions (Feddersen, Talbot et al. 2012). In some cases, the majority of Hg(p) appeared to exist on particles larger than 2.5 microns in size, although this was not always found. Keeler et al. (1995) found that, on average, about 88% of Hg(p) was associated with particles less than 2.5 microns in measurements in Detroit, but this varied from 60% - 100%, depending on conditions. The modeled values of Hg(p) and Hg2s considered here represent mercury on all particle sizes – both smaller and larger than 2.5 µm – and so, all things being equal, would be expected to be larger than the measured values of FPM. As can be seen in all of the figures in this section, the modeled particulate mercury does tend to be larger than the measurements of fine particulate mercury, for most sites.

Additionally, the measurement of Hg(p) is somewhat uncertain. In a comparison of Hg(p) measured with manual (filter) and automated (Tekran) methods, Talbot and colleagues (2011) found that manually-measured concentrations 21% higher than automated concentrations, on average. Further, they found that as much as 85% or more of the data showed a difference of greater than 25%.

At the Mauna Loa Observatory site (MLO), the reported measured concentrations of Hg(p) are greater than the modeled estimates. It has been observed at MLO under some conditions that Hg(0) is converted to Hg(p) *within* the measurement system (Luke, Kelley et al. 2016). This artifact appears to occur in very dry air and may occur at other sites as well. However, the occurrence of these conditions at MLO may be much more prevalent than other typical sites. The high elevation MLO site frequently samples free troposphere air with very low water content.

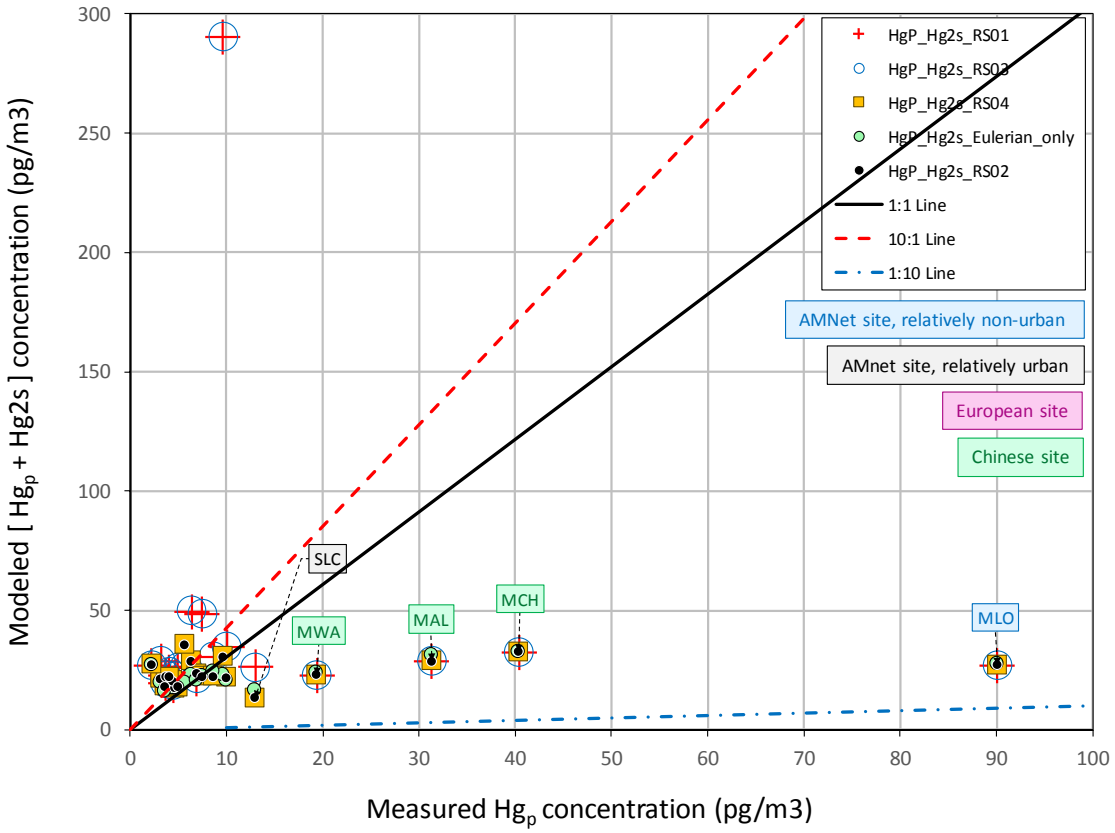

Figure 72. Modeled [HgP + Hg2s] vs. Measured HgP (aka PBM or FPM) Concentrations, Linear Scale.

4.3.4. Comparison of Modeled vs. Measured Non-Elemental Mercury

In light of the numerous issues related to the comparison of modeled Hg(II) and Hg(p) concentrations with measurements, the total modeled "non-Hg(0)" concentrations – Hg(II) + Hg2s + Hg(p) – are compared against the total measured "non-Hg(0)" concentrations – Hg(II) + Hg(p) – in Figure 73 through Figure 75, below. Many of the same general tendencies found in the above sections for Hg(II) and Hg(p) – e.g., for the model estimates to be higher than the reported measurements – are observed here. However, the correlation between modeled and measured values is relatively high. The correlation coefficient (r^2) for a linear regression of the model vs. measurement comparison is 0.38, compared to the 0.33 for Hg(II) and ~0 for Hg(p).

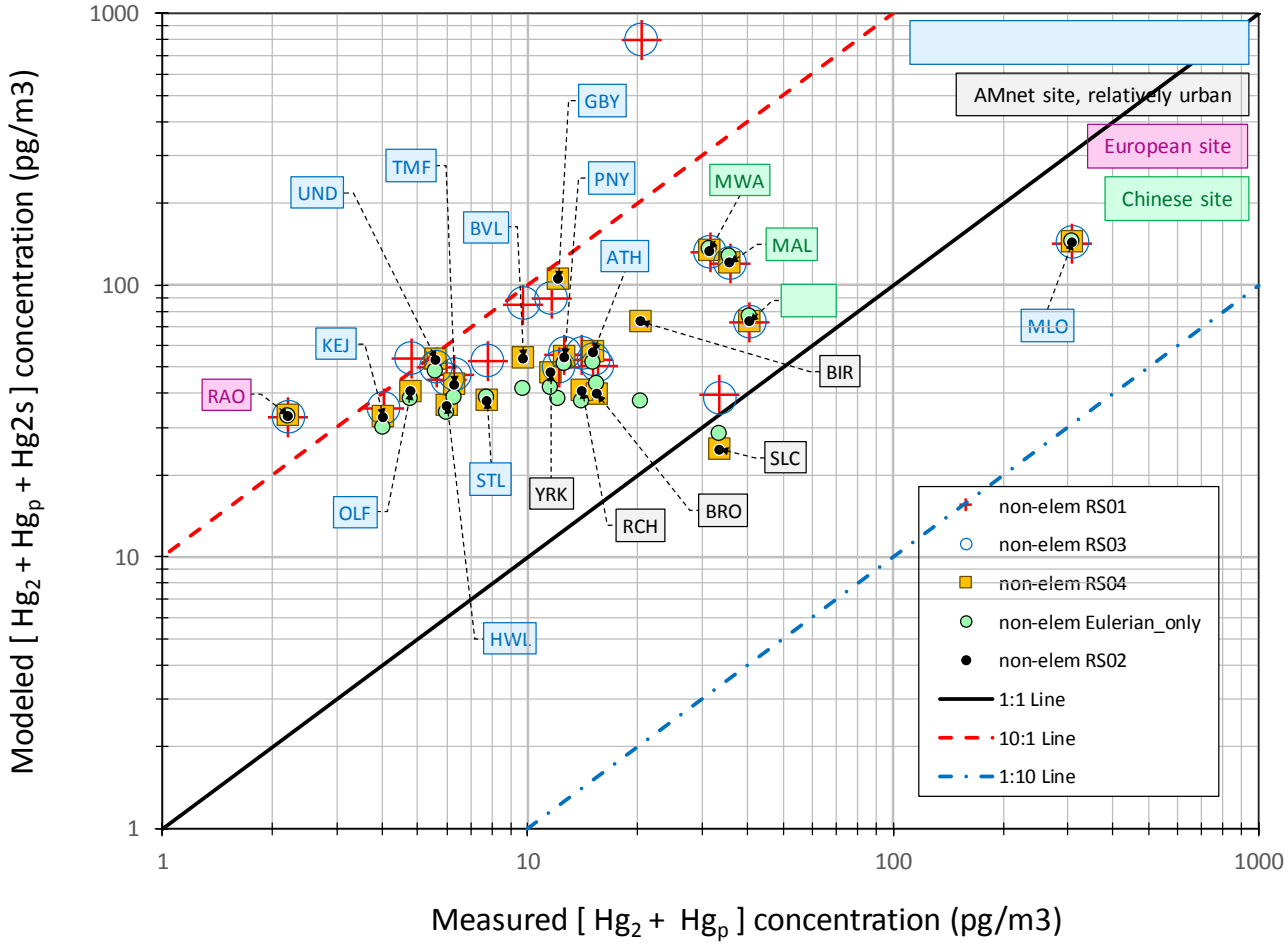

Figure 73. Modeled vs. Measured Total Non-Hg_0 Concentrations, Log Scale.

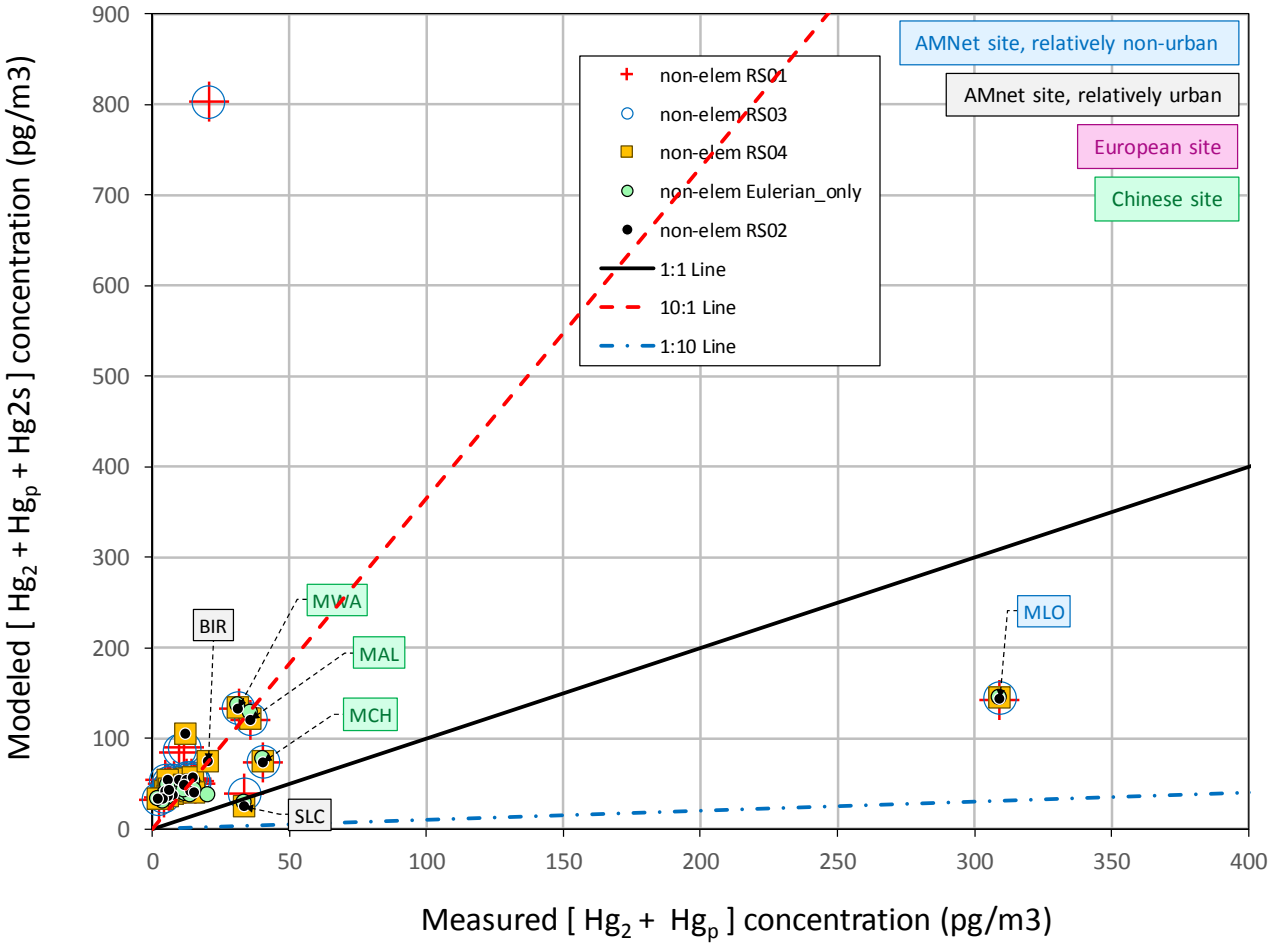

Figure 74. Modeled vs. Measured Total Non-Hg0 Concentrations, Linear Scale.

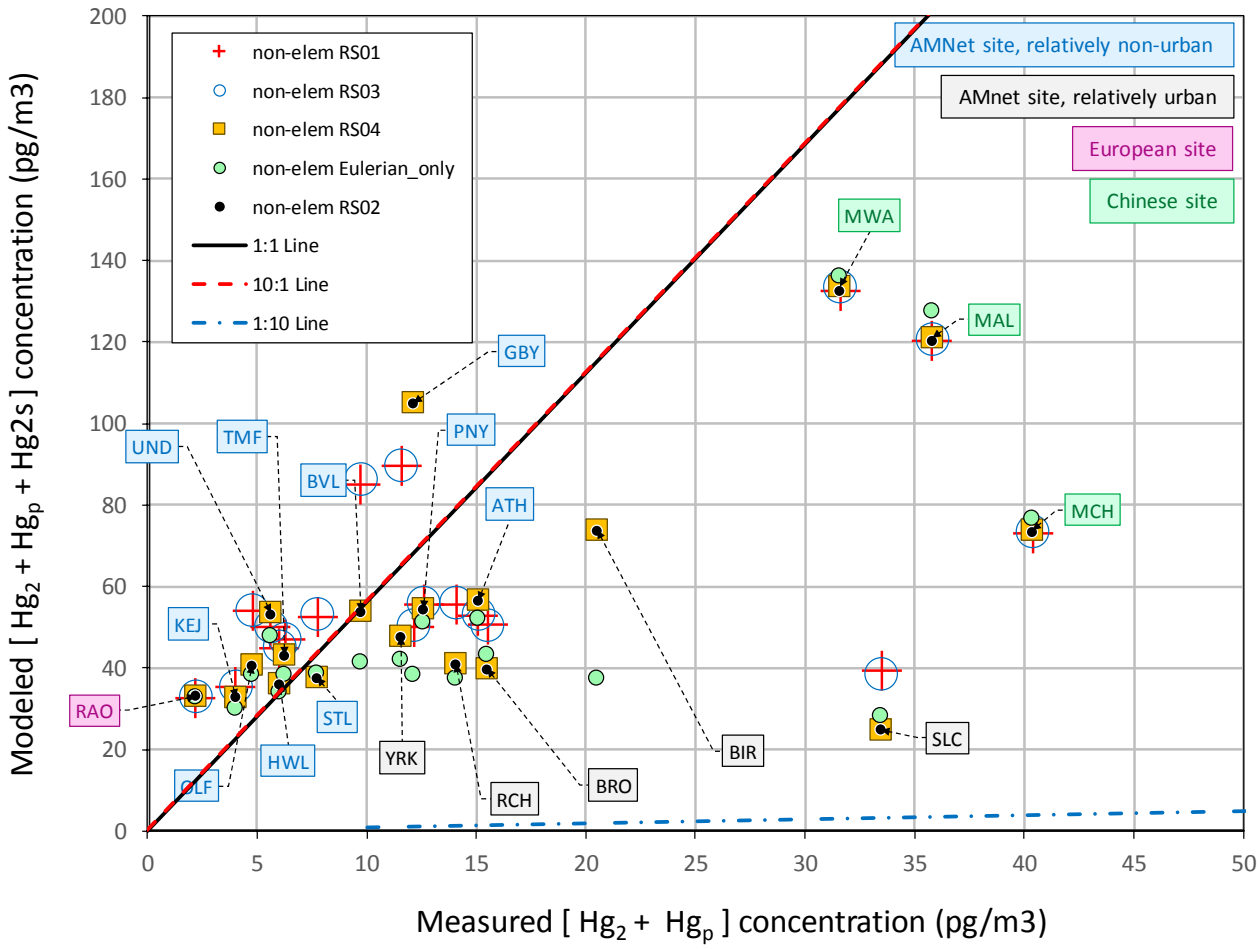

Figure 75. Modeled vs. Measured Total Non-Hg0 Concentrations, Linear Scale, zoomed in.

4.4. Atmospheric mercury wet deposition data used for model evaluation

Measured wet deposition of total mercury in North America was obtained from the Mercury Deposition Network (MDN) (National Atmospheric Deposition Program 2012). A total of 103 MDN sites were operating at the start of 2011 and were still operating at the end of 2011. Of these 103 sites, 31 were in the Great Lakes region, 10 were in the Gulf of Mexico region, 8 were elsewhere in the Southeastern U.S. (but not in States adjacent to the Gulf of Mexico), 7 were in the mid-Atlantic region, 9 were in the Northeast (including Kejimkujik in Nova Scotia, Canada), 9 were in California, Washington or Alaska, 13 were in inland Western states and provinces, and 16 were in the Midwest. These sites are shown with color-coded category designations in Figure 76 through Figure 80. Note that all sites are shown in Figure 76, but in Figure 77 through Figure 80, the sites in Alaska are not shown in order to provide an enlarged view of the remaining sites.

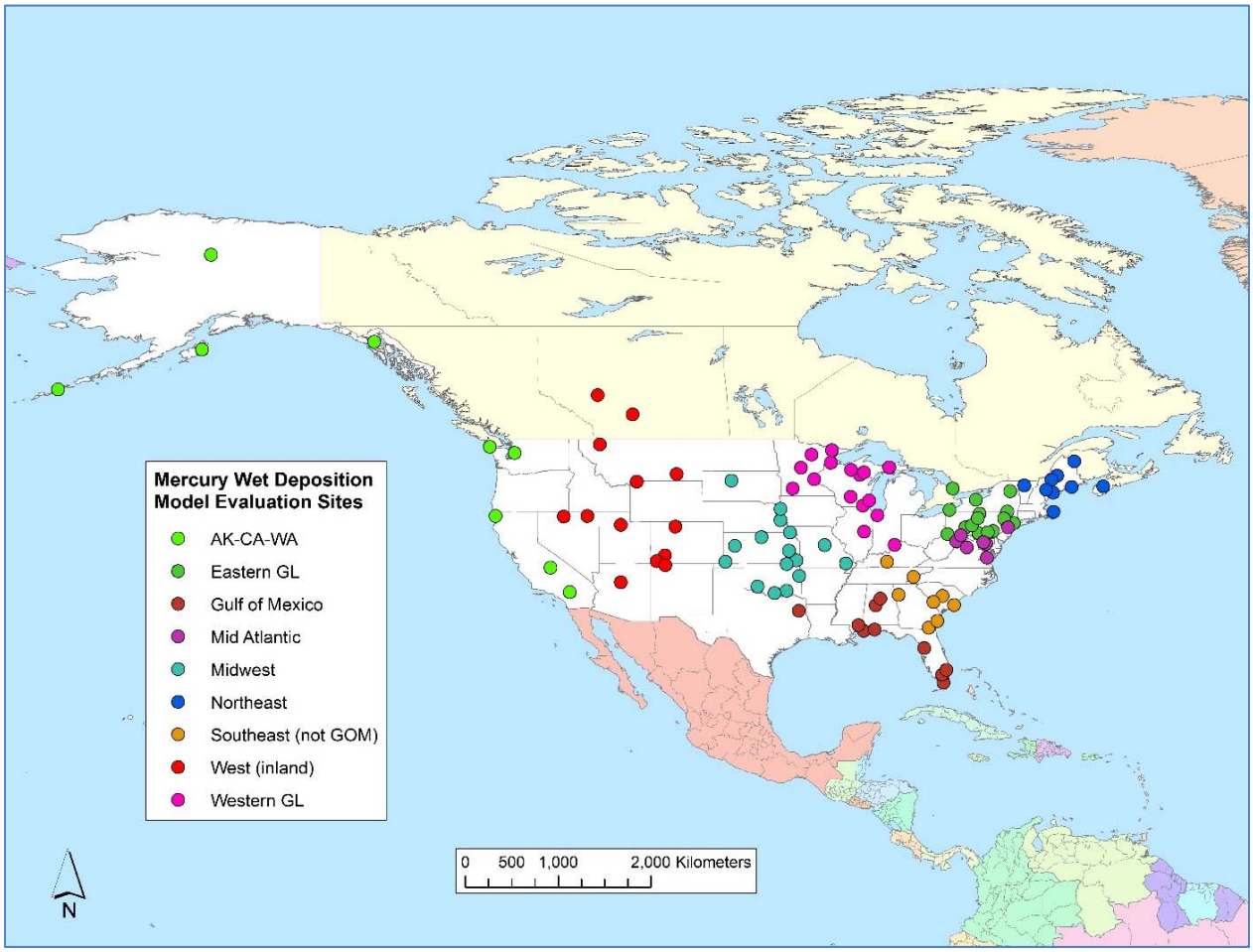

Figure 76. Mercury Deposition Network sites used for model evaluation.

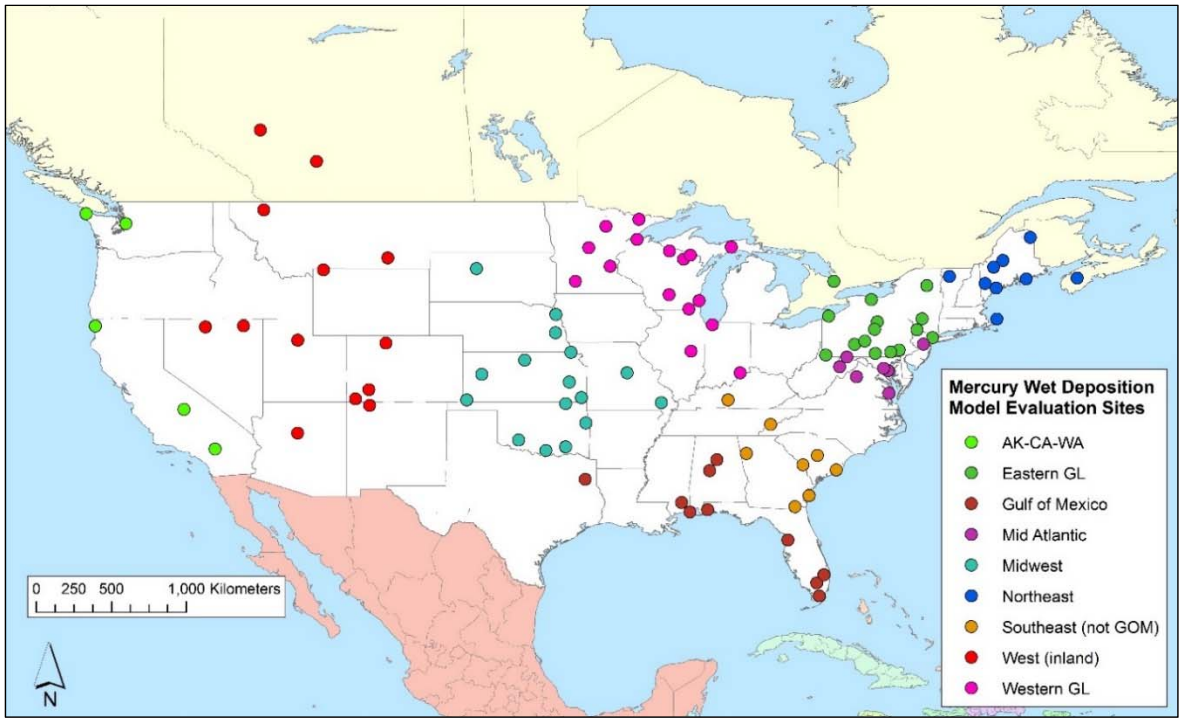

Figure 77. Mercury Deposition Network sites used for model evaluation, except for sites in Alaska.

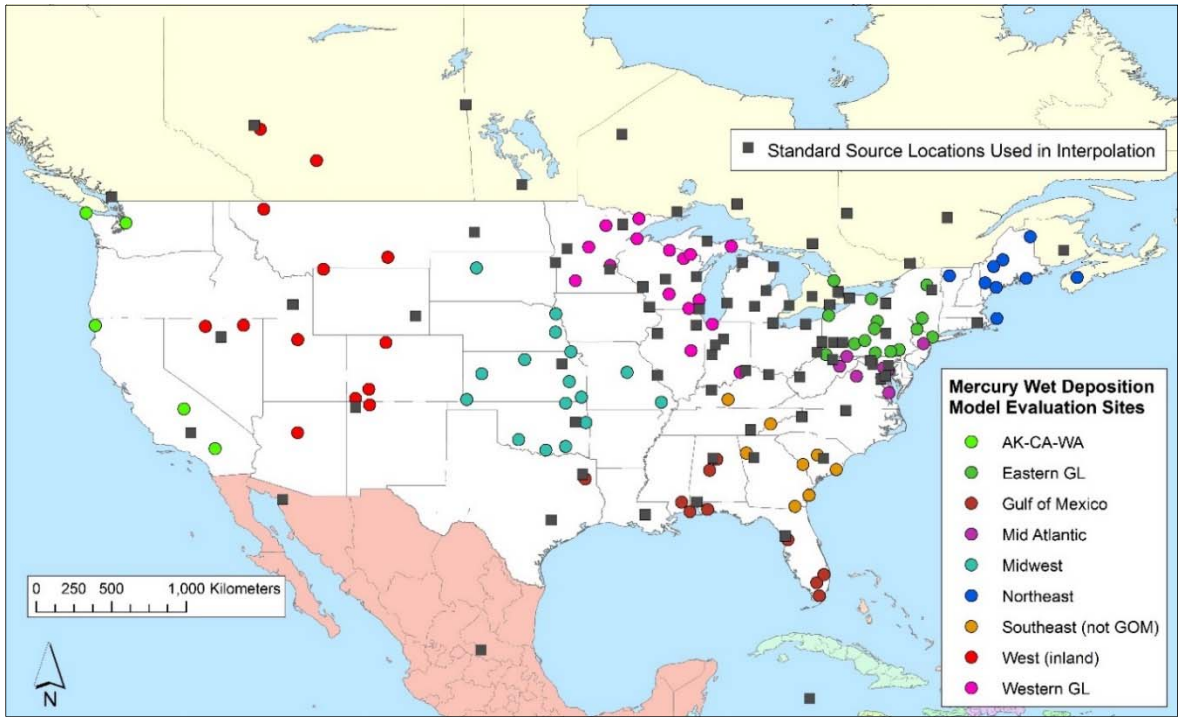

Figure 78. Mercury Deposition Network sites used for model evaluation, except for sites in Alaska. Standard source locations used in the analysis are also shown.

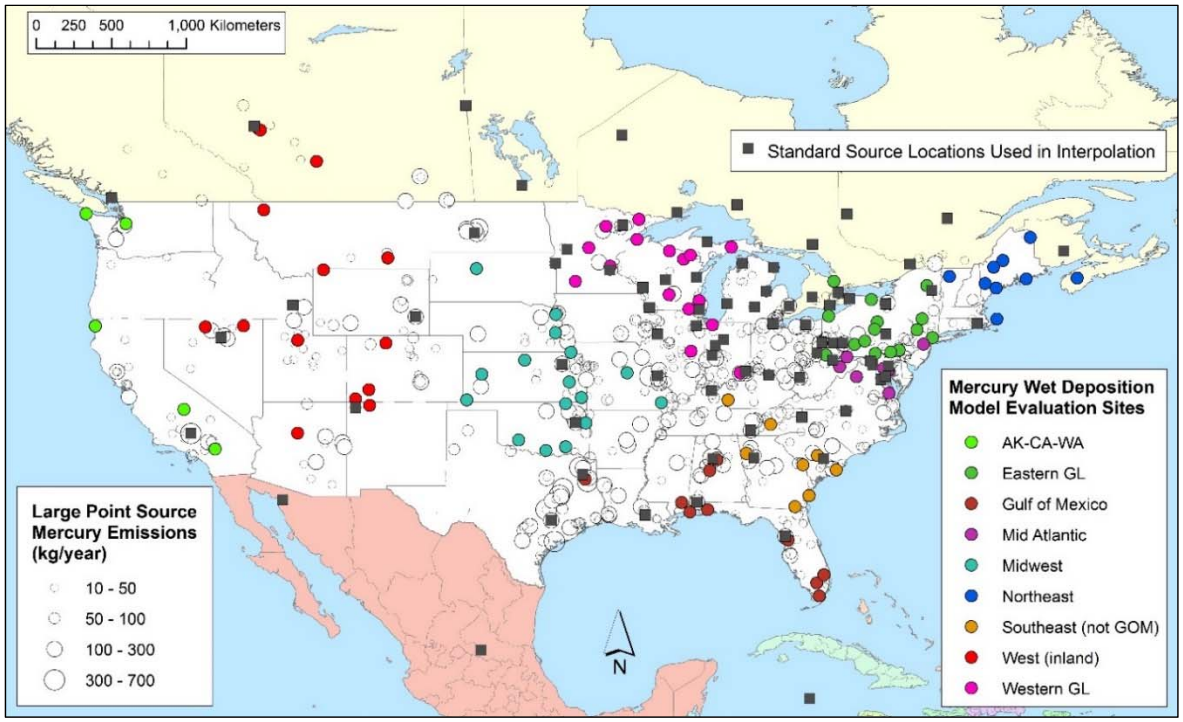

Figure 79. Mercury Deposition Network sites used for model evaluation, except for sites in Alaska. Standard source locations used in the analysis and large mercury point sources are also shown.

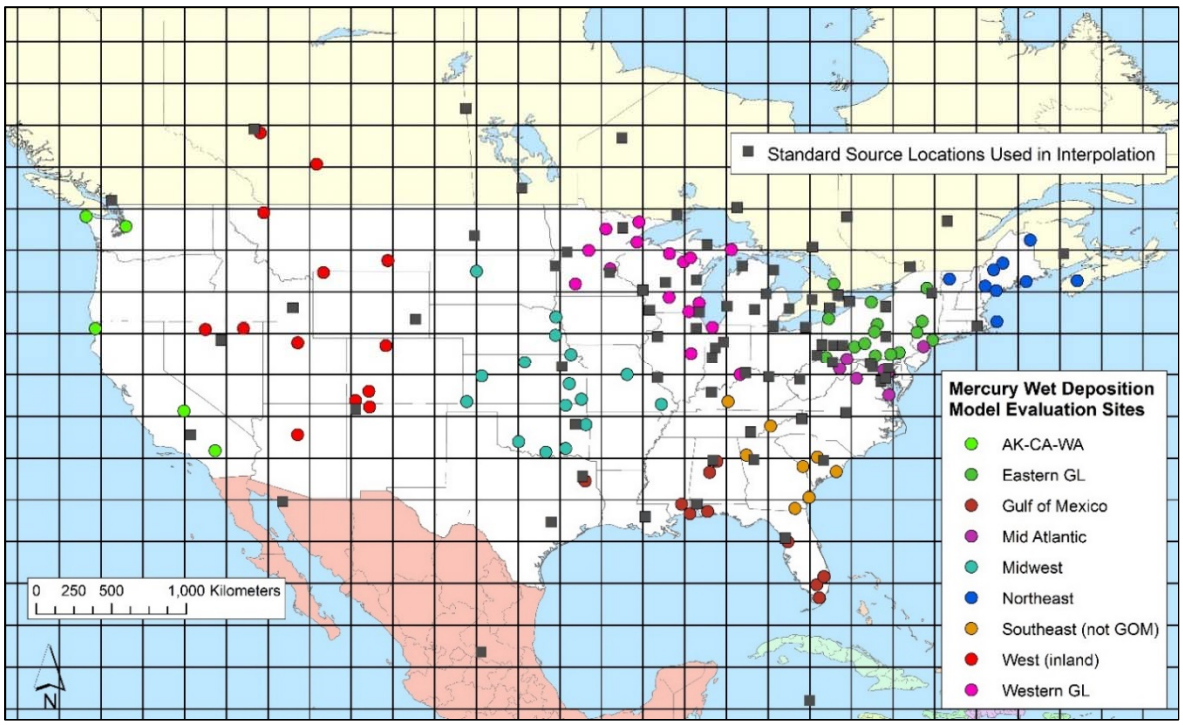

Figure 80. Mercury Deposition Network sites used for model evaluation, except for sites in Alaska. Also shown are the standard source locations used and the 2.5 degree grid used in some of the simulations.

4.5. Comparison of model vs. measured atmospheric mercury wet deposition

As noted above in Section 3.7 above, the precipitation measured at the MDN sites was not identical to the precipitation in the various meteorological datasets used to drive the HYSPLIT-Hg model. Precipitation at a specific location within a meteorological grid cell – e.g., at an MDN site – would not generally be the same as the grid cell average, even if both the model and measurements were "perfect". In comparing HYSPLIT-Hg model output with measured mercury wet deposition, the modeled flux at measurement locations was multiplied by the ratio of measured to modeled precipitation, in a post-processing procedure. It is recognized that the impact of subgrid variations and precipitation errors in the meteorological datasets will introduce complex, non-linear deviations in the simulations. So, using the measured/modeled precipitation ratio at any given site is recognized as an approximation.

Figure 81 shows the modeled wet deposition – using each of the different run schemes, as described in Section 3.3 (beginning on page 36) – compared against the measured wet deposition of mercury at the 15 MDN sites in the Eastern Great Lakes region.

The two run schemes using NCEP/NCAR 2.5 degree meteorological data for their Lagrangian simulation components – RS-01 and RS-03 – are shown as green squares, while the two runs schemes using NARR 32km meteorological data for their Lagrangian simulation components – RS-02 and RS-04 are shown as red squares. Data for the Eulerian-only run scheme using only NCEP/NCAR 2.5 degree meteorological data – RS-00 – are shown as green dots. Note that RS-00 is denoted in the legend as "combined GEM 2.5 deg grid, US/CAN-2011". The "GEM" part of this designation denotes the use of the "Global Eulerian Model", and the US/CAN-2011 denotes the use of 2011 emissions data for the United States and Canada, as described in Section 2 (starting on page 20, above).

It can be seen that RS-01 and RS-03 show very similar results, as might be expected. As described in Section 3.3.3 above (page 43), the only difference between RS-03 and RS-01 is that the Hg(0) and Hg(II) simulations done for the 79 North American Standard Source Locations (SSL's) were carried out using a combined Lagrangian-Eulerian modeling methodology ("COM"). With the COM approach, emissions from any given SSL are first modeled as Lagrangian puffs, and then, after a puff age of 3 weeks, the Lagrangian puff mass was transferred to an Eulerian grid. From that point on, that mass was simulated on a global Eulerian grid.

It can also be seen that the results for the Eulerian-only simulations (green dots) are generally closer to the RS-01 and RS-03 results (green squares) than they are to the RS-02 and RS-04 results (red circles), suggesting that the meteorological dataset used – NCEP/NCAR 2.5 degree vs. NARR 32 km – has a relatively big influence on the overall results.

Figure 82 and Figure 83 show comparable comparisons for MDN sites in the Western Great Lakes and Northeastern U.S. regions, respectively, and the results are seen to be relatively consistent with the general observations made above regarding the similarities and differences among the different run schemes.

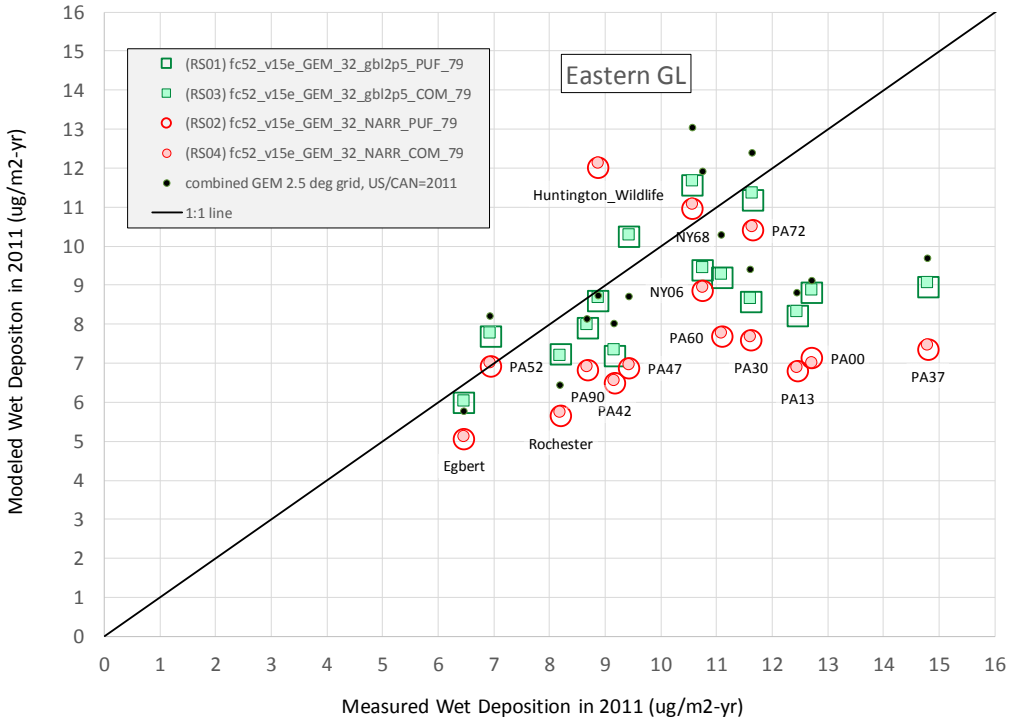

Figure 81. Modeled vs. measured mercury wet deposition at MDN sites in the Eastern Great Lakes region.

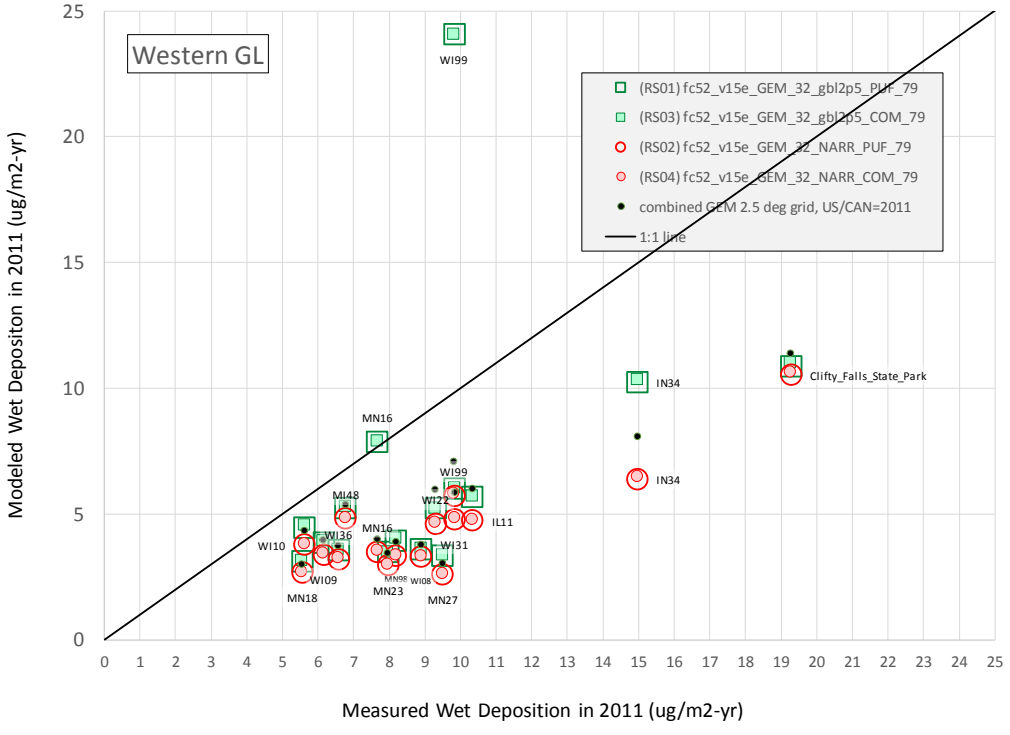

Figure 82. Modeled vs. measured mercury wet deposition at MDN sites in the Western Great Lakes region.

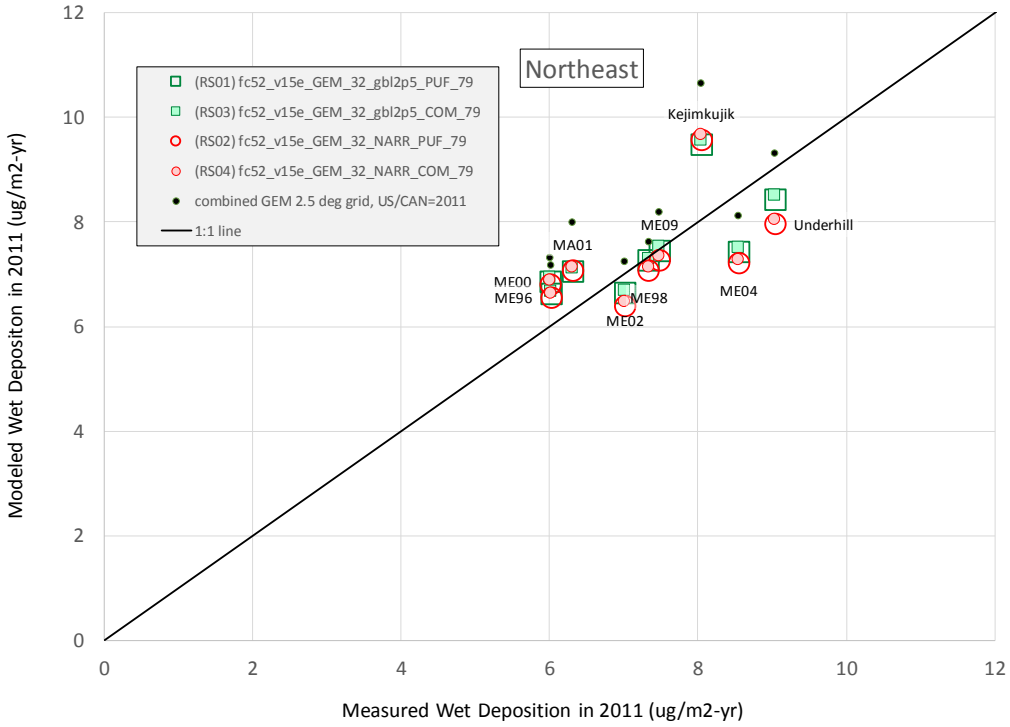

Figure 83. Modeled vs. measured mercury wet deposition at MDN sites in the Northeastern U.S. (and Southeastern Canada).

The focus in this work is the estimation of source-receptor relationships for the Great Lakes, and so, the most computational resources have been expended for the Great Lakes region, i.e., the density of Standard Source Locations (SSL's) is much higher in the Great Lakes region than elsewhere (e.g., see Figure 78). Thus, the results for the Great Lakes region – and the region immediately downwind from this region, the Northeastern U.S. – are considered the most important "test" of the model results. However, even in these regions, the density of SSL's could be increased. Analogous comparisons for MDN sites in other regions are shown in the Appendix, Section 7.3 (beginning on page 173).

Overall, the correlation between modeled and measured values is encouraging, although the model shows a modest tendency to underpredict the measured wet deposition. This finding is in contrast to tendency documented above for the model to overpredict non-elemental mercury concentrations. These countervailing tendencies were also found in previous work with the HYSPLIT-Hg model (Cohen, Draxler et al. 2016), and suggest that the model representation and parameterization of wet deposition phenomena may be biased unrealistically "low". Increased scavenging of non-elemental mercury species by precipitation would increase the predicted wet deposition and decrease the predicted atmospheric concentrations, moving the model predictions of both closer to the measurements.

Nair et al. (2013) carried out cloud-resolving simulations of mercury wet deposition processes in several case studies in the Northeastern and Southeastern U.S. This study is of particular interest as this an many other modeling simulations have tended to underpredict mercury wet deposition in the Southeastern U.S. It was found that wet deposition in typical Northeastern thunderstorms would generally be less than comparable storms in the Southeast – assuming identical atmospheric concentrations of mercury – due to difference in typical cloud dynamics between the two regions. In addition, it was found that stratiform precipitation typically only scavenges mercury from the lowest ~4 km of the atmosphere, while Southeastern thunderstorms can scavenge mercury up to ~10 km.

In another wet deposition process analysis, apparent scavenging ratios, based on ground-level measurements of speciated air concentrations of mercury and total mercury in precipitation, were studied at four sites in the Northeastern U.S. (Huang et al., 2013). While the use of ground-based measurements introduced inherent uncertainties, the authors suggested that GOM concentrations may be underestimated by current measurements, as scavenging ratios based on existing GOM measurements appeared anomalously high.

5. Simulation Results

5.1. Global Mercury Budget

Figure 84 shows a summary of the 2011 emissions and deposition fluxes for the Eulerian-only case (RS-00). The total mercury emissions – using the net emissions of Hg(0) from soil/vegetation and the ocean – was ~5700 Mg/yr, while the total, comparable deposition was ~5450 Mg/yr. Note that more significant figures are shown in this figure than are justified by the accuracy of the estimates, in order to preserve the values for future calculations without introducing unnecessary round-off error. The slight (~3%) imbalance between emissions and deposition may reflect one or more of the following situations:

- The emissions and deposition for any given year will not usually balance out exactly, even if the global system is at "steady state", as both are governed by numerous stochastic processes.
- Like all mercury models, there are numerous uncertainties in characterization of emissions and deposition.
- Emissions during 2011 may have been increased relative to previous years.

Overall, the net flux of Hg(0) from terrestrial surfaces – not including anthropogenic, biomass burning, and geogenic sources – is estimated to be ~560 Mg/yr during 2011, i.e., there was a net upward flux of elemental mercury from terrestrial surfaces. For the ocean, the comparable, model-estimated net Hg(0)flux during 2011 is ~2500 Mg/yr. As shown in Figure 26 above (page 33), these net flux results are reasonably consistent with many other mercury modeling analyses.

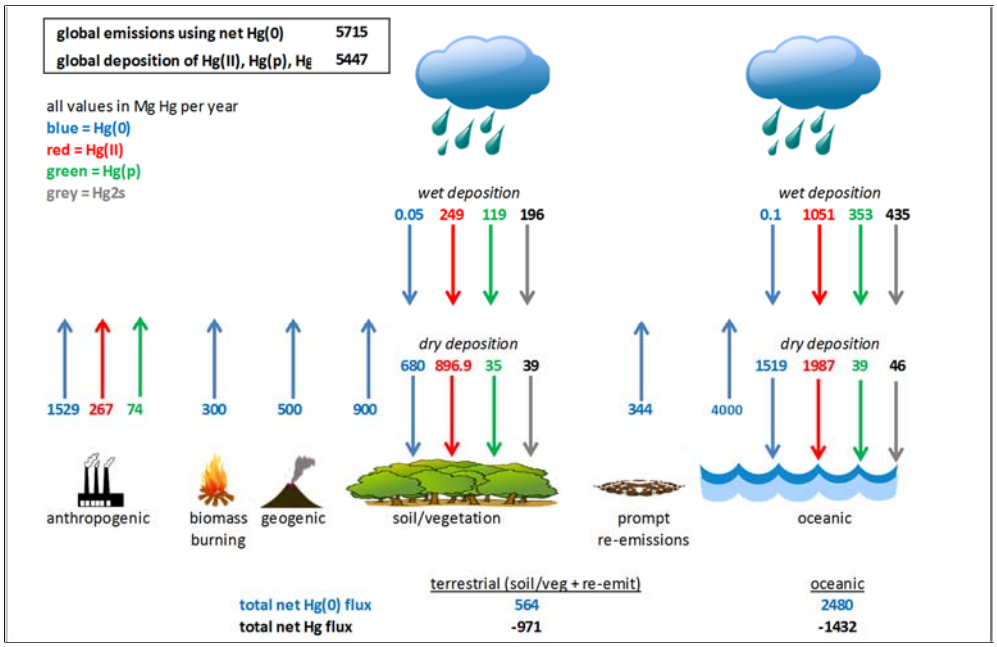

Figure 84. Overall global mass balance (RS-00).

5.2. Source Attribution for Great Lakes Mercury Deposition

The model results presented in this section are for deposition directly to the lakes. Estimates for deposition to each lake's watershed were also made, but are not shown here.

It is important to remember that a significant fraction of the emissions (and associated deposition contributions) from the ocean, land/vegetation, prompt re-emission, and biomass burning represent re-emissions of previously deposited mercury that had been emitted by anthropogenic sources. These re-emissions can be considered to be "indirect anthropogenic emissions". The results presented for the "Total Anthropogenic" category, and for specific countries (e.g., the U.S., Canada, China, etc.) include only the impacts from "direct anthropogenic emissions sources", i.e., manufacturing facilities, power plants burning fossil fuels, metallurgical operations, waste incineration, and other activities that result in mercury emissions. Thus, the "direct" anthropogenic contributions reported here are only fractions of the true contributions from "direct" and "indirect" anthropogenic emissions. As noted earlier, a recent study has estimated that the largest mercury contributor to the global oceanic and terrestrial environment has been North America, even though emissions from Asia have exceeded emissions from North America since the 1970's (Chen, Zhang et al. 2018).

Overall, as will see shortly from the results presented in this section, contributions to the Great Lakes from global oceanic and terrestrial reservoirs – containing significant amounts of previously deposited anthropogenic emissions – are on the order of ~60% of the total modeled deposition. A large fraction of these contributions – likely on the order of 67% or more – can be attributed originally to anthropogenic emissions. The value of 67% or more cited here is estimated based on typical mercury enrichment factors in the global oceanic and terrestrial environment of 2x - 4x, as compared to pre-industrial levels (e.g., Chen, Zhang et al. 2018). An enrichment factor of 2x can be interpreted as meaning that 2/3 (67%) of the mercury present came from anthropogenic activities and 1/3 is present due to natural processes. An enrichment factor of 3x would imply that ¾ (75%) of the mercury present is due to anthropogenic activities and ¼ (25%) is present due to natural processes.

While consideration of the results from each of the various Run Schemes is interesting, the most important results here are for Run Scheme 04, the most advanced, computationally intense, hybrid Lagrangian/Eulerian approach, and Run Scheme 00, the Eulerian-only approach. Run Schemes 01, 02, and 03, which also variants of the hybrid approach in Run Scheme 04, can be considered inherently less "accurate" than Run Scheme 04 given limitations due to the resolution of the meteorological data used and/or the ability of U.S./Canadian emissions to impact the Great Lakes after circling the world one or more times. The utility of considering the results of these less-accurate schemes lies in the quantification of the "trade-offs" made by the choice of less computationally intensive approaches.

Figure 85 through Figure 89 show the model-estimated contributions to atmospheric mercury deposition in 2011 to each of the Great Lakes, arising from direct anthropogenic emissions worldwide, aggregated on a 2.5^{o} x 2.5^{o} grid. Figure 90 through Figure 94 show analogous maps for the Great Lakes, just for U.S. and Canadian direct anthropogenic emissions, aggregated on a 1^{o} x 1^{o} grid.

Figure 95 shows the fraction of modeled atmospheric mercury deposition to Lake Superior from different source categories – anthropogenic (for selected specific countries, and all other countries), geogenic, biomass burning, prompt reemission, land/vegetation, and the ocean – for Run Scheme 04, the most advanced hybrid Lagrangian/Eulerian methodology used.

Figure 96 shows analogous results for Lake Superior, based on Run Scheme 00, the Eulerian-only modeling approach.

Figure 97 through Figure 104 show analogous results for the other Great Lakes, for both Run Scheme 04 and Run Scheme 00.

Figure 105 and Figure 106 show results for the total deposition to the Great Lakes, for Run Scheme 04 and Run Scheme 00, respectively.

Figure 107 and Figure 108 show analogous results for the Great Lakes, using a weighted average based on lake area.

The above figures show lake-by-lake (or average) results, for a particular run-scheme methodology. In the following figures, all of the lakes and all of the run-scheme methodologies are shown on the same plot, so that they can be more easily compared.

Figure 112 shows the shows the deposition attributed to different source types to each of the Great Lakes, for each of the run-scheme methodologies used Estimates are shown for each of the different run-scheme methodologies used. Figure 113 shows the same data, but scaled to 100% for each estimate for each lake, to illustrate the relative fractions each source sector contributed to each lake, for the various model estimates. Figure 114 and Figure 115 show just the data from the above figures for anthropogenic emissions.

Several observations can be made regarding these results.

- Run Schemes 01 and 03 employed a hybrid Lagrangian/Eulerian approach but used only the 2.5-degree NCEP/NCAR global reanalysis meteorological data would be expected to be more vulnerable to subgrid variations in the Lagrangian component of the analysis. It can be seen (e.g., Figure 109) that results for these schemes are indeed somewhat different than the analogous results for RS-02 and RS-04, especially for Lakes Erie and Ontario, as there is a much higher density of local and regional sources around these lakes.

- The differences between RS-02 and RS-04 are relatively small, even though the creation of the RS-04 results required 2.5x the computational resources than creation of the RS-02 results (see Table 4, page 18).

- A large fraction (on the order of 2/3 or more) of the emissions from the ocean, biomass burning, and terrestrial surfaces (“Land/Vegetation” and “Prompt Re-emission”, but excluding

"Geogenic" contributions) can be considered to be *indirect* anthropogenic sources, as the mercury being emitted is actually mercury previously emitted from anthropogenic sources that was previously deposited. So, while the combined contribution of these source categories ranges from 54% for Lake Erie to 67% for Lake Superior of the model-estimated deposition, 2/3 or more of this (i.e., 36% - 45% or more of the total modeled deposition to Lakes Erie and Superior, respectively) is likely attributable to *indirect* anthropogenic emissions.

- Thus, the total *direct* and *indirect* anthropogenic contributions to the Great Lakes is likely on the order of ~70% or more, with the following RS-04 estimates for each lake: Superior (69%), Huron (70%), Michigan (71%), Erie (75%), Ontario (72%). These estimates assume 2/3 of the emissions from oceanic and terrestrial reservoirs in 2011 were *indirect* anthropogenic emissions, but the fraction could be higher.
- *Direct* anthropogenic emissions tended to have the highest impact on Lake Erie (~38-40% of total estimated deposition) and the lowest impact on Lake Superior (~23-24%), with intermediate impacts on the other lakes.
- The importance of US *direct* anthropogenic emissions contributions to individual lakes varied from a high of ~21% for Lake Erie to a low of ~4% for Lake Superior.
- China was generally the country with the 2nd highest *direct* anthropogenic contribution, behind the United States, contributing on the order of ~5-7% of 2011 deposition to the Great Lakes basin. The importance of Chinese direct anthropogenic emissions contributions to individual lakes was much more uniform than that for the U.S., as expected, given their relative distance from the Great Lake region.
- Canada's *direct* anthropogenic sources were estimated to be most important for Lake Ontario (~7%) and least important for Lake Superior and Lake Michigan (<1%). Direct emissions from India, Mexico, and Russia were all estimated to contribute on the order of ~0.5–1% of the total 2011 deposition.
- The total *direct* anthropogenic contribution from all "other" countries in the world during 2011 was on the order of ~7-9% of the total model-estimated deposition.
- The remainder of the deposition came from oceanic natural emissions and re-emissions of previously deposited mercury from the oceans (~35-46%), terrestrial natural emissions and re-emissions (11-13%), prompt re-emissions (4-5%), biomass burning (~3-4%) and geogenic emissions (~7-9%).
- As noted above, for all of these non-direct-anthropogenic categories (except for geogenic sources, e.g., volcanoes), a significant fraction can be regarded as indirect anthropogenic contributions, i.e., they likely originally came from previously deposited direct anthropogenic emissions.

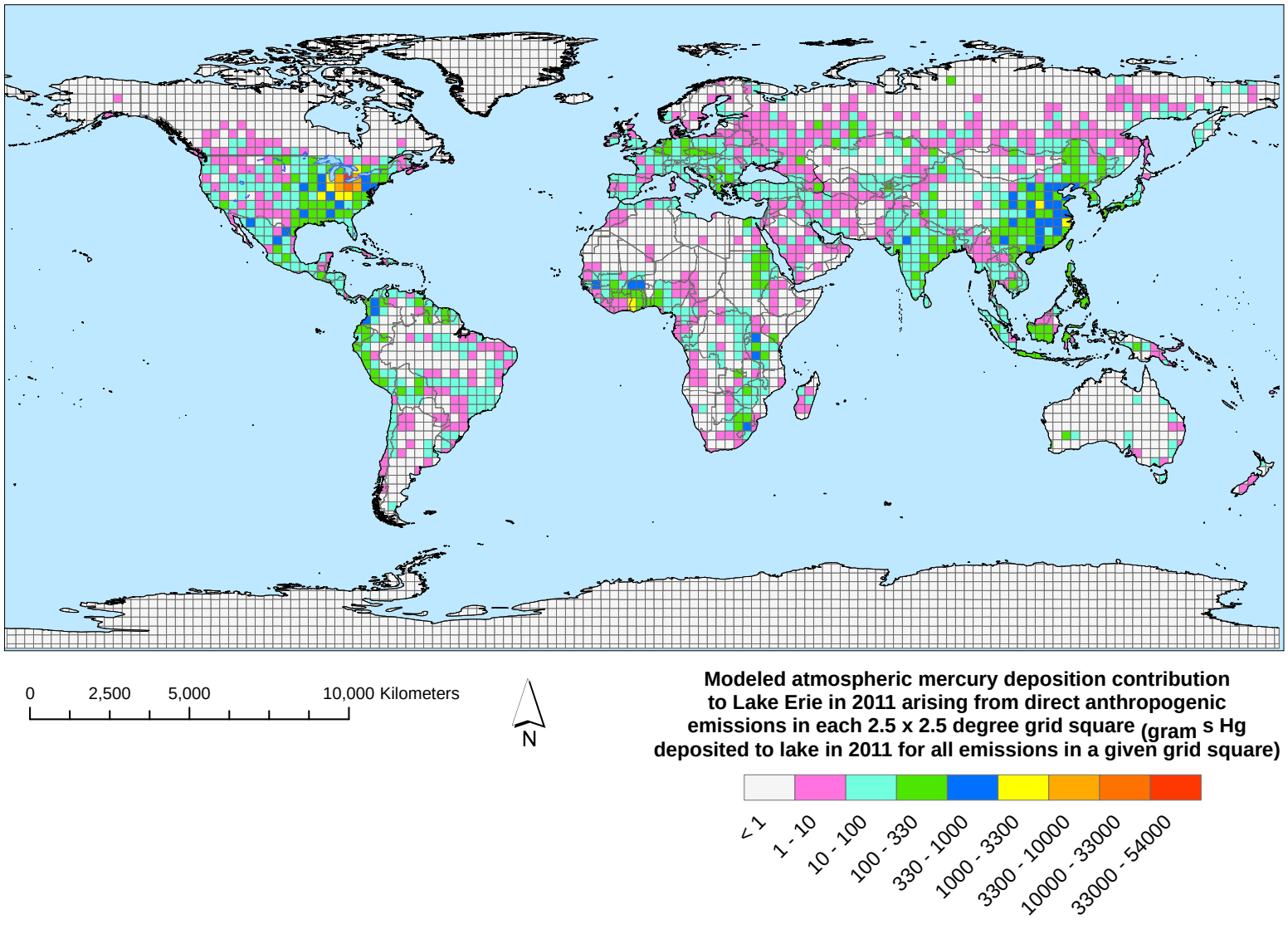

Figure 85. Modeled, gridded atmospheric mercury deposition contribution to Lake Erie in 2011 arising from direct anthropogenic emissions.

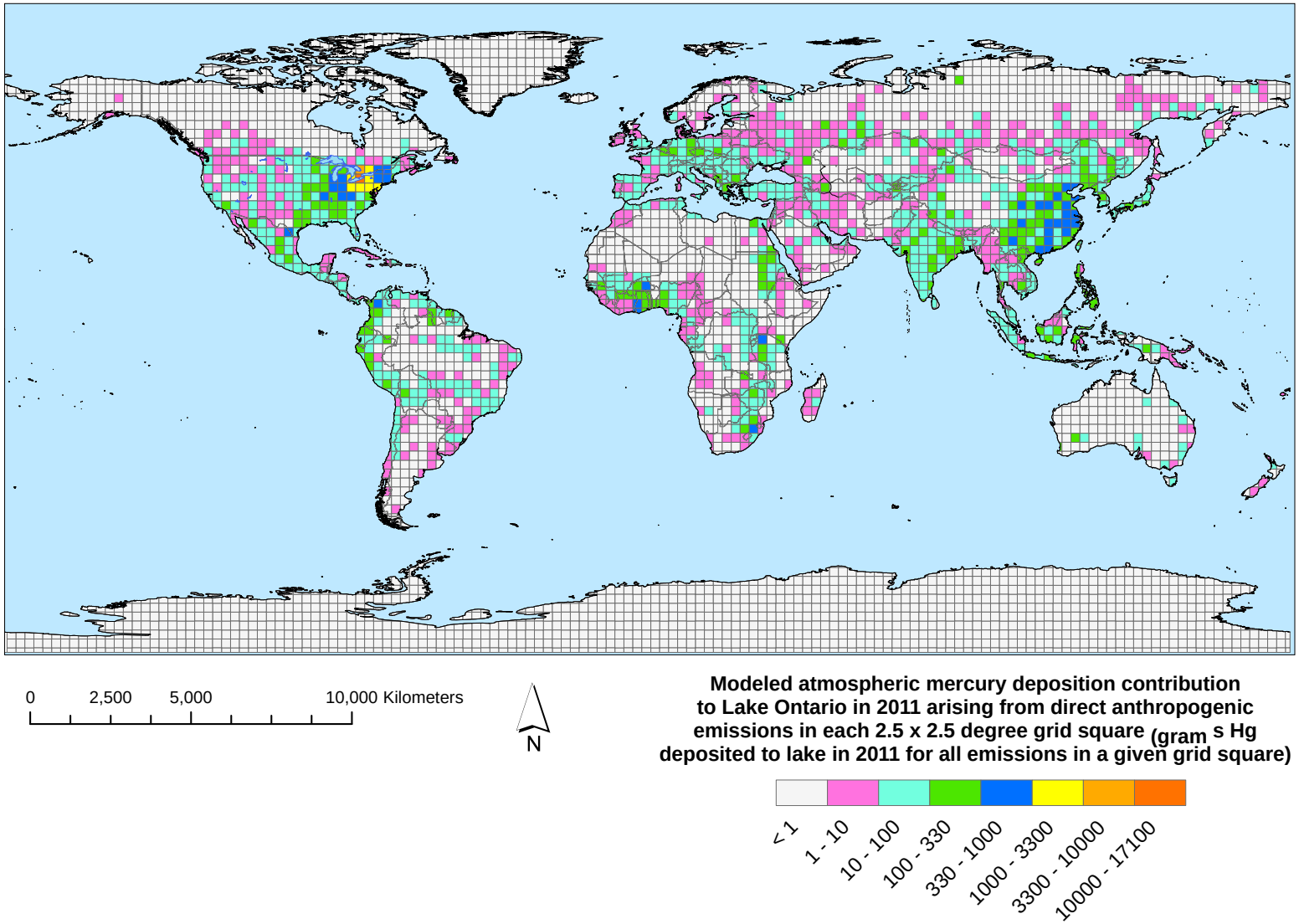

Figure 86. Modeled, gridded atmospheric mercury deposition contribution to Lake Ontario in 2011 arising from direct anthropogenic emissions.

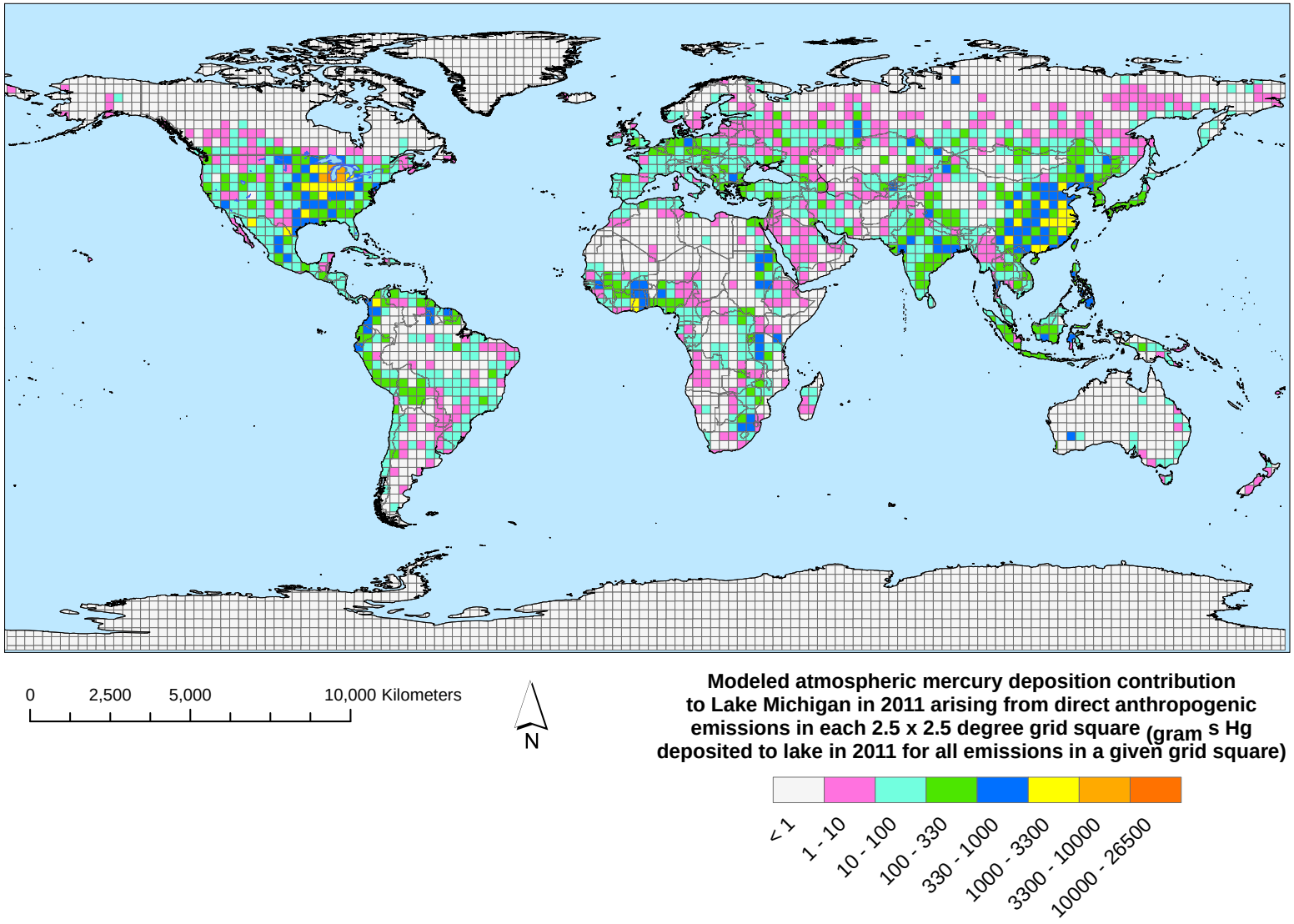

Figure 87. Modeled, gridded atmospheric mercury deposition contribution to Lake Michigan in 2011 arising from direct anthropogenic emissions.

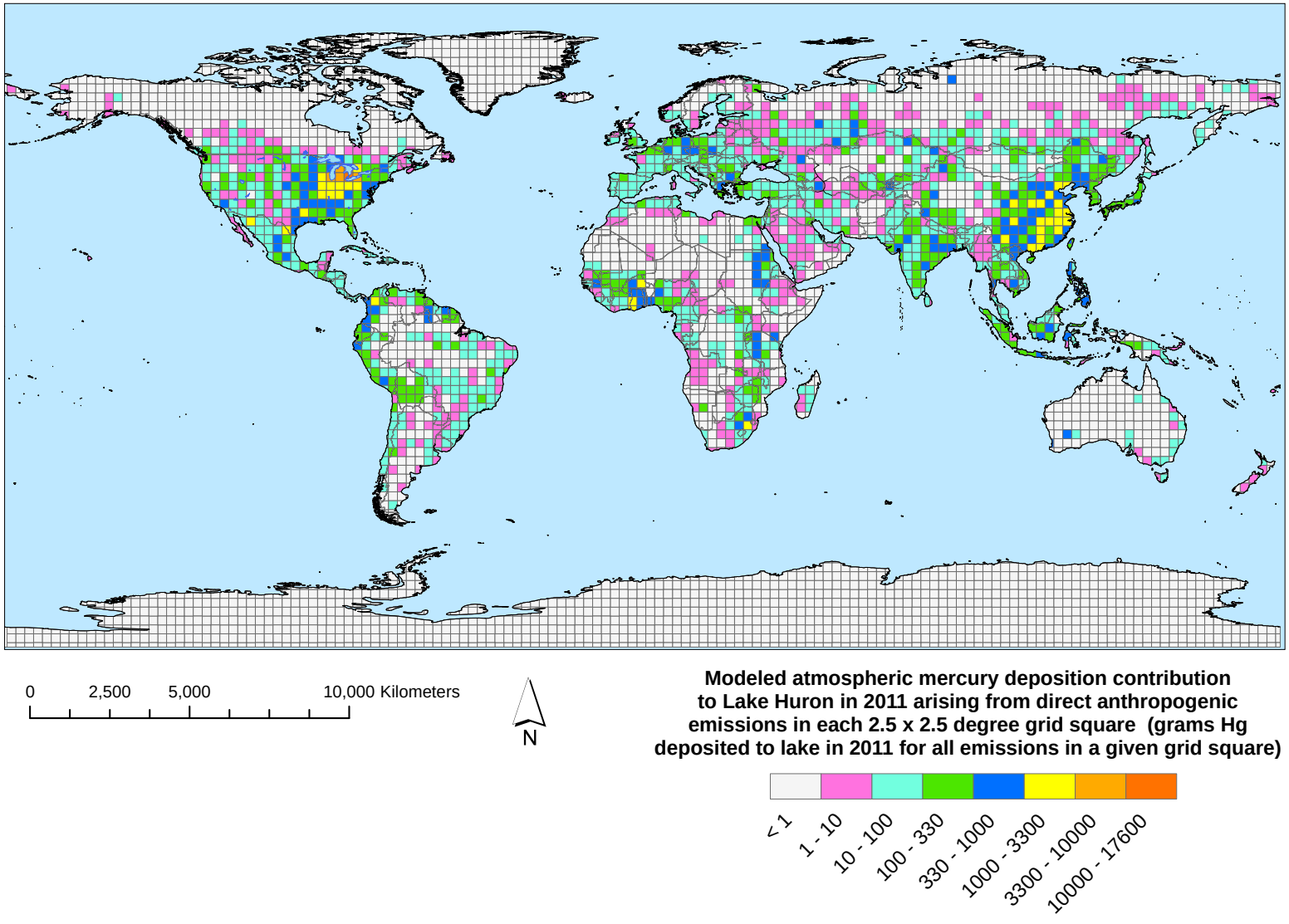

Figure 88. Modeled, gridded atmospheric mercury deposition contribution to Lake Huron in 2011 arising from direct anthropogenic emissions.

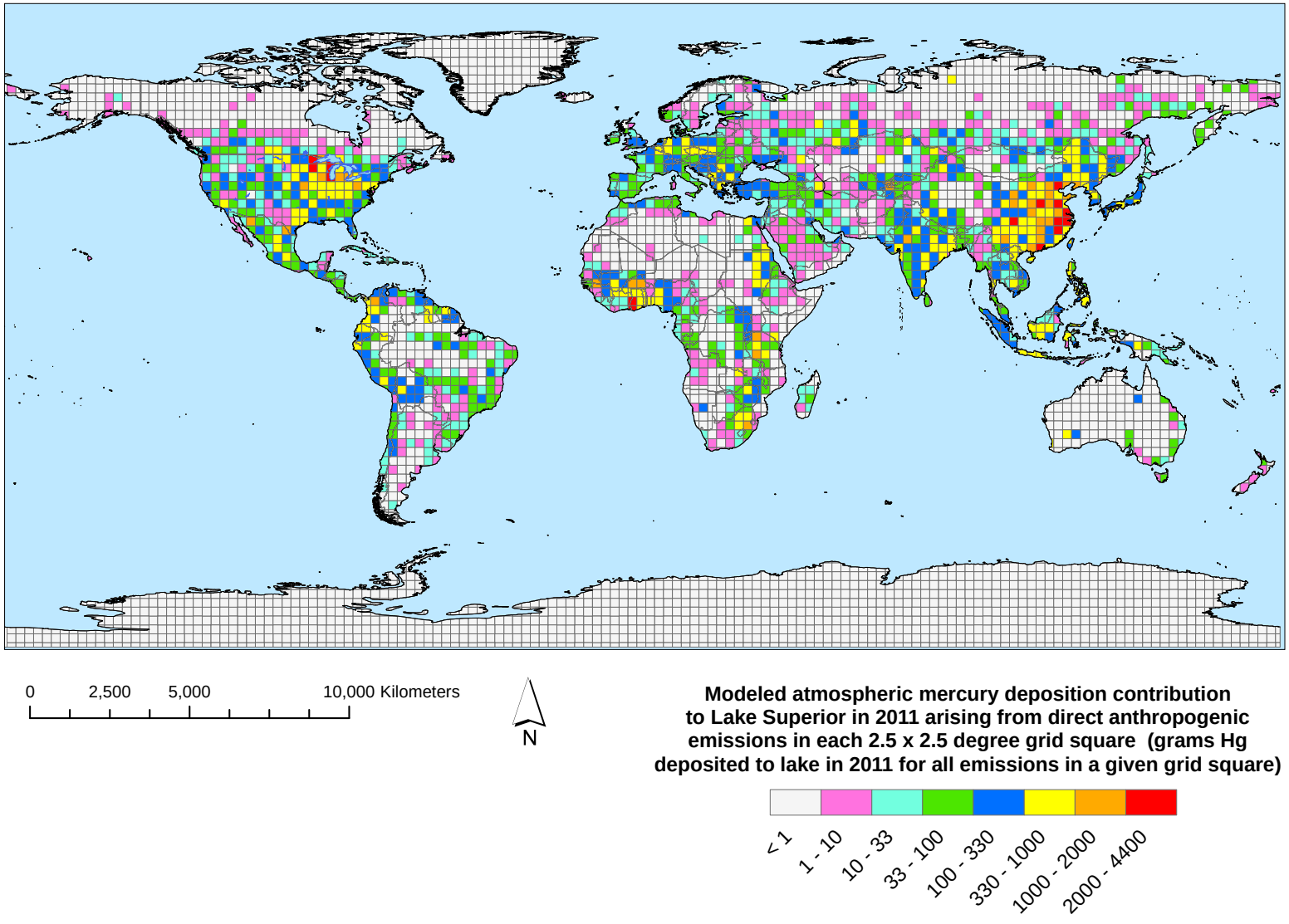

Figure 89. Modeled, gridded atmospheric mercury deposition contribution to Lake Superior in 2011 arising from direct anthropogenic emissions.

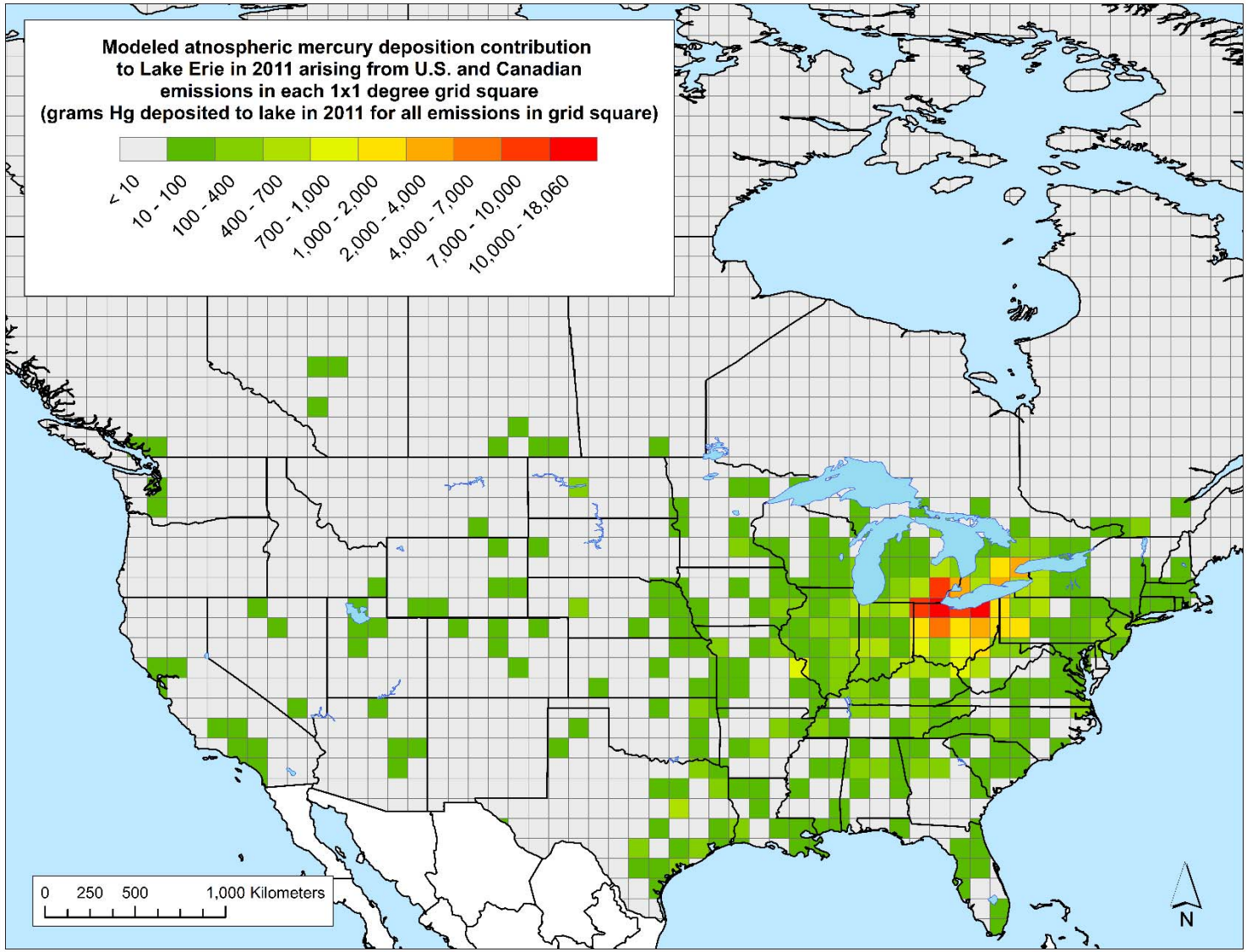

Figure 90. Modeled, gridded atmospheric mercury deposition contribution to Lake Erie in 2011 arising from U.S. and Canadian emissions.

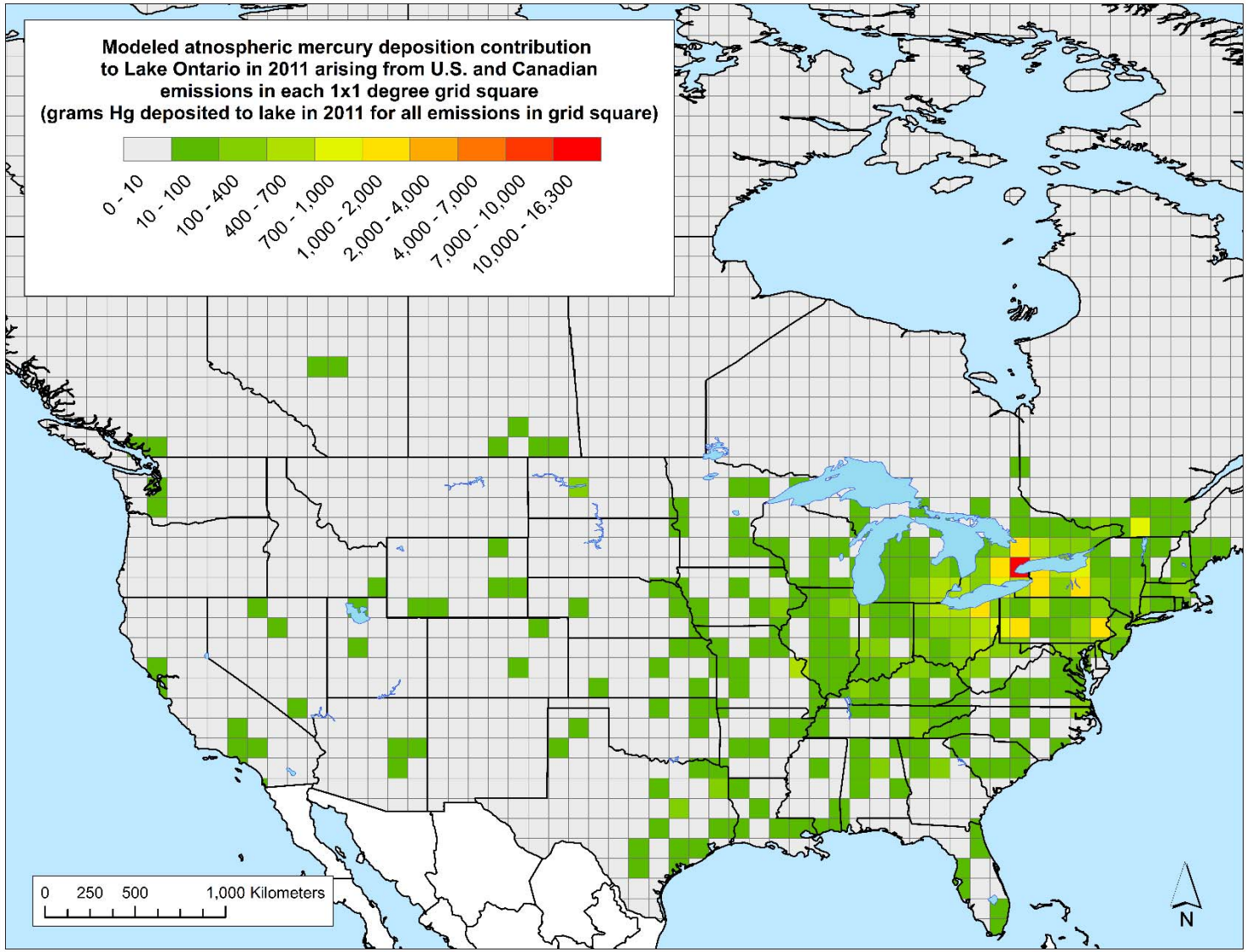

Figure 91. Modeled, gridded atmospheric mercury deposition contribution to Lake Ontario in 2011 arising from U.S. and Canadian emissions.

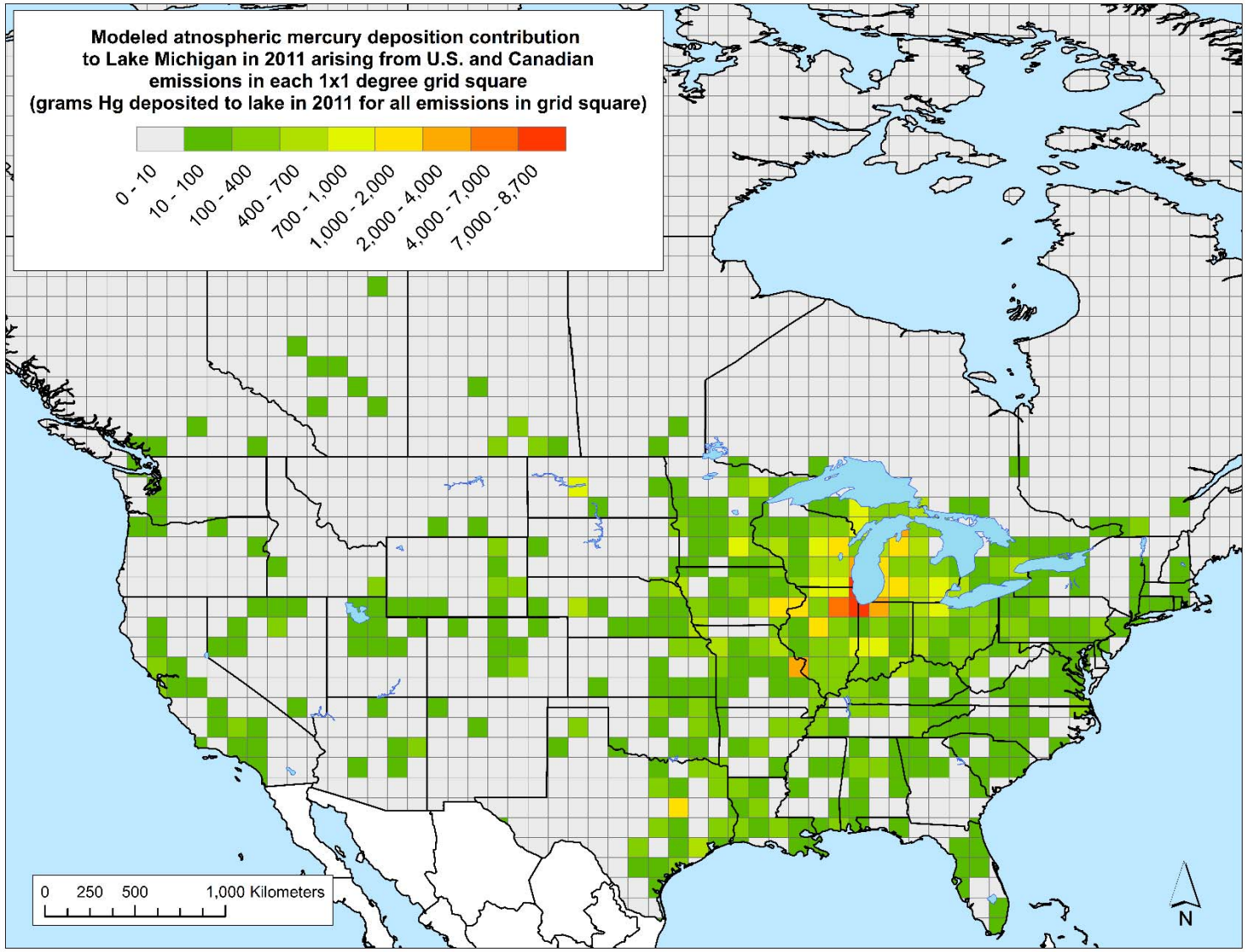

Figure 92. Modeled, gridded atmospheric mercury deposition contribution to Lake Michigan in 2011 arising from U.S. and Canadian emissions.

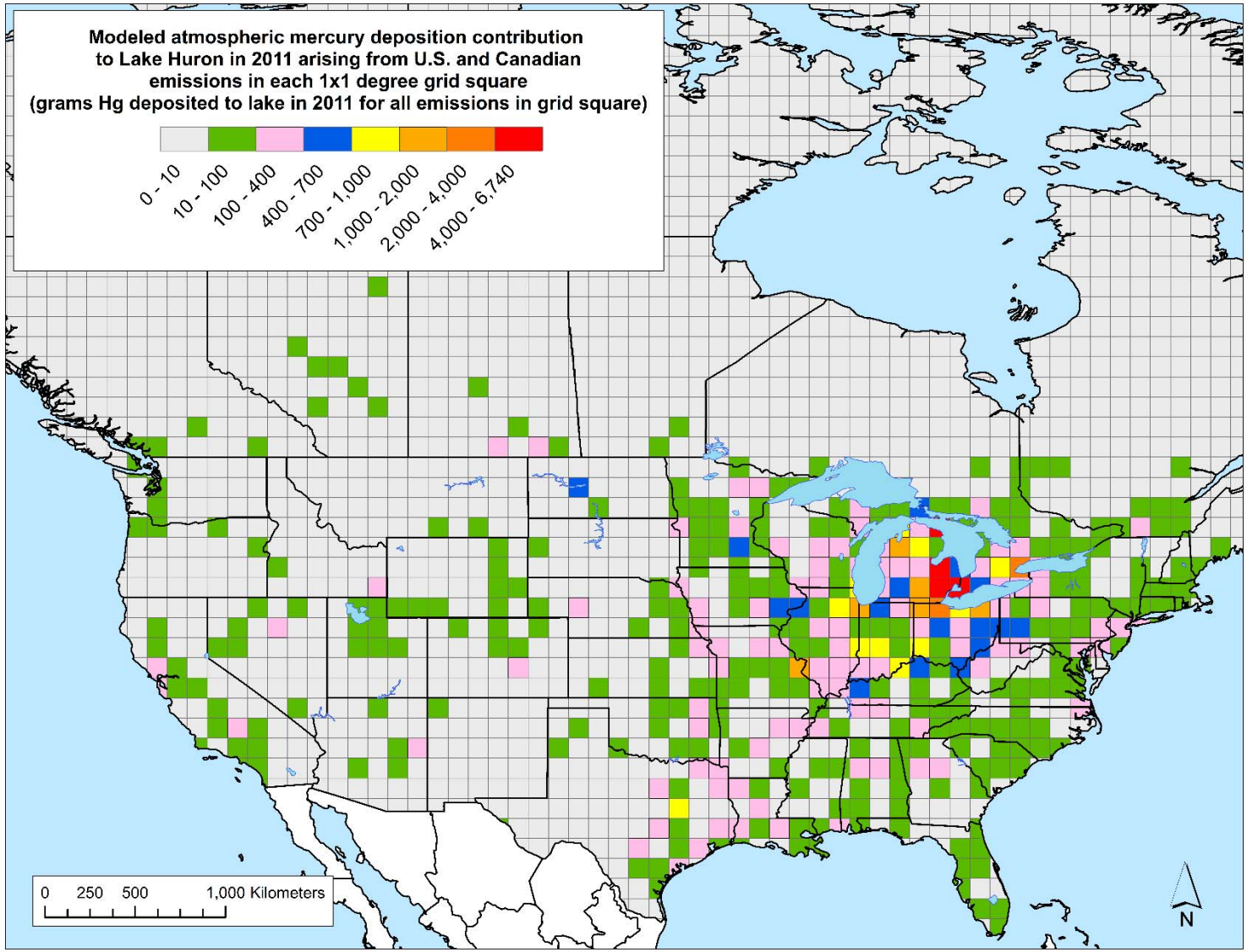

Figure 93. Modeled, gridded atmospheric mercury deposition contribution to Lake Huron in 2011 arising from U.S. and Canadian emissions.

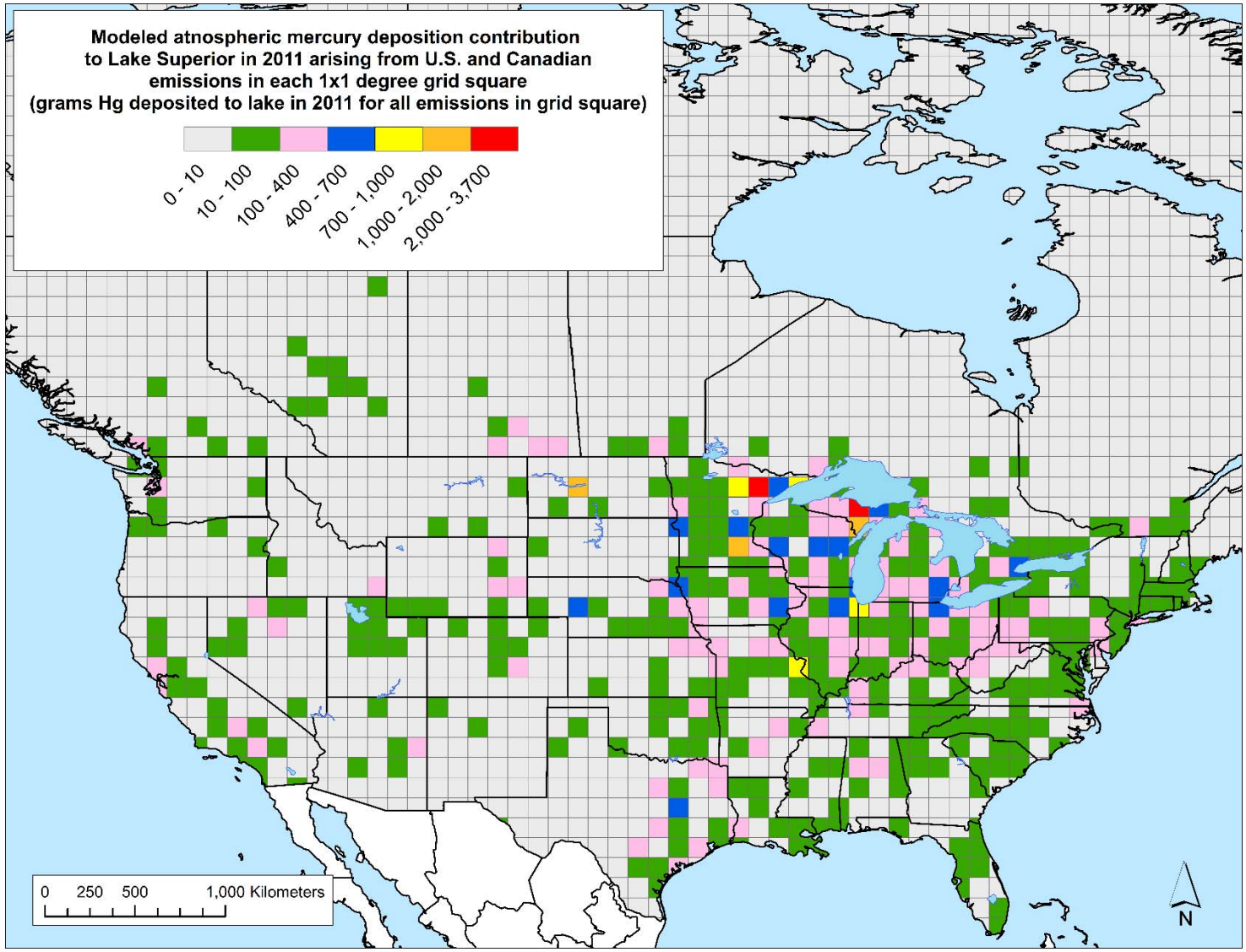

Figure 94. Modeled, gridded atmospheric mercury deposition contribution to Lake Superior in 2011 arising from U.S. and Canadian emissions.

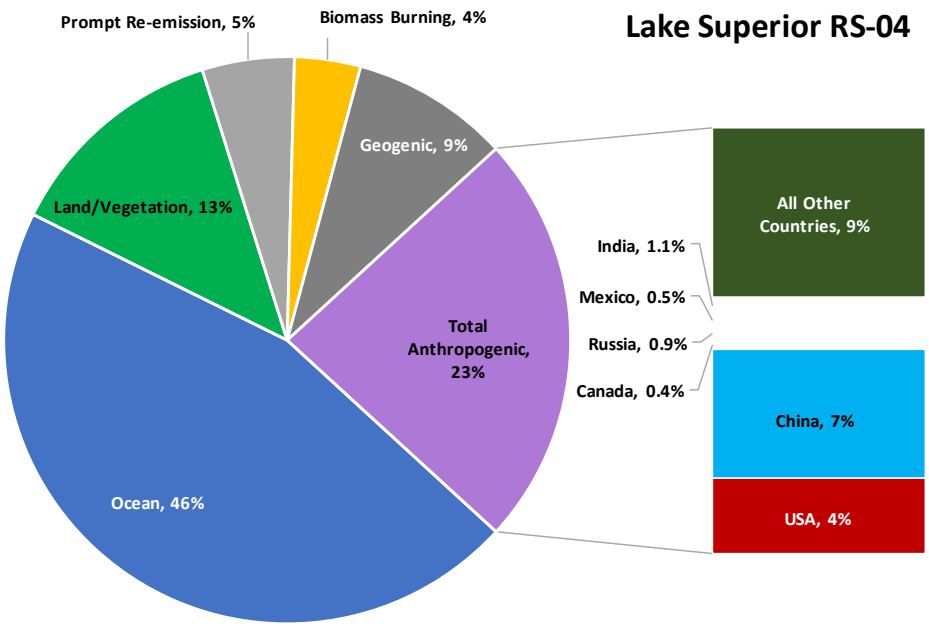

Figure 95. Fraction of total modeled mercury deposition contributed by each source category, Lake Superior, Run Scheme 04 (Hybrid Eulerian/Lagrangian).

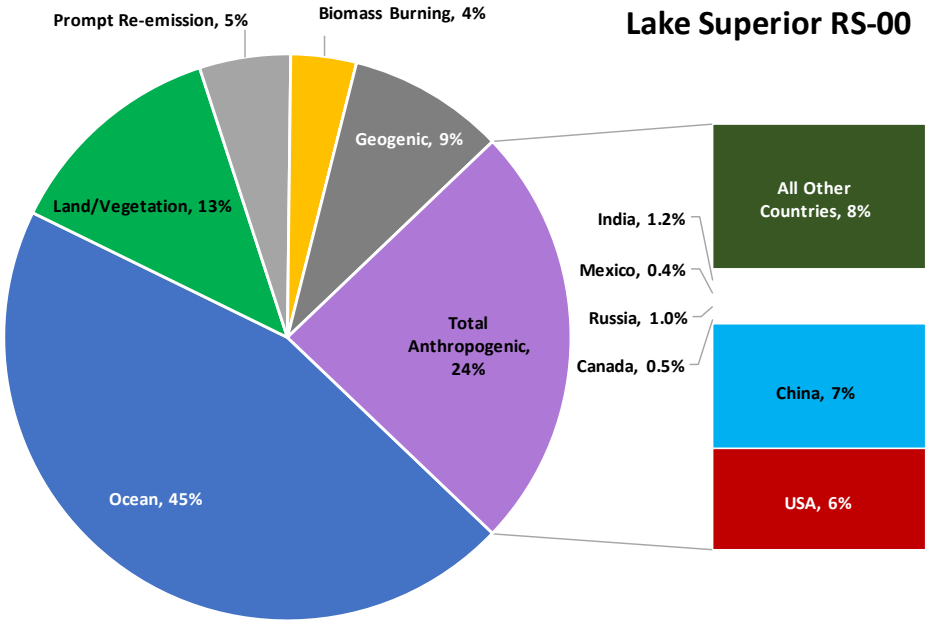

Figure 96. Fraction of total modeled mercury deposition contributed by each source category, Lake Superior, Run Scheme 00 (Eulerian Only).

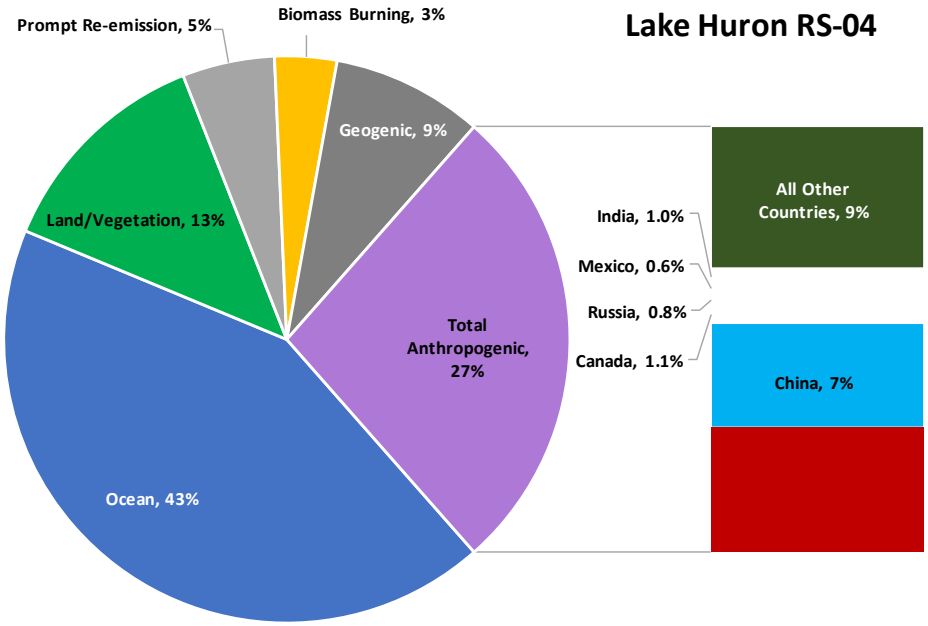

Figure 97. Fraction of total modeled mercury deposition contributed by each source category, Lake Huron, Run Scheme 04 (Hybrid Eulerian/Lagrangian).

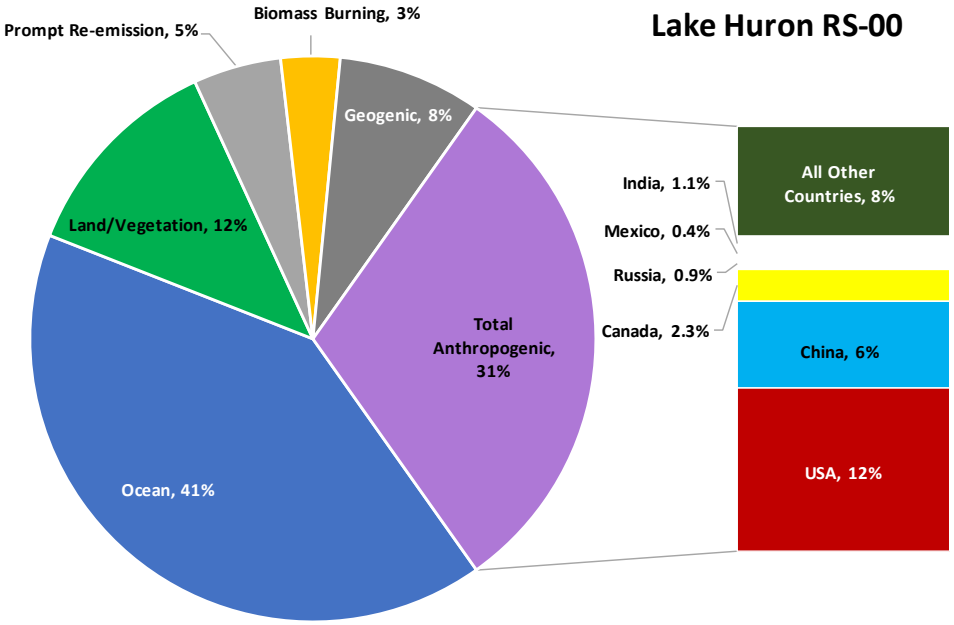

Figure 98. Fraction of total modeled mercury deposition contributed by each source category, Lake Huron, Run Scheme 00 (Eulerian Only).

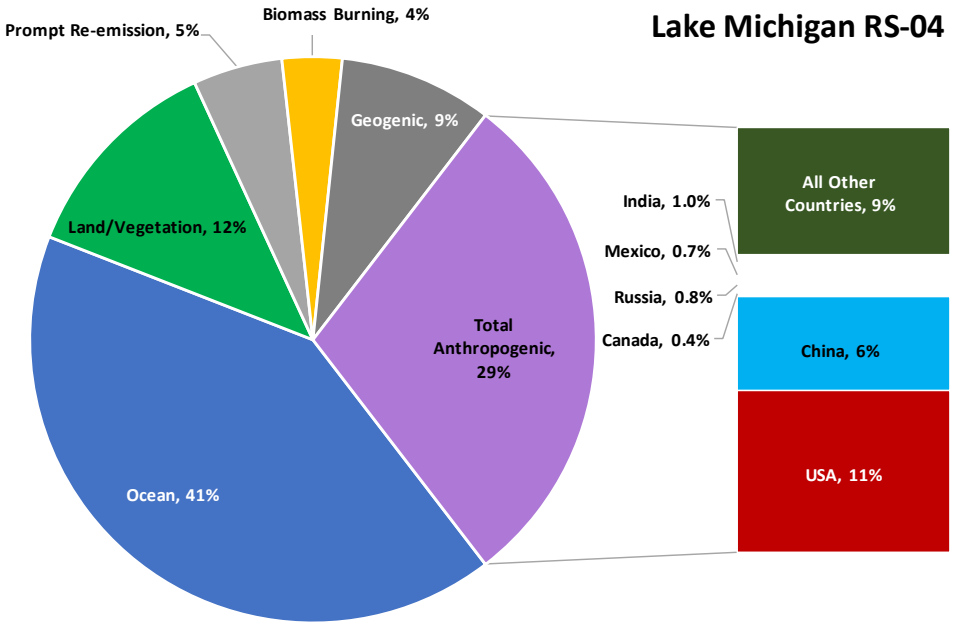

Figure 99. Fraction of total modeled mercury deposition contributed by each source category, Lake Michigan, Run Scheme 04 (Hybrid Eulerian/Lagrangian).

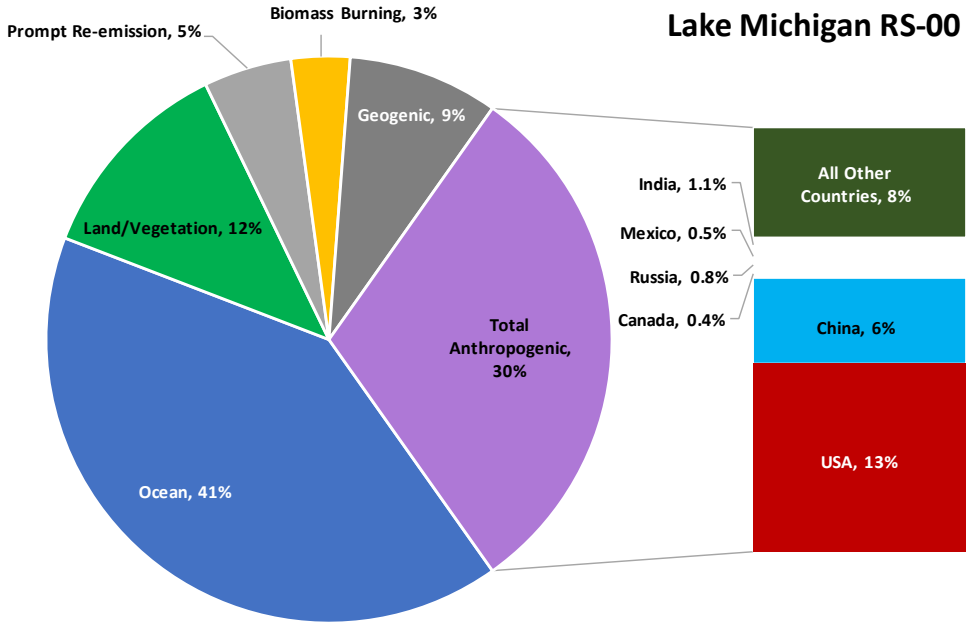

Figure 100. Fraction of total modeled mercury deposition contributed by each source category, Lake Michigan, Run Scheme 04 (Eulerian Only).

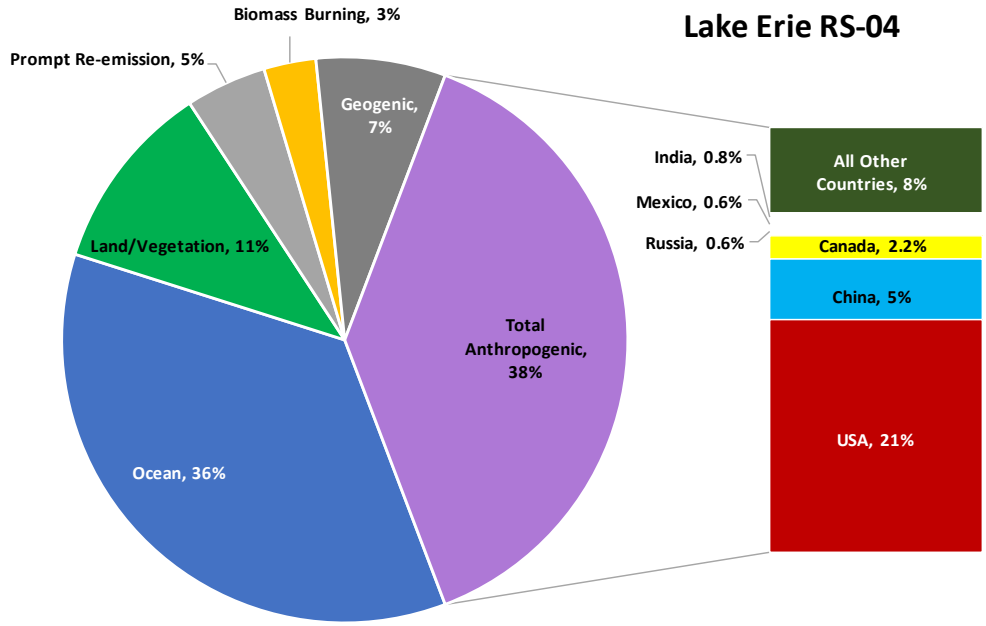

Figure 101. Fraction of total modeled mercury deposition contributed by each source category, Lake Erie, Run Scheme 04 (Hybrid Eulerian/Lagrangian).

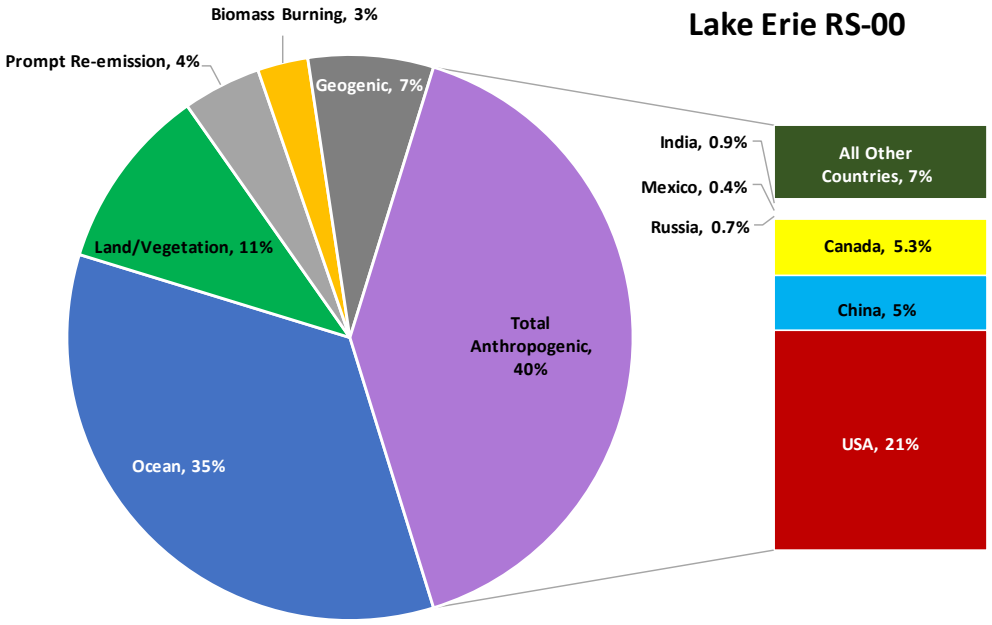

Figure 102. Fraction of total modeled mercury deposition contributed by each source category, Lake Erie, Run Scheme 00 (Eulerian Only).

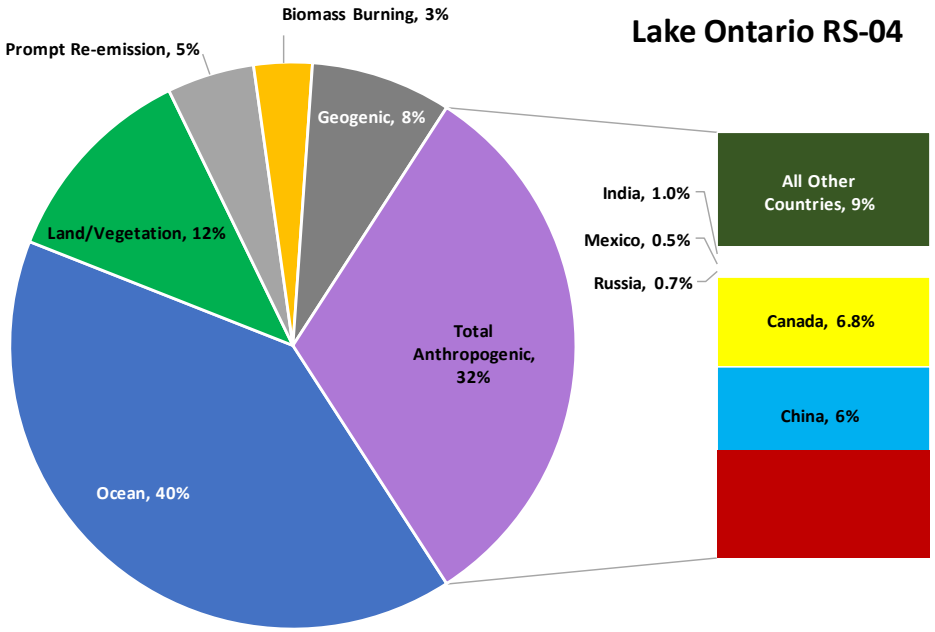

Figure 103. Fraction of total modeled mercury deposition contributed by each source category, Lake Ontario, Run Scheme 04 (Hybrid Eulerian/Lagrangian).

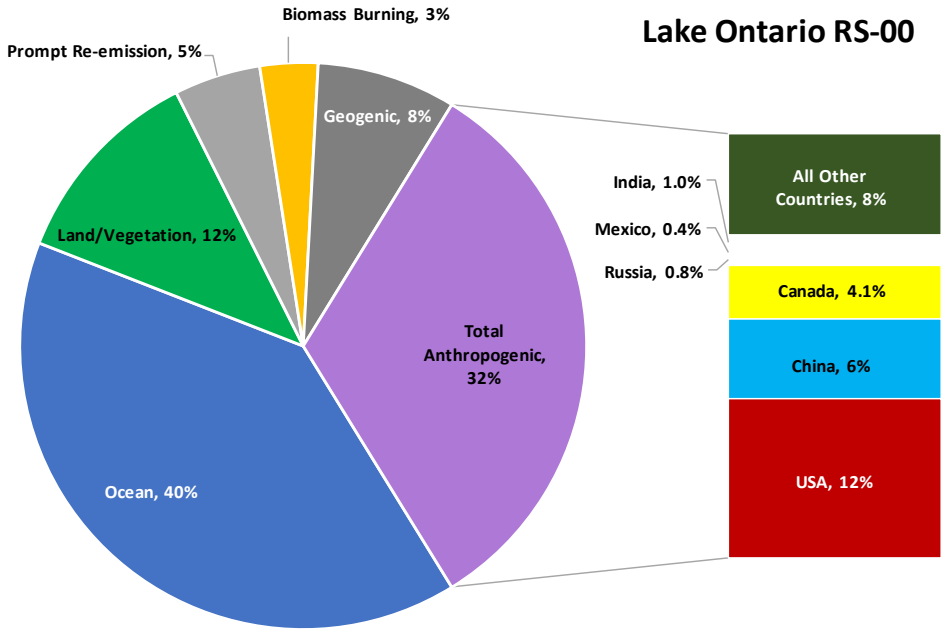

Figure 104. Fraction of total modeled mercury deposition contributed by each source category, Lake Ontario, Run Scheme 00 (Eulerian Only).

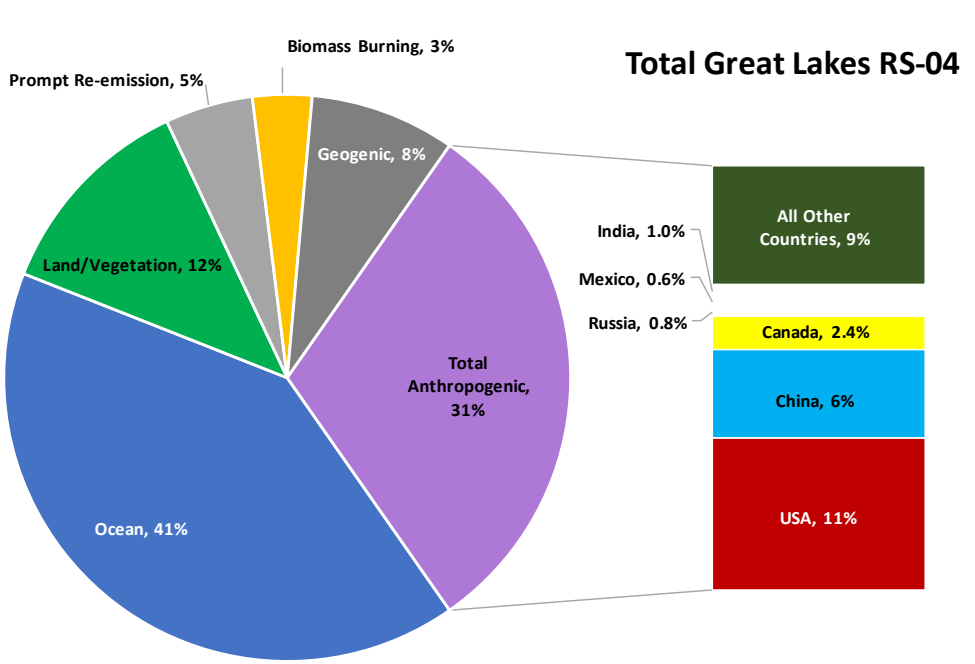

Figure 105. Fraction of total modeled mercury deposition contributed by each source category, Great Lakes Total, Run Scheme 04 (Hybrid Eulerian/Lagrangian).

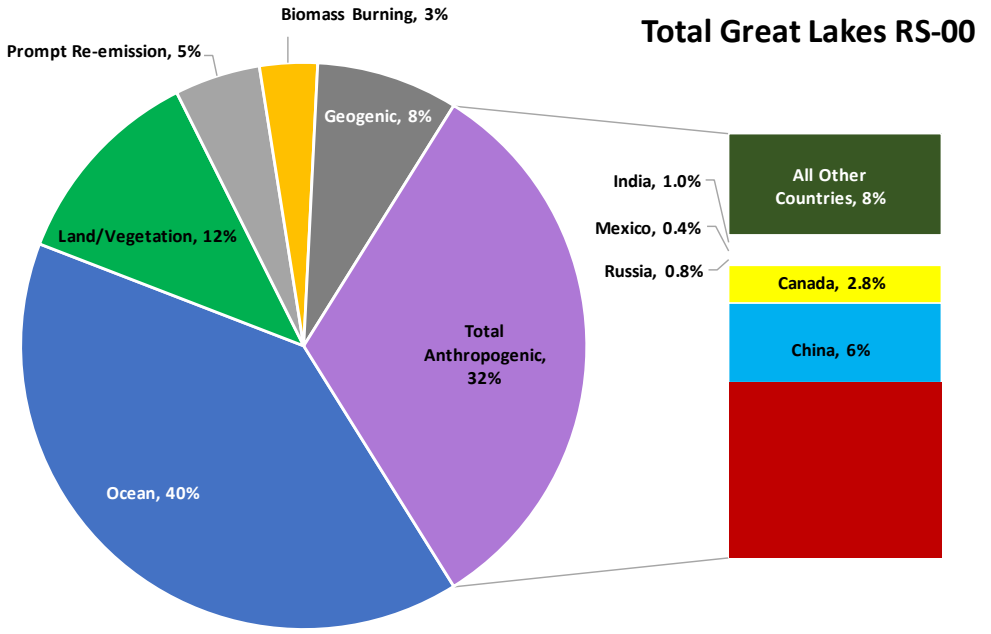

Figure 106. Fraction of total modeled mercury deposition contributed by each source category, Great Lakes Total, Run Scheme 00 (Eulerian Only).

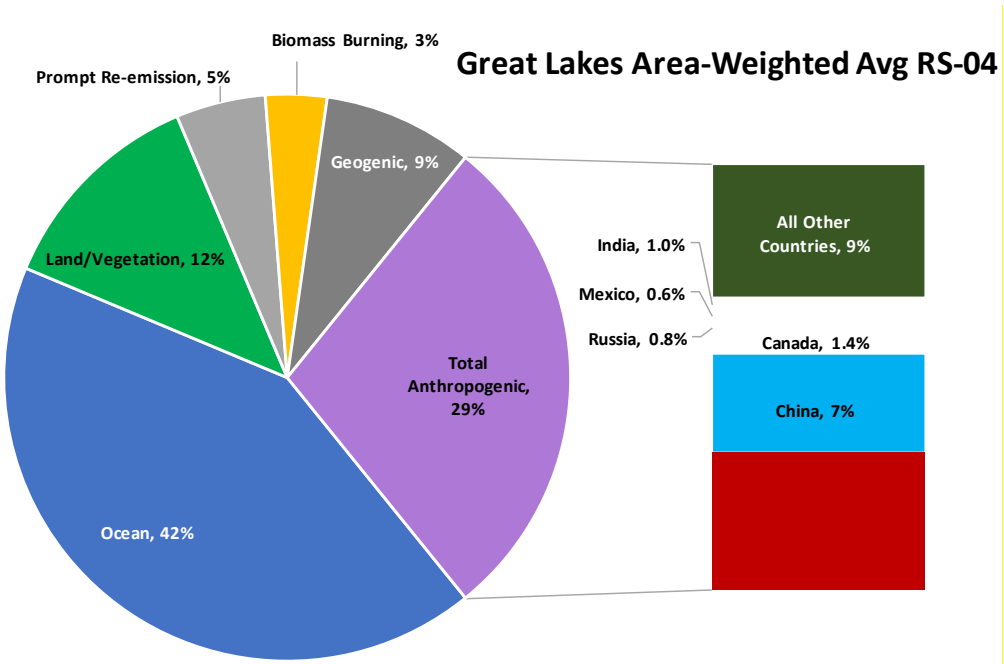

Figure 107. Fraction of total modeled mercury deposition contributed by each source category, Great Lakes, Area-Weighted Average, Run Scheme 04 (Hybrid Eulerian/Lagrangian).

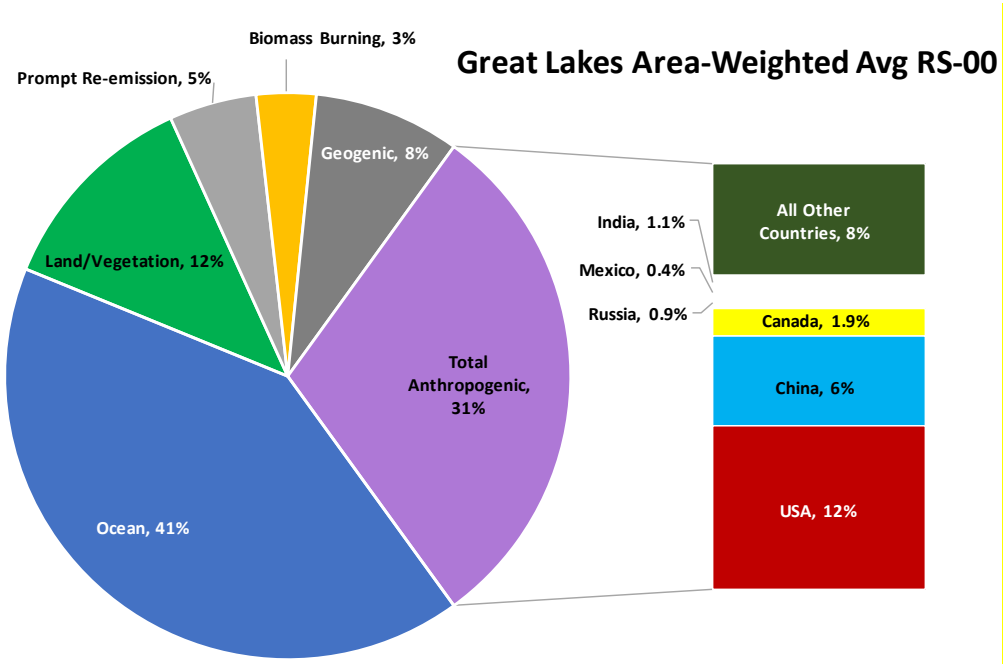

Figure 108. Fraction of total modeled mercury deposition contributed by each source category, Great Lakes, Area-Weighted Average, Run Scheme 00 (Eulerian Only).

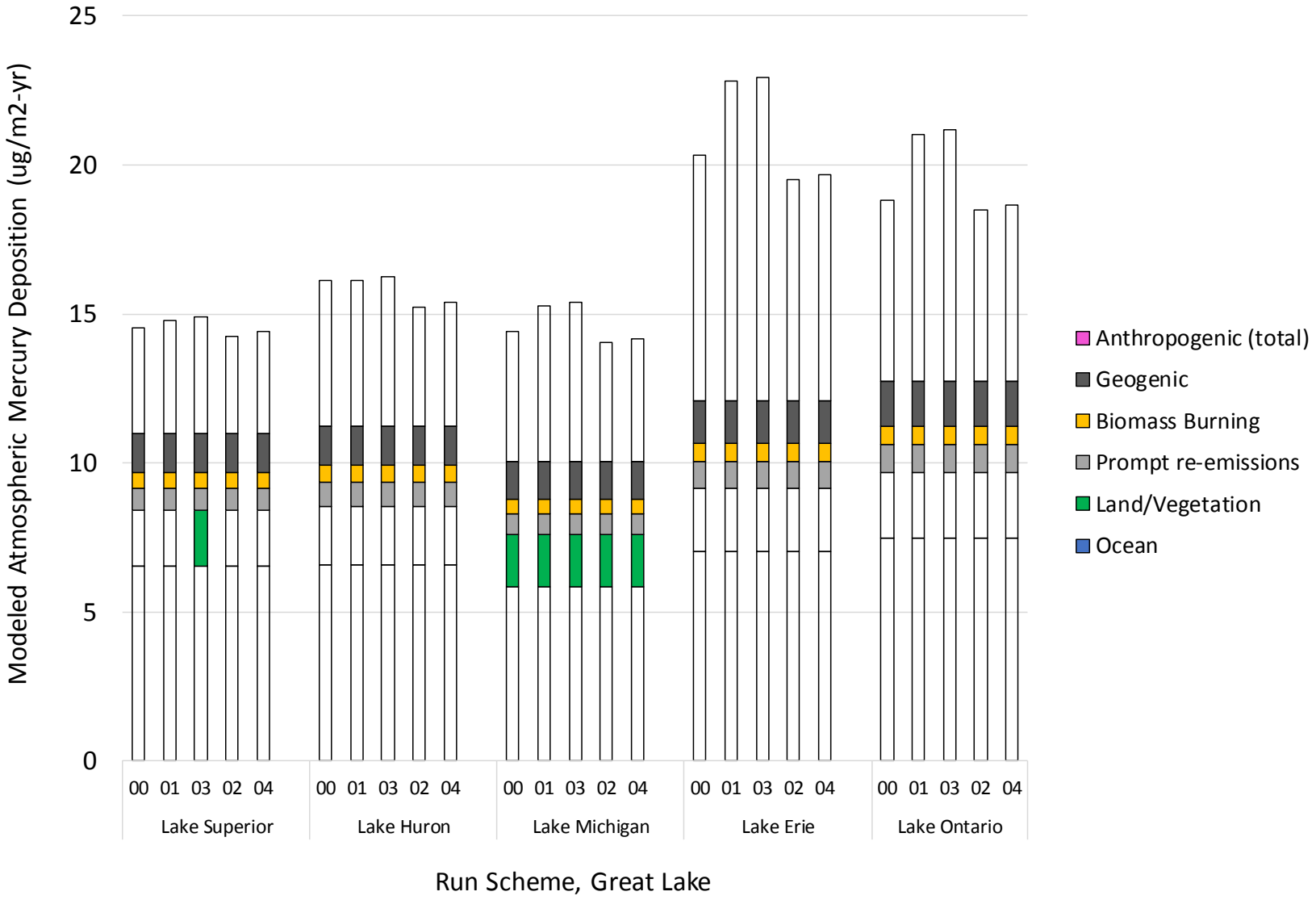

Figure 109. Model estimated atmospheric mercury deposition to the Great Lakes arising from different source types during 2011, for each run-scheme methodology.

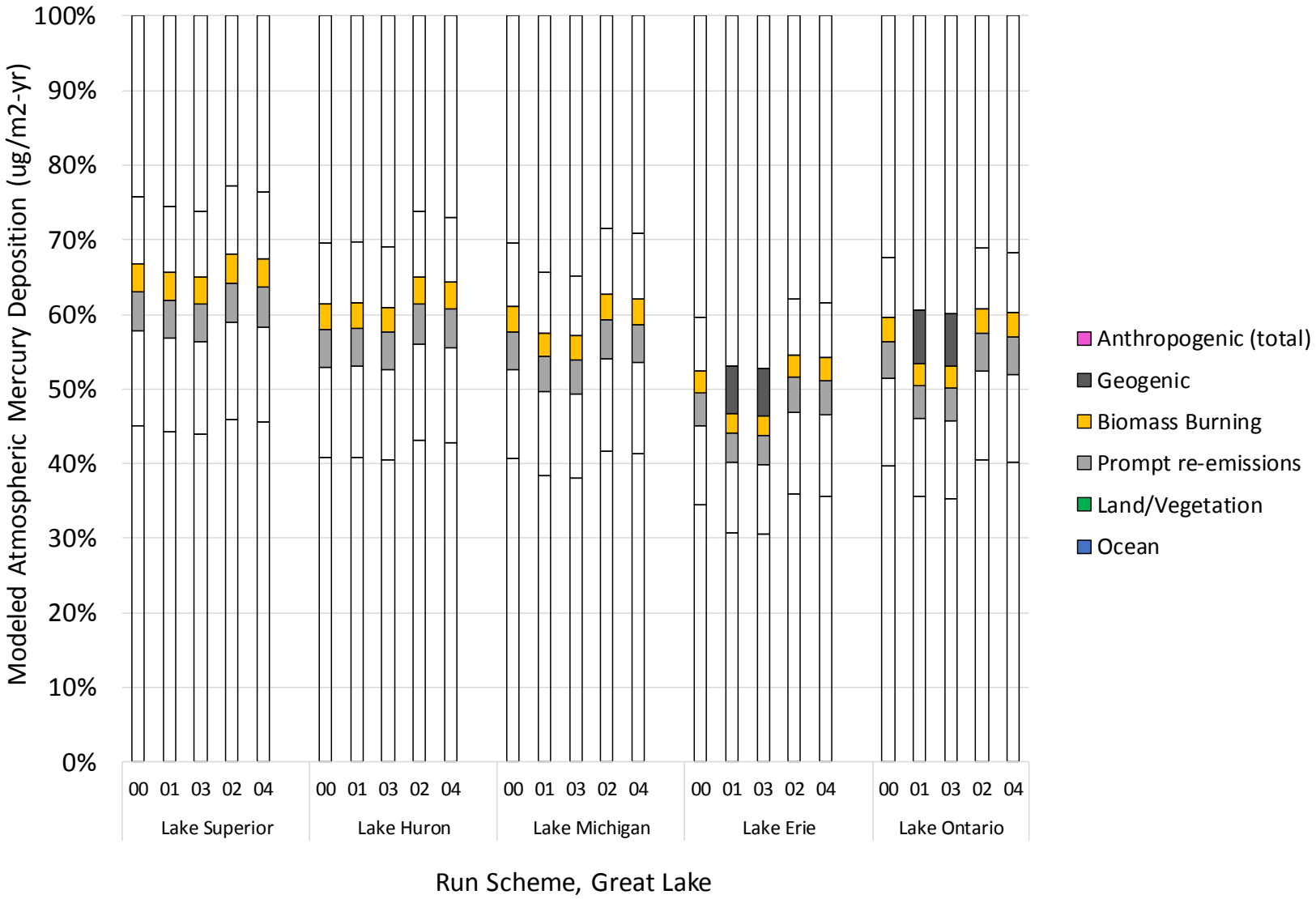

Figure 110. Model estimated atmospheric mercury deposition to the Great Lakes arising from different source types during 2011, for each run-scheme methodology, as a fraction of the total deposition for each overall estimate.

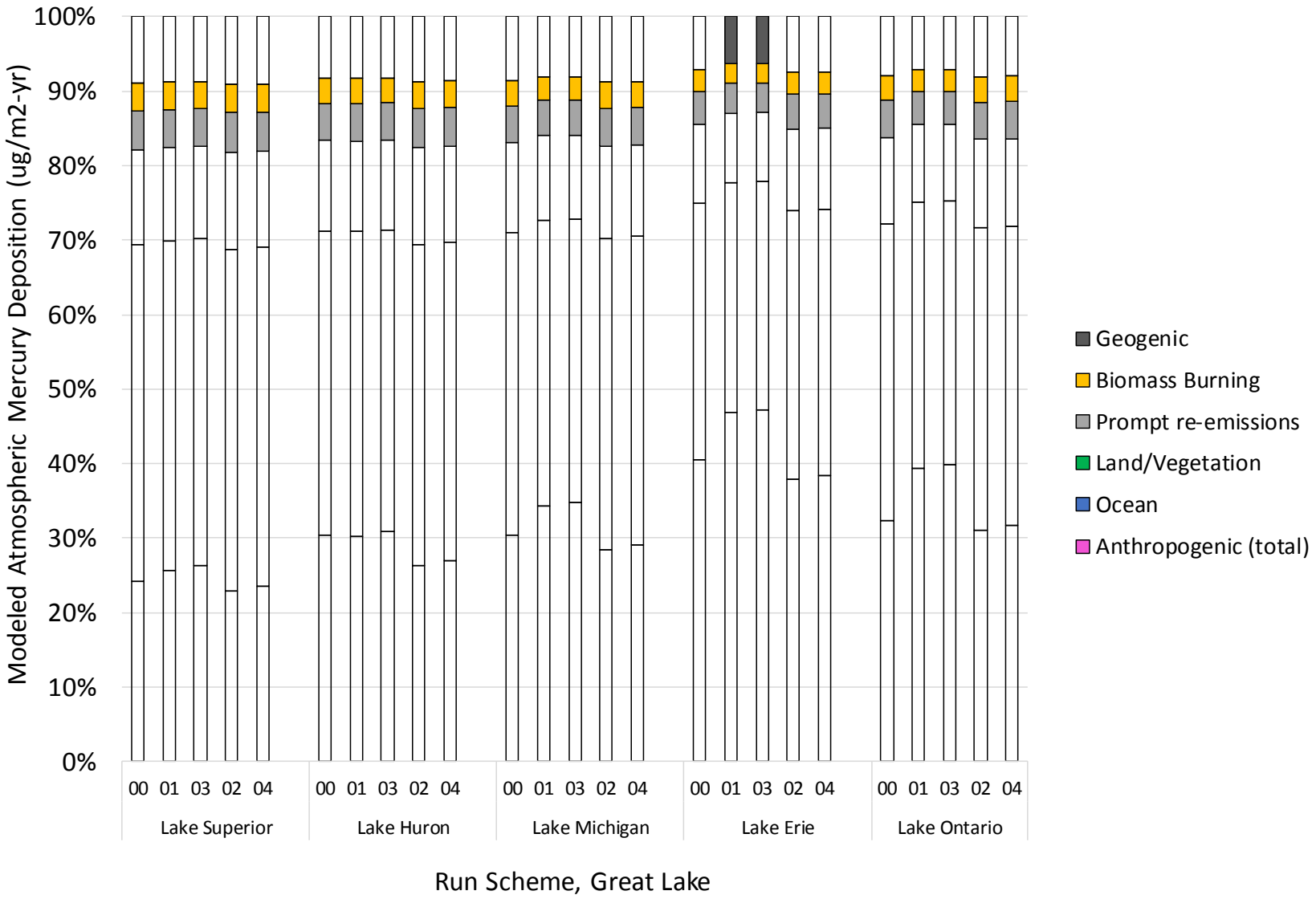

Figure 111. Model estimated atmospheric mercury deposition to the Great Lakes arising from different source types during 2011, for each run-scheme methodology, as a fraction of the total deposition for each overall estimate, showing anthropogenic as first component of stacked bar graph.

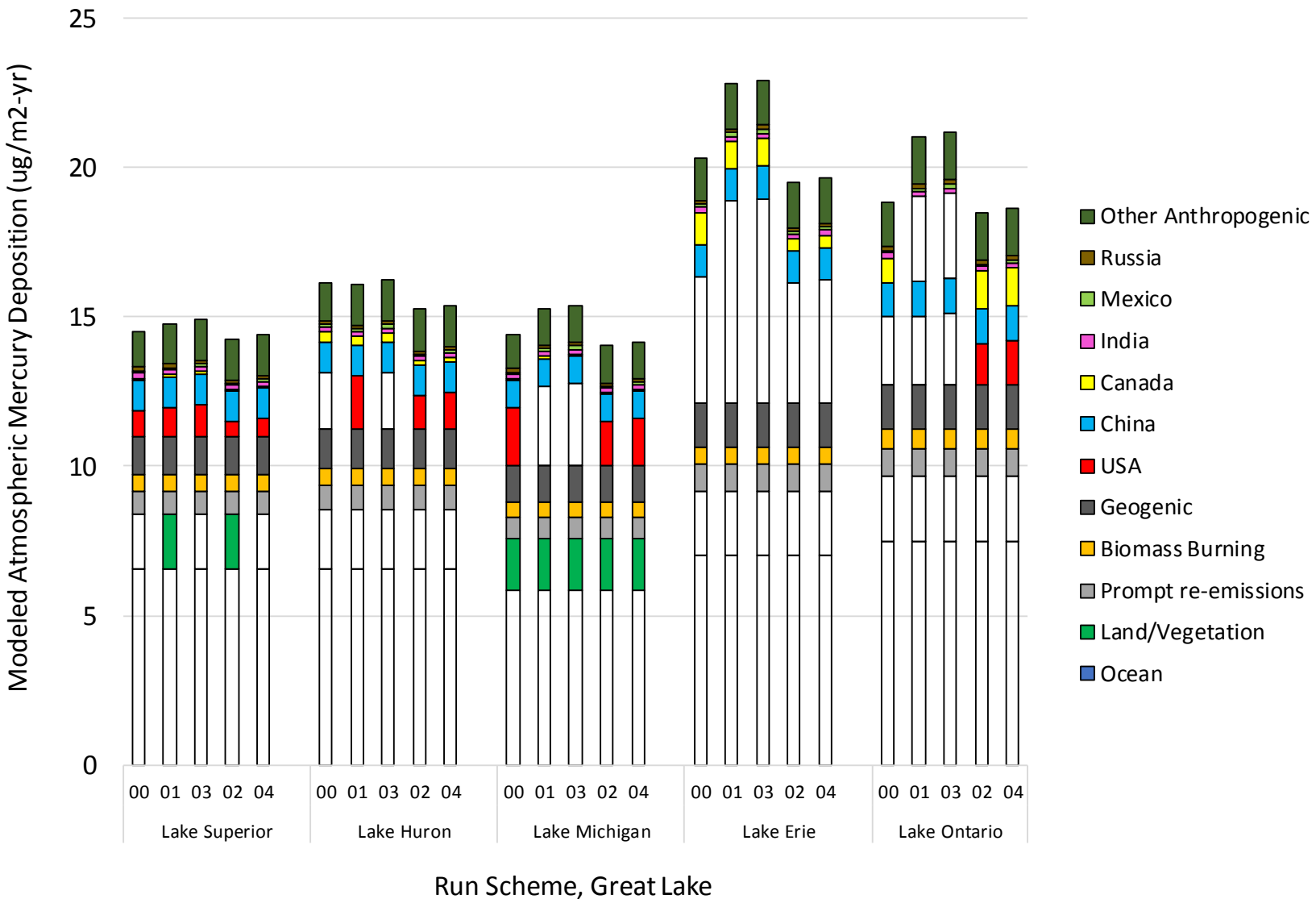

Figure 112. Model estimated atmospheric mercury deposition to the Great Lakes arising from different source types during 2011, for each run-scheme methodology.

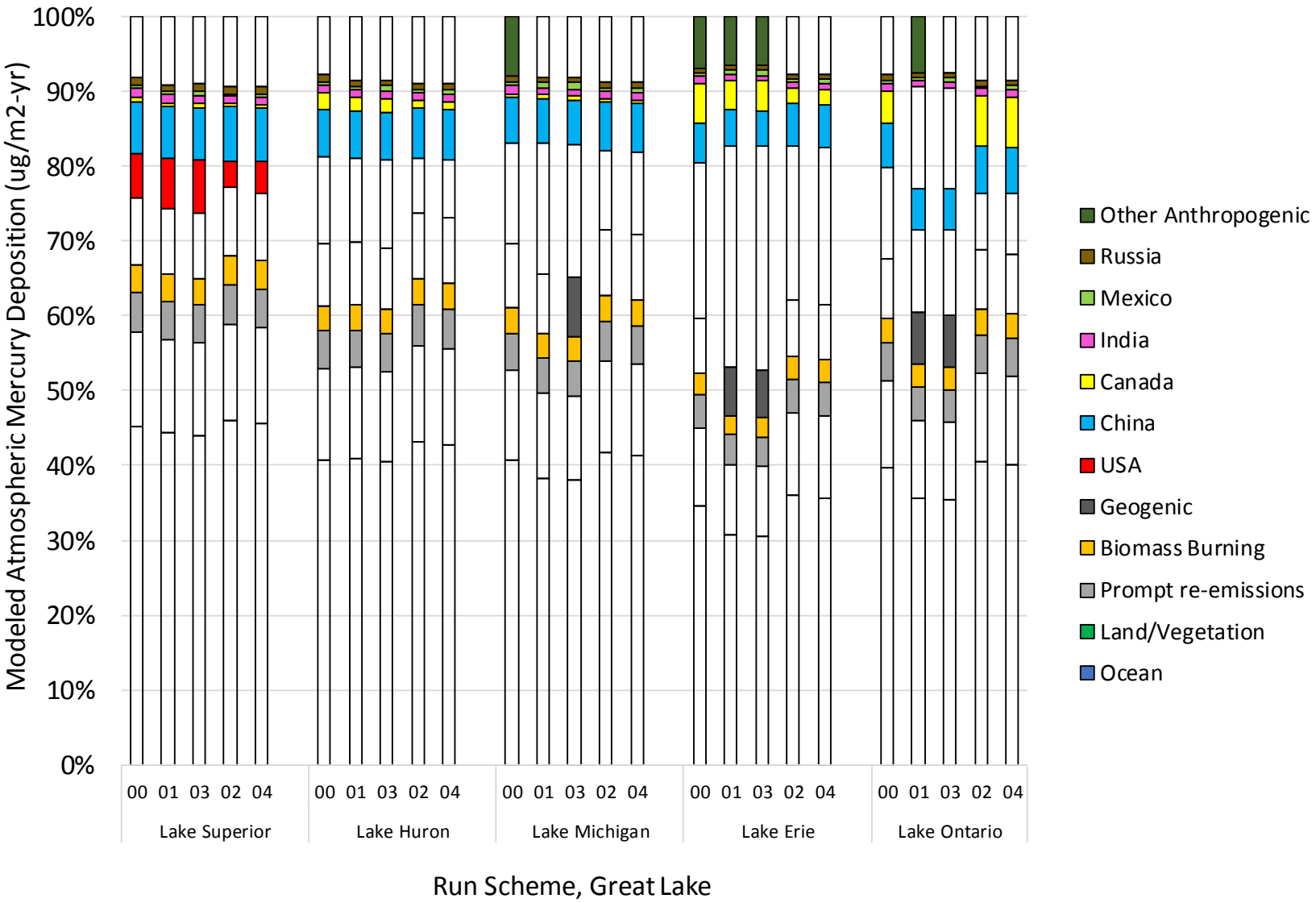

Figure 113. Model estimated atmospheric mercury deposition to the Great Lakes arising from different source types during 2011, for each run-scheme methodology, as a fraction of the total deposition for each overall estimate.

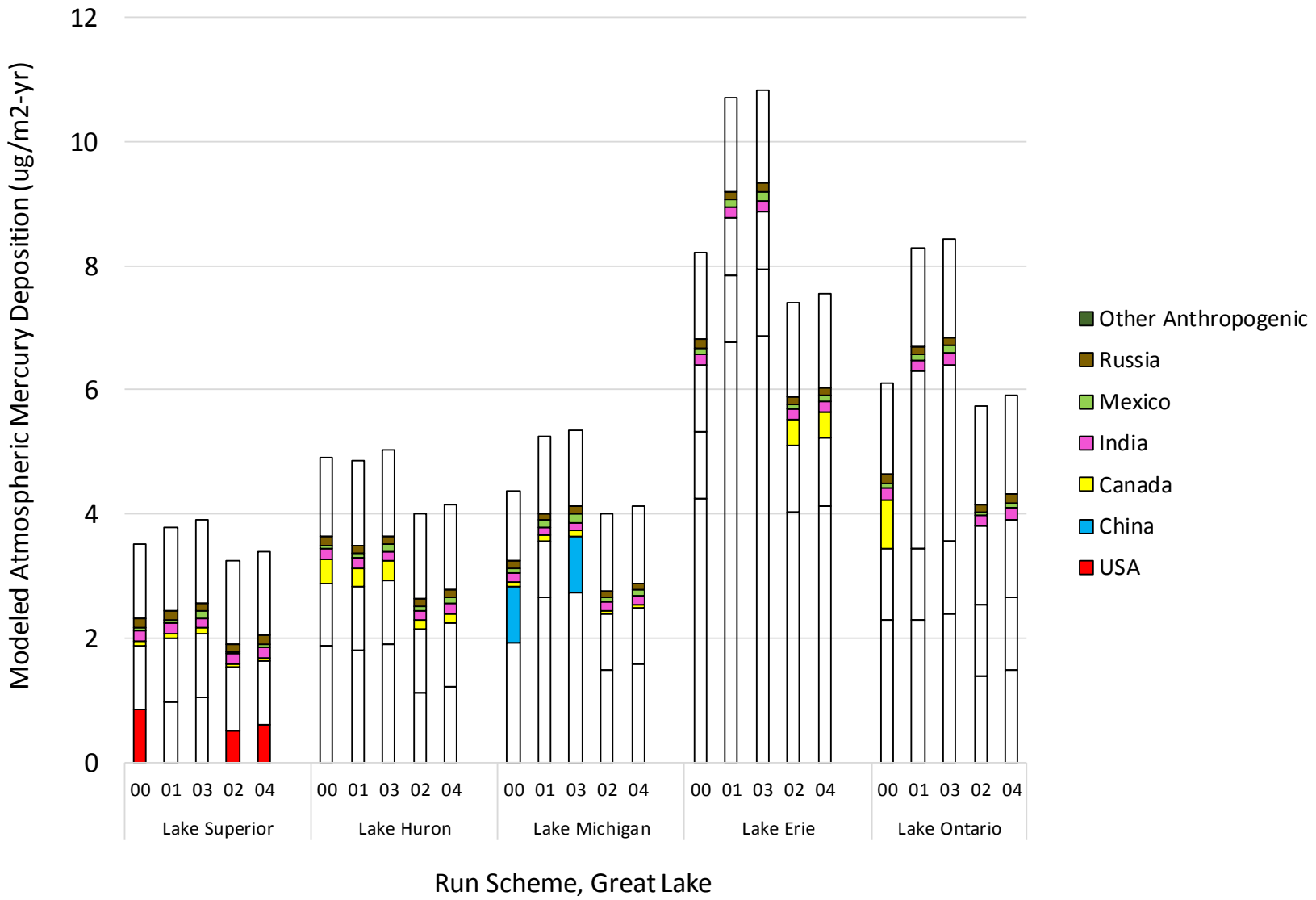

Figure 114. Model estimated atmospheric mercury deposition to the Great Lakes arising from anthropogenic emissions during 2011, for each run-scheme methodology.

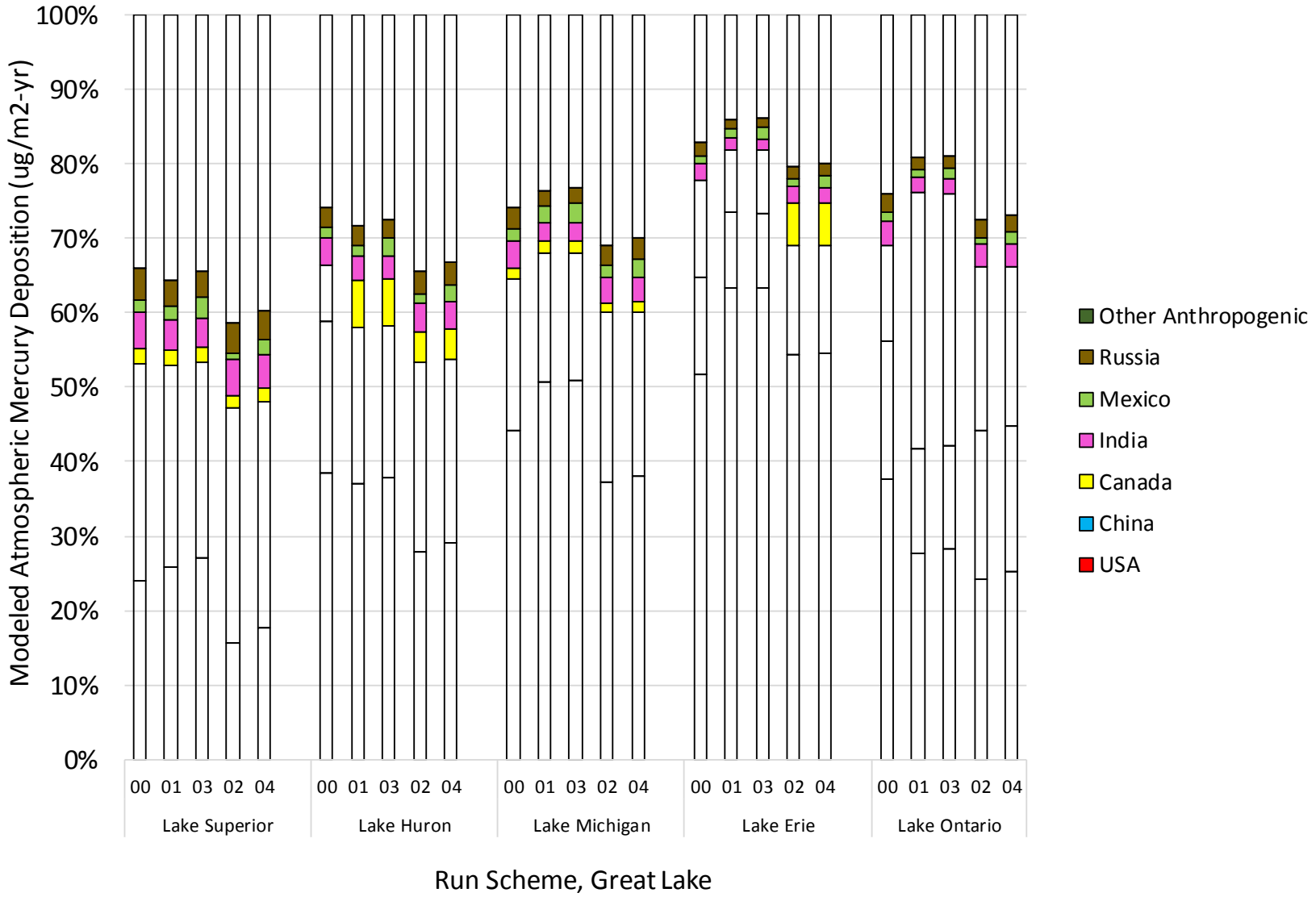

Figure 115. Model estimated atmospheric mercury deposition to the Great Lakes arising from anthropogenic emissions during 2011, for each run-scheme methodology, as a fraction of the total deposition from anthropogenic emissions for each overall estimate.

5.3. Contributions to the Great Lakes as a function of distance

As described in Section 3.3 (beginning on page 36), the individual contribution of each direct anthropogenic emissions inventory record to each Great Lake and watershed is estimated in each of the run-scheme calculations except for the Eulerian-only approach (RS-00). The direct anthropogenic emissions inventory records include active 2011 point and area sources in the U.S. and Canada, and gridded, overall, direct anthropogenic emissions in the rest of the world.

Note that indirect anthropogenic contributions arising from re-emissions of previously deposited direct anthropogenic emissions are tabulated elsewhere in the analysis, i.e., in the Eulerian-only estimates of contributions from oceanic and terrestrial surfaces. The distance between the location of the emissions inventory source and the centroid of each Great Lake (and watershed) can be calculated.

Figure 117 shows the fraction of the total model-estimated deposition arising from anthropogenic sources that came from inventory records in different distance ranges away from the lake and watershed centroids. In Figure 117, separate values are given for dry and wet deposition. In Figure 118, the deposition flux values associated with the percentages in Figure 116 are shown, with the values in the closest (0-500 km) and furthest (>10,000 km) labeled.

It can be seen that for Lake Erie, more than 50% of the total model-estimated contributions from direct anthropogenic emissions arise from sources within 500 km of the lake centroid, and that significant contributions are made from both dry and wet deposition. The results are similar for the Lake Erie watershed. In contrast, only about 5% of the analogous deposition arises from sources within 500 km of the lake centroid for Lake Superior. This difference is of course in part due to the much larger size of Lake Superior, but is mostly influenced by the relative scarcity of emissions nearby the lake.

For Lake Erie, approximately 25% of the deposition arises from sources greater than 10,000 km from the lake centroid, but for Lake Superior, nearly 50% of the deposition arising from direct anthropogenic emissions sources comes from sources greater than 10,000 km from the lake centroid.

While the fraction that the sources greater than 10000 km away from the receptor centroids varies, the absolute amount of deposition flux for these sources is relatively similar among all receptors shown, varying only from 1.5 to 1.9 $\mu g\ m^{-2}\ yr^{-1}$. In contrast, the absolute deposition flux arising from sources within 500 km of the receptor centroid varies greatly, e.g., from 0.2 $\mu g\ m^{-2}\ yr^{-1}$ for Lake Superior to 3.9 $\mu g\ m^{-2}\ yr^{-1}$ for Lake Erie.

Results for the watersheds of each lake (Figure 11) and for Lake St. Clair (part of Lake Erie's watershed) were also estimated in this modeling analysis and are shown in Figure 117. Due to the small size of the watersheds relative to the lakes – as compared to most lakes – and the fact that only a small fraction of the mercury deposited in the watershed is transported to the lake, the focus in this analysis has been on the mercury deposited directly to surface of each lake. However, results for each watershed and for Lake St. Clair were estimated and could be used in further analysis.

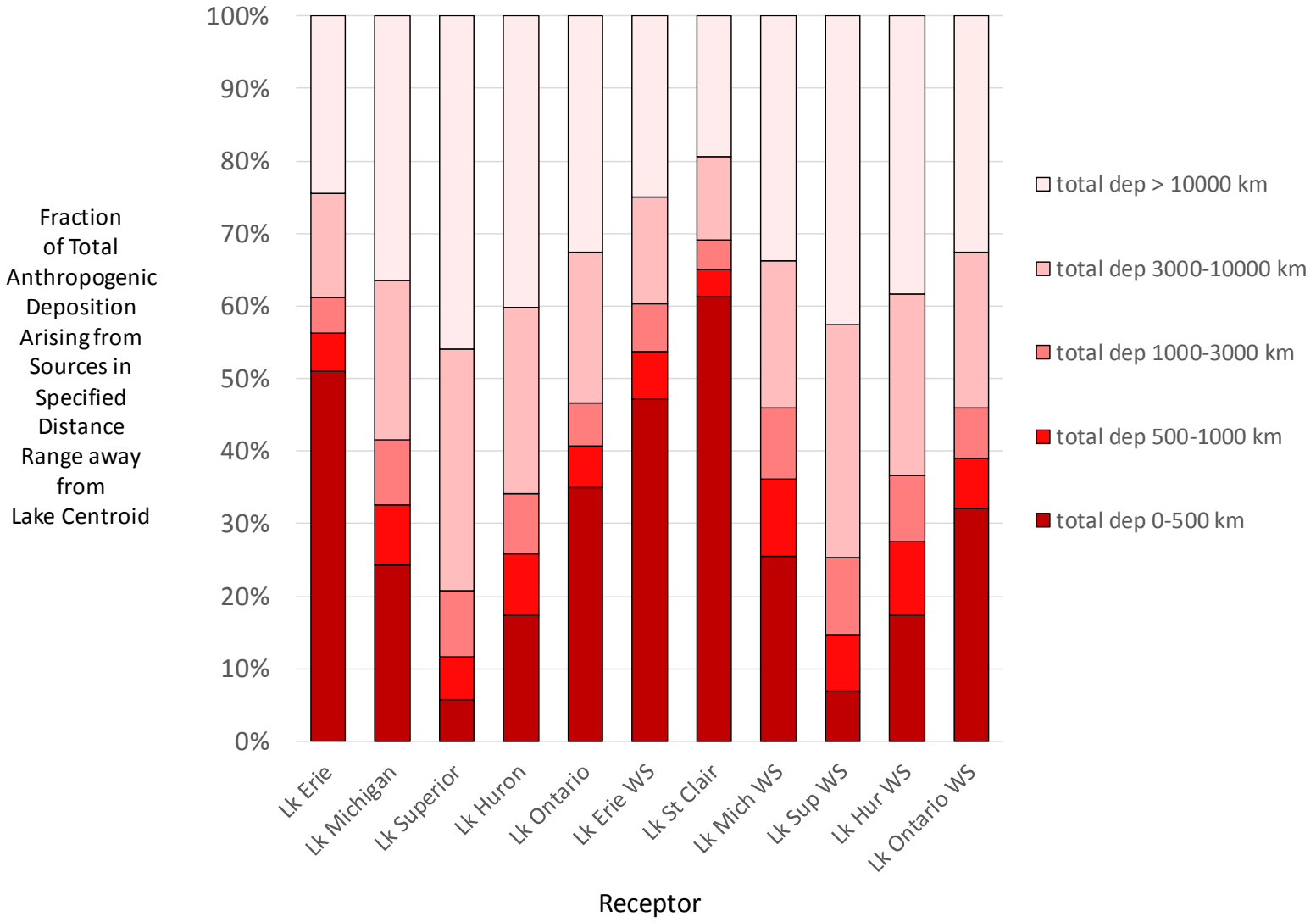

Figure 116. Fraction of total deposition contributions to the Great Lakes from direct anthropogenic emissions arising from sources within different distance ranges away from the centroid of the lake or watershed (WS) (for methodology = RS-04).

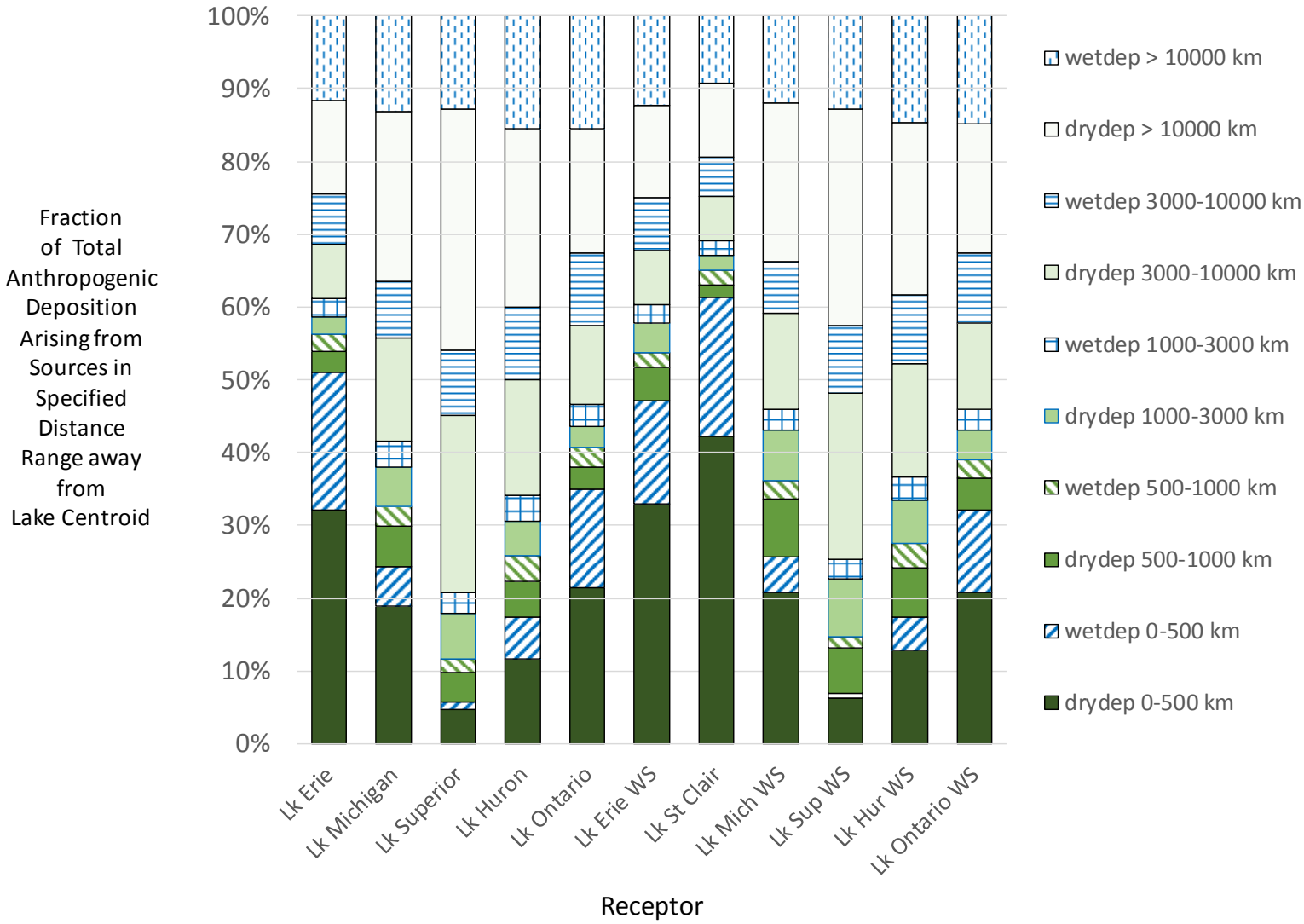

Figure 117. Fraction of total deposition contributions to the Great Lakes from direct anthropogenic emissions arising from sources within different distance ranges (RS-04), divided into dry and wet deposition components.

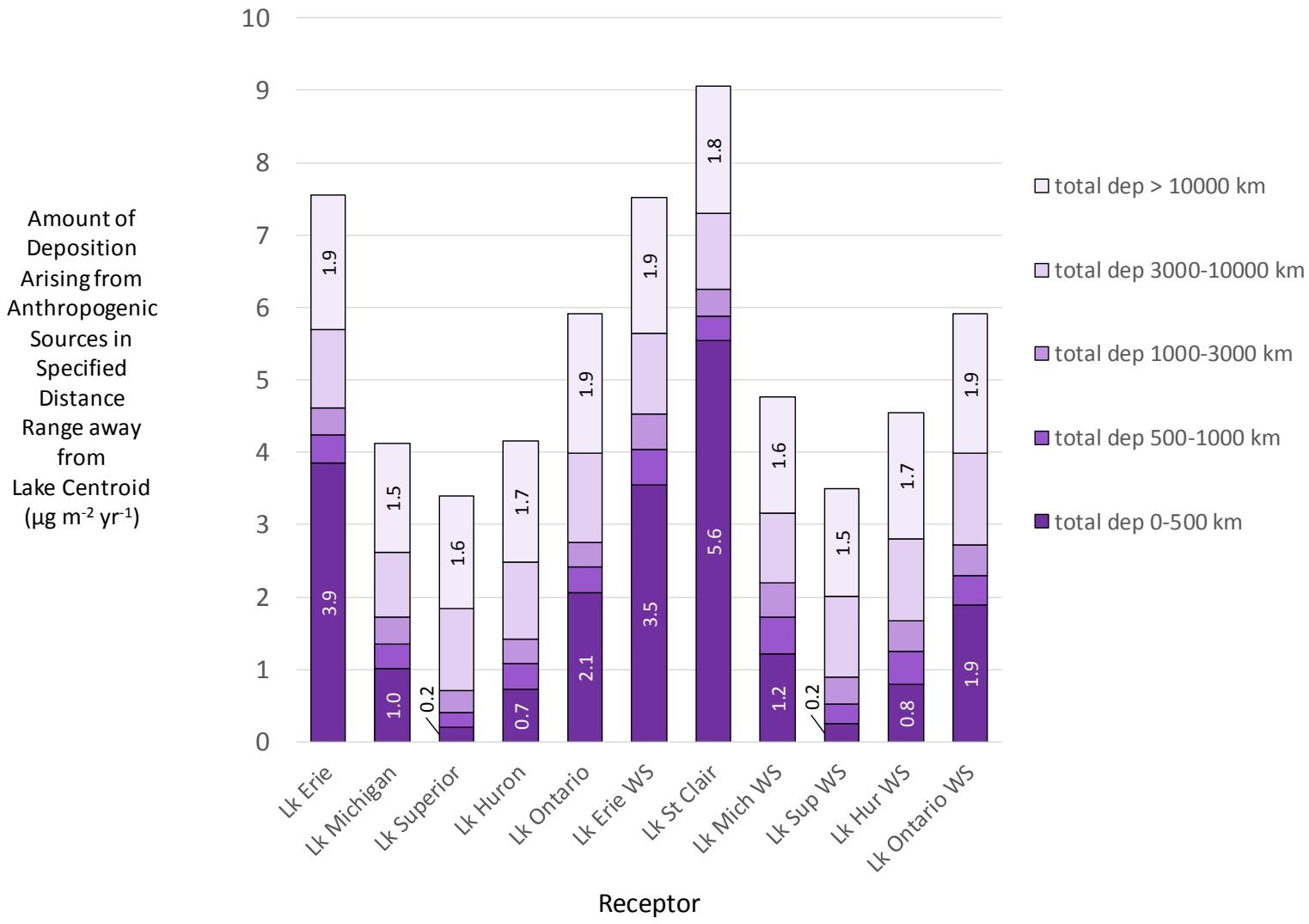

Figure 118. Amount of deposition contributed to the Great Lakes from direct anthropogenic emissions arising from sources within different distance ranges away from the centroid of the lake or watershed (WS) (for methodology = RS-04).

In addition to the results presented above based on the distance of the emissions source to the centroid of the lake, an analysis was also conducted based on the distance of the source to the shore of the lake. Distances were estimated using the NEAR geo-processing tool in ArcGIS 10.4, using a geodesic-based algorithm to factor in the curvature of the earth. The results are shown below for each of the Great Lakes in Figure 119 through Figure 123 below, all for the RS-04 modeling methodology.

Figure 119 shows that nearly half (47.5%) of the modeled atmospheric mercury deposition to Lake Erie from direct anthropogenic emissions comes from sources within 200 km of the lake. These sources, within 200 km of the lake, represent only 0.3% of the total global direct anthropogenic emissions used in the modeling. For Lake Erie, 96% of all direct anthropogenic emissions are from sources more than 3000 km away from the lake, but these sources only contribute a little more than 38% of the corresponding deposition.

For Lake Ontario, Figure 120 shows that about a quarter (25.7%) of the modeled atmospheric mercury deposition from direct anthropogenic emissions comes from sources within 200 km of the lake. These nearby sources represent only 0.1% of the total global direct anthropogenic emissions used in the modeling. For Lake Ontario, 96% of all direct anthropogenic emissions are from sources more than 3000 km away from the lake, but these sources only contribute a little more than half (21.2% + 31.9% = 53.1%) of the deposition due to direct anthropogenic emissions.

Figure 121 shows that about a fifth (20.5%) of the modeled atmospheric mercury deposition to Lake Michigan from direct anthropogenic emissions comes from sources within 200 km of the lake. These nearby sources represent only 0.1% of total global direct anthropogenic emissions. For Lake Michigan, 96% of all direct anthropogenic emissions are from sources more than 3000 km away from the lake, but these sources only contribute a little more than half (22.8% + 35.2% = 58%) of the deposition due to direct anthropogenic emissions.

For Lake Huron, Figure 122 shows that about 15% of the modeled atmospheric mercury deposition from direct anthropogenic emissions comes from sources within 200 km of the lake. These nearby sources represent only 0.2% of total global direct anthropogenic emissions. For Lake Huron, 96% of all direct anthropogenic emissions are from sources more than 3000 km away from the lake, and these sources contribute about 2/3 (26.1% + 39.2% = 65.3%) of the deposition due to direct anthropogenic emissions.

Finally, Figure 123 shows that less than 5% of the modeled atmospheric mercury deposition to Lake Superior from direct anthropogenic emissions comes from sources within 200 km of the lake. These nearby sources represent only 0.1% of total global direct anthropogenic emissions. For Lake Superior, 96% of all direct anthropogenic emissions are from sources more than 3000 km away from the lake, and these sources contribute nearly 80% of the deposition due to direct anthropogenic emissions.

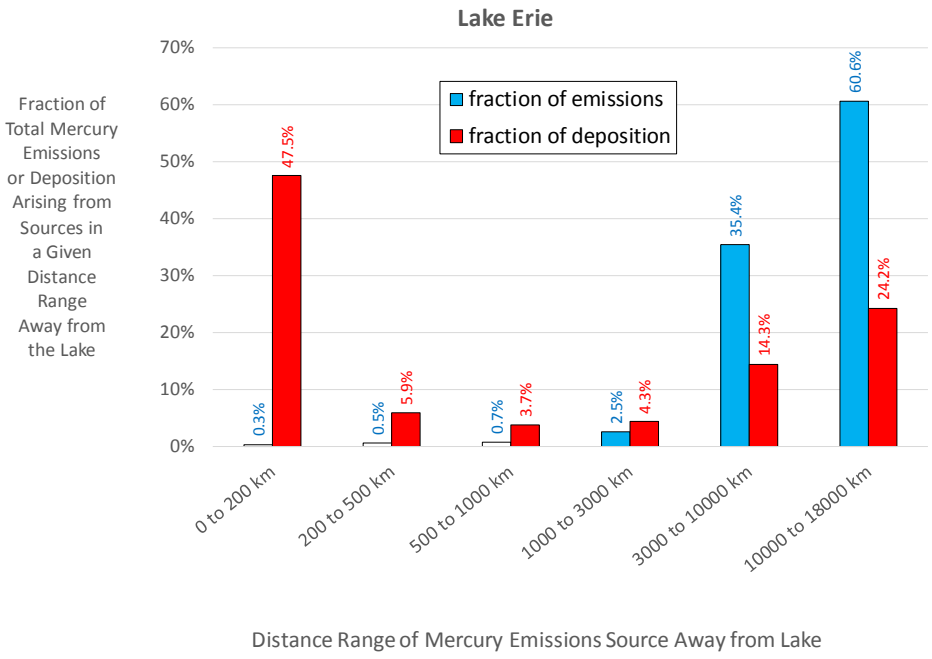

Figure 119. Fraction of direct anthropogenic contributions to atmospheric mercury deposition to Lake Erie arising from direct anthropogenic emissions in different distance ranges away from the lake.

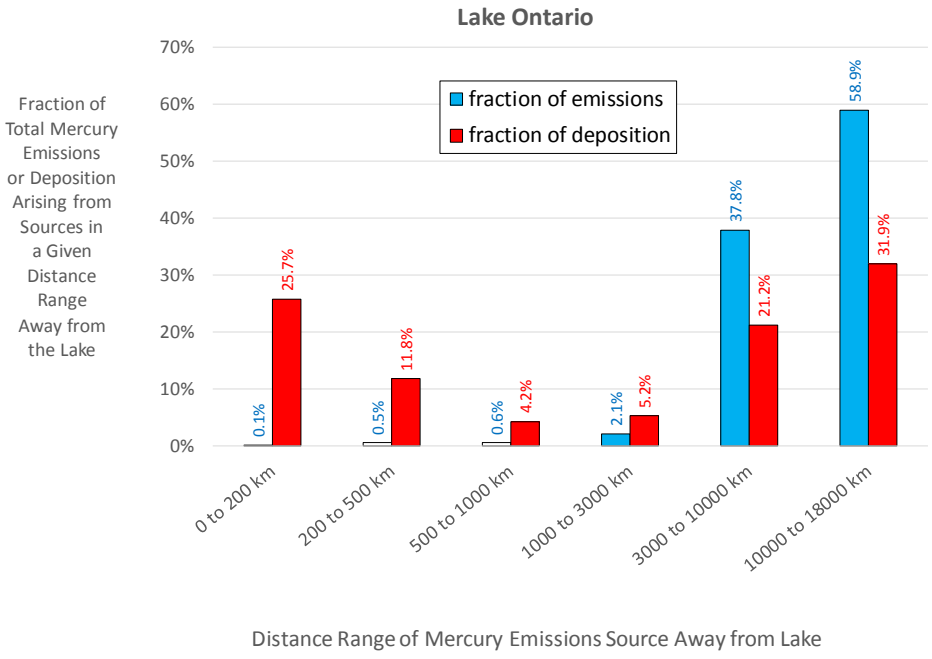

Figure 120. Fraction of direct anthropogenic contributions to atmospheric mercury deposition to Lake Erie arising from direct anthropogenic emissions in different distance ranges away from the lake.

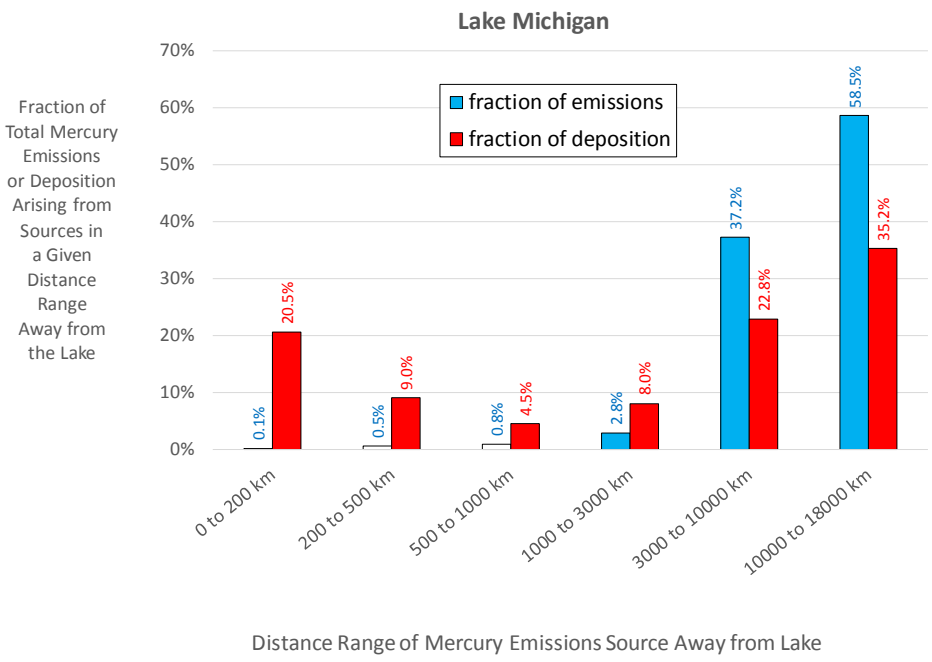

Figure 121. Fraction of direct anthropogenic contributions to atmospheric mercury deposition to Lake Michigan arising from direct anthropogenic emissions in different distance ranges away from the lake.

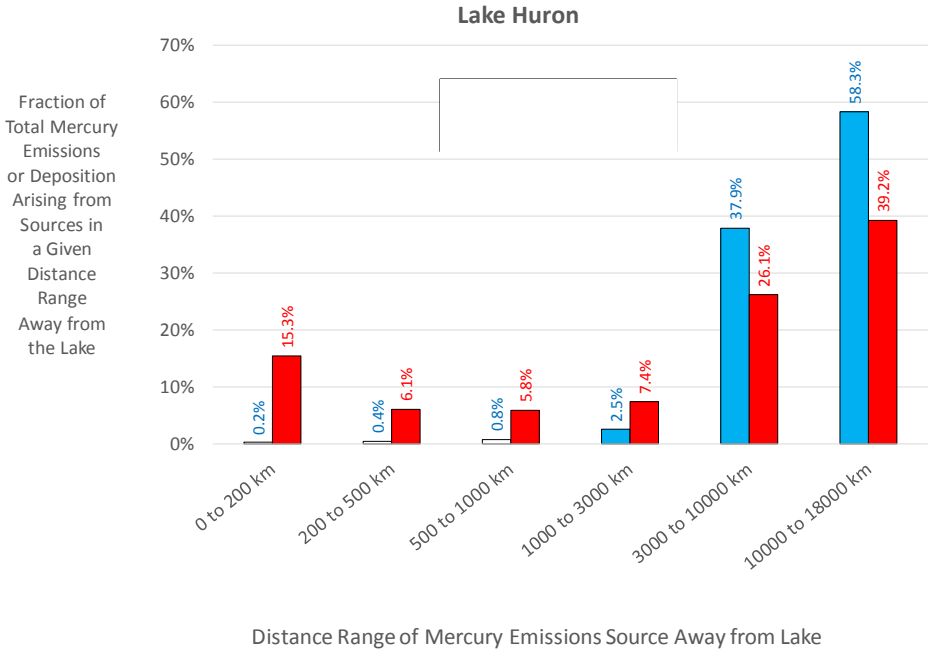

Figure 122. Fraction of direct anthropogenic contributions to atmospheric mercury deposition to Lake Huron arising from direct anthropogenic emissions in different distance ranges away from the lake.

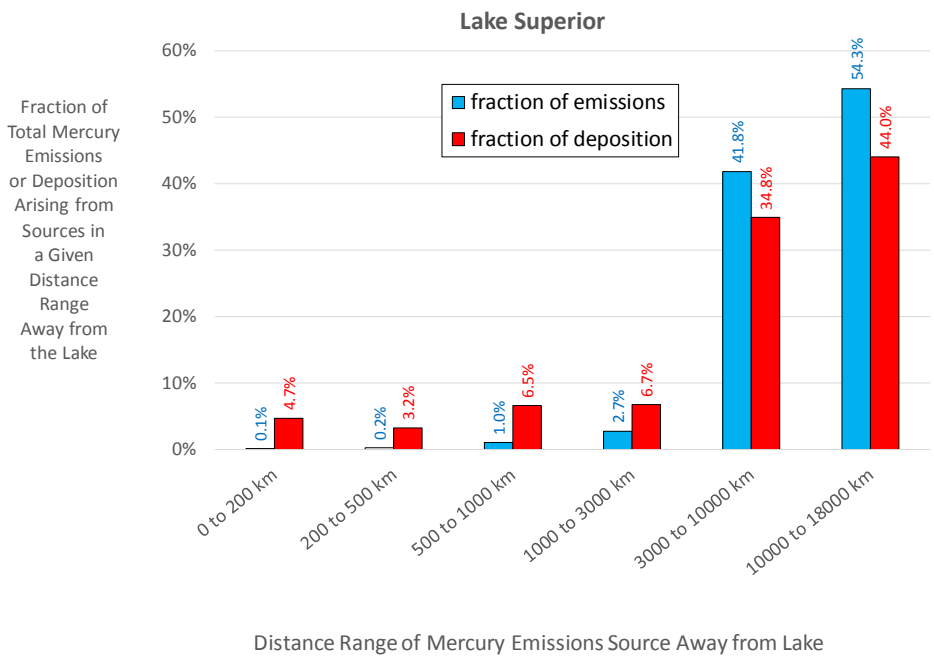

Figure 123. Fraction of direct anthropogenic contributions to atmospheric mercury deposition to Lake Superior arising from direct anthropogenic emissions in different distance ranges away from the lake.

In Figure 124, analogous results for Lake St. Clair are provided, and it can be seen that the results are similar to those for Lake Erie (Figure 119).

In the remaining figures of this section, comparable results for each of the Great Lakes watersheds are shown. An additional "distance" category is shown in these watershed-associated figures: "within or adjacent" refers to sources within the watershed or immediately adjacent to the watershed border.

Figure 125 shows results for the Lake Erie watershed, not including Lake St. Clair. It can be seen that more than 30% of the deposition from direct anthropogenic emissions arises from sources within or adjacent to the watershed, even though these sources represent only ~0.1% of emissions. Results for the other lake watersheds follow a similar pattern to the differences in source-receptor relationships for the Great Lakes themselves presented earlier in this section. That is, the importance of local sources decreases for the other lake watersheds, with the smallest local contribution for the watersheds of Lakes Huron and Superior.

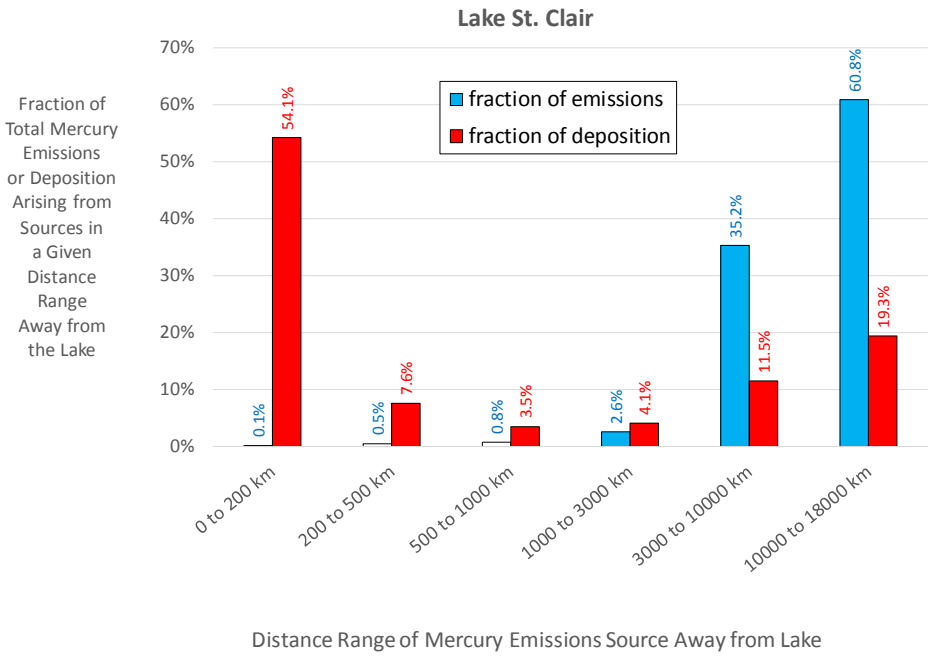

Figure 124. Fraction of direct anthropogenic contributions to atmospheric mercury deposition to Lake St. Clair arising from direct anthropogenic emissions in different distance ranges away from the lake.

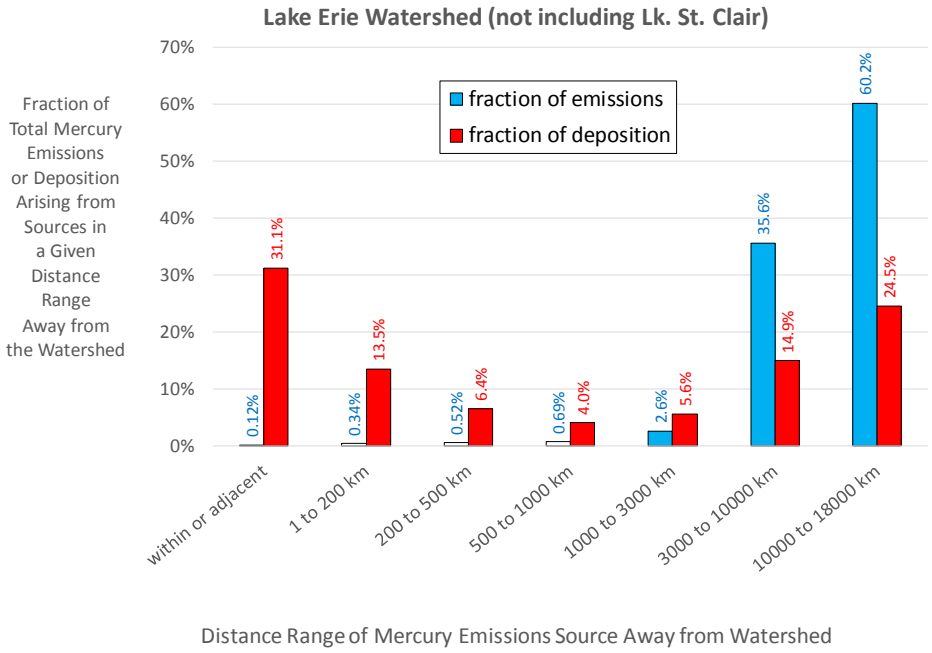

Figure 125. Fraction of direct anthropogenic contributions to atmospheric mercury deposition to the Lake Erie watershed (not including Lake St. Clair) arising from direct anthropogenic emissions in different distance ranges away from the watershed.

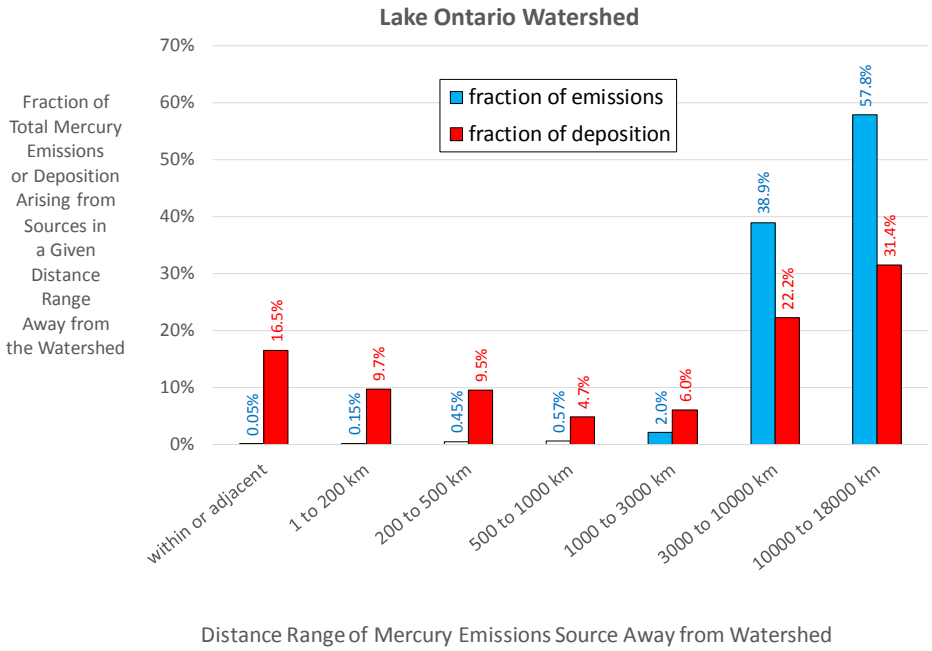

Figure 126. Fraction of direct anthropogenic contributions to atmospheric mercury deposition to the Lake Ontario watershed arising from direct anthropogenic emissions in different distance ranges away from the watershed.

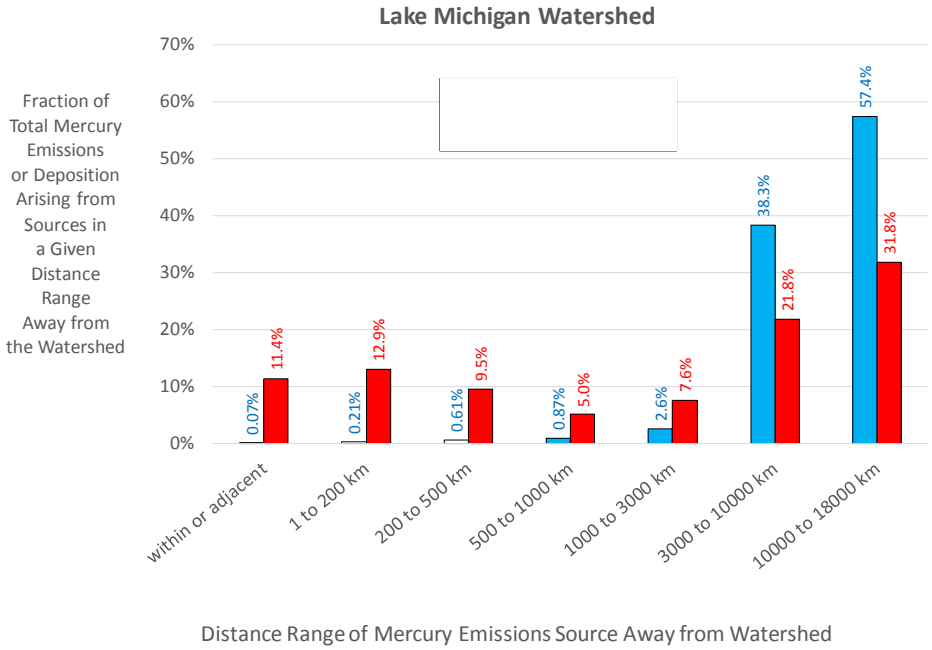

Figure 127. Fraction of direct anthropogenic contributions to atmospheric mercury deposition to the Lake Michigan watershed arising from direct anthropogenic emissions in different distance ranges away from the watershed.

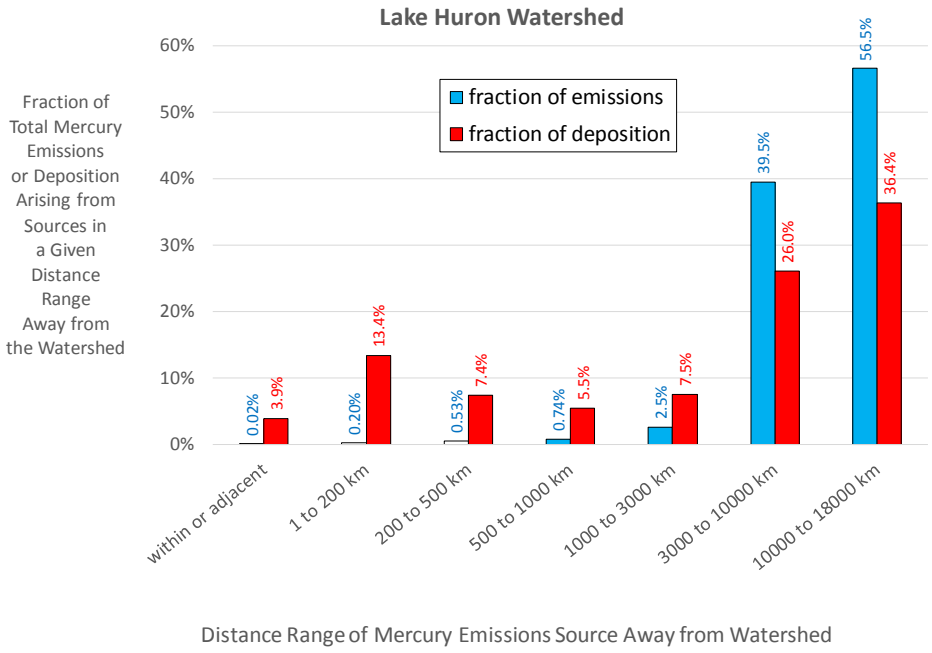

Figure 128. Fraction of direct anthropogenic contributions to atmospheric mercury deposition to the Lake Huron watershed arising from direct anthropogenic emissions in different distance ranges away from the watershed.

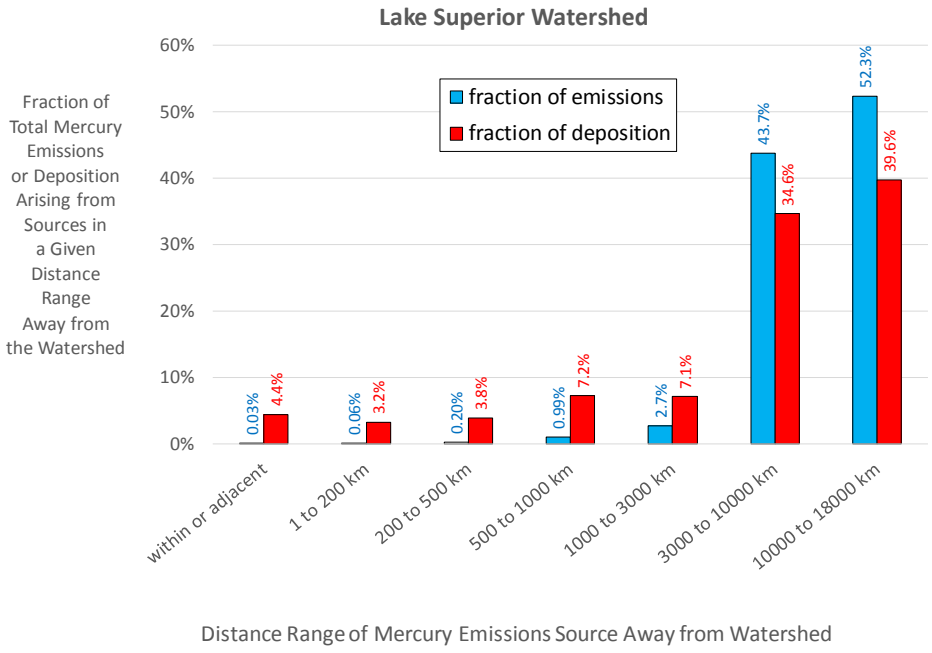

Figure 129. Fraction of direct anthropogenic contributions to atmospheric mercury deposition to the Lake Superior watershed arising from direct anthropogenic emissions in different distance ranges away from the watershed.

5.4. Comparison of these 2011 results with earlier 2005 results

In this section, these new 2011 results will be compared with the 2005 results reported previously (Cohen, Draxler et al. 2016). The 2005 analysis was carried out with an Eulerian-only approach, analogous to the RS-00 methodology utilized here. Therefore, the most relevant comparison will be to compare the results of the two Eulerian-only analyses.

Figure 130 shows the model-estimated deposition flux from all emissions types to each of the Great Lakes for the 2005 and 2011 analyses. For each lake, it is seen that the modeled 2011 deposition is less than the modeled 2005 deposition. Figure 131 shows these same data, but expressed as fractions of the total modeled deposition for each lake. It can be seen that the model-estimated amount and fraction due to U.S. emissions declined significantly for all of the lakes.

Figure 132 and Figure 133 show the same data, but the direct anthropogenic contributions are aggregated into a single category so that the overall impact of these emissions can be more clearly seen.

Figure 134 and Figure 135 are analogous but show only the direct anthropogenic emissions contributions for each lake, in absolute amount (Figure 134) and fraction of total anthropogenic contributions (Figure 135). It can be clearly seen from Figure 134 that the most dramatic change in the model estimates is the decrease in mercury deposition attributable to direct anthropogenic emissions in the United States.

The primary reason for this is that the emissions in the U.S. declined dramatically between 2005 and 2011, especially in the Great Lakes region. This decline can be seen in Figure 136 and Figure 137, in which the direct anthropogenic emissions from the U.S. and Canada for 2005 and 2011 are aggregated onto a 1-degree grid. These two figures were developed in conjunction with the analysis by Zhou et al. (2017) and show the three monitoring sites used in that analysis (the three white stars in the maps in the Northeastern U.S.).

This decline can also be clearly seen in Figure 138, which shows the total point source mercury emissions from U.S. and Canadian sources over different distances ranges away from each Great Lake. Over all distance ranges considered, the emissions declined significantly between 2005 and 2011. This figure identical to Figure S8 in the Supplementary Information associated with the Zhou et al. (2017) analysis (prepared by the author).

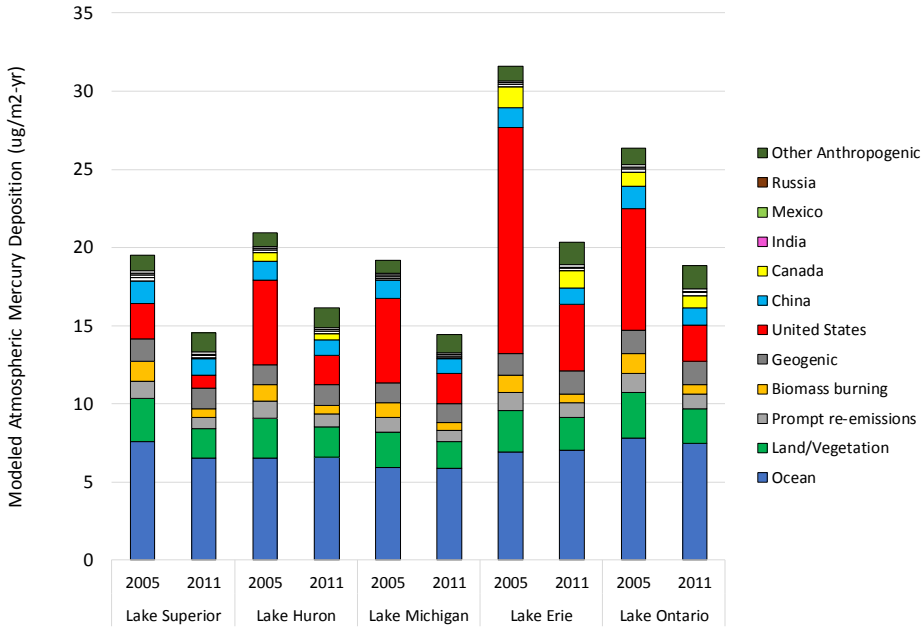

Figure 130. Comparison of Eulerian-only (RS-00) model-estimated 2005 and 2011 atmospheric mercury deposition flux to the Great Lakes.

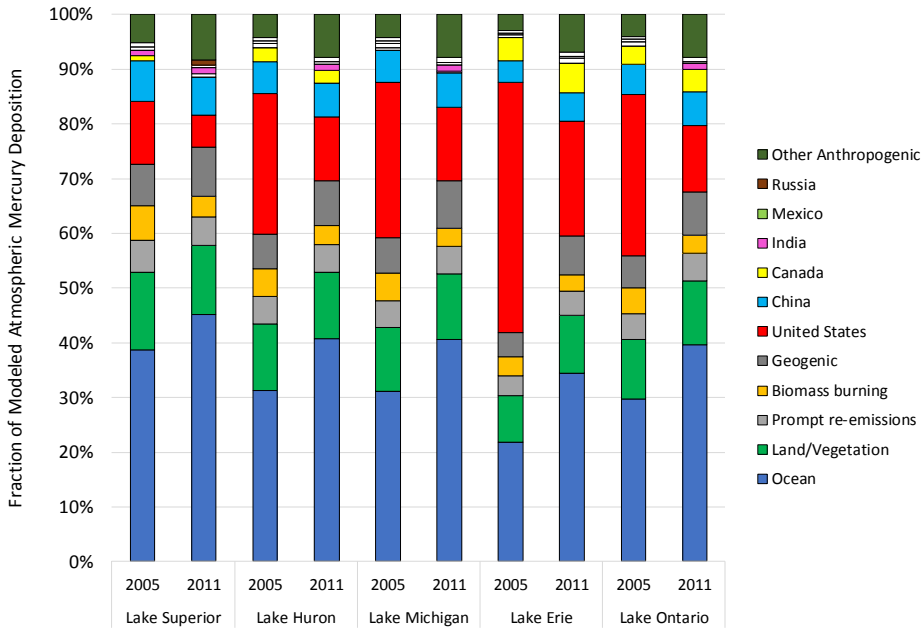

Figure 131. Comparison of Eulerian-only (RS-00) model-estimated 2005 and 2011 atmospheric mercury deposition flux to the Great Lakes. These are the same data as in the previous plot, but plotted as a 100% stacked bar graph, i.e., so that the fractions of deposition arising from each source type are shown.

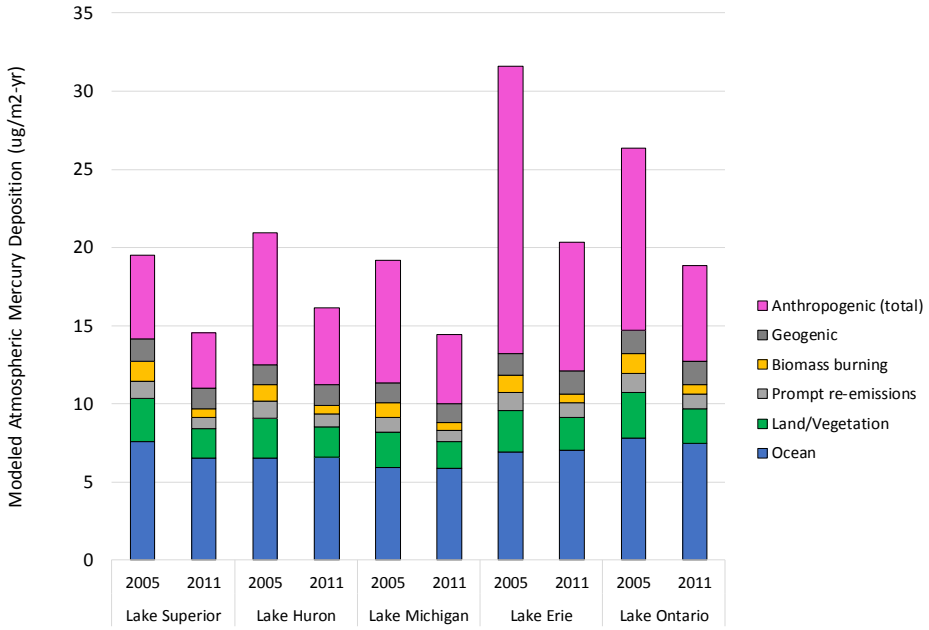

Figure 132. Comparison of Eulerian-only (RS-00) model-estimated 2005 and 2011 atmospheric mercury deposition flux to the Great Lakes. Contributions from direct anthropogenic emissions are aggregated into a single category.

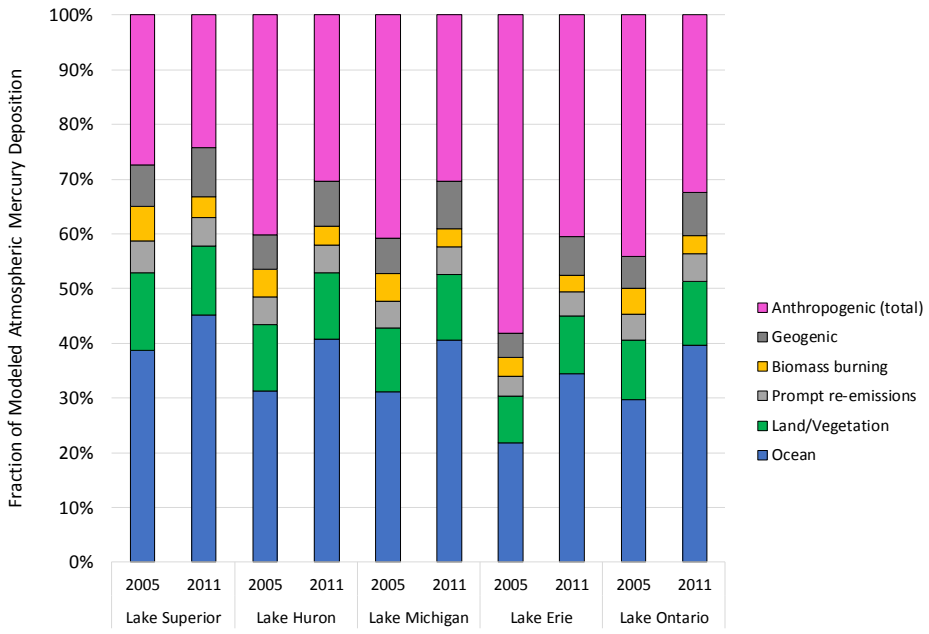

Figure 133. Comparison of Eulerian-only (RS-00) model-estimated 2005 and 2011 atmospheric mercury deposition flux to the Great Lakes. Contributions from direct anthropogenic emissions are aggregated into a single category. Fractions of total model-estimated deposition are shown.

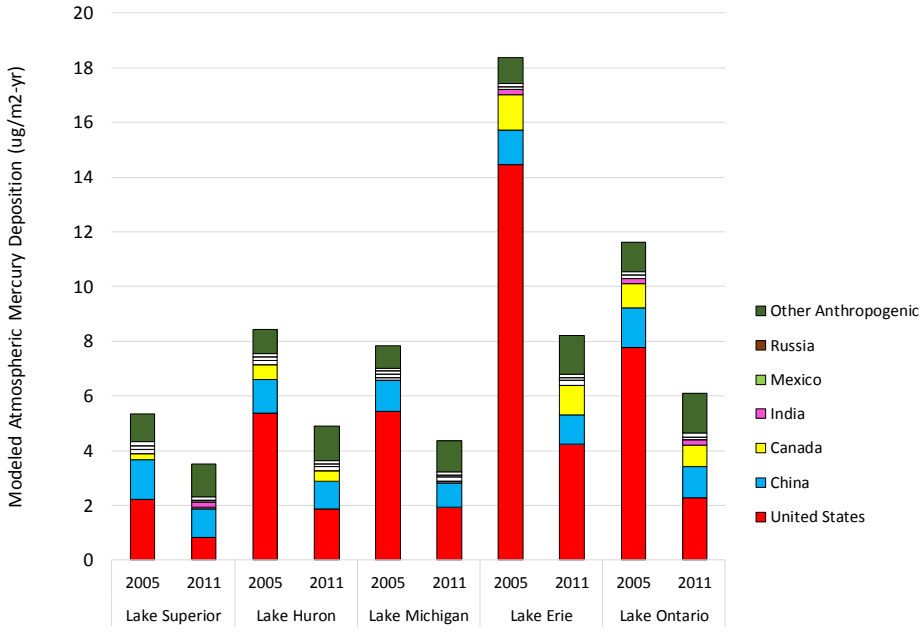

Figure 134. Comparison of Eulerian-only (RS-00) model-estimated 2005 and 2011 atmospheric mercury deposition flux to the Great Lakes from direct anthropogenic emissions.

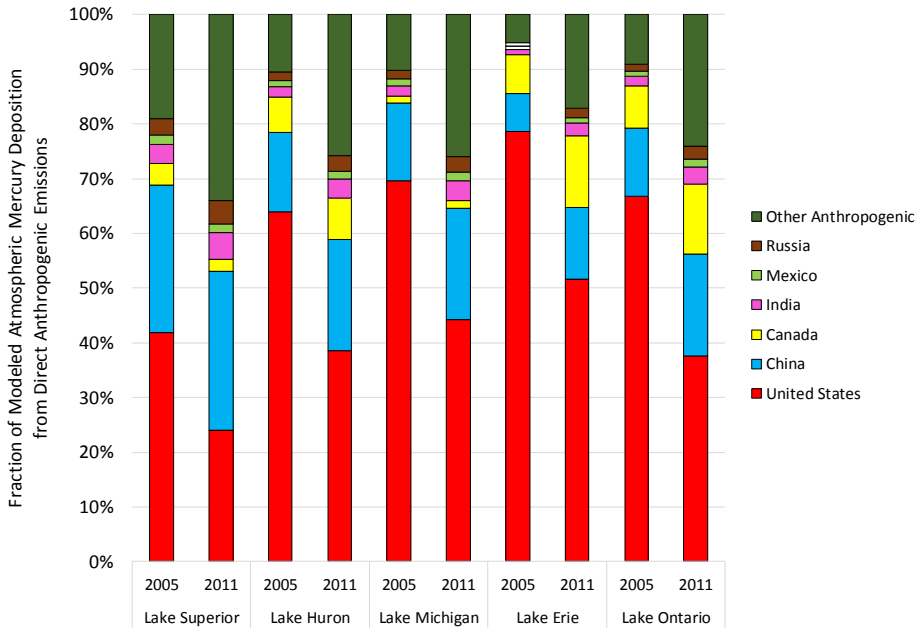

Figure 135. Comparison of Eulerian-only (RS-00) model-estimated 2005 and 2011 atmospheric mercury deposition flux to the Great Lakes from direct anthropogenic emissions. Fractions of total model-estimated deposition from direct anthropogenic emissions are shown.

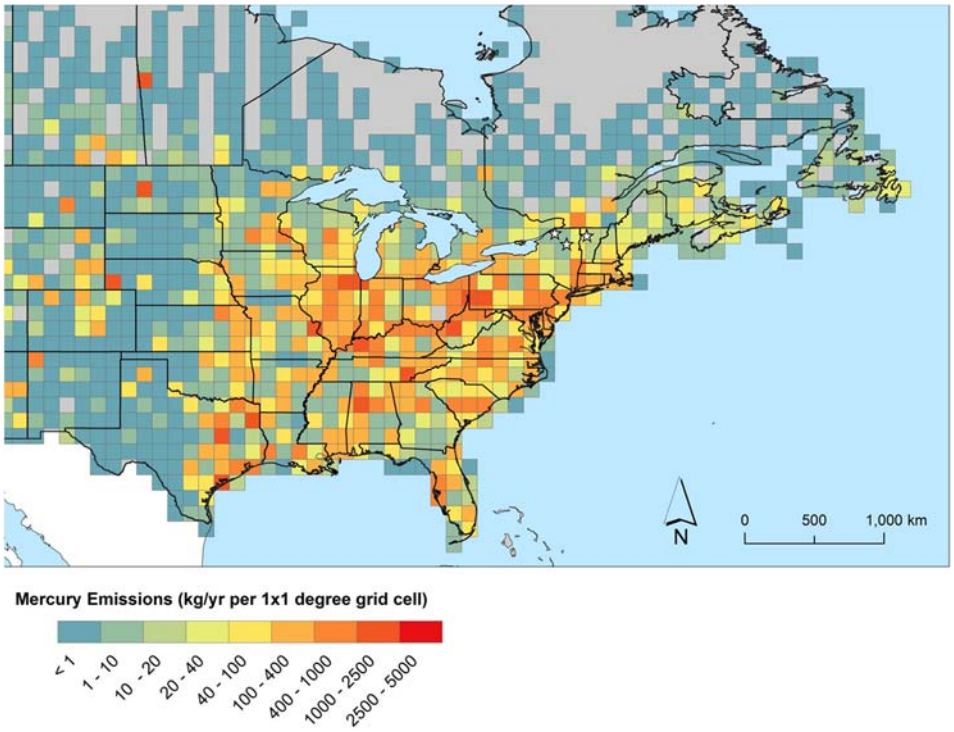

Figure 136. 2005 anthropogenic emissions from U.S. and Canadian sources aggregated onto a 1-degree grid.

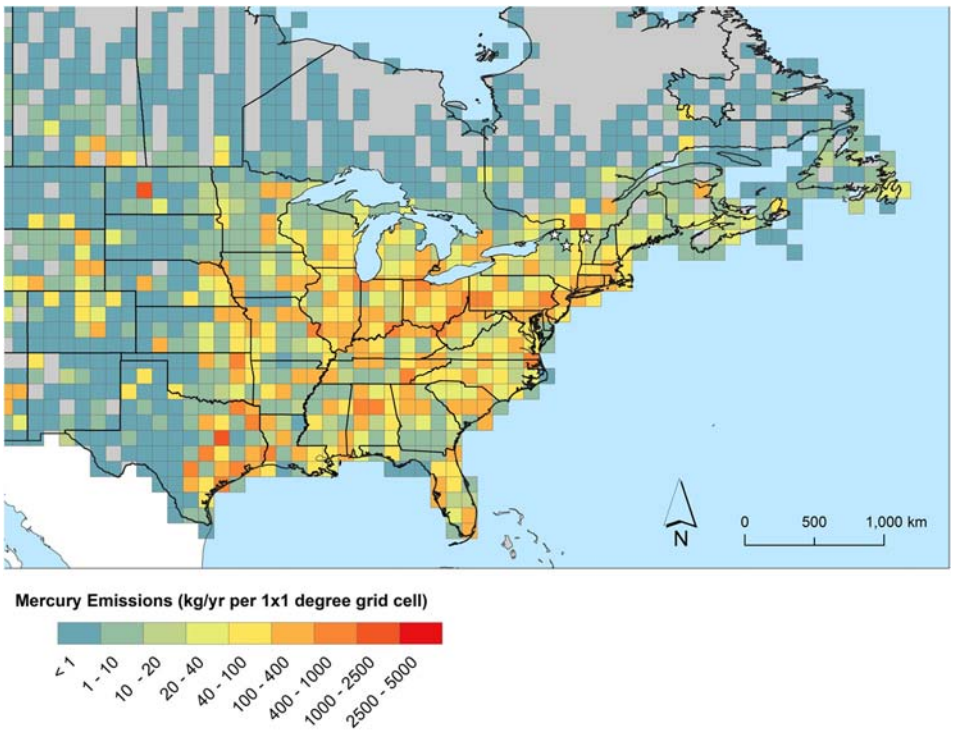

Figure 137. 2011 anthropogenic emissions from U.S. and Canadian sources aggregated onto a 1-degree grid.

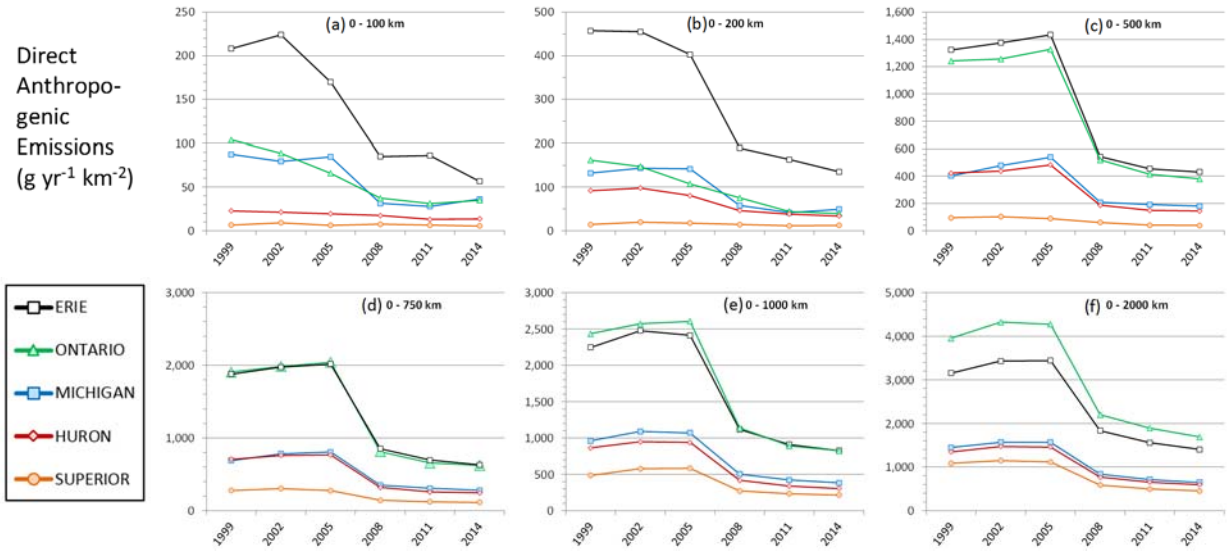

Figure 138. Total Hg point source emissions from the USEPA National Emissions Inventory and the Canadian National Pollutant Release Inventory within (a) 100 km, (b) 200 km, (c) 500 km, (d) 750 km, (e) 1000 km, and (f) 2000 km of each Great Lake. [Figure S8 from Zhou et al. (2017)].

5.5. Comparison of these results with other modeling results

These results show that contributions from U.S. anthropogenic sources contribute significantly to the Great Lakes. This general finding is consistent with a number of other recent analyses, including the following:

- Using a weight-of-evidence approach Sunderland et al. (2016) argued that historical EPA CMAQ-based modeling may have underestimated the impact of local and regional sources on near-field mercury deposition in the U.S., and consequently underestimated the benefits of mercury emissions reductions.

- The GEOS-Chem model was used to estimate the cumulative benefits of domestic and international mercury controls for atmospheric deposition – and subsequent public health impacts – in the U.S. through 2050 (Giang and Selin 2016). For the same amount of avoided mercury emissions, domestic reductions were estimated to have nearly an order of magnitude higher public health benefit than international actions.

- In a hybrid analysis combining fate-and-transport modeling with measurements, GEOS-Chem was used to examine trends in mercury wet deposition over the United States over the 2004-2010 period (Zhang and Jaegle, 2013). The modeling results were subtracted from the observations to assess the roles of changing meteorology and emissions on observed wet deposition at 47 U.S. sites. In the Northeast and Midwest U.S., approximately half of the decreasing trend in mercury concentrations in precipitation could be explained by decreasing U.S. emissions over the study period.

5.6. Visualization of these results in Great Lakes ERMA

U.S. and Canadian source-receptor results using Run Scheme 04 – the analysis using the most advanced and computationally resource-intensive dispersion simulation methodology – are being incorporated into NOAA's Great Lakes Environmental Response Management Application (ERMA) system to allow enhanced data visualization:

https://response.restoration.noaa.gov/maps-and-spatial-data/environmental-response-management-application-erma

https://response.restoration.noaa.gov/maps-and-spatial-data/environmental-response-management-application-erma/great-lakes-erma.html

The deposition contribution of each point and area source in the U.S. and Canadian emissions inventories to each Great Lake (and each watershed) is included in the ERMA dataset. The "model configuration" referenced with the data is designated as "RS_04_111", referring to Run Scheme 04, using a total of 111 Standard Source Locations (SSL's). These 111 SSL's are described in Section 3.3, beginning on page 36.

5.7. Source-by-Source Results

To illustrate the source-by-source results, the top 25 contributors to each of the Great Lakes among the emissions inventory records in the U.S. and Canada are presented in Figure 139 through Figure 143. These figures show the cumulative fraction of the total contribution from direct anthropogenic emissions for the top 25 U.S. and Canadian contributors. The results shown are for RS-04, the most "advanced"and computationally intense modeling methodology used.

Before considering these figures, note that contributions from anthropogenic sources in China, India, Russia, Mexico and elsewhere are included in the analysis, but the emissions inventories used are gridded, overall emissions estimates. Each 2.5^{o} x 2.5^{o} grid can contain 100's or even 1000's of point and area source entities, and so, they cannot be directly compared in these figures. However, an example will provide context on the relative magnitude of the contributions. For the Lake Erie results in Figure 139, if the global gridded emissions inventory records were included, the 17th largest contributor would be a grid square in Western Africa whose centroid is latitude 7.5^{o} North and longitude is 2.5^{0} West. This is an area with high emissions from gold mining, and the total mercury emissions in that grid square were ~23,200 kg/yr, according to the 2010 AMAP-UNEP inventory used in this analysis (as described in Section 2). The 18th largest contributor would be a grid cell in China (lat = 30^{o}, long = 120^{o}) with emissions estimated to be 23,600 kg/yr.

By comparison, the largest emissions source in the top 25 U.S./Canadian contributors to Lake Erie is the 2nd ranked contributor, a coal-fired electric generating power plant that was estimated to emit a total of 248 kg/yr of mercury in 2011. This emissions amount is seen to be ~100x smaller than the gridded emissions contributors noted above. This illustrates why the global source contributions cannot be meaningfully compared with the U.S./Canadian emissions sources in these particular figures. The total emissions from *all* 25 emissions inventory entities represented in Figure 139 are ~1700 kg/yr, more than 10x less than gridded emissions contributors noted above. Thus, while the combined impact of all sources within a few grid squares are comparable to the impact of individual U.S./Canadian sources, the emissions from those grid squares are equivalent to ~100 or more "large" *individual* emissions contributors within the within the grid squares.

In the top-25 contributor figures below, only the type of emissions source is shown (e.g., coal-fired electric generator, primary metal producer, etc.) and the inventory data set it came from (i.e., U.S. point source, U.S. area source, Canadian point source, or Canadian area source). The sources of these data are described in Section 2 above.

It can be seen from Figure 139 that U.S. point sources – i.e., individual facilities – make up most of the top 25 contributors. There are also three U.S. area sources in the top 25 (human cremation in three different counties near the lake) and one Canadian point source. The source names are not included in these figures, but are included in the DIVER/ERMA dataset noted in the previous section. It can also be seen in this figure that the top 25 contributors account for ~30% of the model-estimated deposition in 2011 to Lake Erie from direct anthropogenic emissions.

For Lake Ontario (Figure 140), it is seen that the top 25 contributors only represent about 13% of the total model-estimated deposition in 2011 from direct anthropogenic emissions worldwide, and the mix of sources is very different. For this lake, there are many more Canadian contributors, including both area and point sources.

For Lake Michigan (Figure 141), the top 25 contributors are all U.S. point sources and represent a little more than 12% of the total model-estimated deposition in 2011 from direct anthropogenic emissions worldwide.

For Lake Huron (Figure 142), the top 25 contributors are primarily U.S. point sources and represent ~10% of total model-estimated deposition in 2011 from direct anthropogenic emissions worldwide.

Finally, for Lake Superior (Figure 143), the top 25 contributors are mostly U.S. point sources and represent less than 5% of the total model-estimated deposition in 2011 from direct anthropogenic emissions worldwide.

In Figure 144 through Figure 148, maps of significant U.S. and Canadian point and area source contributors of atmospheric mercury deposition are shown for each of the Great Lakes. The size and shape of the symbols in the maps indicate the amount of mercury each source contributes to a given lake, and the color of the symbol indicates the type of source.

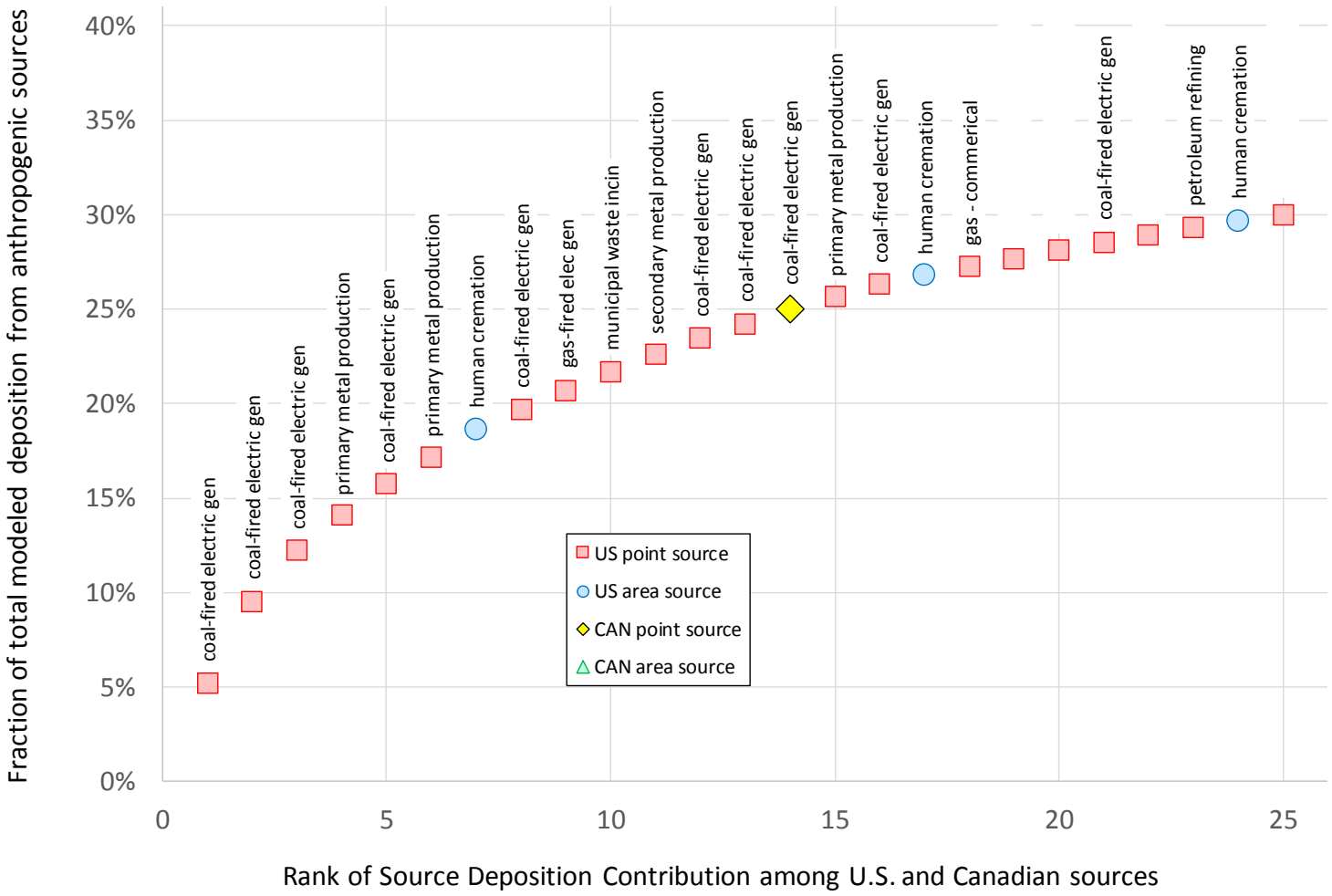

Figure 139. Top 25 U.S./Canadian Contributors to Lake Erie Hg Deposition.

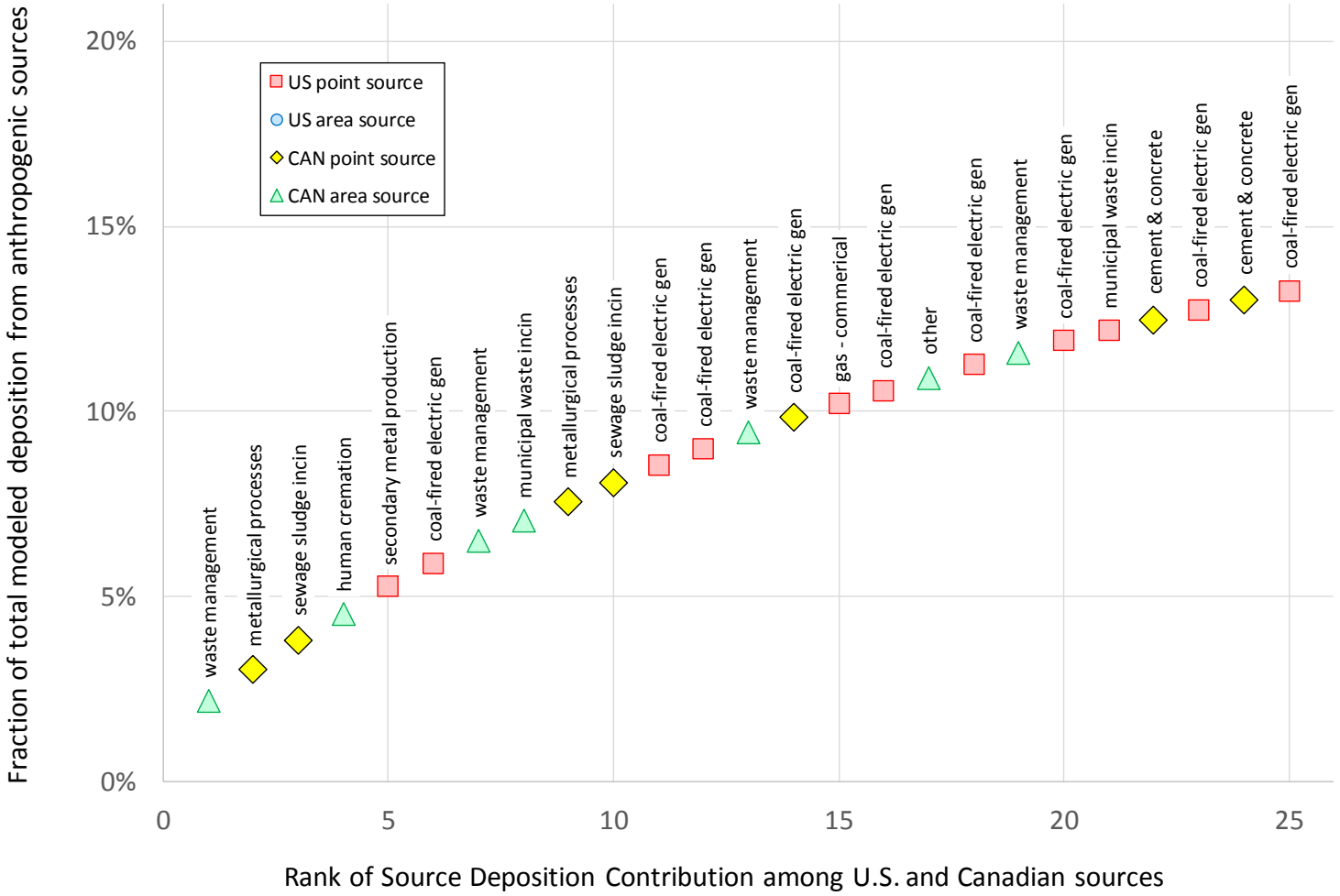

Figure 140. Top 25 U.S./Canadian Contributors to Lake Ontario Hg Deposition.

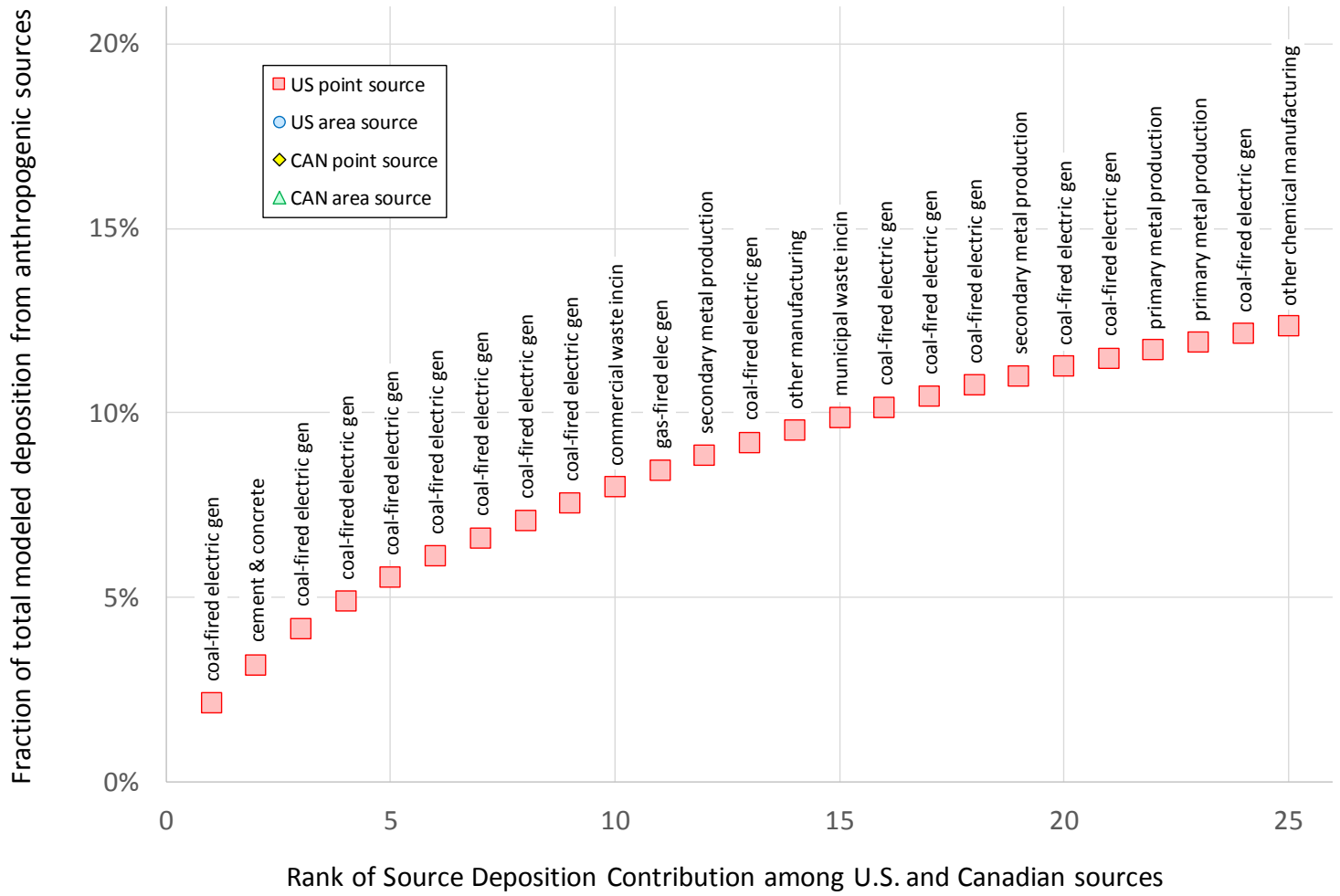

Figure 141. Top 25 U.S./Canadian Contributors to Lake Michigan Hg Deposition.

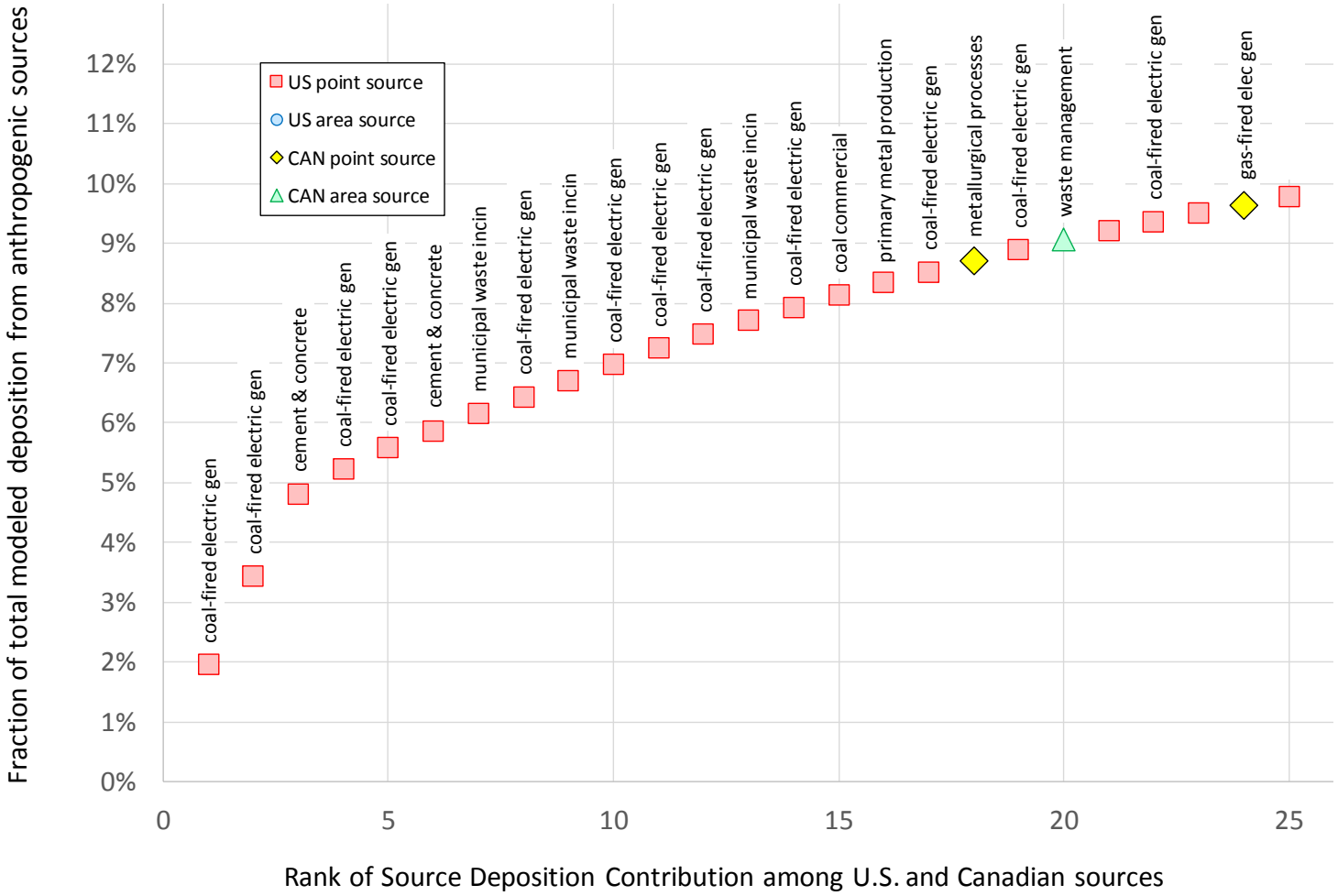

Figure 142. Top 25 U.S./Canadian Contributors to Lake Huron Hg Deposition.

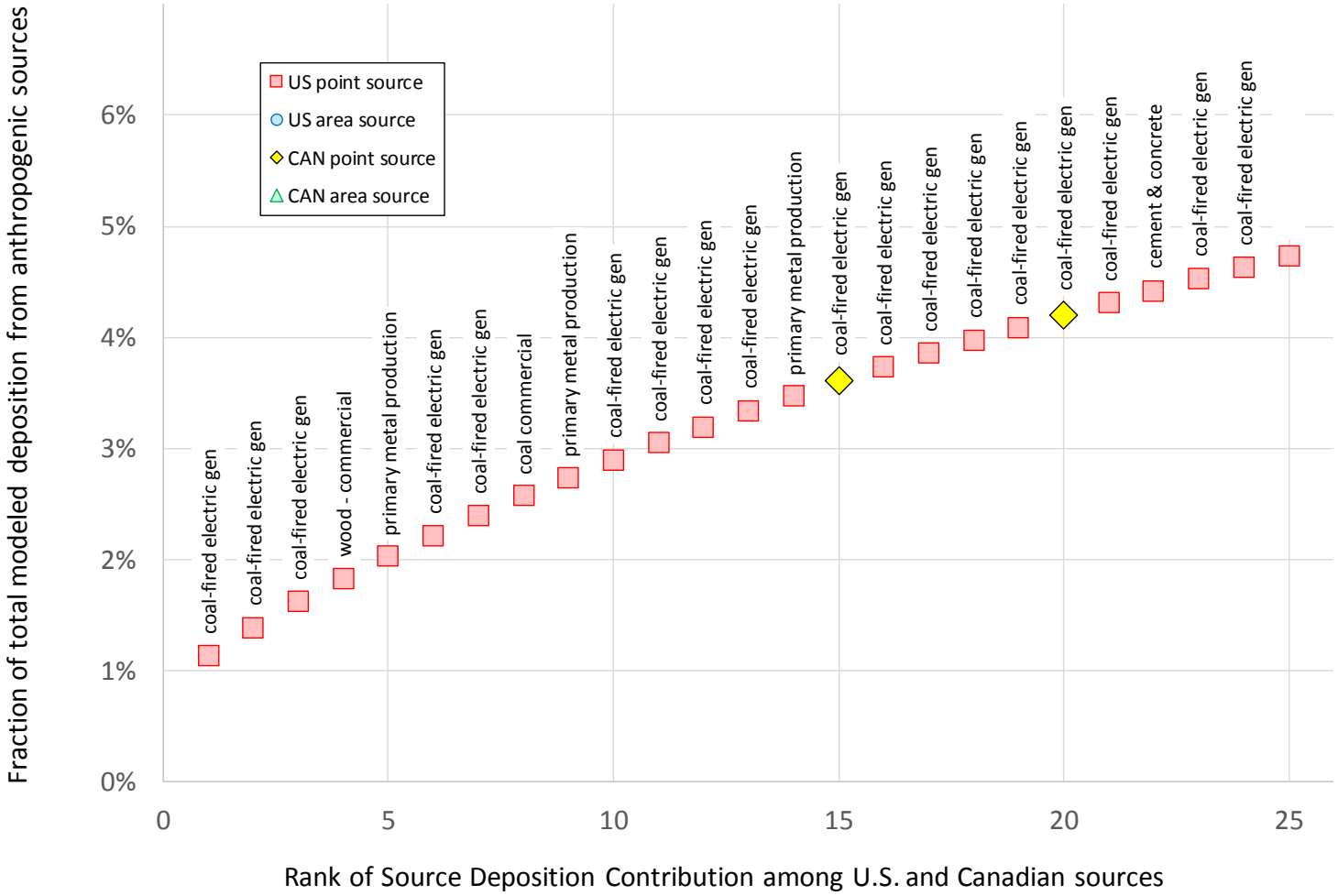

Figure 143. Top 25 U.S./Canadian Contributors to Lake Superior Hg Deposition.

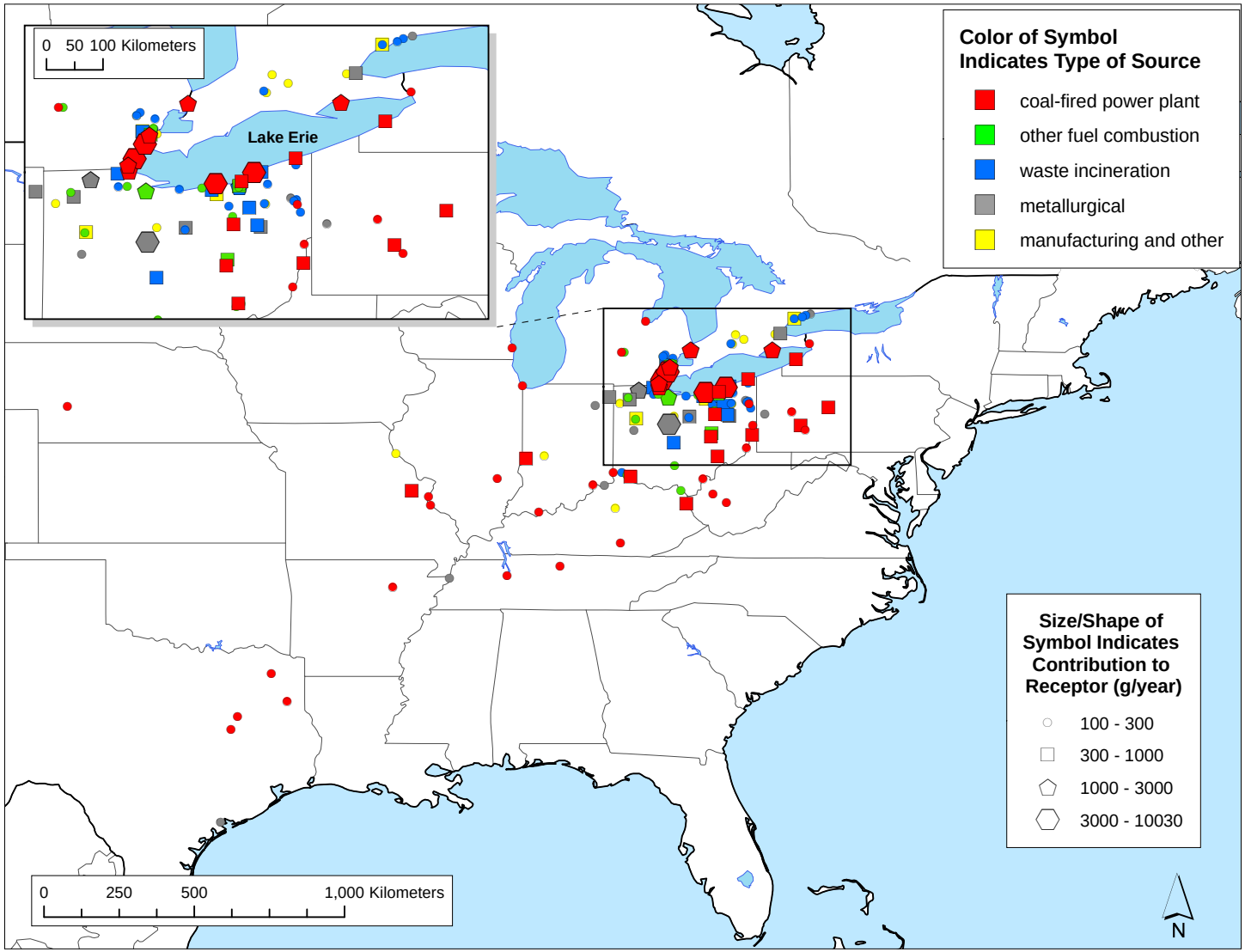

Figure 144. Significant U.S. and Canadian point and area source contributors to 2011 atmospheric deposition of mercury to Lake Erie.

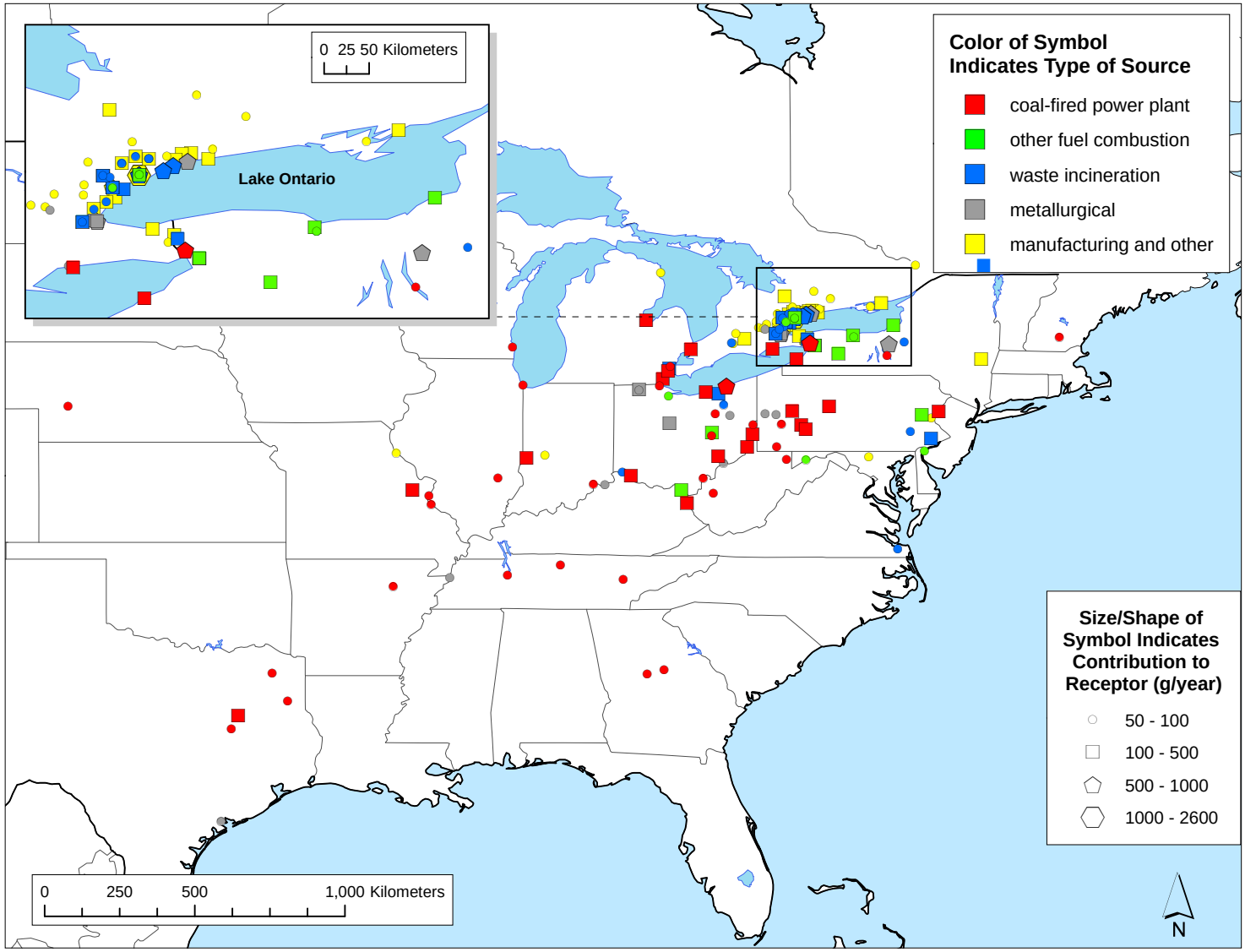

Figure 145. Significant U.S. and Canadian point and area source contributors to 2011 atmospheric deposition of mercury to Lake Ontario.

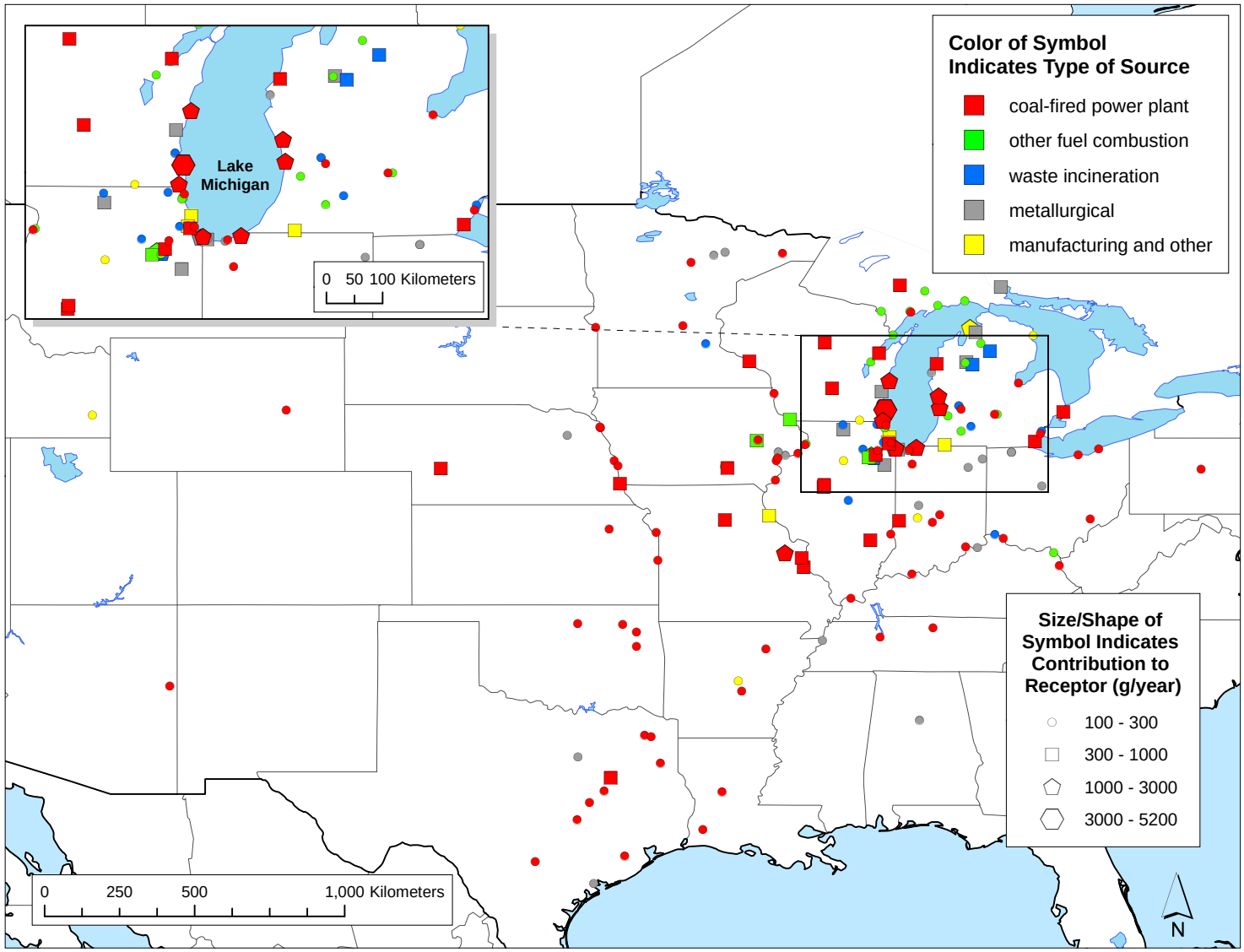

Figure 146. Significant U.S. and Canadian point and area source contributors to 2011 atmospheric deposition of mercury to Lake Michigan.

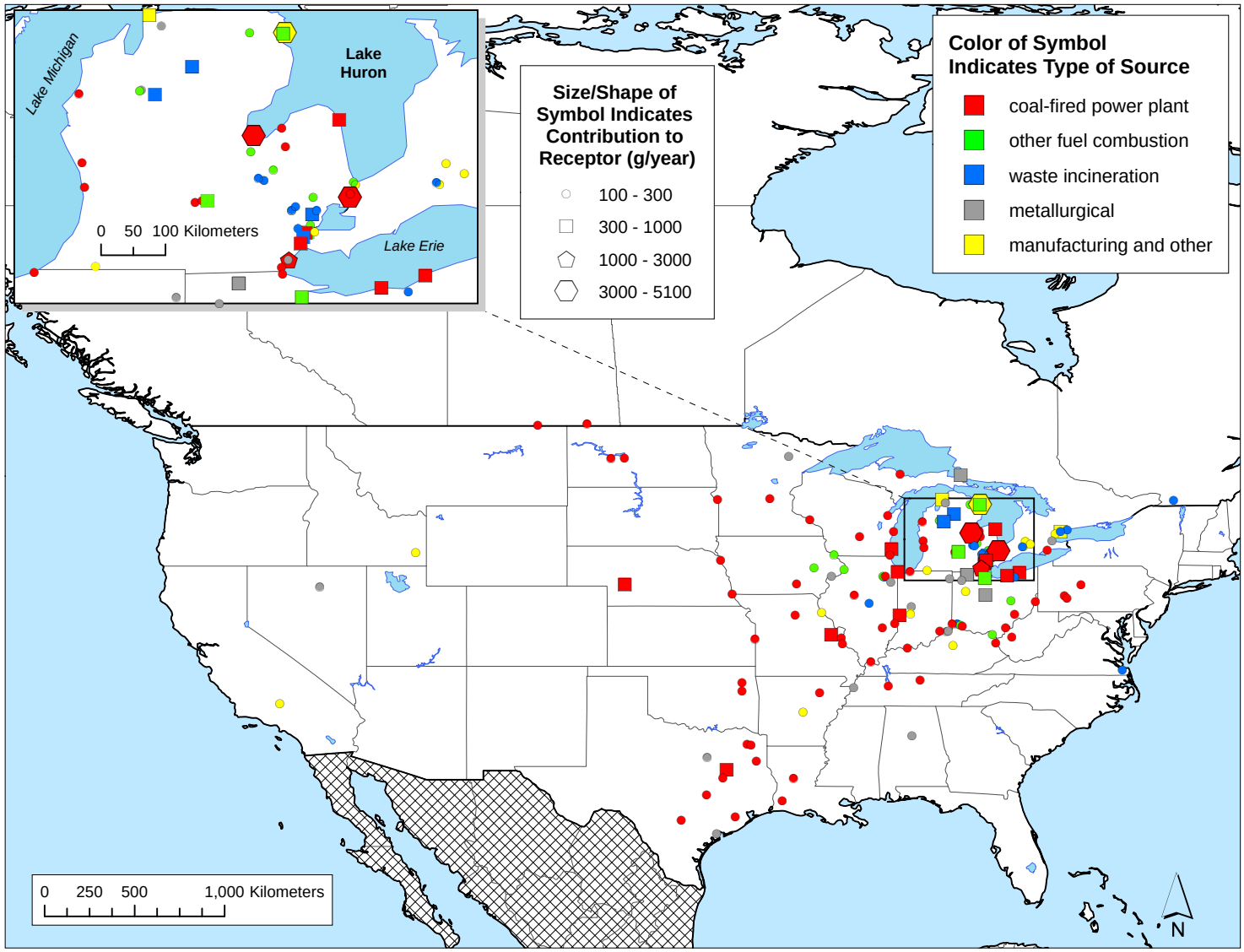

Figure 147. Significant U.S. and Canadian point and area source contributors to 2011 atmospheric deposition of mercury to Lake Huron.

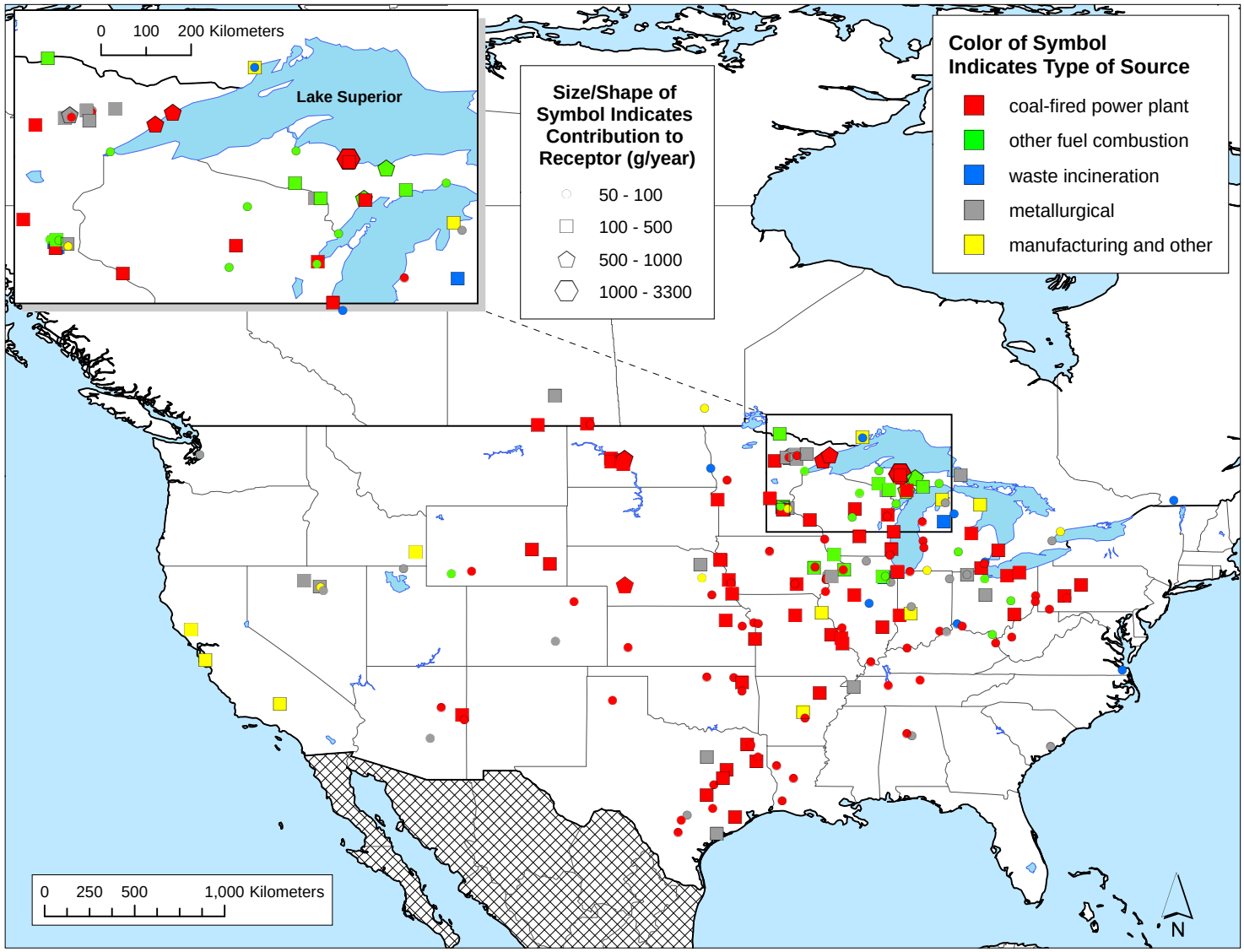

Figure 148. Significant U.S. and Canadian point and area source contributors to 2011 atmospheric deposition of mercury to Lake Superior.

6. References

Agnan, Y., T. Le Dantec, C. W. Moore, G. C. Edwards and D. Obrist (2016). "New constraints on terrestrial surface atmosphere fluxes of gaseous elemental mercury using a global database." Environmental Science & Technology **50**(2): 507-524.

AMAP/UNEP. (2013, July 27, 2015). "AMAP/UNEP geospatially distributed mercury emissions dataset 2010v1." from https://www.amap.no/mercury-emissions/datasets.

AMAP/UNEP (2013). Technical Background Report for the Global Mercury Assessment. Oslo, Norway**:** 263 pages.

Amos, H. M., D. J. Jacob, C. D. Holmes, J. A. Fisher, Q. Wang, R. M. Yantosca, E. S. Corbitt, E. Galarneau, A. P. Rutter, M. S. Gustin, A. Steffen, J. J. Schauer, J. A. Graydon, V. L. St Louis, R. W. Talbot, E. S. Edgerton, Y. Zhang and E. M. Sunderland (2012). "Gas-particle partitioning of atmospheric Hg(II) and its effect on global mercury deposition." Atmospheric Chemistry and Physics **12**(1): 591-603.

Ariya, P. A., M. Amyot, A. Dastoor, D. Deeds, A. Feinberg, G. Kos, A. Poulain, A. Ryjkov, K. Semeniuk, M. Subir and K. Toyota (2015). "Mercury physicochemical and biogeochemical transformation in the atmosphere and at atmospheric interfaces: a review and future directions." Chemical Reviews **115**(10): 3760-3802.

Bash, J. O., A. G. Carlton, W. T. Hutzell and O. R. Bullock, Jr. (2014). "Regional Air Quality Model Application of the Aqueous-Phase Photo Reduction of Atmospheric Oxidized Mercury by Dicarboxylic Acids." Atmosphere **5**(1): 1-15.

Bash, J. O. and D. R. Miller (2009). "Growing season total gaseous mercury (TGM) flux measurements over an Acer rubrum L. stand." Atmospheric Environment **43**(37): 5953-5961.

Bergan, T. and H. Rodhe (2001). "Oxidation of elemental mercury in the atmosphere; Constraints imposed by global scale modelling." Journal of Atmospheric Chemistry **40**(2): 191-212.

Bhavsar, S. P., S. B. Gewurtz, D. J. McGoldrick, M. J. Keir and S. M. Backus (2010). "Changes in Mercury Levels in Great Lakes Fish Between 1970s and 2007." Environmental Science & Technology **44**(9): 3273-3279.

Bieser, J., F. De Simone, C. Gencarelli, B. Geyer, I. Hedgecock, V. Matthias, O. Travnikov and A. Weigelt (2014). "A diagnostic evaluation of modeled mercury wet depositions in Europe using atmospheric speciated high-resolution observations." Environmental Science and Pollution Research **21**(16): 9995-10012.

Bieser, J., F. Slemr, J. Ambrose, C. Brenninkmeijer, S. Brooks, A. Dastoor, F. DeSimone, R. Ebinghaus, C. N. Gencarelli, B. Geyer, L. E. Gratz, I. M. Hedgecock, D. Jaffe, P. Kelley, C. J. Lin, L. Jaegle, V. Matthias, A. Ryjkov, N. E. Selin, S. J. Song, O. Travnikov, A. Weigelt, W. Luke, X. R. Ren, A. Zahn, X. Yang, Y. Zhu and N. Pirrone (2017). "Multi-model study of mercury dispersion in the atmosphere: vertical and interhemispheric distribution of mercury species." Atmospheric Chemistry and Physics **17**(11): 6925-6955.

Bullock, O. R. and K. A. Brehme (2002). "Atmospheric mercury simulation using the CMAQ model: formulation description and analysis of wet deposition results." Atmospheric Environment **36**(13): 2135-2146.

Bullock, O. R., Jr., D. Atkinson, T. Braverman, K. Civerolo, A. Dastoor, D. Davignon, J.-Y. Ku, K. Lohman, T. C. Myers, R. J. Park, C. Seigneur, N. E. Selin, G. Sistla and K. Vijayaraghavan (2008). "The North American Mercury Model Intercomparison Study (NAMMIS): Study description and model-to-model comparisons." Journal of Geophysical Research-Atmospheres **113**(D17).

Bullock, O. R., Jr., D. Atkinson, T. Braverman, K. Civerolo, A. Dastoor, D. Davignon, J.-Y. Ku, K. Lohman, T. C. Myers, R. J. Park, C. Seigneur, N. E. Selin, G. Sistla and K. Vijayaraghavan (2009). "An analysis of simulated wet deposition of mercury from the North American Mercury Model Intercomparison Study." Journal of Geophysical Research-Atmospheres **114**.

Calhoun, J. A. and E. Prestbo (2001). Kinetic studyof the gas phase reactions of elemental mercury by molecular chlorine. Seattle, WA, Frontier Geosciences.

Calvert, J. G. and S. E. Lindberg (2005). "Mechanisms of mercury removal by O3 and OH in the atmosphere." Atmospheric Environment **39**(18): 3355-3367.

Chen, L., H. H. Wang, J. F. Liu, Y. D. Tong, L. B. Ou, W. Zhang, D. Hu, C. Chen and X. J. Wang (2014). "Intercontinental transport and deposition patterns of atmospheric mercury from anthropogenic emissions." Atmospheric Chemistry and Physics **14**(18): 10163-10176.

Chen, L., W. Zhang, Y. X. Zhang, Y. D. Tong, M. D. Liu, H. H. Wang, H. Xie and X. J. Wang (2018). "Historical and future trends in global source-receptor relationships of mercury." Science of the Total Environment **610**: 24-31.

Cheng, I., L. Zhang, P. Blanchard, J. Dalziel, R. Tordon, J. Huang and T. M. Holsen (2013). "Comparisons of mercury sources and atmospheric mercury processes between a coastal and inland site." Journal of Geophysical Research-Atmospheres **118**(5): 2434-2443.

Christensen, K. Y., B. A. Thompson, M. Werner, K. Malecki, P. Imm and H. A. Anderson (2016). "Levels of persistent contaminants in relation to fish consumption among older male anglers in Wisconsin." International Journal of Hygiene and Environmental Health **219**(2): 184-194.

Clever, H. L., S. A. Johnson and M. E. Derrick (1985). "The solubility of mercury and some sparingly soluble mercury salts in water and aqueous-electrolyte solutions." Journal of Physical and Chemical Reference Data **14**(3): 631-681.

Cohen, M. (2016). Modeling Atmospheric Mercury Deposition to the Great Lakes: Updated Analysis. Final Report for work conducted with FY2013 funding from the Great Lakes Restoration Initiative. College Park, MD, USA, NOAA Air Resources Laboratory**:** 80.

Cohen, M., R. Artz, R. Draxler, P. Miller, L. Poissant, D. Niemi, D. Ratte, M. Deslauriers, R. Duval, R. Laurin, J. Slotnick, T. Nettesheim and J. McDonald (2004). "Modeling the atmospheric transport and deposition of mercury to the Great Lakes." Environmental Research **95**(3): 247-265.

Cohen, M., R. Draxler and R. Artz (2011). Modeling Atmospheric Mercury Deposition to the Great Lakes. Final Report for work conducted with FY2010 funding from the Great Lakes Restoration Initiative. Silver Spring, MD, USA, NOAA Air Resources Laboratory**:** 160.

Cohen, M., R. Draxler and R. Artz (2013). Modeling Atmospheric Mercury Deposition to the Great Lakes: Examination of the Influence of Variations in Model Inputs, Parameters, and Algorithms on Model Results. Final Report for work conducted with FY2011 funding from the Great Lakes Restoration Initiative. College Park, MD, NOAA Air Resources Laboratory**:** 157.

Cohen, M., R. Draxler and R. Artz (2014). Modeling Atmospheric Mercury Deposition to the Great Lakes: Projected Consequences of Alternative Future Emissions Scenarios. Final Report for work conducted with FY2012 funding from the Great Lakes Restoration Initiative. College Park, MD, NOAA Air Resources Laboratory**:** 193.

Cohen, M. D., R. S. Artz and R. R. Draxler (2007). Report to Congress: Mercury Contamination in the Great Lakes. Silver Spring, MD, NOAA Air Resources Laboratory**:** 162 pages.

Cohen, M. D., R. R. Draxler, R. S. Artz, P. Blanchard, M. S. Gustin, Y. Han, T. A. Holsen, D. A. Jaffe, P. Kelley, H. Lei, C. P. Loughner, W. T. Luke, S. L. Lyman, D. Niemi, J. M. Pacyna, M. Pilote, L. Poissant, D. Ratte, X. Ren, F. Steenhuisen, A. Steffen, R. Tordon and S. Wilson (2016). "Modeling the global atmospheric transport and deposition of mercury to the Great Lakes." Elementa **4:000118**.

Connelly, N. A., T. B. Lauber, J. Niederdeppe and B. A. Knuth (2017). "Are women anglers of childbearing age in the Great Lakes region following fish consumption guidelines?" Journal of Great Lakes Research **43**(3): 187-191.

Corbitt, E. S., D. J. Jacob, C. D. Holmes, D. G. Streets and E. M. Sunderland (2011). "Global Source-Receptor Relationships for Mercury Deposition Under Present-Day and 2050 Emissions Scenarios." Environmental Science & Technology **45**(24): 10477-10484.

Dastoor, A. P. and Y. Larocque (2004). "Global circulation of atmospheric mercury: a modelling study." Atmospheric Environment **38**(1): 147-161.

De Simone, F., C. N. Gencarelli, I. M. Hedgecock and N. Pirrone (2014). "Global atmospheric cycle of mercury: a model study on the impact of oxidation mechanisms." Environmental Science and Pollution Research **21**(6): 4110-4123.

Draxler, R. R. (2007). "Demonstration of a global modeling methodology to determine the relative importance of local and long-distance sources." Atmospheric Environment **41**(4): 776-789.

Draxler, R. R. and G. D. Hess (1997). Description of the HYSPLIT_4 modeling system. NOAA Tech. Memo. Silver Spring, MD, USA, NOAA Air Resources Laboratory. **ERL ARL-224 (Revised 2014):** 24 pages.

Draxler, R. R. and G. D. Hess (1998). "An overview of the HYSPLIT_4 modeling system of trajectories, dispersion, and deposition." Aust. Meteor. Mag. **47**: 295-308.

Draxler, R. R. and A. D. Taylor (1982). "Horizontal dispersion parameters for long-range transport modeling." Journal of Applied Meteorology **21**: 367-372.

Driscoll, C. T., R. P. Mason, H. M. Chan, D. J. Jacob and N. Pirrone (2013). "Mercury as a Global Pollutant: Sources, Pathways, and Effects." Environmental Science & Technology **47**(10): 4967-4983.

Durnford, D., A. Dastoor, D. Figueras-Nieto and A. Ryjkov (2010). "Long range transport of mercury to the Arctic and across Canada." Atmospheric Chemistry and Physics **10**(13): 6063-6086.

Edwards, G. C. and D. A. Howard (2013). "Air-surface exchange measurements of gaseous elemental mercury over naturally enriched and background terrestrial landscapes in Australia." Atmospheric Chemistry and Physics **13**(10): 5325-5336.

Environment and Climate Change Canada (2016). 1990-2015 Air Pollutant Emissions Inventory Report. ECCC Public Inquiries Centre**:** 97.

Environment and Climate Change Canada. (2017, March 30, 2017). "Air Pollutant Emissions Inventory (APEI)." from http://ec.gc.ca/inrp-npri/donnees-data/ap/index.cfm?lang=En.

Environment Canada. (2016). "Environment Canada 2011 National Pollutant Release Inventory (NPRI)." 2011. Retrieved Feb 11, 2016, 2016, from http://www.ec.gc.ca/inrp-npri.

Evers, D. C., J. G. Wiener, N. Basu, R. A. Bodaly, H. A. Morrison and K. A. Williams (2011). "Mercury in the Great Lakes region: bioaccumulation, spatiotemporal patterns, ecological risks, and policy." Ecotoxicology **20**(7): 1487-1499.

Feddersen, D. M., R. Talbot, H. Mao and B. C. Sive (2012). "Size distribution of particulate mercury in marine and coastal atmospheres." Atmospheric Chemistry and Physics **12**(22): 10899-10909.

Finlayson-Pitts, B. J. and J. N. Pitts (2000). Chemistry of the Upper and Lower Atmosphere. San Diego, Academic Press.

Fu, X. W., H. Zhang, B. Yu, X. Wang, C. J. Lin and X. B. Feng (2015). "Observations of atmospheric mercury in China: a critical review." Atmospheric Chemistry and Physics **15**(16): 9455-9476.

Gandhi, N., K. G. Drouillard, G. B. Arhonditsis, S. B. Gewurtz and S. P. Bhavsar (2017). "Are Fish Consumption Advisories for the Great Lakes Adequately Protective against Chemical Mixtures?" Environmental Health Perspectives **125**(4): 586-593.

Gandhi, N., R. W. K. Tang, S. P. Bhavsar and G. B. Arhonditsis (2014). "Fish Mercury Levels Appear to Be Increasing Lately: A Report from 40 Years of Monitoring in the Province of Ontario, Canada." Environmental Science & Technology **48**(10): 5404-5414.

Gatz, D. F. (1976). "Wet Deposition Estimation Using Scavenging Ratios." Journal of Great Lakes Research **2, Supplement 1**: 21-29.

Gencarelli, C. N., J. Bieser, F. Carbone, F. De Simone, I. M. Hedgecock, V. Matthias, O. Travnikov, X. Yang and N. Pirrone (2017). "Sensitivity model study of regional mercury dispersion in the atmosphere." Atmospheric Chemistry and Physics **17**(1): 627-643.

Giang, A. and N. E. Selin (2016). "Benefits of mercury controls for the United States." Proceedings of the National Academy of Sciences of the United States of America **113**(2): 286-291.

Graedel, T. E. and W. C. Keene (1995). "Tropospheric Budget of Reactive Chlorine." Global Biogeochemical Cycles **9**(1): 47-77.

Grandjean, P., P. Weihe, R. F. White, F. Debes, S. Araki, K. Yokoyama, K. Murata, N. Sorensen, R. Dahl and P. J. Jorgensen (1997). "Cognitive deficit in 7-year-old children with prenatal exposure to methylmercury." Neurotoxicology and Teratology **19**(6): 417-428.

Grant, S. L., M. Kim, P. Lin, K. C. Crist, S. Ghosh and V. R. Kotamarthi (2014). "A simulation study of atmospheric mercury and its deposition in the Great Lakes." Atmospheric Environment **94**: 164-172.

Groth, E. (2017). "Scientific foundations of fish-consumption advice for pregnant women: Epidemiological evidence, benefit-risk modeling, and an integrated approach." Environmental Research **152**: 386-406.

Gustin, M., Amos, H., Huang, J., Miller, M., Heidecorn, K. (2015). "Successes and challenges of measuring and modeling atmospsheric mercury at the part per quadrillion level: a critical review." Atmospheric Chemistry and Physics Discussions **15**: 3777-3821.

Gustin, M. S., J. Huang, M. B. Miller, C. Peterson, D. A. Jaffe, J. Ambrose, B. D. Finley, S. N. Lyman, K. Call, R. Talbot, D. Feddersen, H. Mao and S. E. Lindberg (2013). "Do We Understand What the Mercury Speciation Instruments Are Actually Measuring? Results of RAMIX." Environmental Science & Technology **47**(13): 7295-7306.

Hall, B. (1995). "The gas-phase oxidation of elemental mercury by ozone." Water Air and Soil Pollution **80**(1-4): 301-315.

Hartman, J. S., P. J. Weisberg, R. Pillai, J. A. Ericksen, T. Kuiken, S. E. Lindberg, H. Zhang, J. J. Rytuba and M. S. Gustin (2009). "Application of a Rule-Based Model to Estimate Mercury Exchange for Three Background Biomes in the Continental United States." Environmental Science & Technology **43**(13): 4989-4994.

Holloway, T., C. Voigt, J. Morton, S. N. Spak, A. P. Rutter and J. J. Schauer (2012). "An assessment of atmospheric mercury in the Community Multiscale Air Quality (CMAQ) model at an urban site and a rural site in the Great Lakes Region of North America." Atmospheric Chemistry and Physics **12**(15): 7117-7133.

Holmes, C. D., D. J. Jacob, E. S. Corbitt, J. Mao, X. Yang, R. Talbot and F. Slemr (2010). "Global atmospheric model for mercury including oxidation by bromine atoms." Atmospheric Chemistry and Physics **10**(24): 12037-12057.

Holmes, C. D., D. J. Jacob, A. L. Soerensen and E. S. Corbitt (2010). "Global atmospheric budget of mercury including oxidation of Hg(0) by bromine atoms." Geochimica Et Cosmochimica Acta **74**(12): A413-A413.

Horowitz, H. M., D. J. Jacob, Y. X. Zhang, T. S. Dibble, F. Slemr, H. M. Amos, J. A. Schmidt, E. S. Corbitt, E. A. Marais and E. M. Sunderland (2017). "A new mechanism for atmospheric mercury redox chemistry: implications for the global mercury budget." Atmospheric Chemistry and Physics **17**(10): 6353-6371.

Horowitz, L. W., S. Walters, D. L. Mauzerall, L. K. Emmons, P. J. Rasch, C. Granier, X. X. Tie, J. F. Lamarque, M. G. Schultz, G. S. Tyndall, J. J. Orlando and G. P. Brasseur (2003). "A global simulation of tropospheric ozone and related tracers: Description and evaluation of MOZART, version 2." Journal of Geophysical Research-Atmospheres **108**(D24).

Jaffe, D. A., S. Lyman, H. M. Amos, M. S. Gustin, J. Huang, N. E. Selin, L. Levin, A. ter Schure, R. P. Mason, R. Talbot, A. Rutter, B. Finley, L. Jaegle, V. Shah, C. McClure, J. Arnbrose, L. Gratz, S. Lindberg, P. Weiss-Penzias, G.-R. Sheu, D. Feddersen, M. Horvat, A. Dastoor, A. J. Hynes, H. Mao, J. E. Sonke, F. Slemr, J. A. Fisher, R. Ebinghaus, Y. Zhang and G. Edwards (2014). "Progress on Understanding Atmospheric Mercury Hampered by Uncertain Measurements." Environmental Science & Technology **48**(13): 7204-7206.

Jeremiason, J. D., L. A. Kanne, T. A. Lacoe, M. Hulting and M. F. Simcik (2009). "A comparison of mercury cycling in Lakes Michigan and Superior." Journal of Great Lakes Research **35**(3): 329-336.

Jung, G., I. M. Hedgecock and N. Pirrone (2009). "ECHMERIT V1.0-a new global fully coupled mercury-chemistry and transport model." Geoscientific Model Development **2**(2): 175-195.

Keeler, G., G. Glinsorn and N. Pirrone (1995). "Particulate mercury in the atmosphere - its significance, transport, transformation and sources." Water Air and Soil Pollution **80**(1-4): 159-168.

Kikuchi, T., H. Ikemoto, K. Takahashi, H. Hasome and H. Ueda (2013). "Parameterizing Soil Emission and Atmospheric Oxidation-Reduction in a Model of the Global Biogeochemical Cycle of Mercury." Environmental Science & Technology **47**(21): 12266-12274.

Kos, G., A. Ryzhkov, A. Dastoor, J. Narayan, A. Steffen, P. A. Ariya and L. Zhang (2013). "Evaluation of discrepancy between measured and modelled oxidized mercury species." Atmospheric Chemistry and Physics **13**(9): 4839-4863.

Lei, H., X. Z. Liang, D. J. Wuebbles and Z. Tao (2013). "Model analyses of atmospheric mercury: present air quality and effects of transpacific transport on the United States." Atmospheric Chemistry and Physics **13**(21): 10807-10825.

Lei, H., D. J. Wuebbles, X. Z. Liang, Z. Tao, S. Olsen, R. Artz, X. Ren and M. Cohen (2014). "Projections of atmospheric mercury levels and their effect on air quality in the United States." Atmospheric Chemistry and Physics **14**(2): 783-795.

Lepak, R. F., R. S. Yin, D. P. Krabbenhoft, J. M. Ogorek, J. F. DeWild, T. M. Holsen and J. P. Hurley (2015). "Use of Stable Isotope Signatures to Determine Mercury Sources in the Great Lakes." Environmental Science & Technology Letters **2**(12): 335-341.

Lin, C.-J., P. Pongprueksa, S. E. Lindberg, S. O. Pehkonen, D. Byun and C. Jang (2006). "Scientific uncertainties in atmospheric mercury models I: Model science evaluation." Atmospheric Environment **40**(16): 2911-2928.

Lin, C.-J., P. Pongprueksa, O. Russell Bullock, Jr., S. E. Lindberg, S. O. Pehkonen, C. Jang, T. Braverman and T. C. Ho (2007). "Scientific uncertainties in atmospheric mercury models II: Sensitivity analysis in the CONUS domain." Atmospheric Environment **41**(31): 6544-6560.

Lin, C.-J., S. K. Shetty, L. Pan, P. Pongprueksa, C. Jang and H.-w. Chu (2012). "Source attribution for mercury deposition in the contiguous United States: Regional difference and seasonal variation." Journal of the Air & Waste Management Association **62**(1): 52-63.

Lin, C. J. and S. O. Pehkonen (1997). "Aqueous free radical chemistry of mercury in the presence of iron oxides and ambient aerosol." Atmospheric Environment **31**(24): 4125-4137.

Lin, C. J. and S. O. Pehkonen (1998). "Oxidation of elemental mercury by aqueous chlorine (HOCl/OCl-): Implications for tropospheric mercury chemistry." Journal of Geophysical Research-Atmospheres **103**(D21): 28093-28102.

Lindqvist, O. and H. Rodhe (1985). "Atmospheric mercury - a review." Tellus Series B-Chemical and Physical Meteorology **37**(3): 136-159.

Lohman, K., C. Seigneur, M. Gustin and S. Lindberg (2008). "Sensitivity of the global atmospheric cycle of mercury to emissions." Applied Geochemistry **23**(3): 454-466.

Lu, Y. and M. A. K. Khalil (1991). "Tropospheric OH – model calculations of spatial, temporal, and secular variations." Chemosphere **23**(3): 397-444.

Luke, W., P. Kelley, X. Ren, M. Cohen, R. Artz, M. Olsen and D. Schmeltz (2016). Assessment of Measurement Artifacts of Atmospheric Mercury Species. NOAA Air Resources Laboratory Science Review. College Park, MD, USA.

Lyman, S., C. Jones, T. O'Neil, T. Allen, M. Miller, M. S. Gustin, A. M. Pierce, W. Luke, X. R. Ren and P. Kelley (2016). "Automated Calibration of Atmospheric Oxidized Mercury Measurements." Environmental Science & Technology **50**(23): 12921-12927.

Lyman, S. N., D. A. Jaffe and M. S. Gustin (2010). "Release of mercury halides from KCl denuders in the presence of ozone." Atmospheric Chemistry and Physics **10**(17): 8197-8204.

Martin, L. G., C. Labuschagne, E. G. Brunke, A. Weigelt, R. Ebinghaus and F. Slemr (2017). "Trend of atmospheric mercury concentrations at Cape Point for 1995-2004 and since 2007." Atmospheric Chemistry and Physics **17**(3): 2393-2399.

Mason, R. P. and G. R. Sheu (2002). "Role of the ocean in the global mercury cycle." Global Biogeochemical Cycles **16**(4).

Mason, R. P. and K. A. Sullivan (1997). "Mercury in Lake Michigan." Environmental Science & Technology **31**(3): 942-947.

Munthe, J. (1992). "The aqueous oxidation of elemental mercury by ozone." Atmospheric Environment Part a-General Topics **26**(8): 1461-1468.

National Atmospheric Deposition Program. (2012, April 18, 2012). "Mercury Deposition Network." from http://nadp.sws.uiuc.edu/MDN/.

National Centers for Environmental Prediction, N. W. S., NOAA, U.S. Department of Commerce. (2017). "NCEP North American Regional Reanalysis (NARR). Research Data Archive at the National Center for Atmospheric Research,

Computational and Information Systems Laboratory, Boulder, CO.", from http://rda.ucar.edu/datasets/ds608.0/.

NOAA Air Resources Laboratory. (2017). "North American Regional Reanalysis (NARR, 1979 - present)." from http://www.ready.noaa.gov/archives.php.

Pal, B. and P. A. Ariya (2004). "Gas-phase HO-Initiated reactions of elemental mercury: Kinetics, product studies, and atmospheric implications." Environmental Science & Technology **38**(21): 5555-5566.

Pan, L., G. R. Carmichael, B. Adhikary, Y. Tang, D. Streets, J.-H. Woo, H. R. Friedli and L. F. Radke (2008). "A regional analysis of the fate and transport of mercury in East Asia and an assessment of major uncertainties." Atmospheric Environment **42**(6): 1144-1159.

Pan, L., C.-J. Lin, G. R. Carmichael, D. G. Streets, Y. Tang, J.-H. Woo, S. K. Shetty, H.-W. Chu, T. C. Ho, H. R. Friedli and X. Feng (2010). "Study of atmospheric mercury budget in East Asia using STEM-Hg modeling system." Science of the Total Environment **408**(16): 3277-3291.

Pirrone, N., S. Cinnirella, X. Feng, R. B. Finkelman, H. R. Friedli, J. Leaner, R. Mason, A. B. Mukherjee, G. B. Stracher, D. G. Streets and K. Telmer (2010). "Global mercury emissions to the atmosphere from anthropogenic and natural sources." Atmospheric Chemistry and Physics **10**(13): 5951-5964.

Pongprueksa, P., C.-J. Lin, S. E. Lindberg, C. Jang, T. Braverman, O. R. Bullock, Jr., T. C. Ho and H.-W. Chu (2008). "Scientific uncertainties in atmospheric mercury models III: Boundary and initial conditions, model grid resolution, and Hg(II) reduction mechanism." Atmospheric Environment **42**(8): 1828-1845.

Prospero, J. M., R. J. Charlson, V. Mohnen, R. Jaenicke, A. C. Delany, J. Moyers, W. Zoller and K. Rahn (1983). "The atmospheric aerosol system - an overview." Reviews of Geophysics **21**(7): 1607-1629.

Ren, X., W. T. Luke, P. Kelley, M. D. Cohen, R. Artz, M. L. Olson, D. Schmeltz, M. Puchalski, D. L. Goldberg, A. Ring, G. M. Mazzuca, K. A. Cummings, L. Wojdan, S. Preaux and J. W. Stehr (2016). "Atmospheric mercury measurements at a suburban site in the Mid-Atlantic United States: Inter-annual, seasonal and diurnal variations and source-receptor relationships, ." Atmospheric Environment **146**: 141-152

Rolfhus, K. R., H. E. Sakamoto, L. B. Cleckner, R. W. Stoor, C. L. Babiarz, R. C. Back, H. Manolopoulos and J. P. Hurley (2003). "Distribution and fluxes of total and methylmercury in Lake Superior." Environmental Science & Technology **37**(5): 865-872.

Ryaboshapko, A., O. R. Bullock, Jr., J. Christensen, M. Cohen, A. Dastoor, I. Ilyin, G. Petersen, D. Syrakov, R. S. Artz, D. Davignon, R. R. Draxler and J. Munthe (2007). "Intercomparison study of atmospheric mercury models: 1. Comparison of models with short-term measurements." Science of the Total Environment **376**(1-3): 228-240.

Ryaboshapko, A., O. R. Bullock, Jr., J. Christensen, M. Cohen, A. Dastoor, I. Ilyin, G. Petersen, D. Syrakov, O. Travnikov, R. S. Artz, D. Davignon, R. R. Draxler, J. Munthe and J. Pacyna (2007). "Intercomparison

study of atmospheric mercury models: 2. Modelling results vs. long-term observations and comparison of country deposition budgets." Science of the Total Environment **377**(2-3): 319-333.

Ryaboshapko, A., R. Bullock, R. Ebinghaus, I. Ilyin, K. Lohman, J. Munthe, G. Petersen, C. Seigneur and I. Wangberg (2002). "Comparison of mercury chemistry models." Atmospheric Environment **36**(24): 3881-3898.

Seigneur, C., H. Abeck, G. Chia, M. Reinhard, N. S. Bloom, E. Prestbo and P. Saxena (1998). "Mercury adsorption to elemental carbon (soot) particles and atmospheric particulate matter." Atmospheric Environment **32**(14-15): 2649-2657.

Seigneur, C. and K. Lohman (2008). "Effect of bromine chemistry on the atmospheric mercury cycle." Journal of Geophysical Research-Atmospheres **113**(D23).

Seigneur, C., K. Vijayaraghavan, K. Lohman, P. Karamchandani and C. Scott (2004). "Global source attribution for mercury deposition in the United States." Environmental Science & Technology **38**(2): 555-569.

Seigneur, C., J. Wrobel and E. Constantinou (1994). "A chemical kinetic mechanism for atmospheric inorganic mercury." Environmental Science & Technology **28**(9): 1589-1597.

Seinfeld, J. and S. Pandis (1986). "Atmospheric chemistry and air pollution." NY: Wiley Intersci. Publ.

Seinfeld, J. H. and S. N. Pandis (1998). Atmospheric Chemistry and Physics: From Air Pollution to Climate Change. New York, John Wiley and Sons, Inc.

Selin, N. E., D. J. Jacob, R. J. Park, R. M. Yantosca, S. Strode, L. Jaegle and D. Jaffe (2007). "Chemical cycling and deposition of atmospheric mercury: Global constraints from observations." Journal of Geophysical Research-Atmospheres **112**(D2).

Selin, N. E., D. J. Jacob, R. M. Yantosca, S. Strode, L. Jaegle and E. M. Sunderland (2008). "Global 3-D land-ocean-atmosphere model for mercury: Present-day versus preindustrial cycles and anthropogenic enrichment factors for deposition." Global Biogeochemical Cycles **22**(2): 13.

Shia, R. L., C. Seigneur, P. Pai, M. Ko and N. D. Sze (1999). "Global simulation of atmospheric mercury concentrations and deposition fluxes." Journal of Geophysical Research-Atmospheres **104**(D19): 23747-23760.

Slinn, S. A. and W. G. N. Slinn (1980). "Predictions for particle deposition on natural-waters." Atmospheric Environment **14**(9): 1013-1016.

Sommar, J., W. Zhu, L. Shang, X. Feng and C.-J. Lin (2013). "A whole-air relaxed eddy accumulation measurement system for sampling vertical vapour exchange of elemental mercury." Tellus Series B-Chemical and Physical Meteorology **65**.

Song, S., N. E. Selin, A. L. Soerensen, H. Angot, R. Artz, S. Brooks, E. G. Brunke, G. Conley, A. Dommergue, R. Ebinghaus, T. M. Holsen, D. A. Jaffe, S. Kang, P. Kelley, W. T. Luke, O. Magand, K. Marumoto, K. A. Pfaffhuber, X. Ren, G. R. Sheu, F. Slemr, T. Warneke, A. Weigelt, P. Weiss-Penzias, D. C. Wip and Q.

Zhang (2015). "Top-down contraints on atmospheric mercury emissions and implications for global biogeochemical cycling." Atmos. Chem. Phys. **15**: 7103-7125.

Sprovieri, F., N. Pirrone, M. Bencardino, F. D'Amore, F. Carbone, S. Cinnirella, V. Mannarino, M. Landis, R. Ebinghaus, A. Weigelt, E. G. Brunke, C. Labuschagne, L. Martin, J. Munthe, I. Wangberg, P. Artaxo, F. Morais, H. D. J. Barbosa, J. Brito, W. Cairns, C. Barbante, M. D. Dieguez, P. E. Garcia, A. Dommergue, H. Angot, O. Magand, H. Skov, M. Horvat, J. Kotnik, K. A. Read, L. M. Neves, B. M. Gawlik, F. Sena, N. Mashyanov, V. Obolkin, D. Wip, X. Bin Feng, H. Zhang, X. W. Fu, R. Ramachandran, D. Cossa, J. Knoery, N. Marusczak, M. Nerentorp and C. Norstrom (2016). "Atmospheric mercury concentrations observed at ground-based monitoring sites globally distributed in the framework of the GMOS network." Atmospheric Chemistry and Physics **16**(18): 11915-11935.

Stein, A. F., R. R. Draxler, G. D. Rolph, B. J. B. Stunder, M. D. Cohen and F. Ngan (2015). "NOAA's HYSPLIT atmospheric transport and dispersion modeling system." Bulletin of the American Meteorological Society.

Subir, M., P. A. Ariya and A. P. Dastoor (2011). "A review of uncertainties in atmospheric modeling of mercury chemistry I. Uncertainties in existing kinetic parameters - Fundamental limitations and the importance of heterogeneous chemistry." Atmospheric Environment **45**(32): 5664-5676.

Subir, M., P. A. Ariya and A. P. Dastoor (2012). "A review of the sources of uncertainties in atmospheric mercury modeling II. Mercury surface and heterogeneous chemistry - A missing link." Atmospheric Environment **46**: 1-10.

Sullivan, K. A. and R. P. Mason (1998). "The concentration and distribution of mercury in Lake Michigan." Science of the Total Environment **213**(1-3): 213-228.

Sunderland, E. M., C. T. Driscoll, J. K. Hammitt, P. Grandjean, J. S. Evans, J. D. Blum, C. Y. Chen, D. C. Evers, D. A. Jaffe, R. P. Mason, S. Goho and W. Jacobs (2016). "Benefits of Regulating Hazardous Air Pollutants from Coal and Oil Fired Utilities in the United States." Environmental Science & Technology **50**(5): 2117-2120.

Talbot, R., H. Mao, D. Feddersen, M. Smith, S. Y. Kim, B. Sive, K. Haase, J. Ambrose, Y. Zhou and R. Russo (2011). "Comparison of Particulate Mercury Measured with Manual and Automated Methods." Atmosphere **2**(1): 1-20.

Tokos, J. J. S., B. Hall, J. A. Calhoun and E. M. Prestbo (1998). "Homogeneous gas-phase reaction of Hg-0 with H2O2, O-3, CH3I, and (CH3)(2)S: Implications for atmospheric Hg cycling." Atmospheric Environment **32**(5): 823-827.

Travnikov, O. (2005). "Contribution of the intercontinental atmospheric transport to mercury pollution in the Northern Hemisphere." Atmospheric Environment **39**(39): 7541-7548.

Travnikov, O., H. Angot, P. Artaxo, M. Bencardino, J. Bieser, F. D'Amore, A. Dastoor, F. De Simone, M. D. Dieguez, A. Dommergue, R. Ebinghaus, X. B. Feng, C. N. Gencarelli, I. M. Hedgecock, O. Magand, L. Martin, V. Matthias, N. Mashyanov, N. Pirrone, R. Ramachandran, K. A. Read, A. Ryjkov, N. E. Selin, F. Sena, S. Song, F. Sprovieri, D. Wip, I. Wagberg and X. Yang (2017). "Multi-model study of mercury dispersion in the atmosphere: atmospheric processes and model evaluation." Atmospheric Chemistry and Physics **17**(8): 5271-5295.

USEPA. (2006, June 29, 2011). "Mercury Speciation Profiles." Dec 19, 2006. from ftp://ftp.epa.gov/EmisInventory/2002finalnei/documentation/point/augmentation_point/mercuryspeciation12192006.zip.

USEPA (2015). 2011 National Emissions Inventory, version 2. Technical Support Document. Research Triangle Park, North Carolina, U.S. Environmental Protection Agency Office of Air Quality Planning and Standards, Air Quality Assessment Division, Emissions Inventory and Analysis Group.

Van Loon, L., E. Mader and S. L. Scott (2000). "Reduction of the aqueous mercuric ion by sulfite: UV spectrum of HgSO3 and its intramolecular redox reaction." Journal of Physical Chemistry A **104**(8): 1621-1626.

Visha, A., N. Gandhi, S. P. Bhavsar and G. B. Arhonditsis (2015). "A Bayesian assessment of the mercury and PCB temporal trends in lake trout (Salvelinus namaycush) and walleye (Sander vitreus) from lake Ontario, Ontario, Canada." Ecotoxicology and Environmental Safety **117**: 174-186.

Wang, X., C. J. Lin and X. Feng (2014). "Sensitivity analysis of an updated bidirectional air-surface exchange model for elemental mercury vapor." Atmospheric Chemistry and Physics **14**(12): 6273-6287.

Wangberg, I., M. G. N. Mastromonaco, J. Munthe and K. Gardfeldt (2016). "Airborne mercury species at the Rao background monitoring site in Sweden: distribution of mercury as an effect of long-range transport." Atmospheric Chemistry and Physics **16**(21): 13379-13387.

Weiss-Penzias, P., H. M. Amos, N. E. Selin, M. S. Gustin, D. A. Jaffe, D. Obrist, G. R. Sheu and A. Giang (2015). "Use of a global model to understand speciated atmospheric mercury observations at five high-elevation sites." Atmospheric Chemistry and Physics **15**(3): 1161-1173.

Wesely, M. L. (1989). "Parameterization of surface resistances to gaseous dry deposition in regional-scale numerical-models." Atmospheric Environment **23**(6): 1293-1304.

Wesely, M. L. and B. B. Hicks (1977). "Some factors that affect deposition rates of sulfur-dioxide and similar gases on vegetation." Journal of the Air Pollution Control Association **27**(11): 1110-1116.

Whitby, K. T. (1975). Modeling of Atmospheric Aerosol Particle Size Distribution. Particle Technology Laboratory, University of Minnesota (Report #253).

Whitby, K. T. (1978). "Physical characteristics of sulfur aerosols." Atmospheric Environment **12**(1-3): 135-159.

Wiener, J. G., D. C. Evers, D. A. Gay, H. A. Morrison and K. A. Williams (2012). "Mercury contamination in the Laurentian Great Lakes region: Introduction and overview." Environmental Pollution **161**: 243-251.

Wright, L. P. and L. Zhang (2015). "An approach estimating bidirectional air-surface exchange for gaseous elemental mercury at AMNet sites." Journal of Advances in Modeling Earth Systems **7**(1): 35-49.

Xiao, Z., J. Munthe, D. Stromberg and O. Lindqvist (1994). Photochemical behavior of inorganic mercury compounds in aqueous solution. Mercury as a Global Pollutant - Integration and Synthesis. C. Watras and J. Huckabee. New York, Lewis Publishers**:** 581-592.

Zhang, H., X. W. Fu, C. J. Lin, L. H. Shang, Y. P. Zhang, X. B. Feng and C. Lin (2016). "Monsoon-facilitated characteristics and transport of atmospheric mercury at a high-altitude background site in southwestern China." Atmospheric Chemistry and Physics **16**(20): 13131-13148.

Zhang, L., P. Blanchard, D. Johnson, A. Dastoor, A. Ryzhkov, C. J. Lin, K. Vijayaraghavan, D. Gay, T. M. Holsen, J. Huang, J. A. Graydon, V. L. St Louis, M. S. Castro, E. K. Miller, F. Marsik, J. Lu, L. Poissant, M. Pilote and K. M. Zhang (2012). "Assessment of modeled mercury dry deposition over the Great Lakes region." Environmental Pollution **161**: 272-283.

Zhang, L. M., S. Lyman, H. T. Mao, C. J. Lin, D. A. Gay, S. X. Wang, M. S. Gustin, X. B. Feng and F. Wania (2017). "A synthesis of research needs for improving the understanding of atmospheric mercury cycling." Atmospheric Chemistry and Physics **17**(14): 9133-9144.

Zhang, Y., L. Jaegle, A. van Donkelaar, R. V. Martin, C. D. Holmes, H. M. Amos, Q. Wang, R. Talbot, R. Artz, S. Brooks, W. Luke, T. M. Holsen, D. Felton, E. K. Miller, K. D. Perry, D. Schmeltz, A. Steffen, R. Tordon, P. Weiss-Penzias and R. Zsolway (2012). "Nested-grid simulation of mercury over North America." Atmospheric Chemistry and Physics **12**(14): 6095-6111.

Zhou, C. L., M. D. Cohen, B. A. Crimmins, H. Zhou, T. A. Johnson, P. K. Hopke and T. M. Holsen (2017). "Mercury Temporal Trends in Top Predator Fish of the Laurentian Great Lakes from 2004 to 2015: Are Concentrations Still Decreasing?" Environmental Science & Technology **51**(13): 7386-7394.

Zhou, H., C. L. Zhou, M. M. Lynam, J. T. Dvonch, J. A. Barres, P. K. Hopke, M. Cohen and T. M. Holsen (2017). "Atmospheric Mercury Temporal Trends in the Northeastern United States from 1992 to 2014: Are Measured Concentrations Responding to Decreasing Regional Emissions?" Environmental Science & Technology Letters **4**(3): 91-97.

Zhu, W., C. J. Lin, X. Wang, J. Sommar, X. W. Fu and X. B. Feng (2016). "Global observations and modeling of atmosphere-surface exchange of elemental mercury: a critical review." Atmospheric Chemistry and Physics **16**(7): 4451-4480.

7. Appendices

7.1. Emissions

In Figure 149 below, large points sources of mercury in the United States and Canada (2011) are shown, and in Figure 150, these large emissions sources are shown along with the 79 Standard Source Locations (SSL's) used for interpolation in Run Schemes 01-04. The SSL's are more highly concentrated in the Great Lakes region to increase the accuracy of estimating the higher potential impacts of sources close to the Great Lakes. The SSL's are much more sparse outside of the Great Lakes region, but, as discussed in the text (e.g., see discussion of Figure 32, page 42), the tradeoff between accuracy and density of SSL's is much less significant for sources further way from the receptors of interest (in this case, the Great Lakes). However, it is recognized that the sparseness of SSL's – especially outside of the Great Lakes region – will generally limit the accuracy of estimating wet deposition and concentrations at model evaluation locations, i.e., where the model results are compared against ambient measurements. Even for model evaluation locations in the Great Lakes region, the SSL's may be too sparse for optimum model performance in matching measurements.

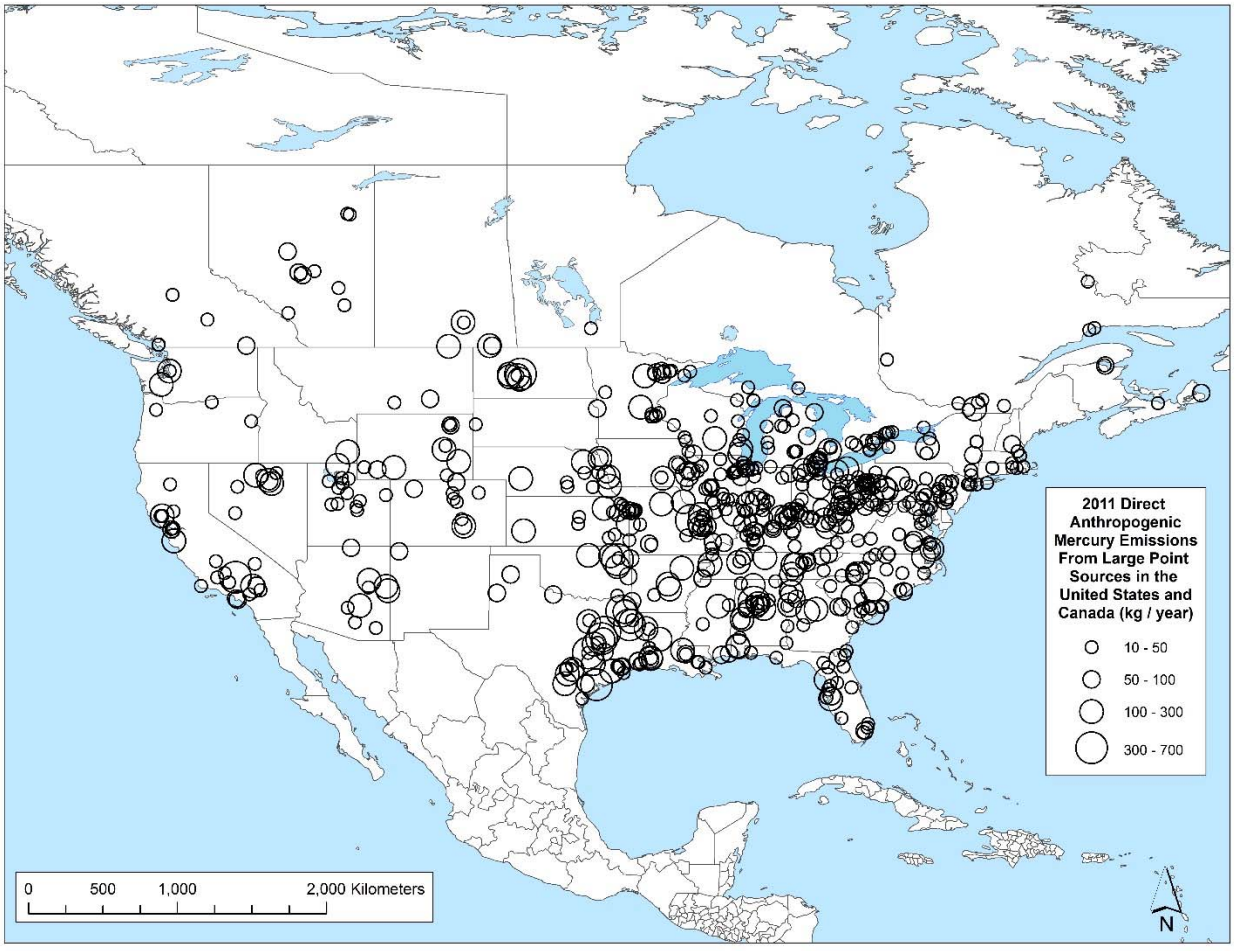

Figure 149. Large Point Sources of Mercury in the United States and Canada (2011). See Section 2 of the main body of the report, beginning on page 20, for information on the data sources used.

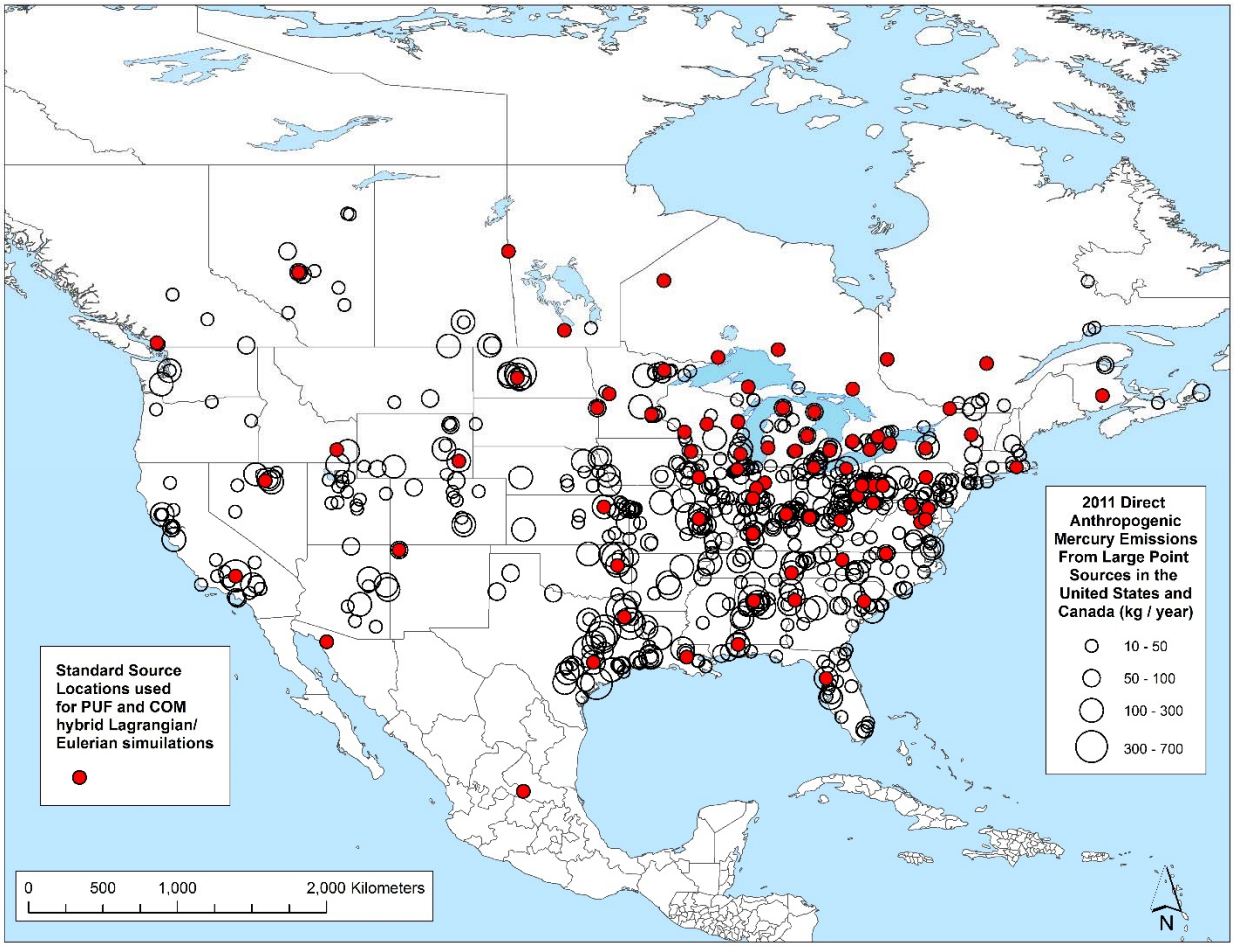

Figure 150. Large Point Sources of Mercury in the United States and Canada (2011) and the 79 Standard Source Locations used for Interpolation in Run Schemes 01-04. See Section 2 of the main body of the report, beginning on page 19, for information on the data sources used.

7.2. Modeled and Measured Precipitation

In Section 3.7 of the main body of this report (beginning on page 51), differences between modeled and measured precipitation are presented and discussed.

A few illustrative examples of comparisons between modeled and measured precipitation are presented in that section (Figure 36, Figure 37, and Figure 38).

In this section of the Appendix, additional comparisons of modeled and measured precipitation are presented, divided into different regions. For the reader's convenience, Figure 76 has been reproduced here (as Figure 151) showing the location of Mercury Deposition Network sites in different regions at which comparisons of modeled and measured precipitation are made.

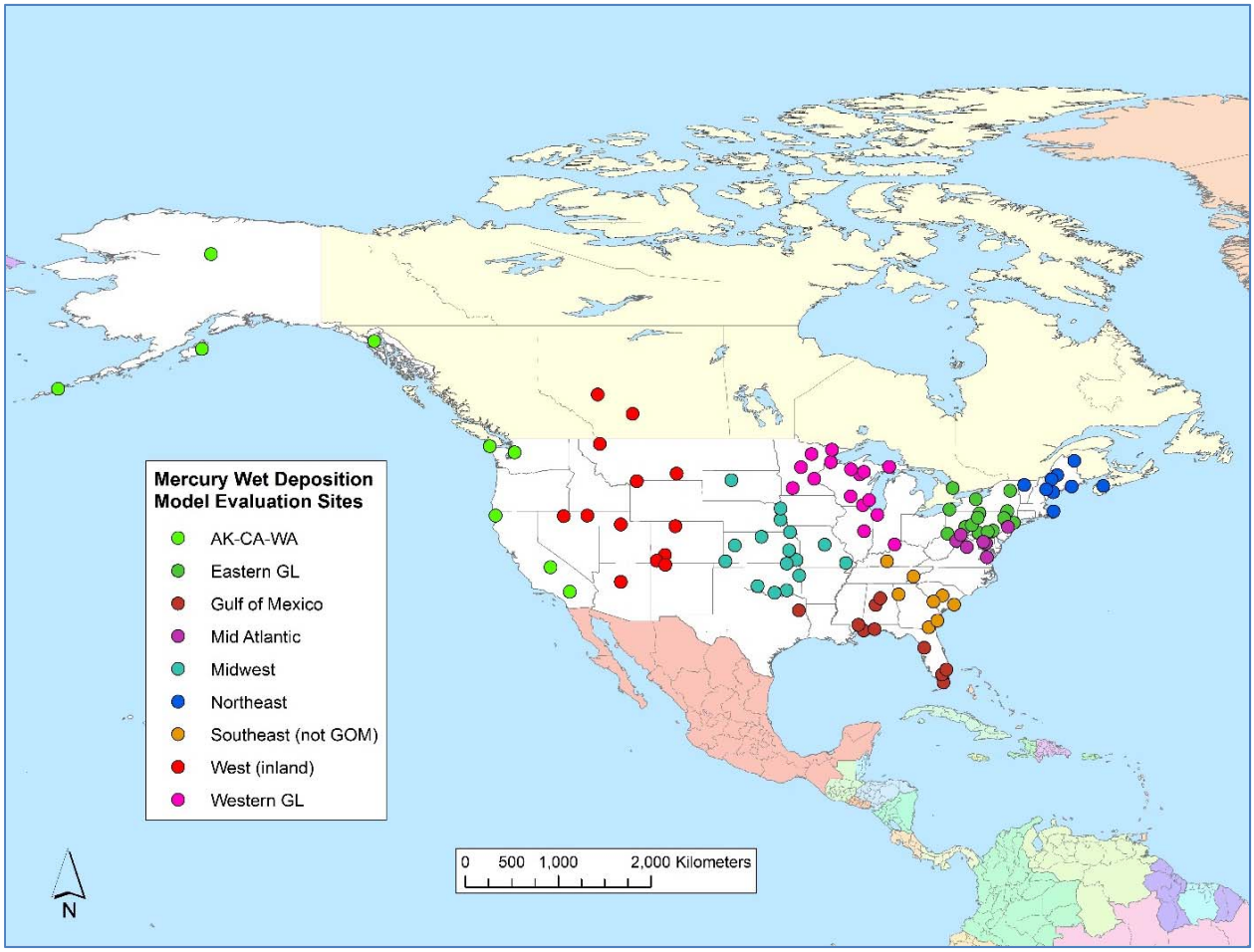

Figure 151. Mercury Deposition Network sites used for model evaluation.

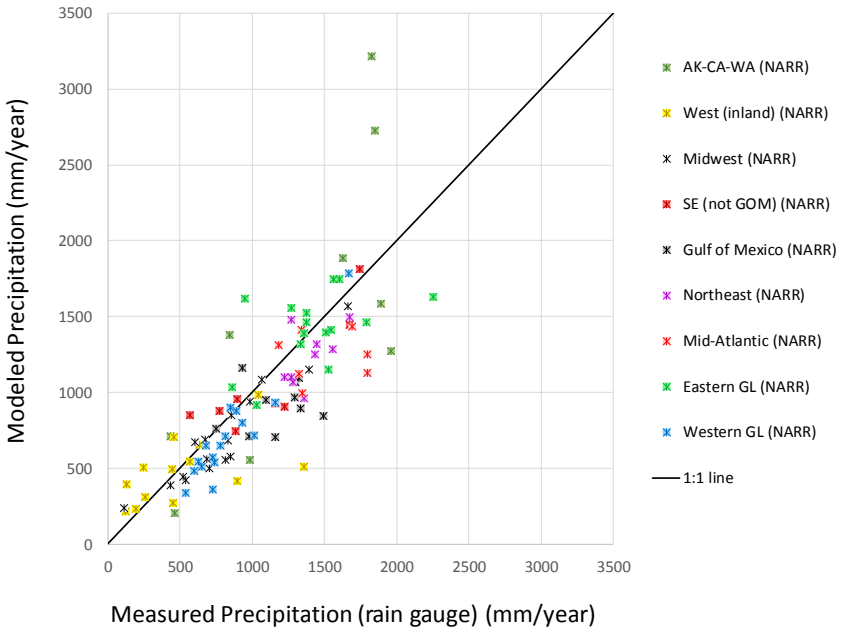

Figure 152. Comparison of 2011 precipitation amount (mm) measured at MDN sites (rain gauge) with amount in NARR.

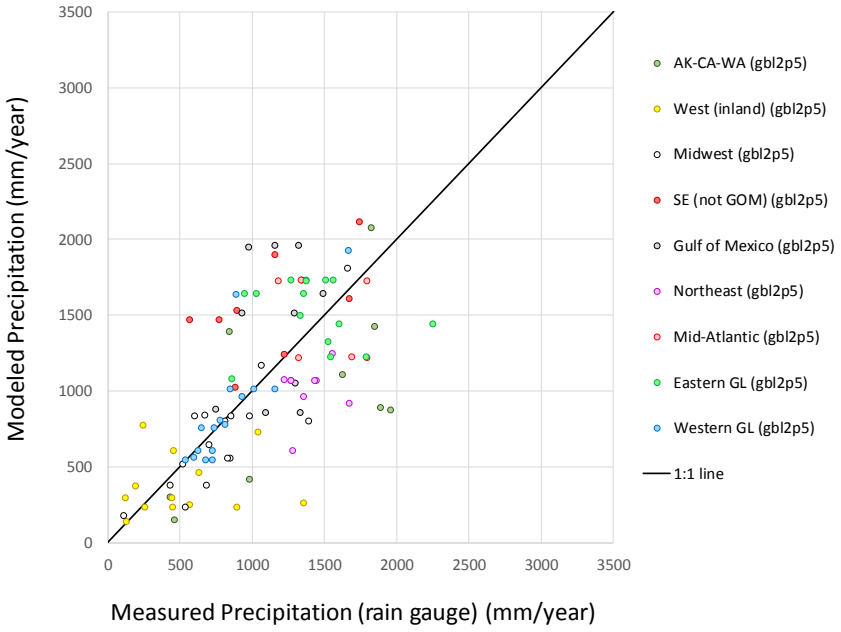

Figure 153. Comparison of 2011 precipitation amount (mm) measured at MDN sites (rain gauge) with amount in NCEP/NCAR Global Reanalysis.

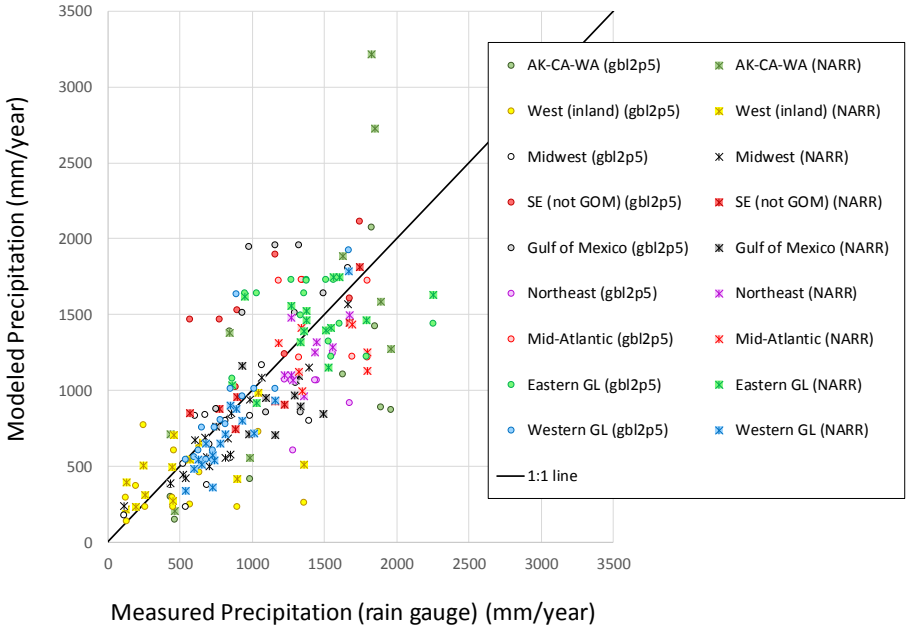

Figure 154. Comparison of 2011 precipitation amount (mm) measured at MDN sites (rain gauge) with amount in NARR and NCEP/NCAR Global Reanalysis.

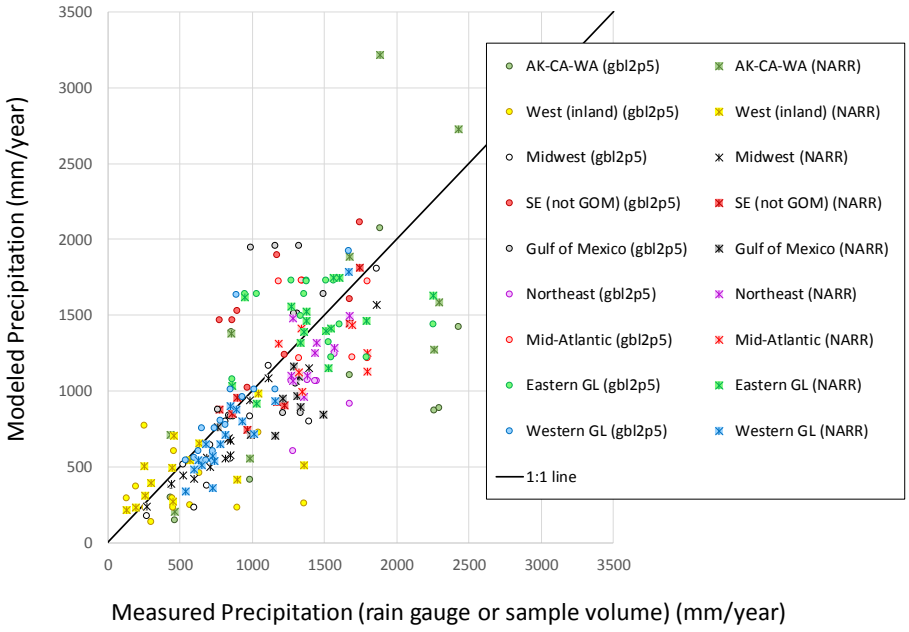

Figure 155. Comparison of 2011 precipitation amount (mm) measured at MDN sites (rain gauge or sample volume) with amount in NARR and NCEP/NCAR Global Reanalysis.

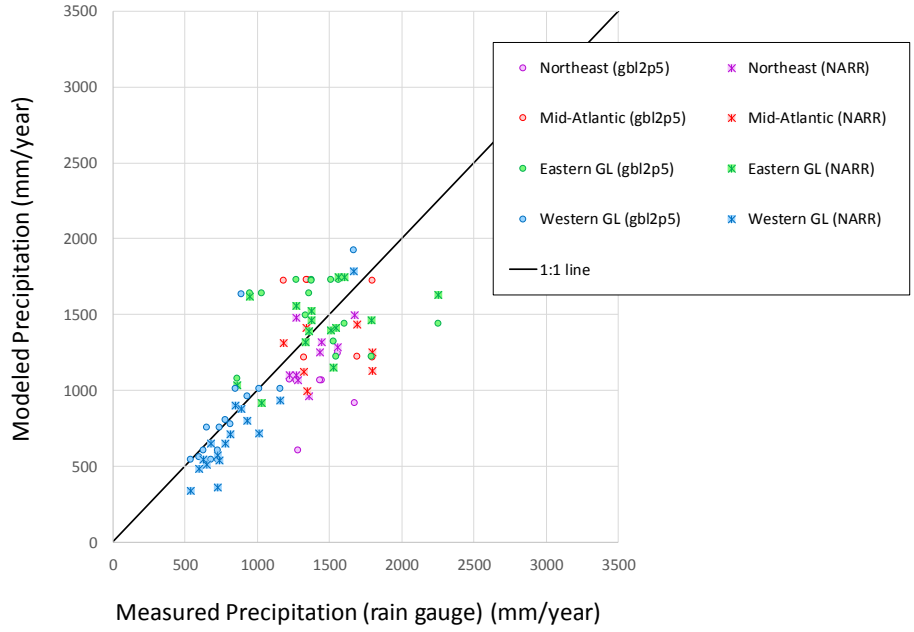

Figure 156. Comparison of 2011 precipitation amount (mm) measured at MDN sites (rain gauge) with amount in NARR and NCEP/NCAR Global Reanalysis (sites in Great Lakes, Northeast, and Mid-Atlantic regions).

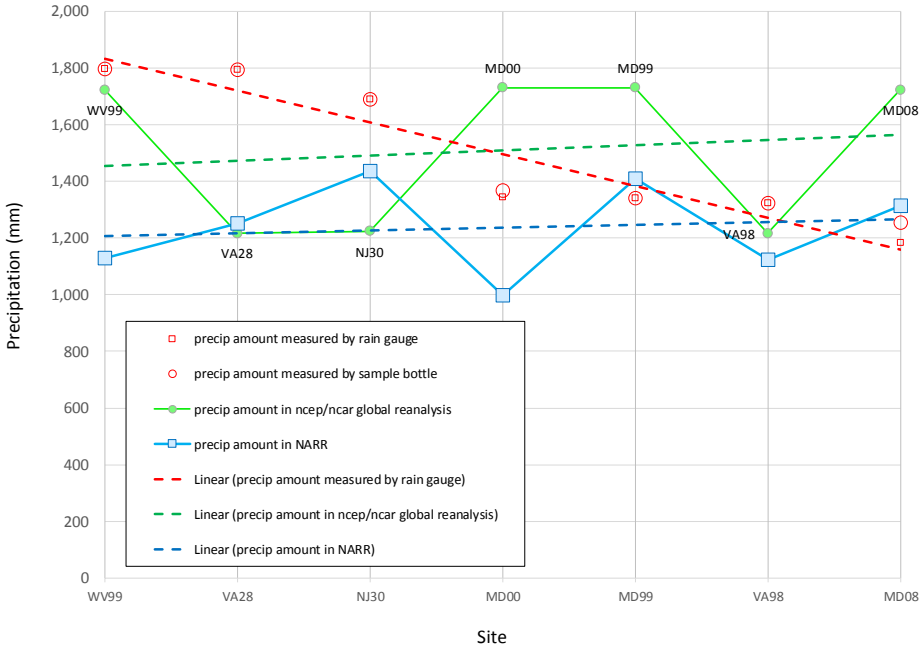

Figure 157. Comparison of 2011 precipitation amount (mm) measured at MDN sites with amount in NARR and NCEP/NCAR Global Reanalysis (sites in Mid-Atlantic region)

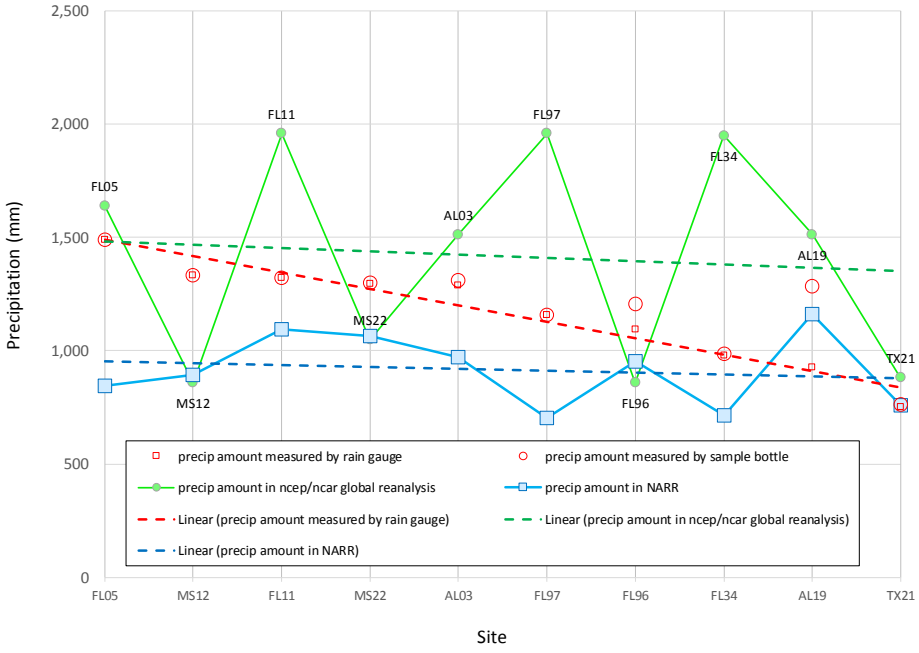

Figure 158. Comparison of 2011 precipitation amount (mm) measured at MDN sites with amount in NARR and NCEP/NCAR Global Reanalysis (sites in Gulf of Mexico region).

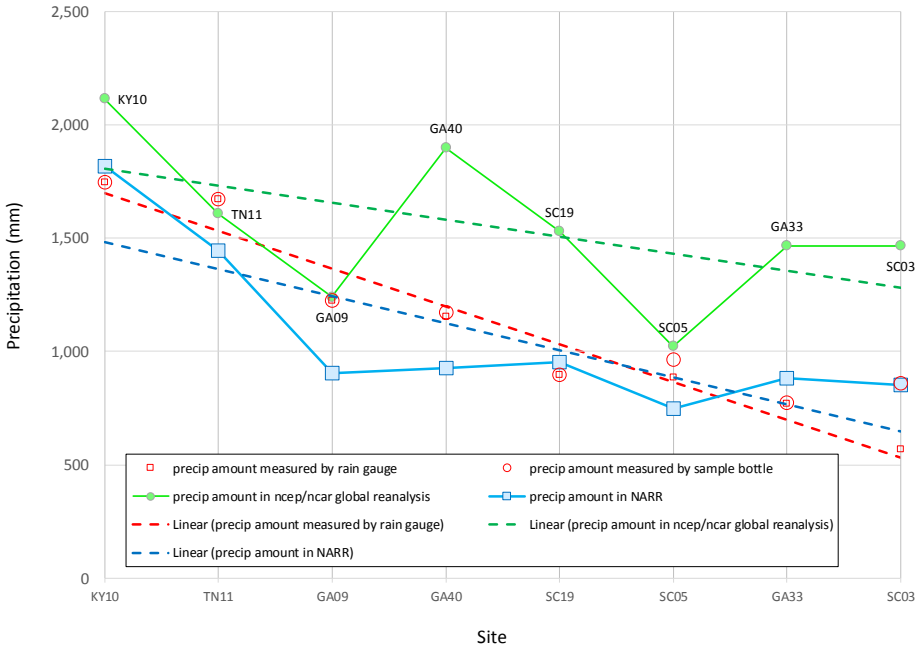

Figure 159. Comparison of 2011 precipitation amount (mm) measured at MDN sites with amount in NARR and NCEP/NCAR Global Reanalysis (sites in Southeast other than Gulf of Mexico).

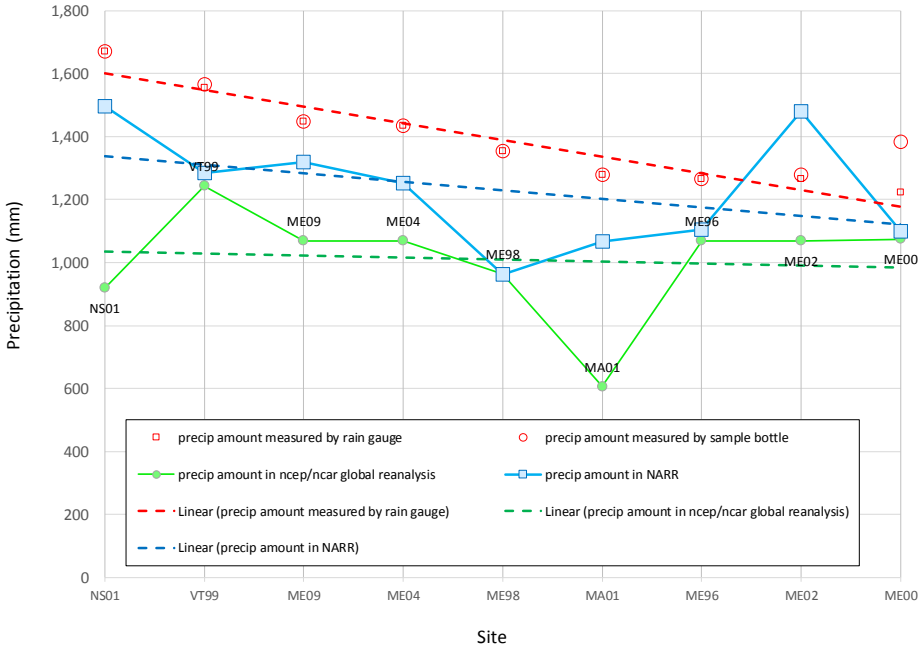

Figure 160. Comparison of 2011 precipitation amount (mm) measured at MDN sites with amount in NARR and NCEP/NCAR Global Reanalysis (sites in Northeast).

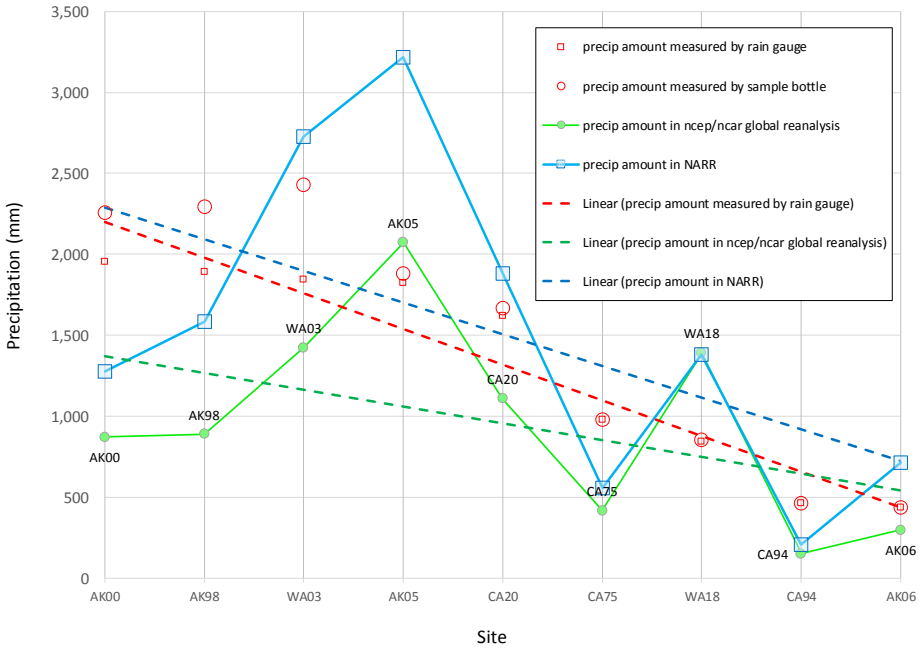

Figure 161. Comparison of 2011 precipitation amount (mm) measured at MDN sites with amount in NARR and NCEP/NCAR Global Reanalysis (sites in Calif, Wash, and Alaska).

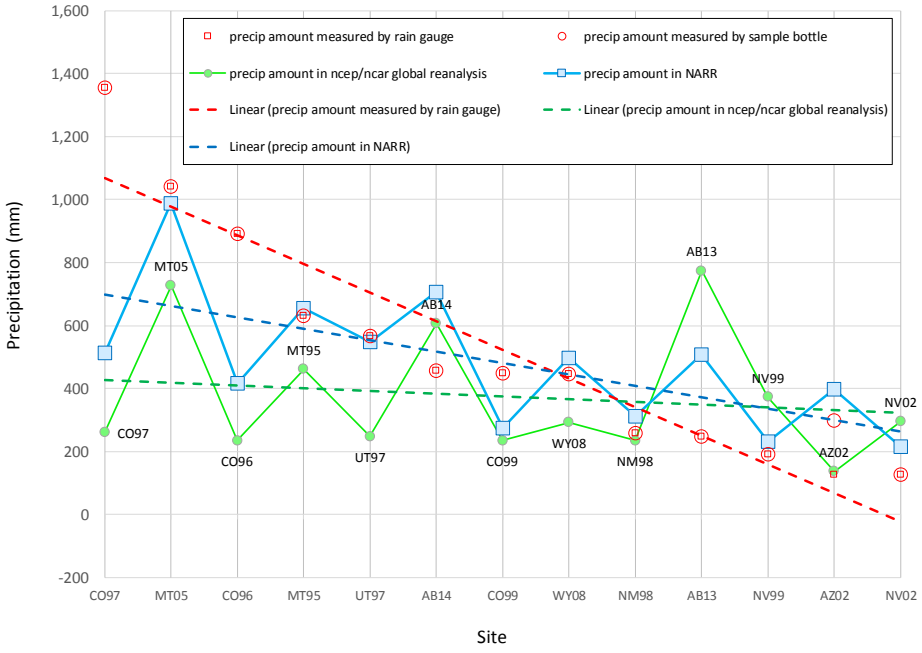

Figure 162. Comparison of 2011 precipitation amount (mm) measured at MDN sites with amount in NARR and NCEP/NCAR Global Reanalysis (sites in Inland West region).

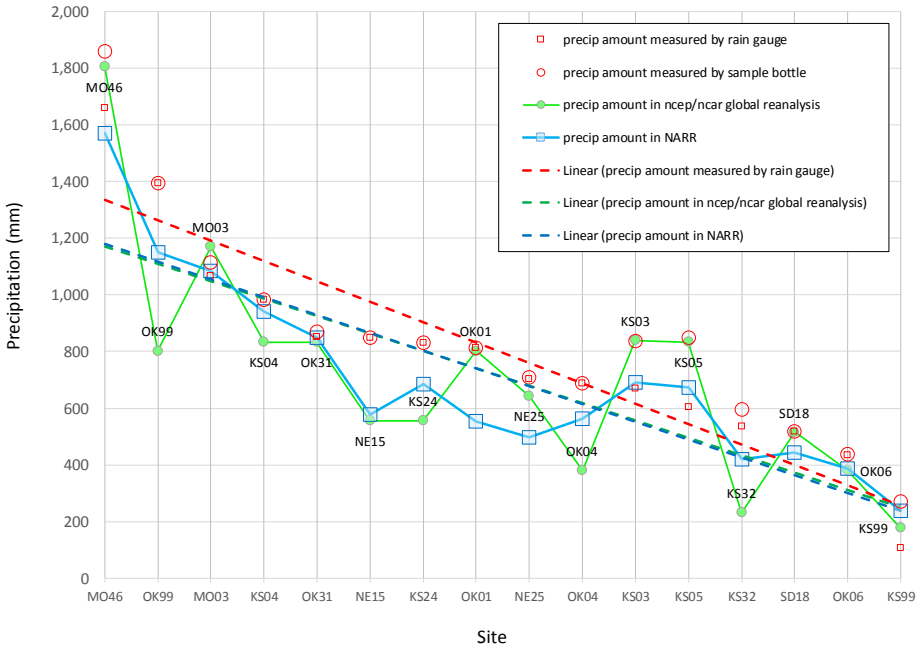

Figure 163. Comparison of 2011 precipitation amount (mm) measured at MDN sites with amount in NARR and NCEP/NCAR Global Reanalysis (sites in Midwest region)

7.3. Modeled and Measured Wet Deposition of Mercury

In Section 4.5 (beginning on page 90), data regarding the comparison of modeled vs. measured mercury wet deposition data are presented and discussed. In that section, data for the Great Lakes region and the Northeastern U.S. and Southeastern Canada are presented, as these regions are the most relevant for this Great Lakes analysis.

In this section of the Appendix, comparison data for these regions are reproduced, for the reader's convenience, and comparisons for all other regions are included as well.

Given the sparsity of Standard Source Locations in some regions (e.g., see Figure 79), it was not expected that the model predictions for wet deposition at most sites would match the measured deposition. However, as discussed in conjunction with Figure 32 (page 42), modeling using the SSL-interpolation approach can be relatively accurate for impacts on large receptors but be very limited in its skill in predicting wet deposition (and other quantities, like atmospheric concentrations) at specific monitoring sites.

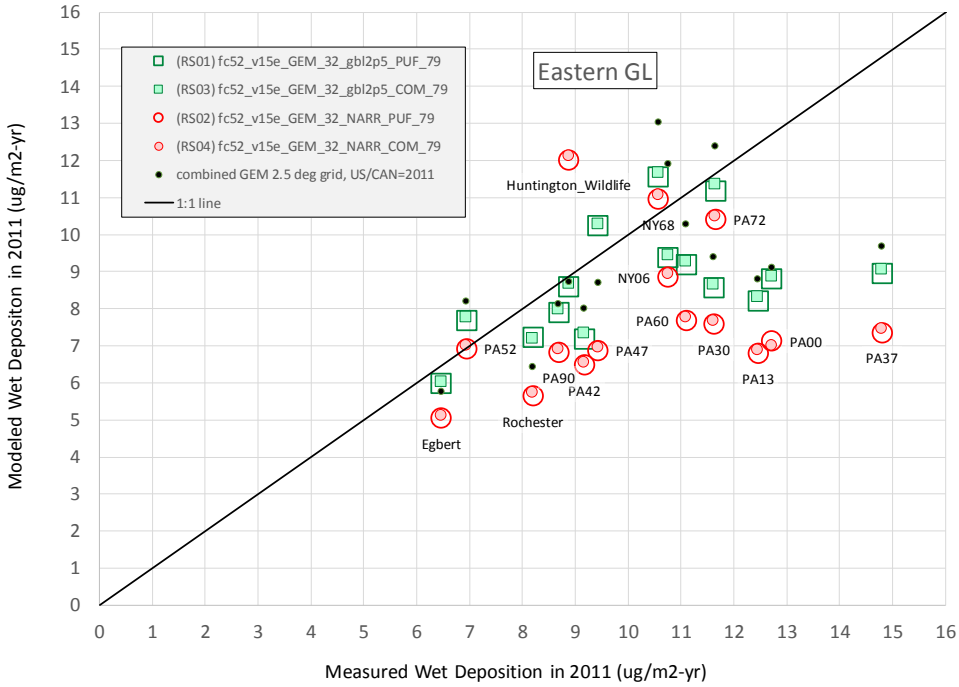

Figure 164. Modeled vs. measured mercury wet deposition at MDN sites in the Eastern Great Lakes region.

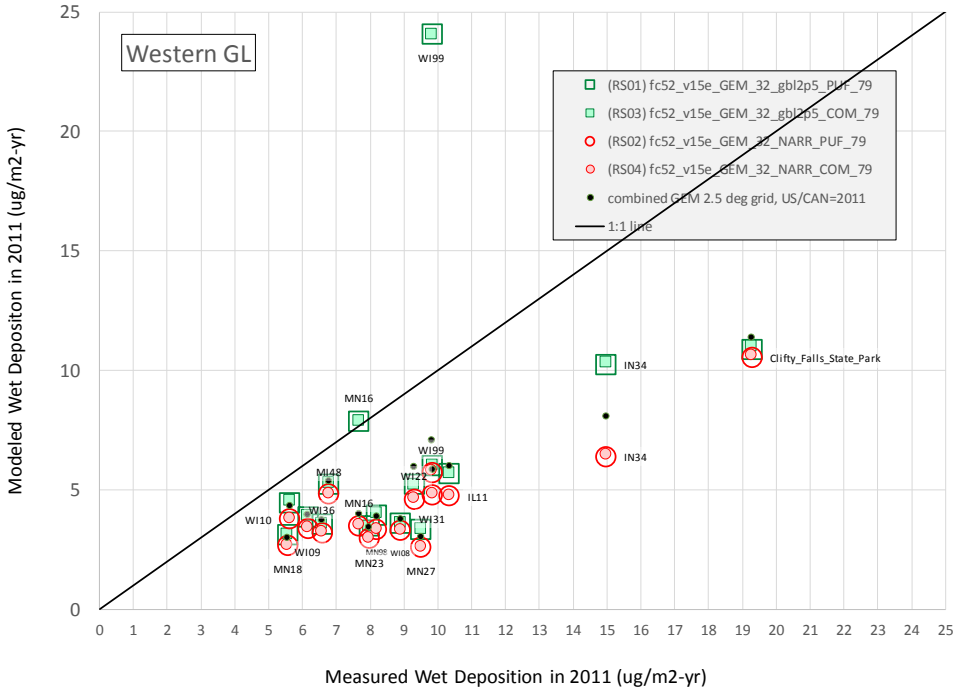

Figure 165. Modeled vs. measured mercury wet deposition at MDN sites in the Western Great Lakes region.

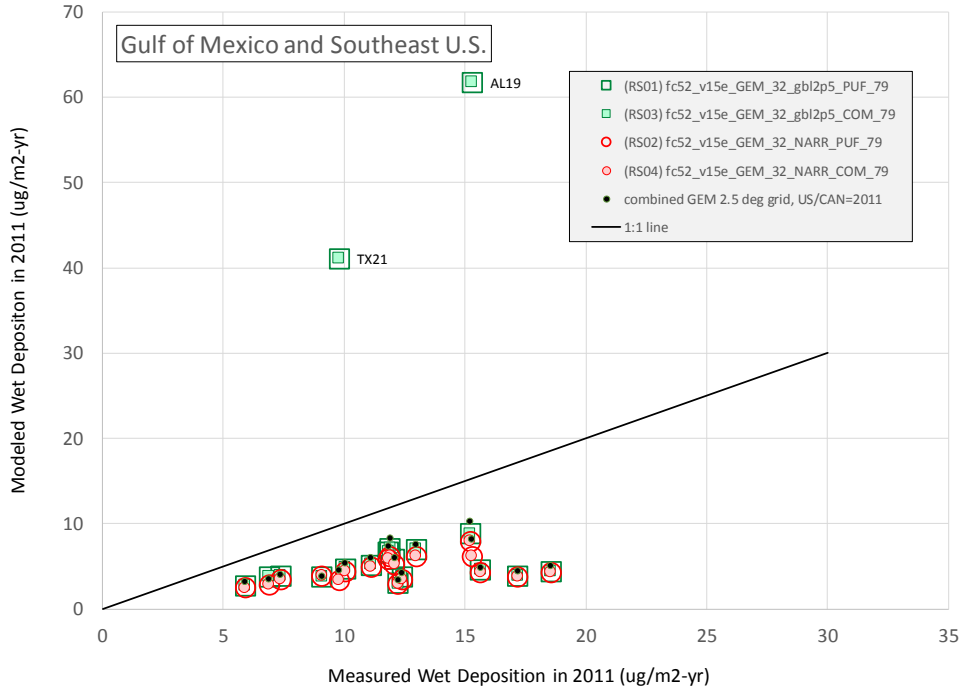

Figure 166. Modeled vs. measured mercury wet deposition at MDN sites in the Gulf of Mexico region and elsewhere in the Southeastern U.S. (all sites).

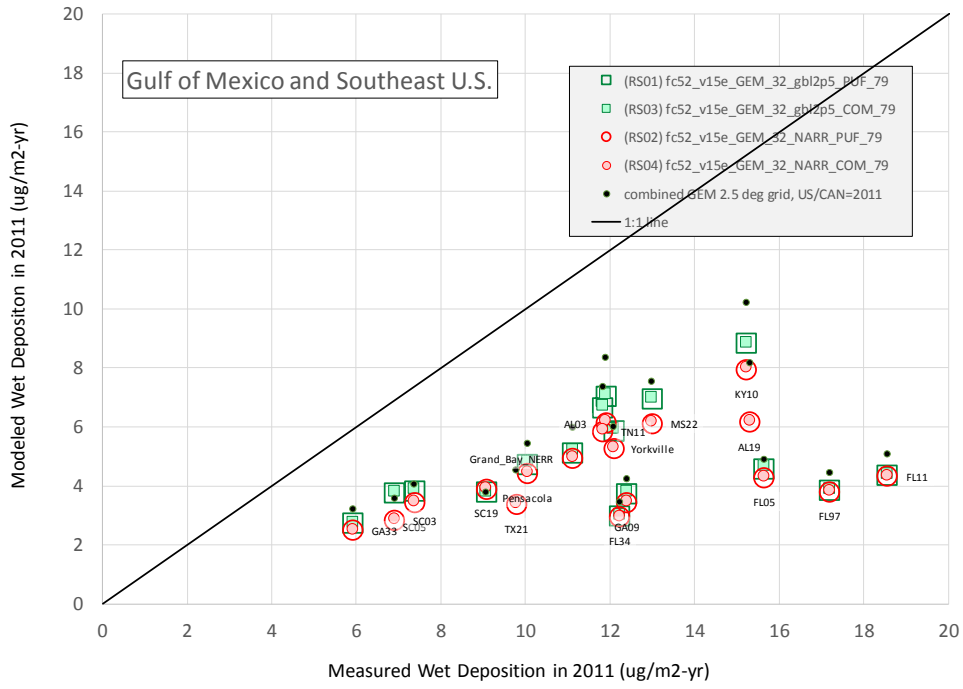

Figure 167. Modeled vs. measured mercury wet deposition at MDN sites in the Gulf of Mexico region and elsewhere in the Southeastern U.S. (all sites except TX21 and AL19, to better show comparison for other sites).

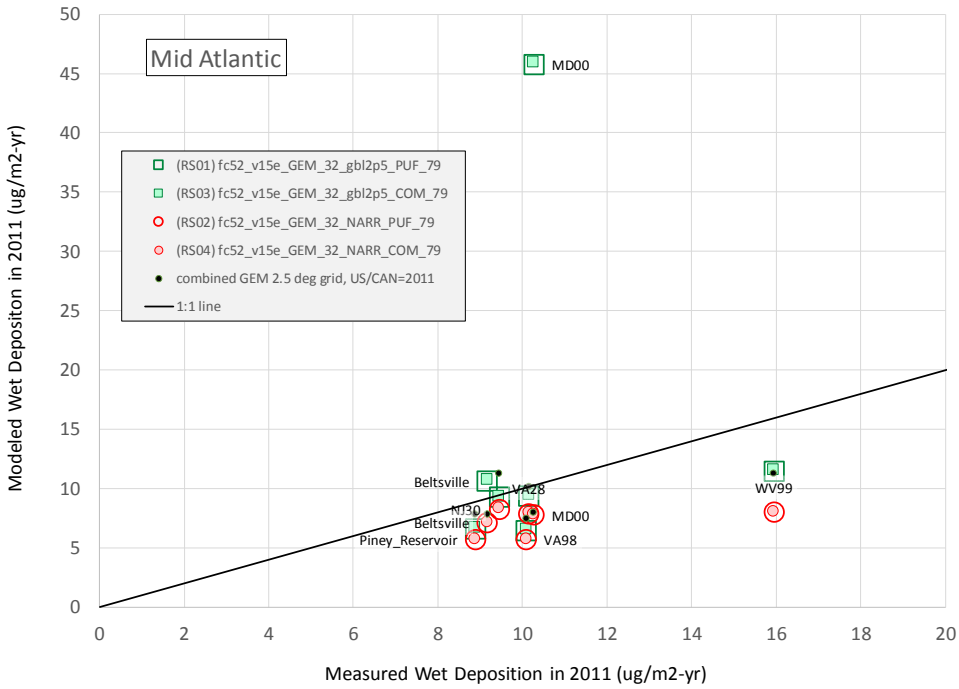

Figure 168. Modeled vs. measured mercury wet deposition at MDN sites in the Mid-Atlantic region of the U.S. (all sites).

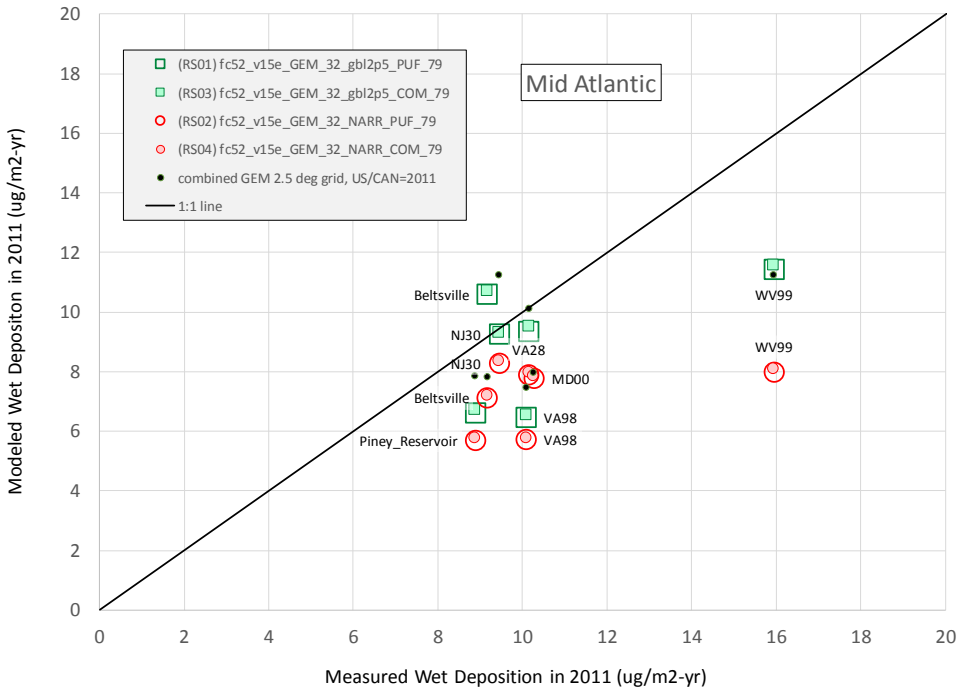

Figure 169. Modeled vs. measured mercury wet deposition at MDN sites in the Mid-Atlantic region of the U.S. (all sites except MD00, to better show details of comparison for remaining sites)

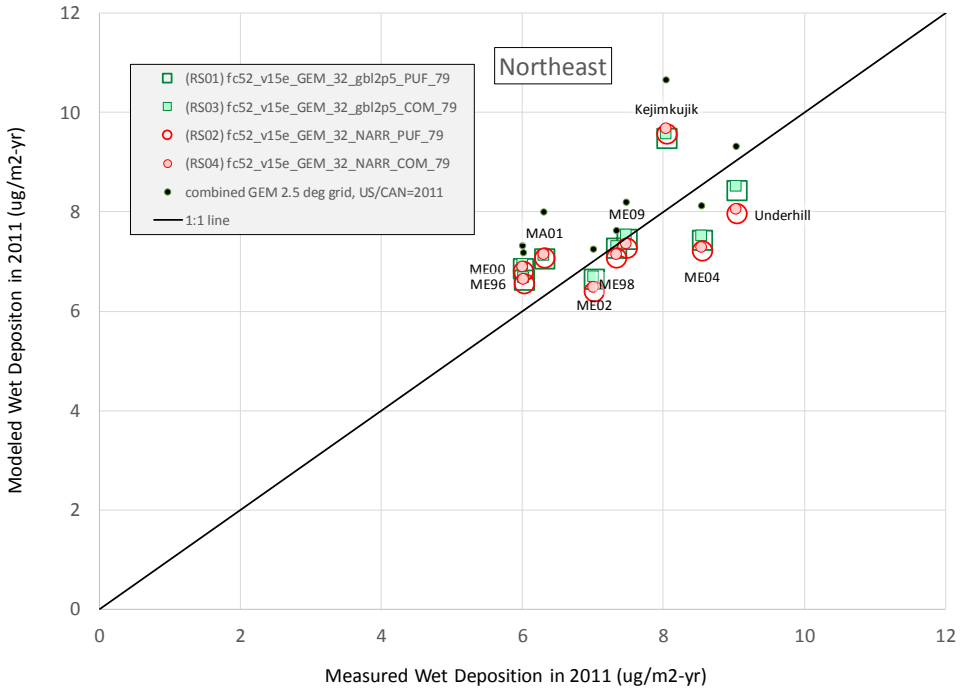

Figure 170. Modeled vs. measured mercury wet deposition at MDN sites in the Northeastern U.S. (and Southeastern Canada).

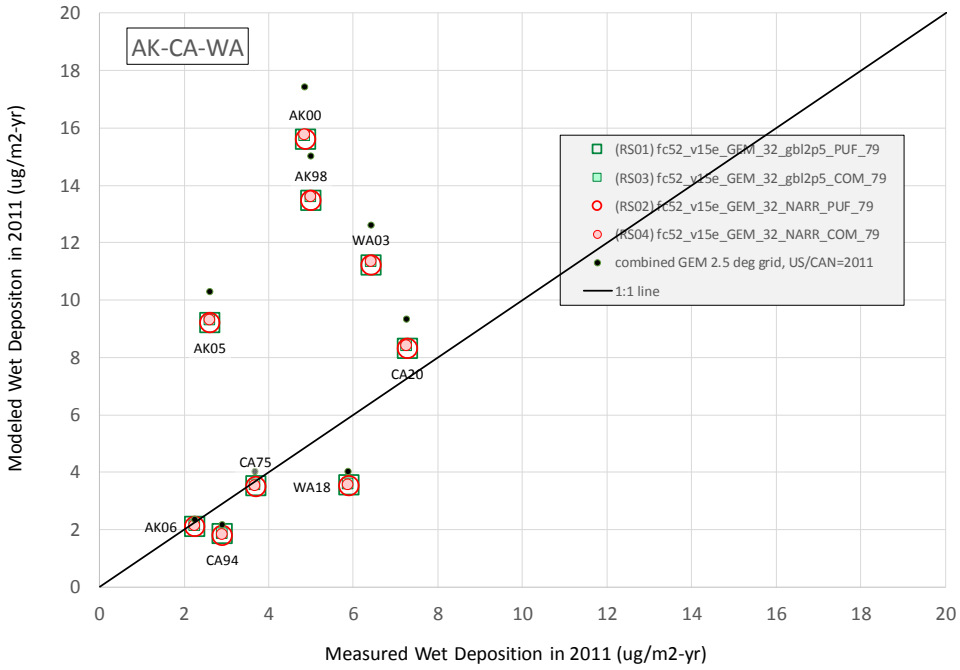

Figure 171. Modeled vs. measured mercury wet deposition at MDN sites in Alaska, Washington, and California.

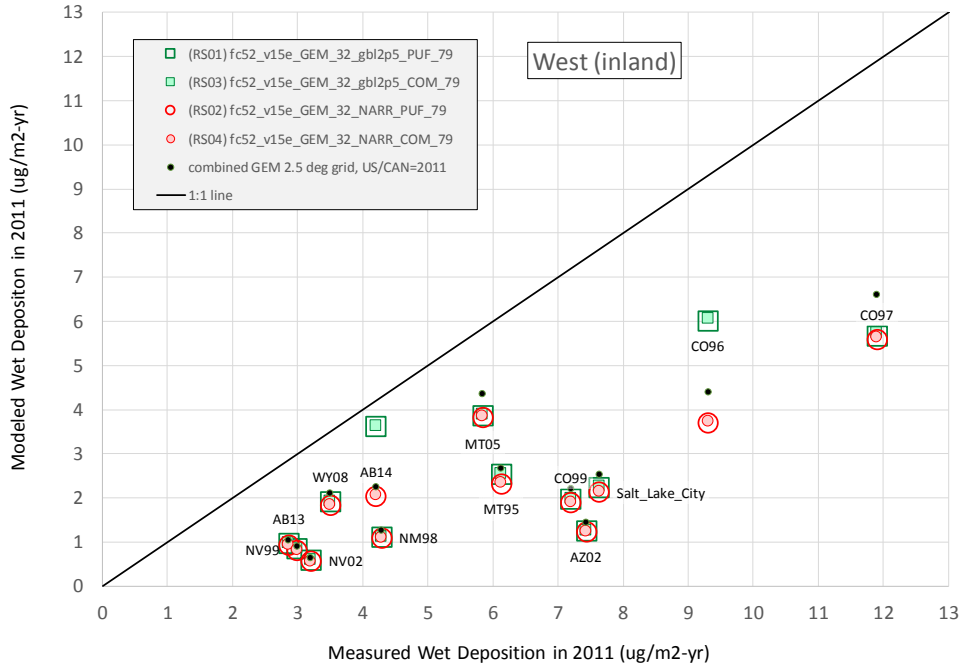

Figure 172. Modeled vs. measured mercury wet deposition at MDN sites in the Inland West region of the U.S. and Canada.

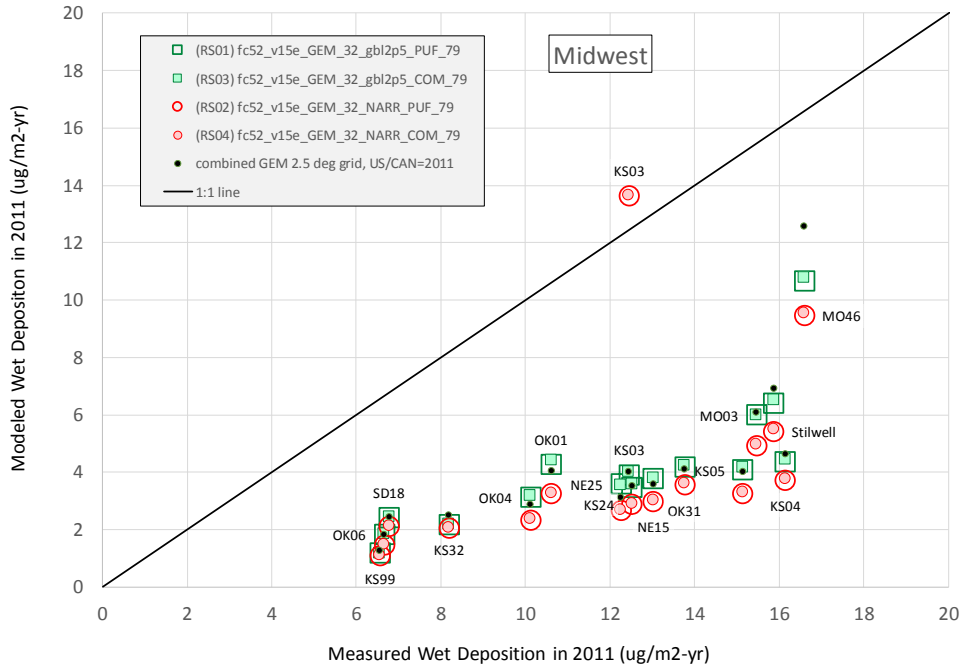

Figure 173. Modeled vs. measured mercury wet deposition at MDN sites in the Midwestern U.S.

7.4. Interpolation Methodology

As described in Section 3.3.1 (beginning on page 37), the impact of direct anthropogenic sources in Run Schemes 01, 02, 03, and 04 (i.e., all schemes except the Eulerian-only scheme RS-00) are estimated using an interpolation-based methodology. As described, the method uses a specific number of the closest Standard Source Locations (SSL's) to the actual source, and calculates a weighted average of the source-receptor results for these closest SSL's based on the distance between the source and the SSL and the difference in angular orientation of the *source to the receptor* and the *SSL to the receptor.*

The default values used in the interpolation approach were the following:

- number of closest SSL's used = 3
- exponent on distance for weighted average = 2 ("*r*" in Equation 1)
- exponent on difference in angular orientation for weighted average = 2 ("*a*" in Equation 1)

In Figure 174 below, the interpolation-based contributions from the U.S., Canada, China, and all other countries is shown for a range of different interpolation parameters, for the RS-04 dispersion methodology. It can be seen the model estimated results are quite similar over the wide range of parameters used. Thus, while there are uncertainties in this approach – e.g., the accuracy is certainly influenced by the number of SSL's used – the choice of interpolation parameters does not appear to introduce significant additional uncertainty.

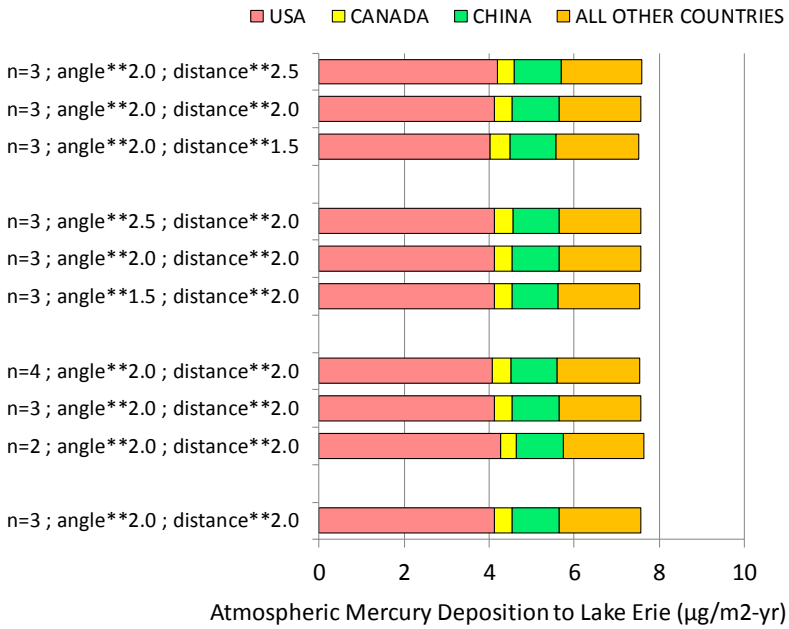

Figure 174. Examples of the influence of different interpolation parameters on the model-estimated contribution of direct anthropogenic emissions (based on the RS-04 dispersion methodology).

7.5. Presentation at ICMGP 2017, Providence Rhode Island

The author of this report (Mark Cohen) gave a presentation at the 13th International Conference on Mercury as a Global Pollutant (ICMGP), July 16-21, 2017, Providence, Rhode Island, USA. This presentation is being included as an Appendix to this Technical Report, as the graphical images and animations may help to further illustrate the methodologies and results in this analysis.

The results presented at this July 2017 conference were based on slightly different model configuration than was ultimately used in the final analysis presented in this report, but the results methodologies – and results – are close enough that the presentation is relevant. The results for contributions of direct anthropogenic emissions are the exactly the same, but there are small differences (~10%) in the contributions estimated from the global ocean, from land/vegetation, and biomass burning.

Note also that results for another type of methodology was examined in this talk. In this alternative methodology, the Lagrangian-Eulerian hybrid approaches were alternatively supplied with U.S. and Canadian emissions aggregated onto a 2.5° by 2.5° grid, and then emitted from the centroid of each grid square. This approach was examined to investigate the relative impact of the spatial resolution of emissions on modeling results. Graphics and results related to this alternative methodology are shown in Slide 21 (Figure 195), Slide 22 (Figure 196), and Slide 25 (Figure 199).

Static images of the slides from the talk are included below, but it is noted that the original PowerPoint presentation has extensive animation that enhances the content. In a few cases, explanatory notes have been added as text boxes on the slides.

As of the time this report was written, the PowerPoint version of the presentation has been made available at:

ftp://1397guest:2018arl@ftp.arl.noaa.gov/.Presentations/.2017/.ICMGP_2017/Cohen_ICMGP_2017.pptx

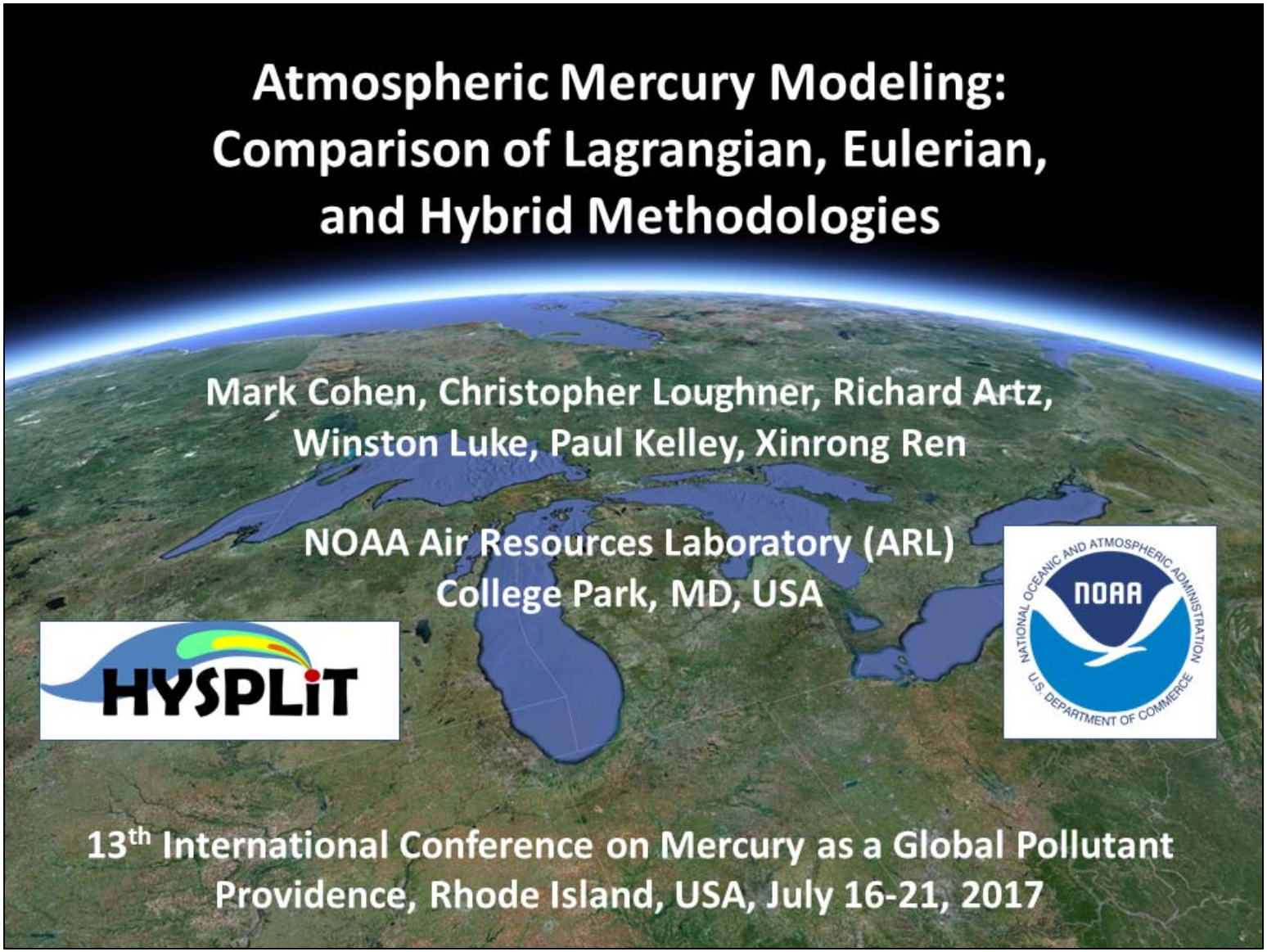

Figure 175. Slide 1

Lagrangian

emissions, fate and transport modeled as a 3-dimensional plume

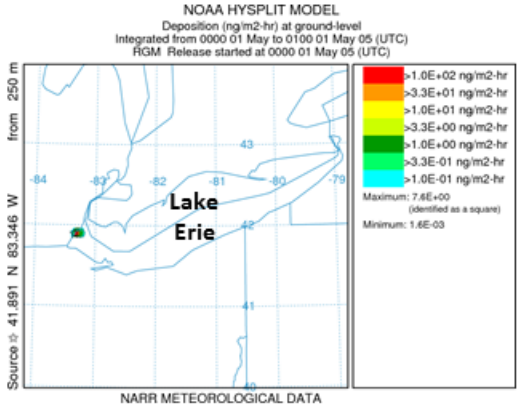

Eulerian

emissions, fate and transport modeled on a 3-dimensional grid

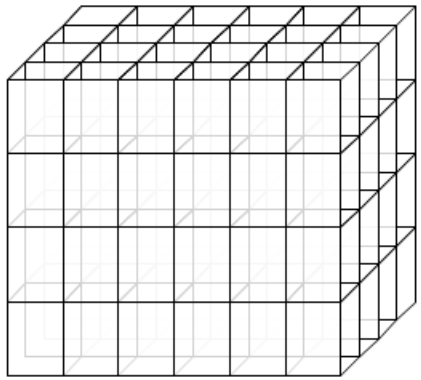

Hybrid **-- a combination of *Lagrangian* and *Eulerian* approaches**

Figure 176. Slide 2

Note: this slide has a lot of animation, and can be best viewed after downloading the PowerPoint version of the presentation.

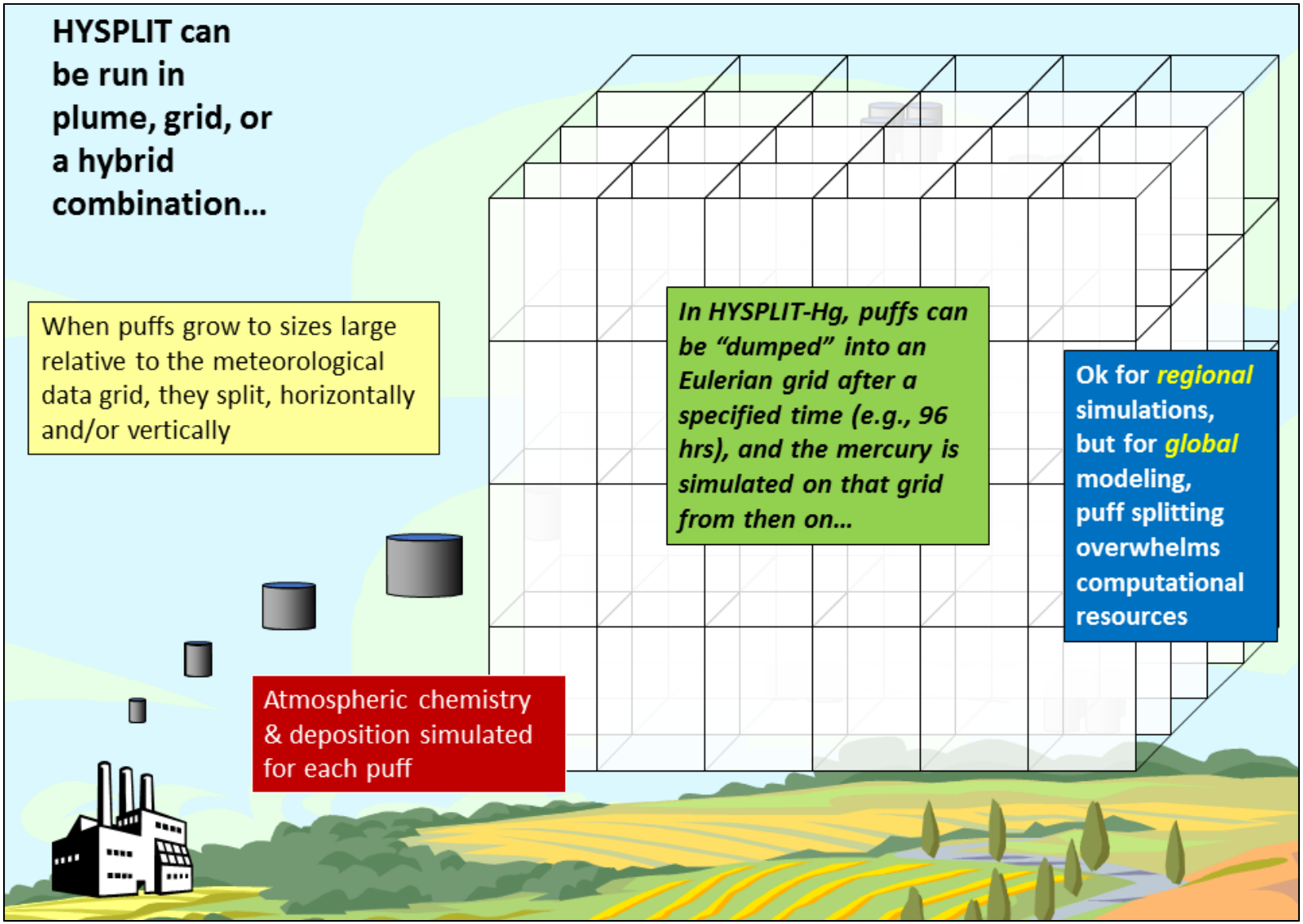

Figure 177. Slide 3

Note: this slide has a lot of animation, and can be best viewed after downloading the PowerPoint version of the presentation.

Running a Lagrangian (plume-based) simulation for ~100,000 sources would take ~**10 years** on a 96-processor Linux workstation, just for one particular model configuration (e.g., parameter choices, etc.)

We want to succeed, but if we fail, **its important to fail fast!**

When using the Lagrangian (plume-based) approach, generally **can't do an explicit simulation for each source** in the emissions inventory

Have developed an **interpolation-based** approach, where only a much smaller number of simulations are required

Figure 178. Slide 4

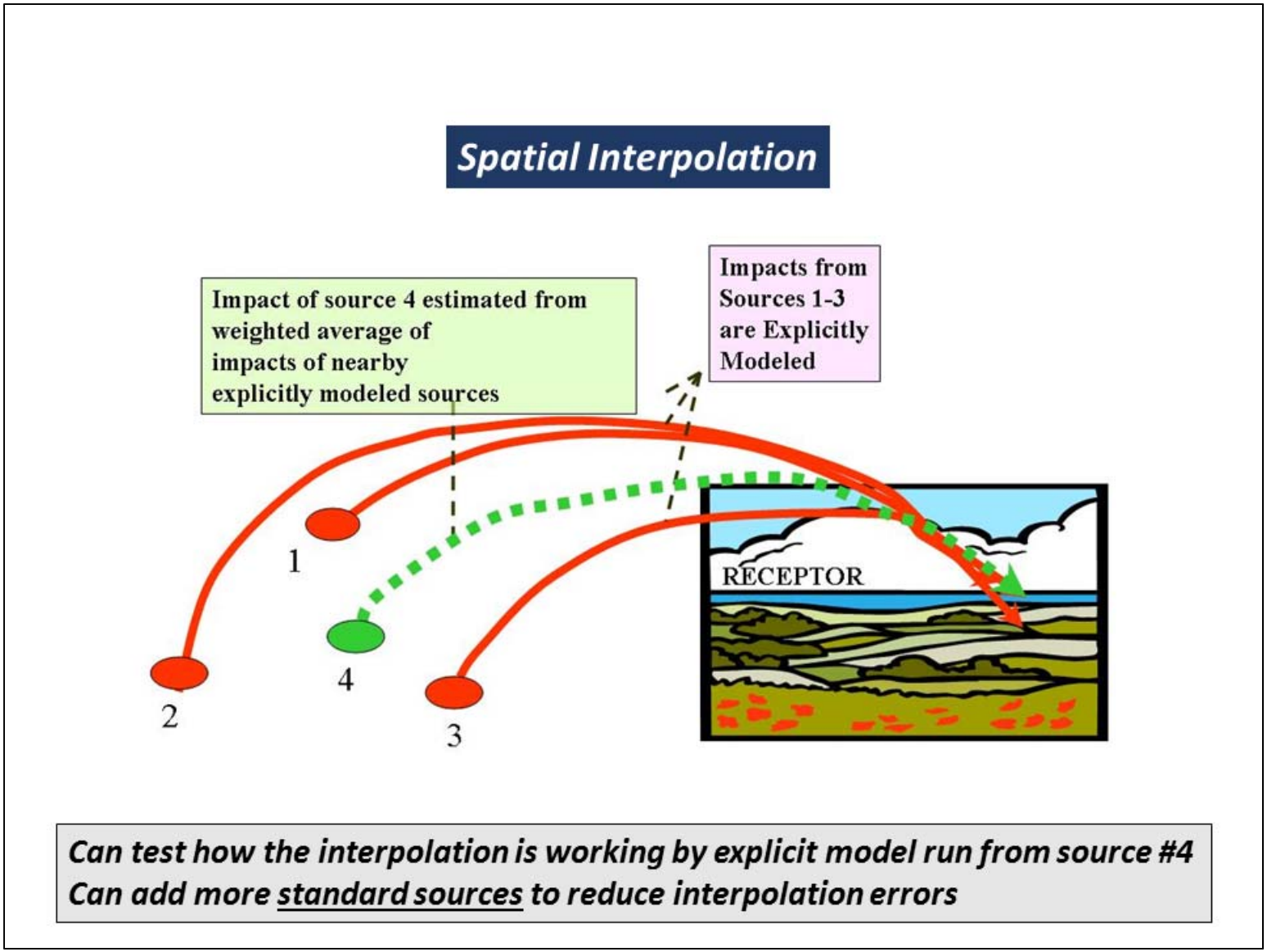

Figure 179. Slide 5

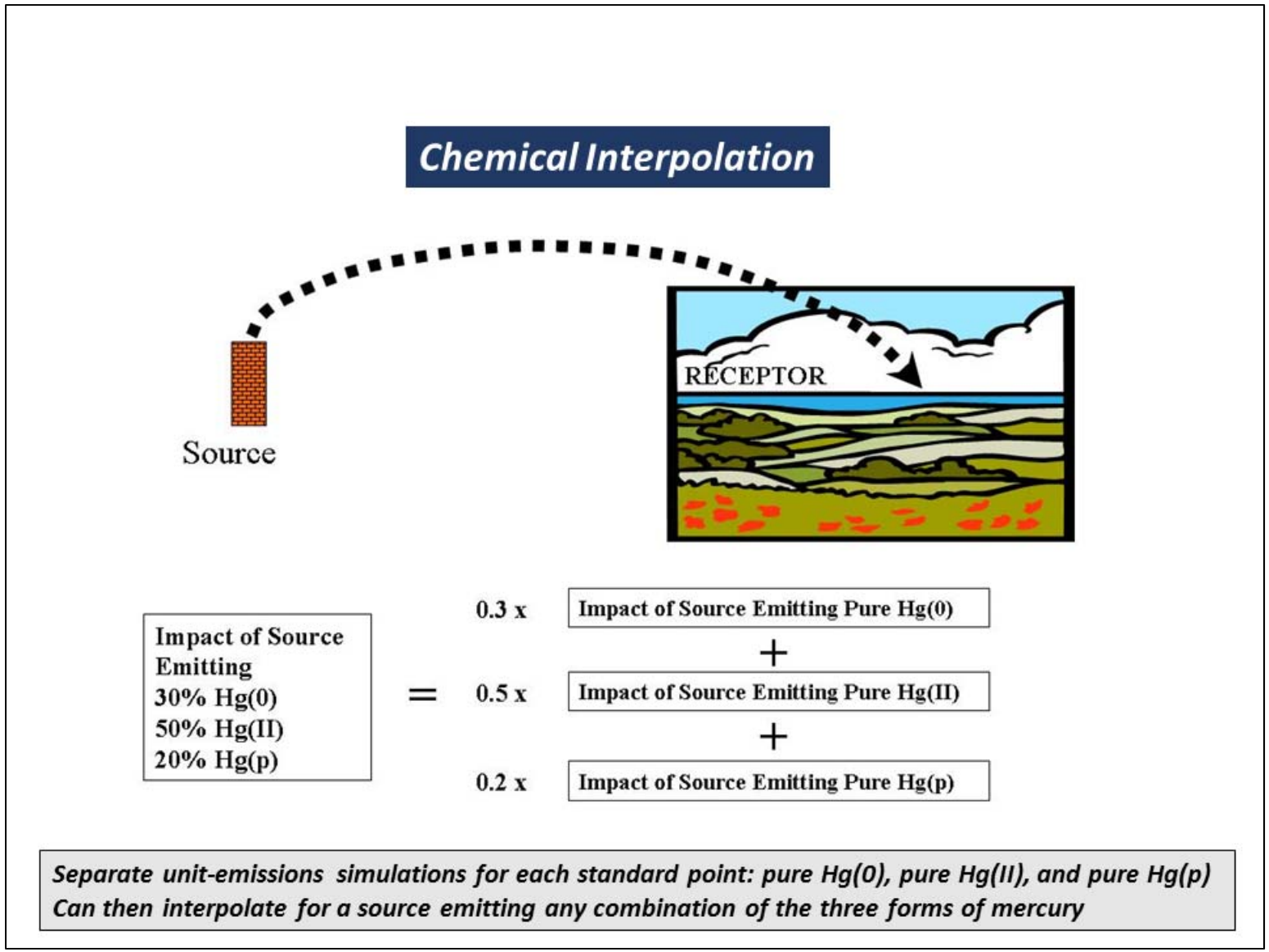

Figure 180. Slide 6

Why use the Lagrangian (plume-based) approach, even though it typically requires more computational resources?

… can get very detailed source-attribution information

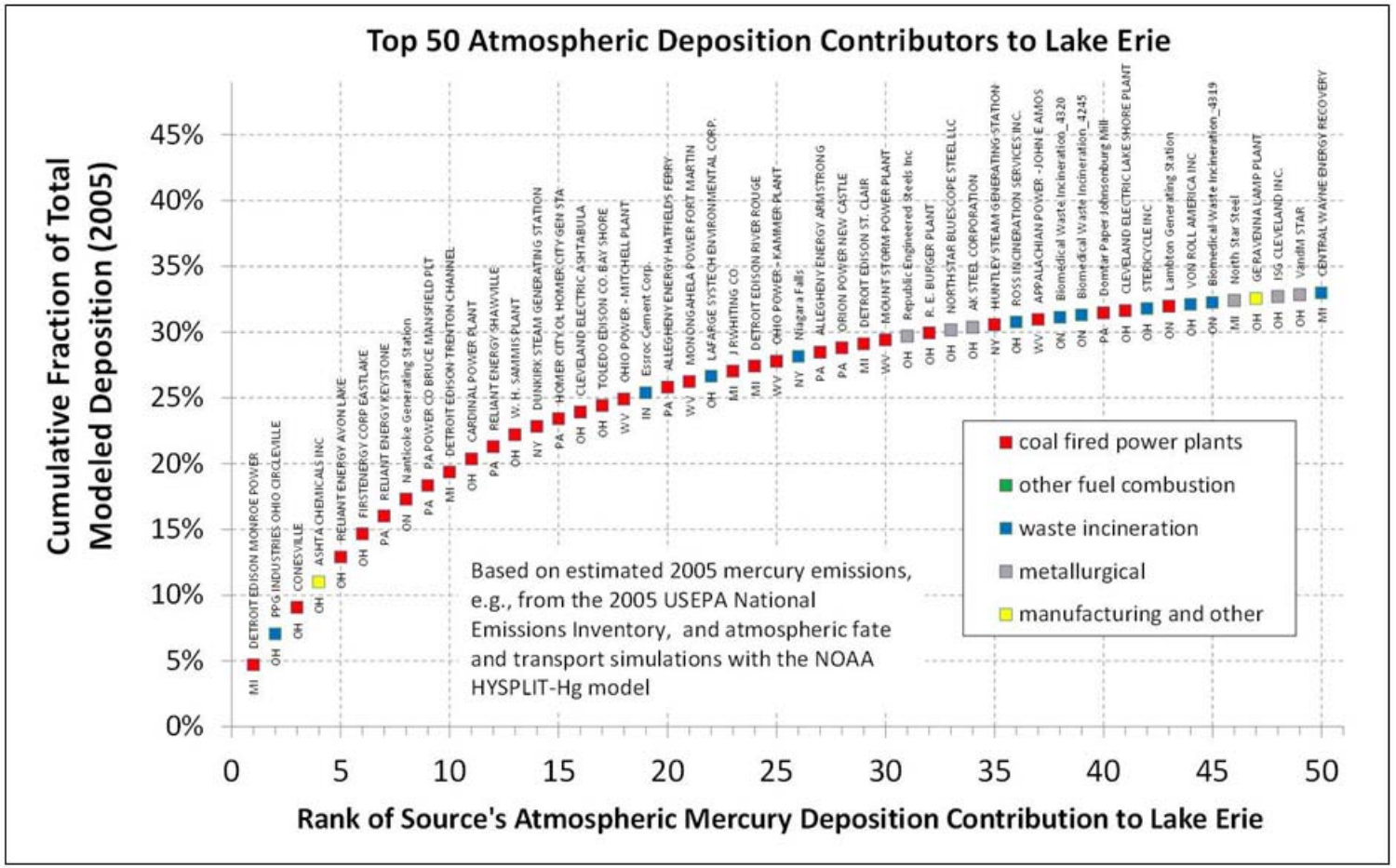

Figure 181. Slide 7

Note: this example was from an earlierl analysis. Examples of source-by-source results for the present analysis are included in the main body of the report (Section 5.7) and can also be developed through the DIVER/ERMA system (Section 5.6).

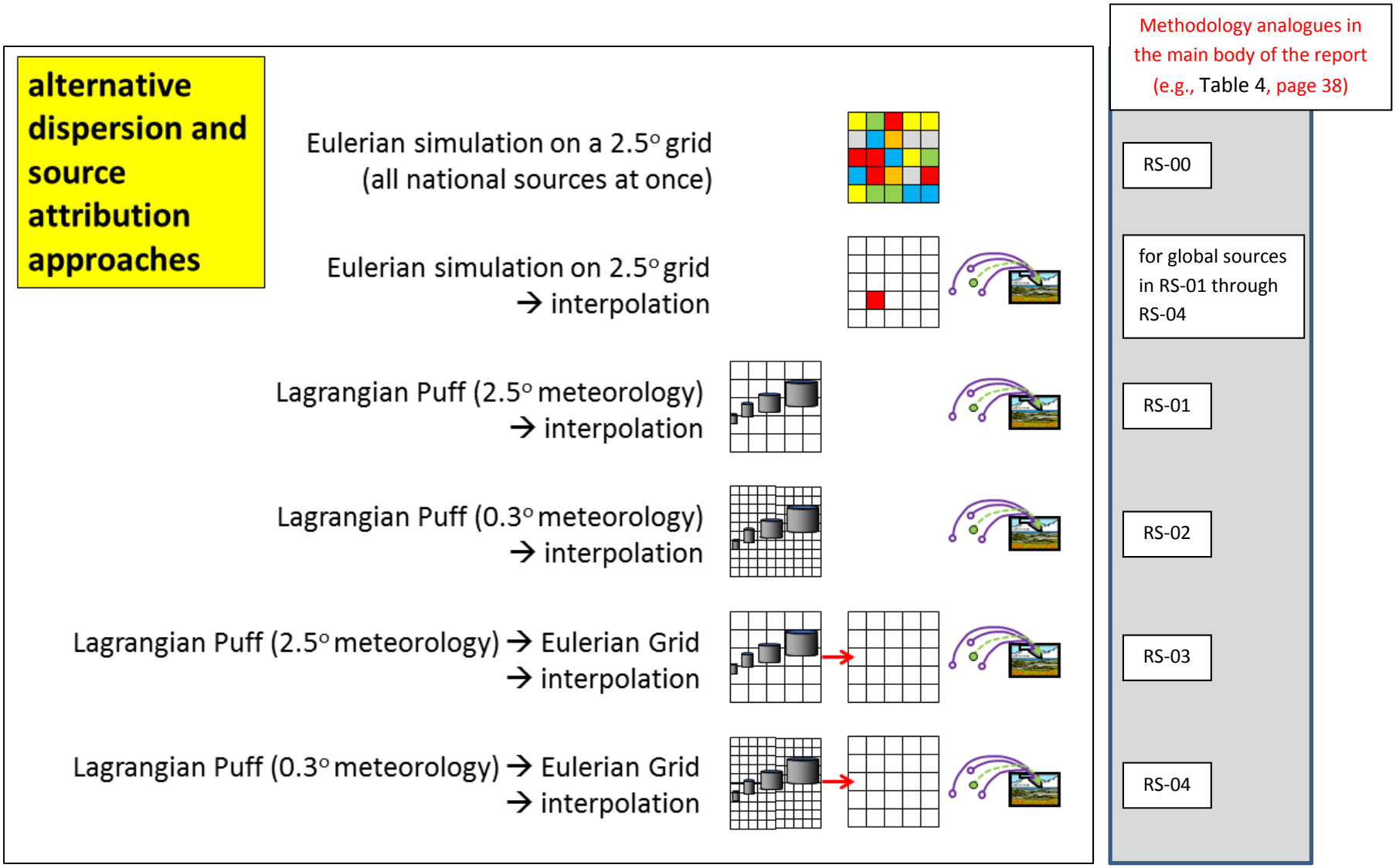

Figure 182. Slide 8

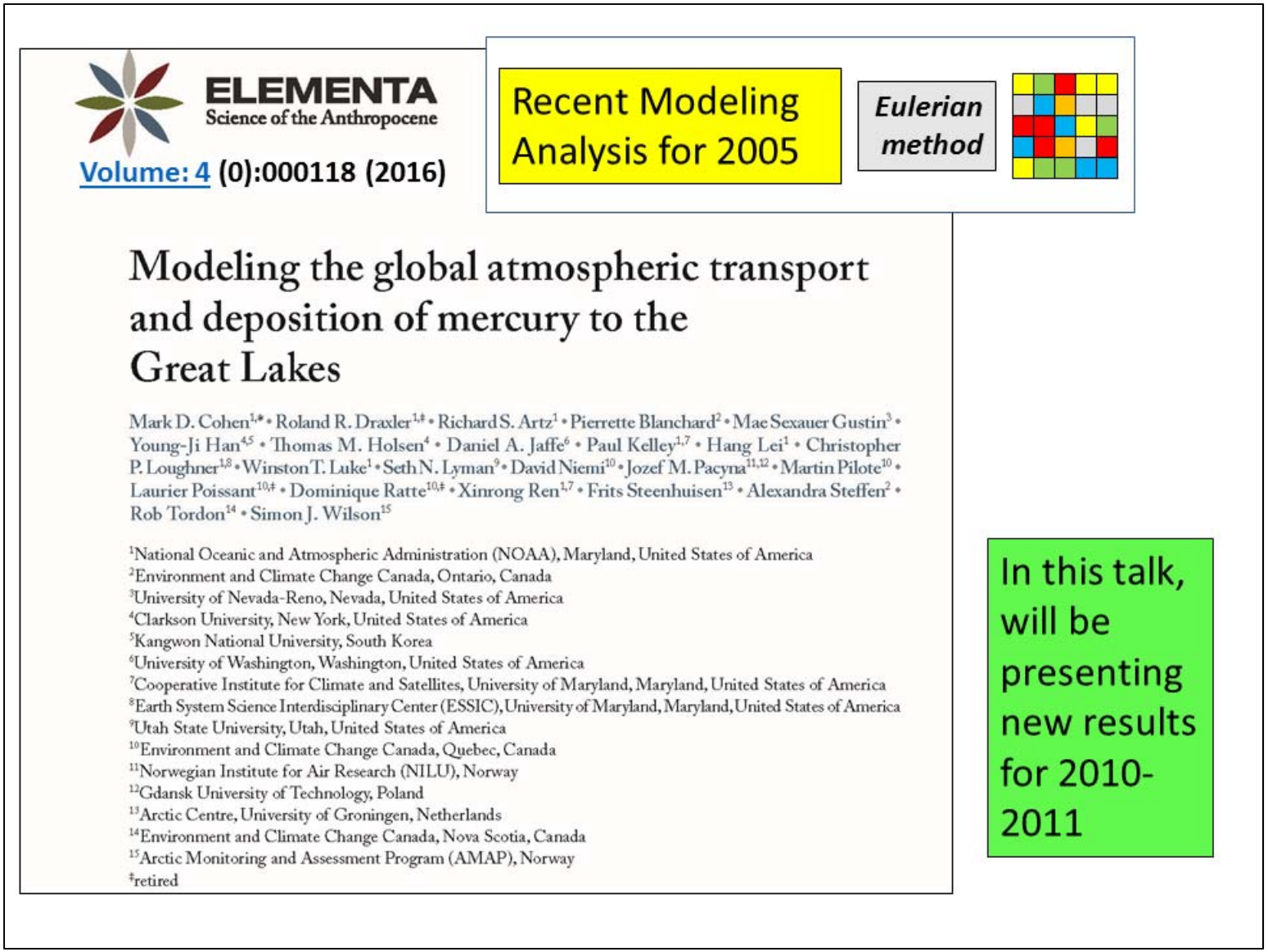

Figure 183. Slide 9

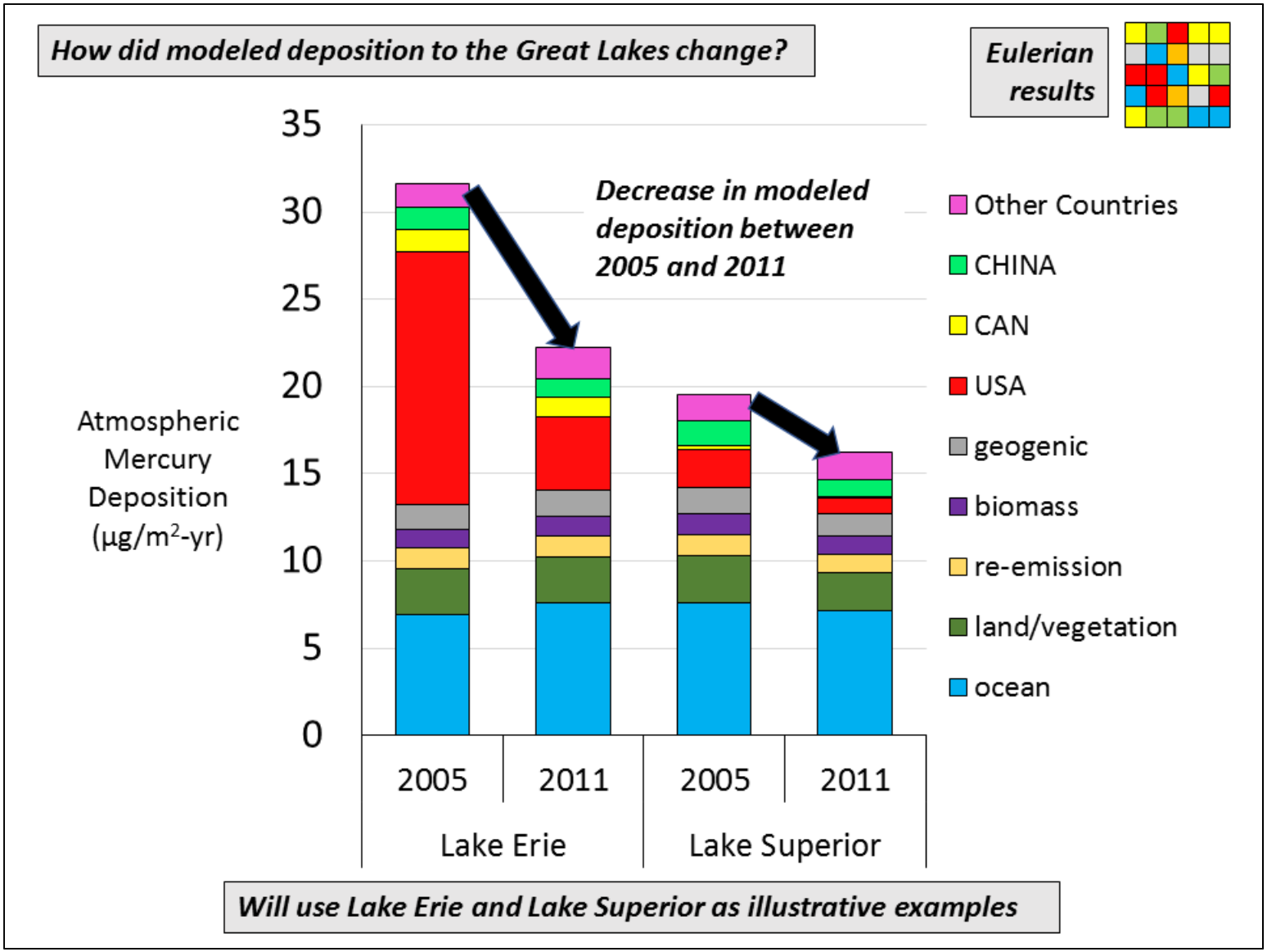

Figure 184. Slide 10

Note: results for ocean, land/vegetation, re-emission, biomass, and geogenic are slightly different in this preliminary analysis than those in the final model configuration presented in the main body of the report.

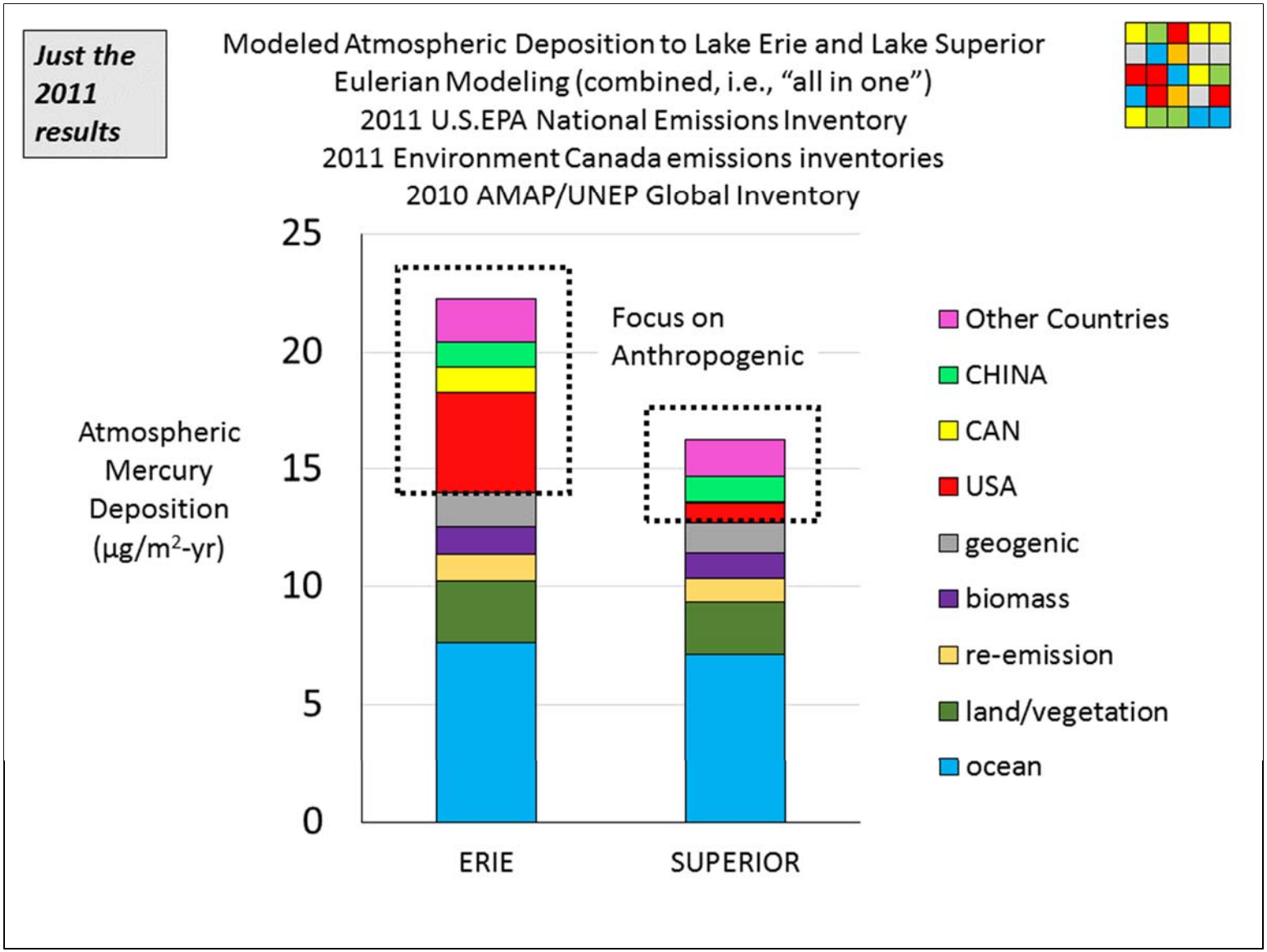

Figure 185. Slide 11

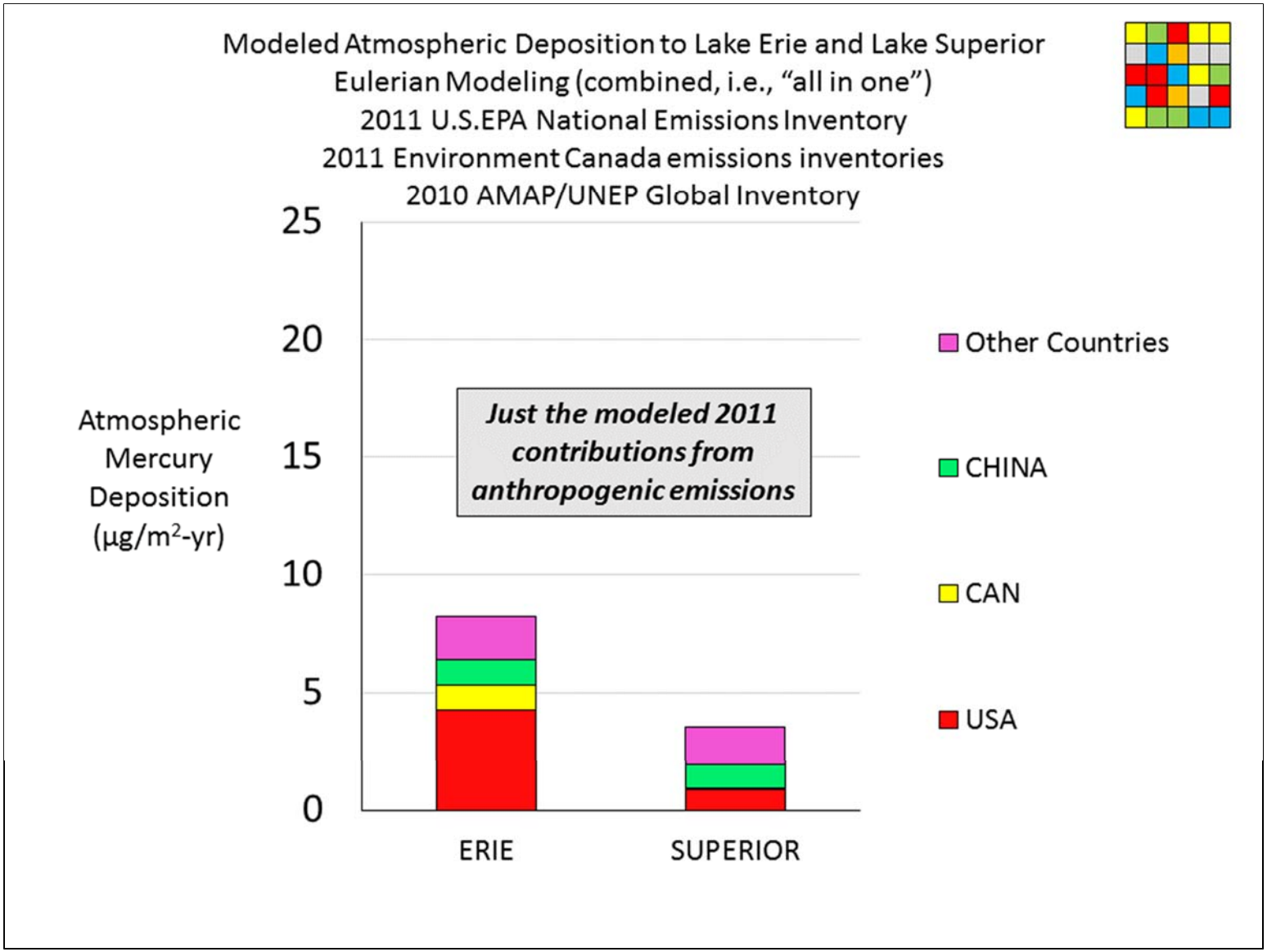

Figure 186. Slide 12

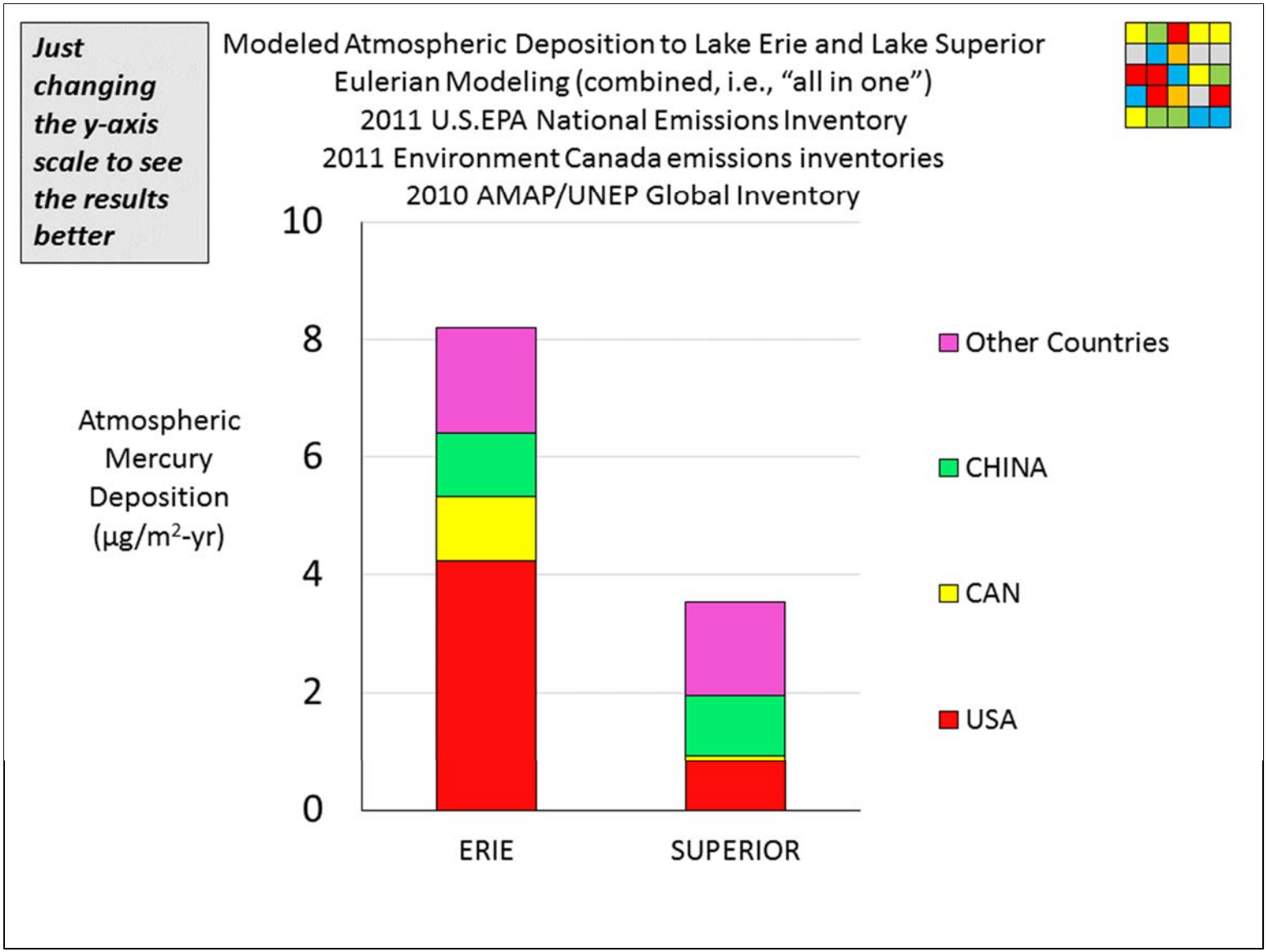

Figure 187. Slide 13

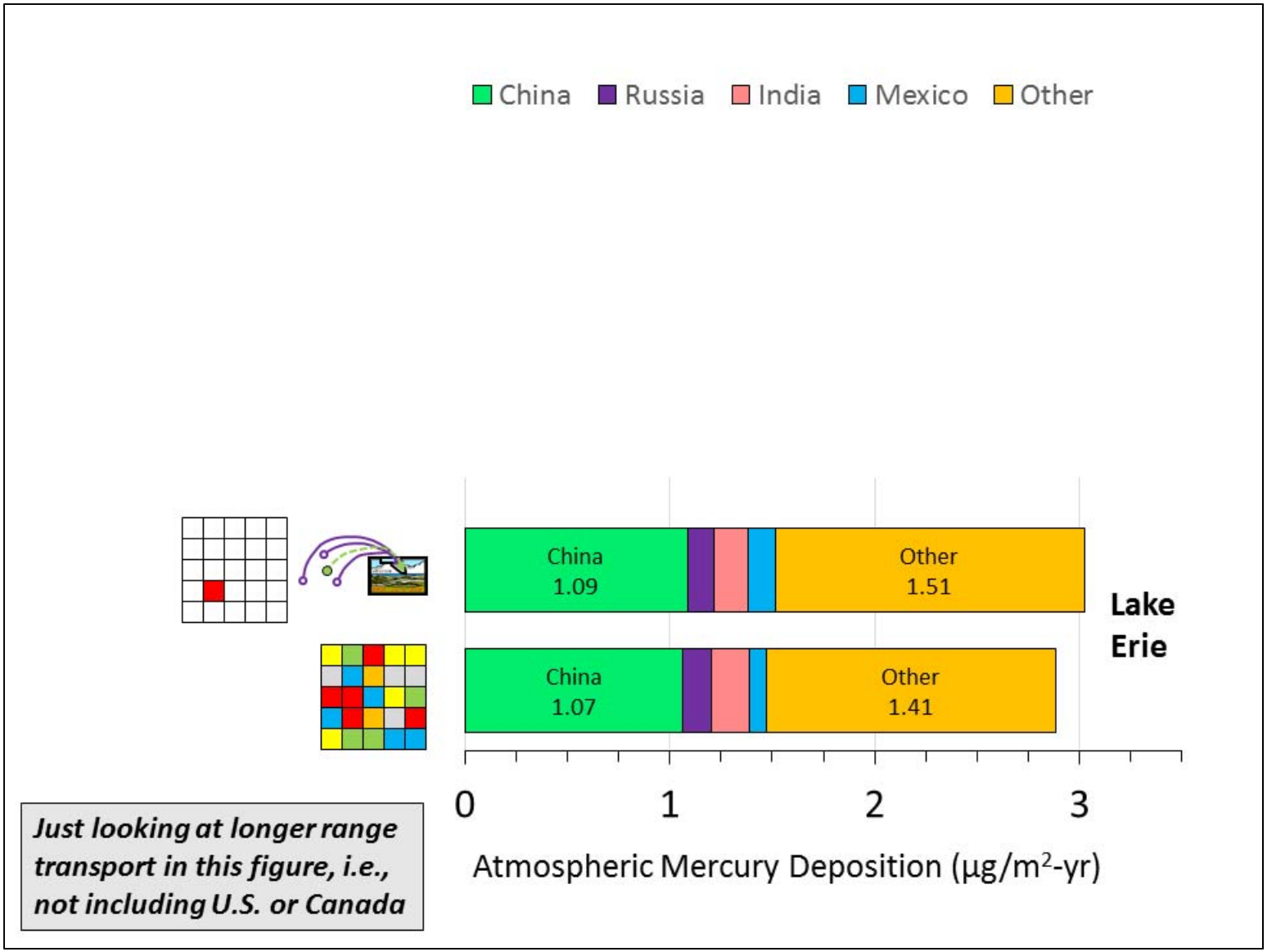

Figure 188. Slide 14

Note: this slide compares the modeling results for the Eulerian-only methodology (RS-00) and the hybrid Lagrangian/Eulerian approach described in the main body of the report. For essentially all sources outside of the U.S. and Canada, all of the hybrid methodologies used were identical. (See Table 4. Summary of Simulation Methodologies Used. Page 18)

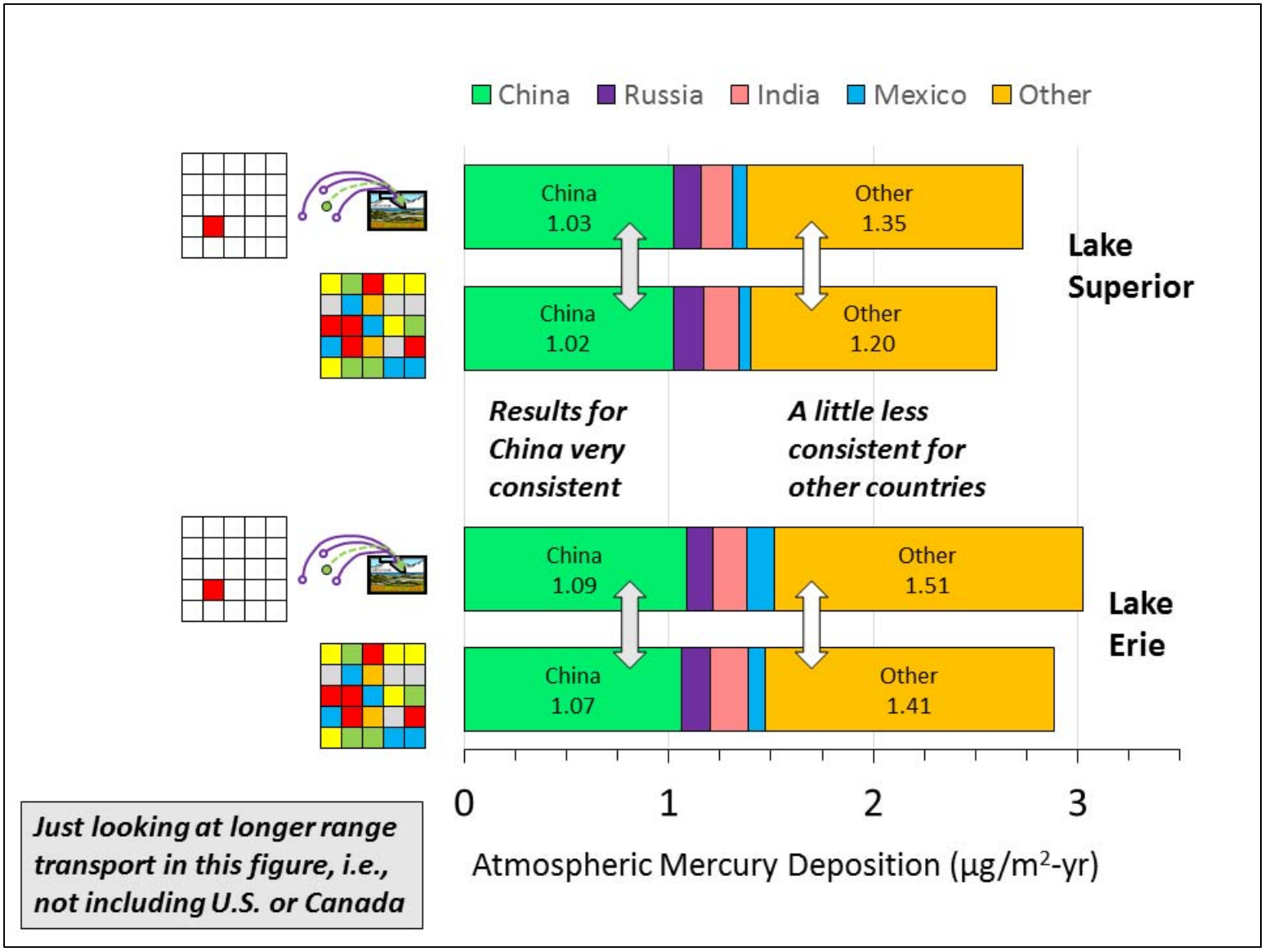

Figure 189. Slide 15

Note: this slide just adds the analogous comparison of results for Lake Superior to the previous slide, which only showed results for Lake Erie.

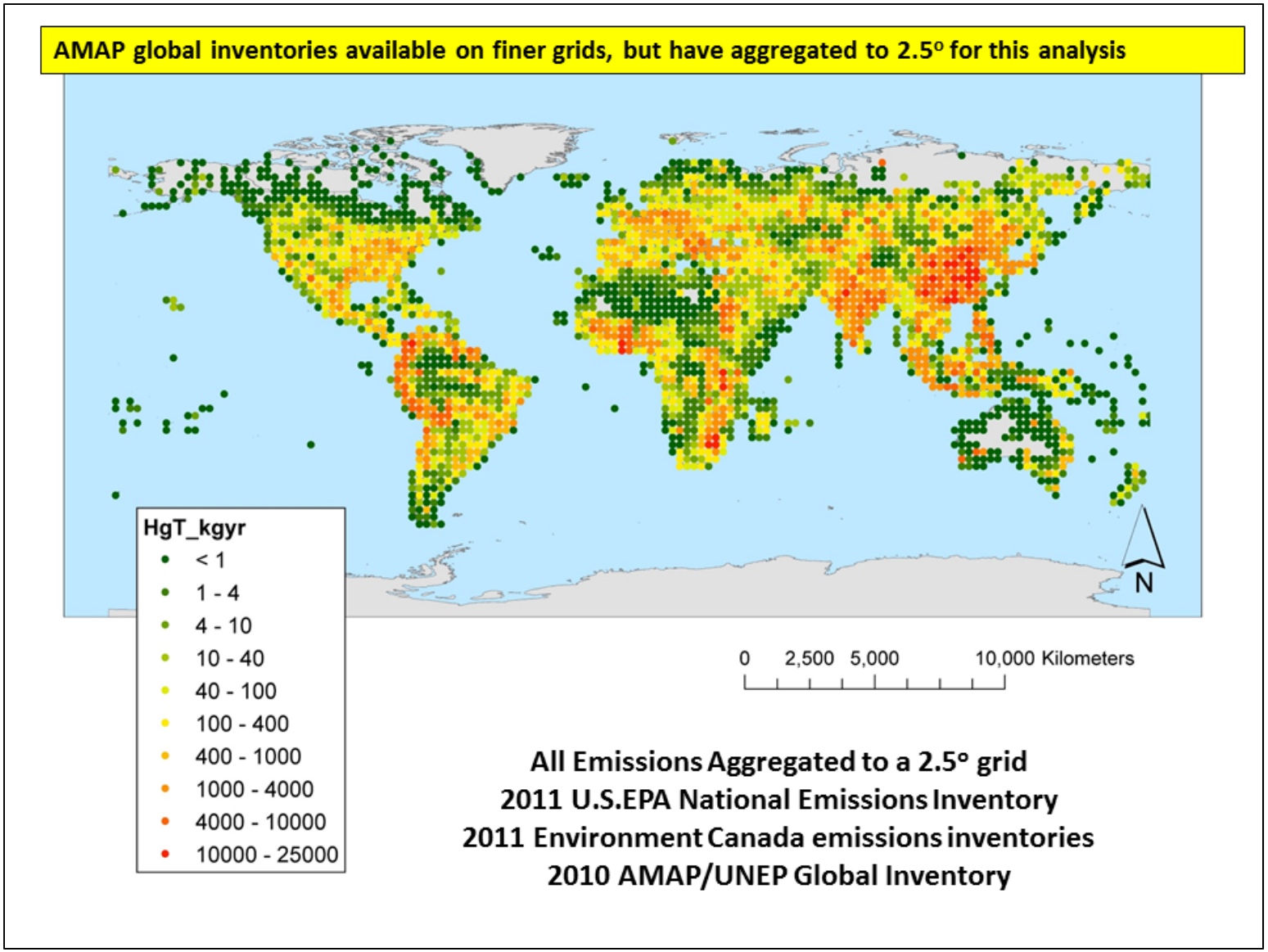

Figure 190. Slide 16

Note: In the methodologies described in the main body of the report, U.S. and Canadian emissions were only aggregated to the 2.5° grid for the Eulerian-only approach (RS-00). For all other approaches (RS-01, RS-02, RS-03, and RS-04), individual point and area sources (each with their own "actual" location) were used in the analysis.

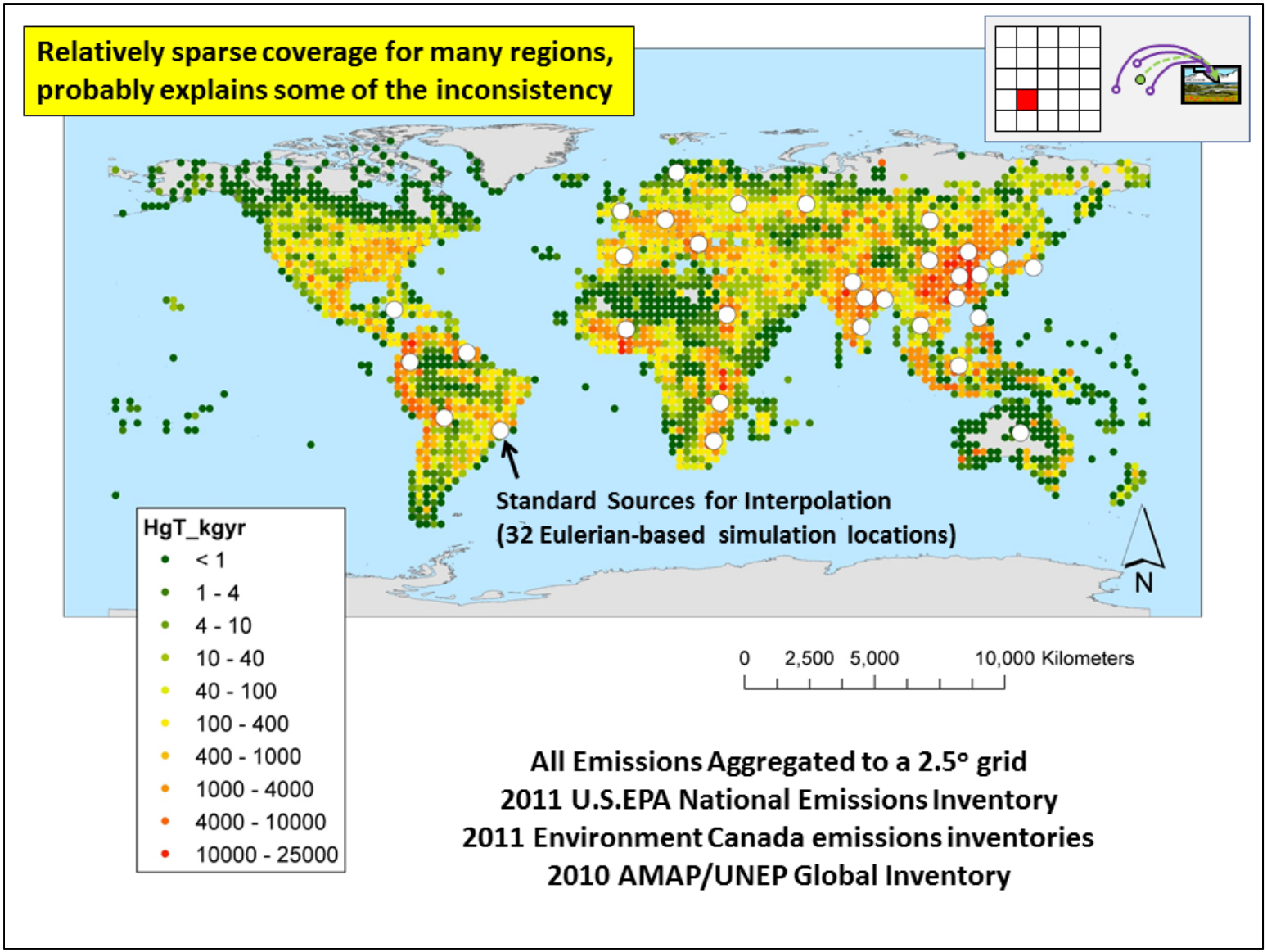

Figure 191. Slide 17

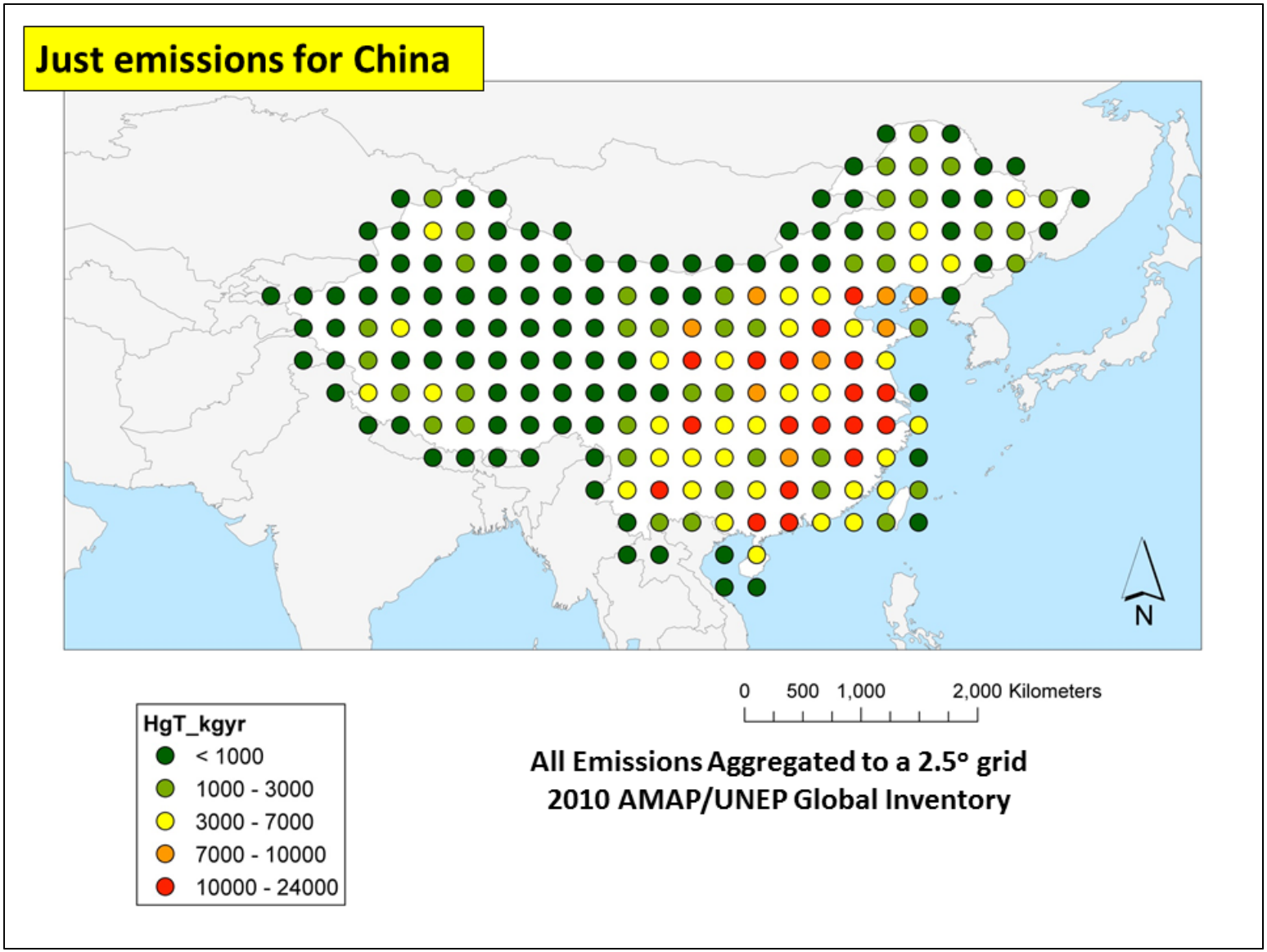

Figure 192. Slide 18

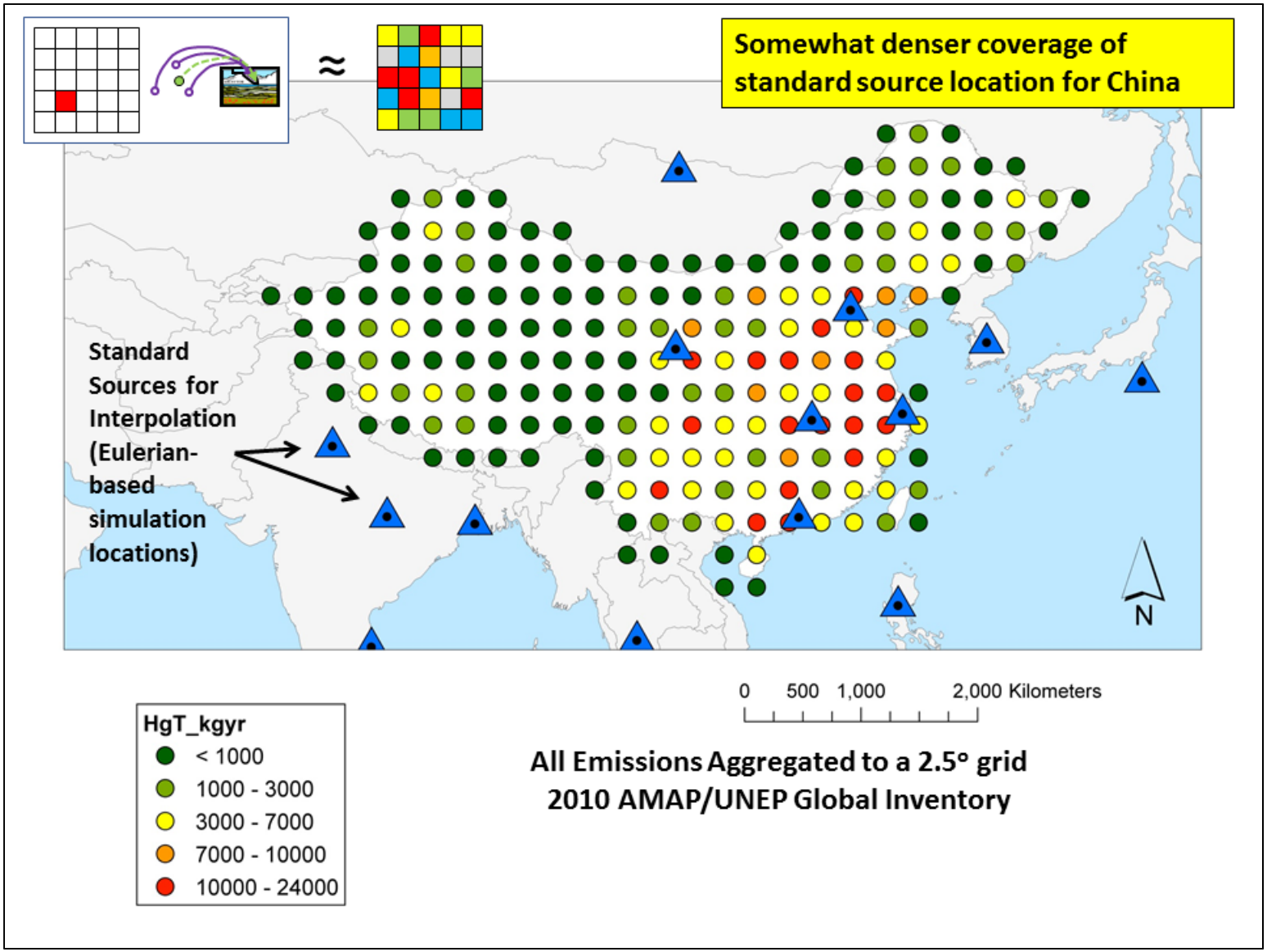

Figure 193. Slide 19

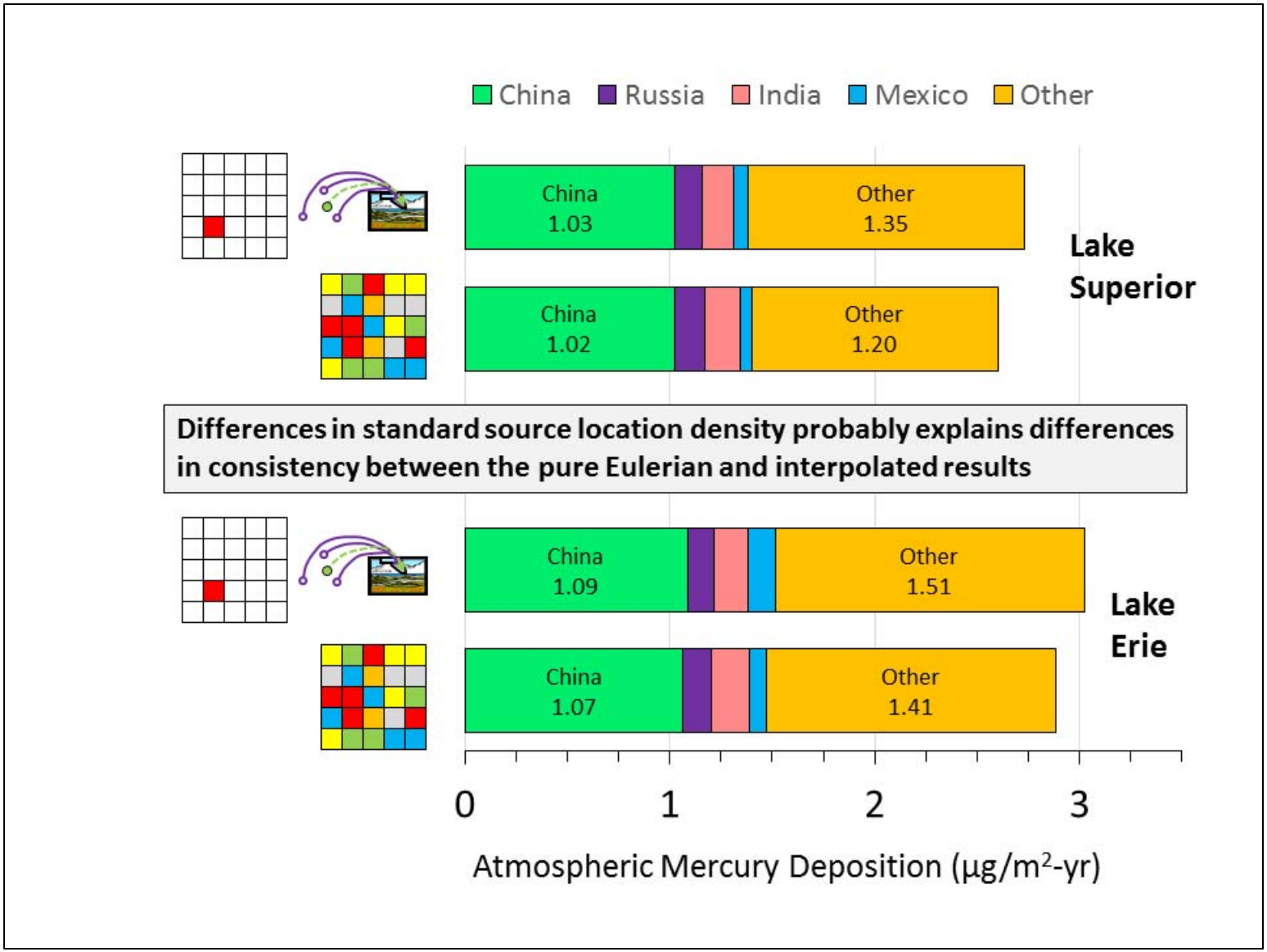

Figure 194. Slide 20

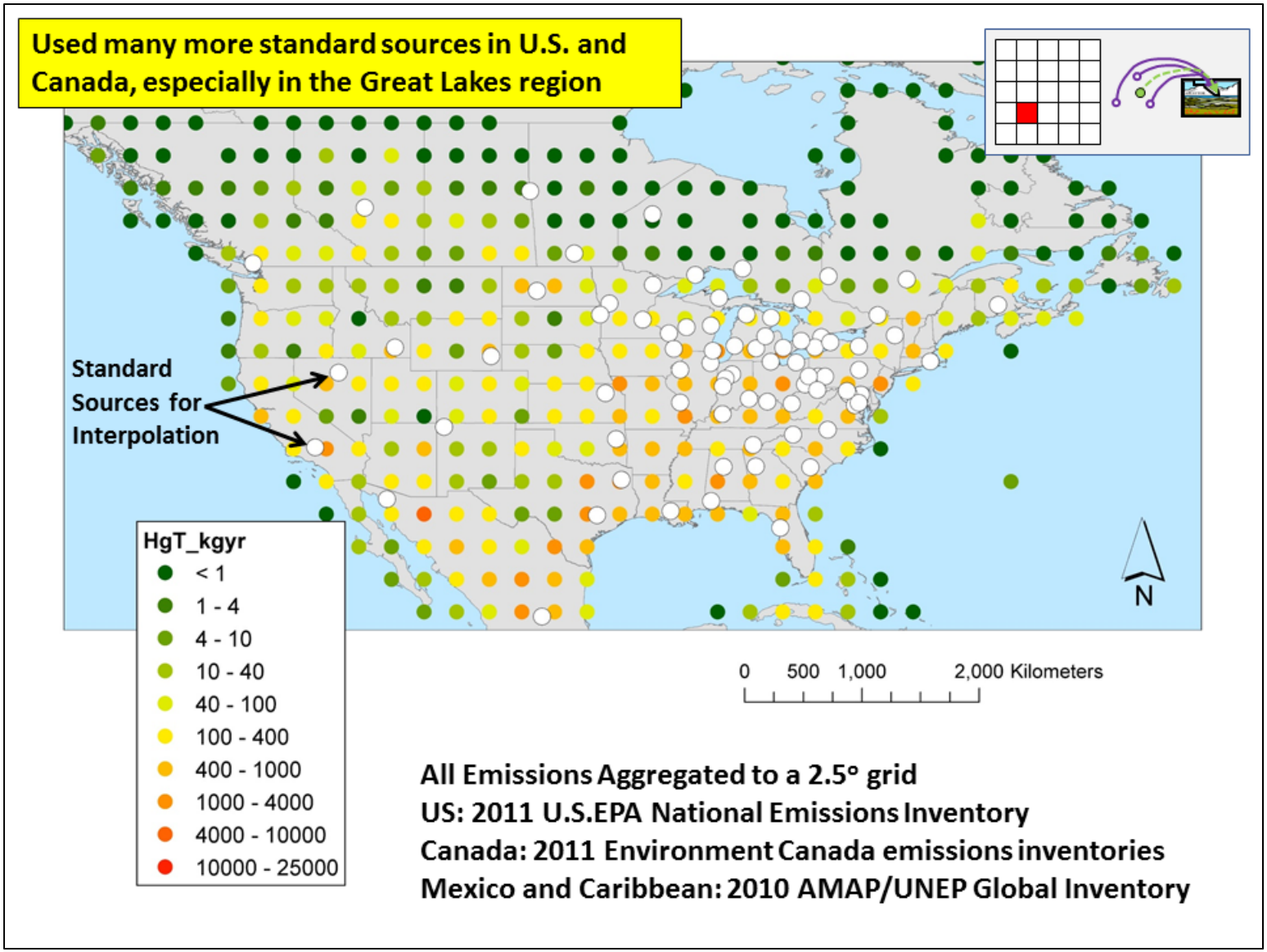

Figure 195. Slide 21

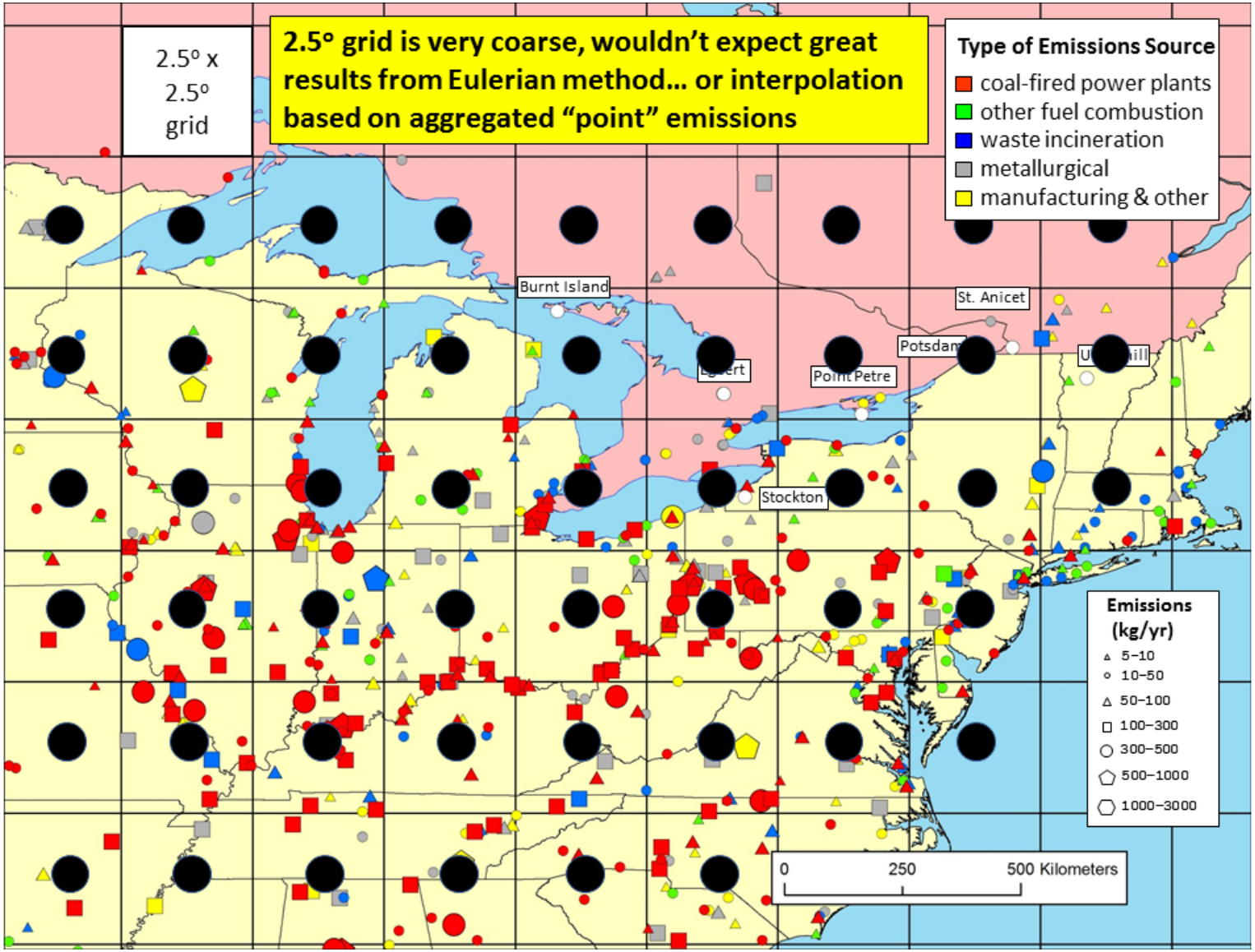

Figure 196. Slide 22

Note: An Eulerian-only approach was used in the main body of the report (RS-00), but results for "***point emissions for the entire grid expressed as a point source at the centroid of the grid square***" were not presented. Results for this approach were discussed in this talk, to explore issues related to source location specificity and interpolation.

Interpolation Methodology

The relative weight (importance) a given standard source simulation is given in estimating the impact of the actual source on a given receptor depends on two factors:

Number of closest standard source locations used

$$\frac{1}{\left[\text{Difference in orientation (angle) of standard source relative to actual source } \textit{in relation to a given receptor}\right]^{\text{Angle Exponent}}} \qquad \frac{1}{\left[\text{Distance between standard source and actual source}\right]^{\text{Distance Exponent}}}$$

Figure 197. Slide 23

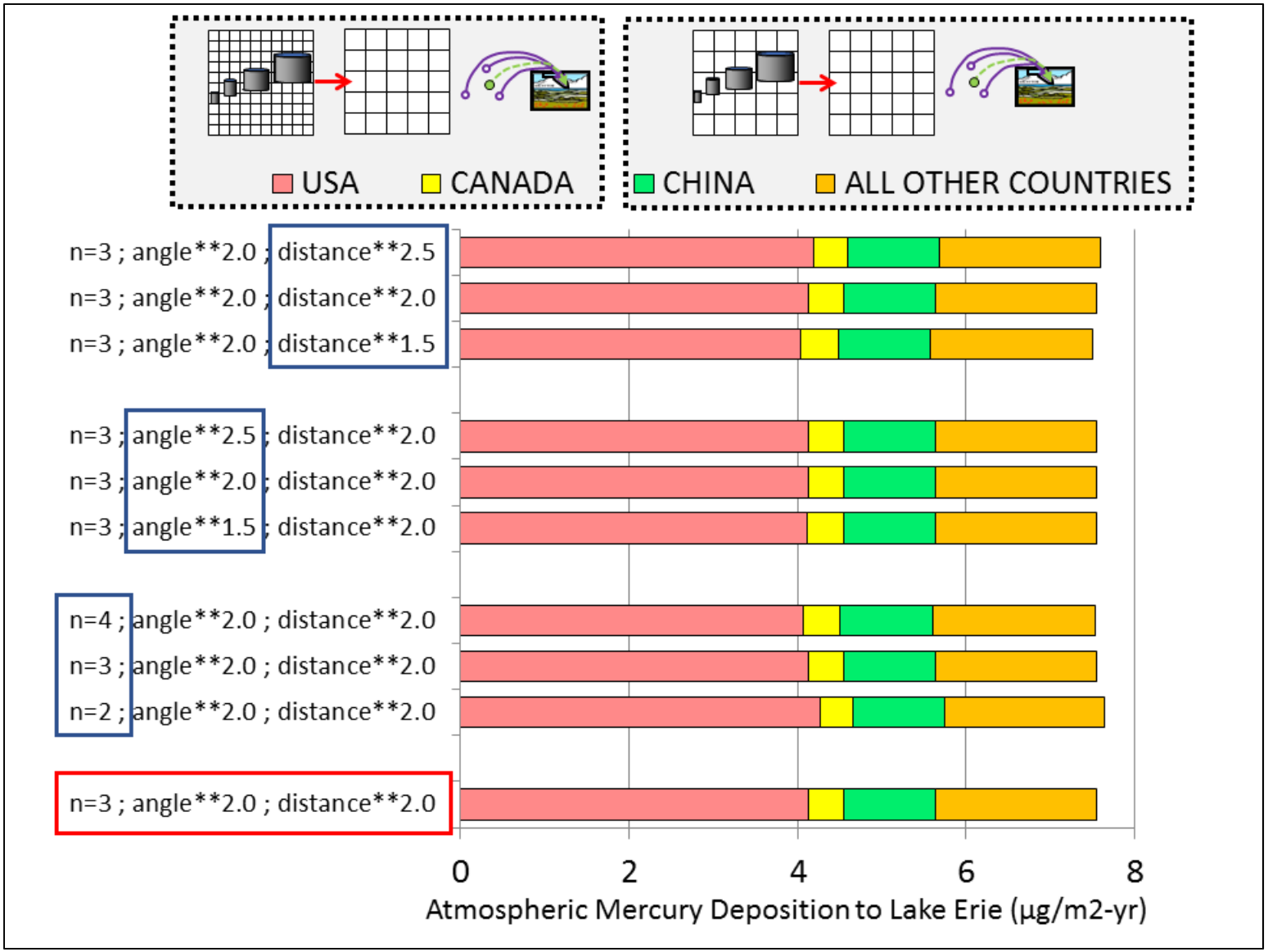

Figure 198. Slide 24

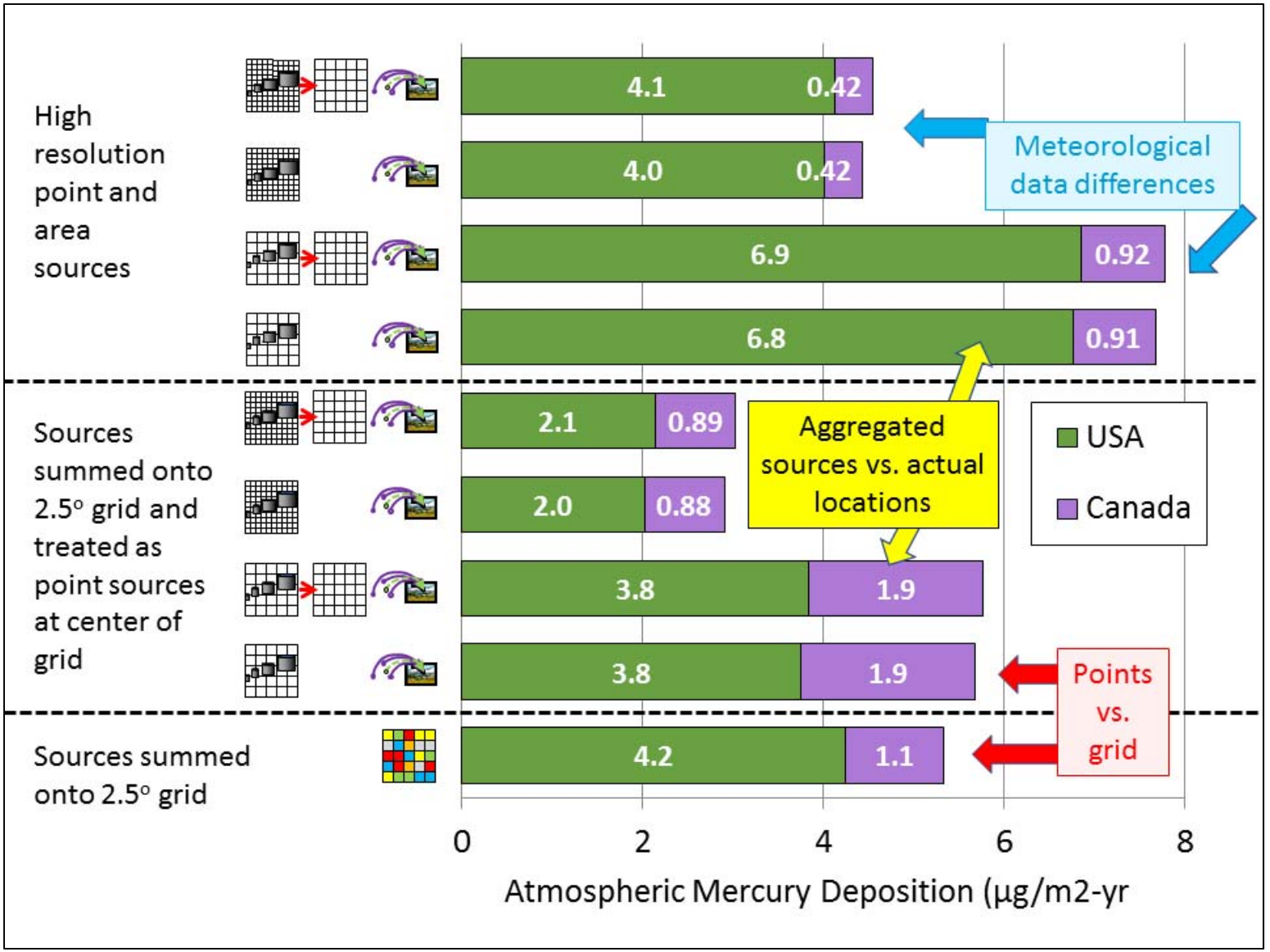

As noted on slide 22, these results are not presented in the main body of the report.

Figure 199. Slide 25

Conclusions

- Lagrangian (plume), Eulerian (grid), and Hybrid approaches can be used in modeling the fate and transport of atmospheric mercury
- Each methodology has advantages and disadvantages
- Similar results for more distant sources, no matter what approach is used
- Some differences in results for local & regional sources, primarily due to:
  - Differences in resolution and source of meteorological data used
  - Are sources aggregated or treated individually?

Next steps

- Detailed model evaluation of results by comparison with ambient measurements
- Eulerian nested-grid capability for HYSPLIT-Hg

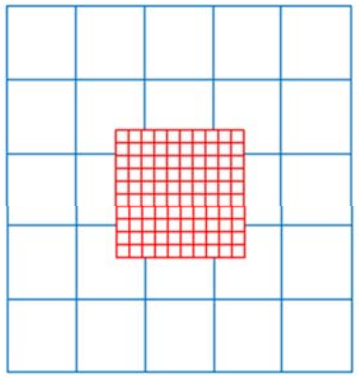

Figure 200. Slide 26

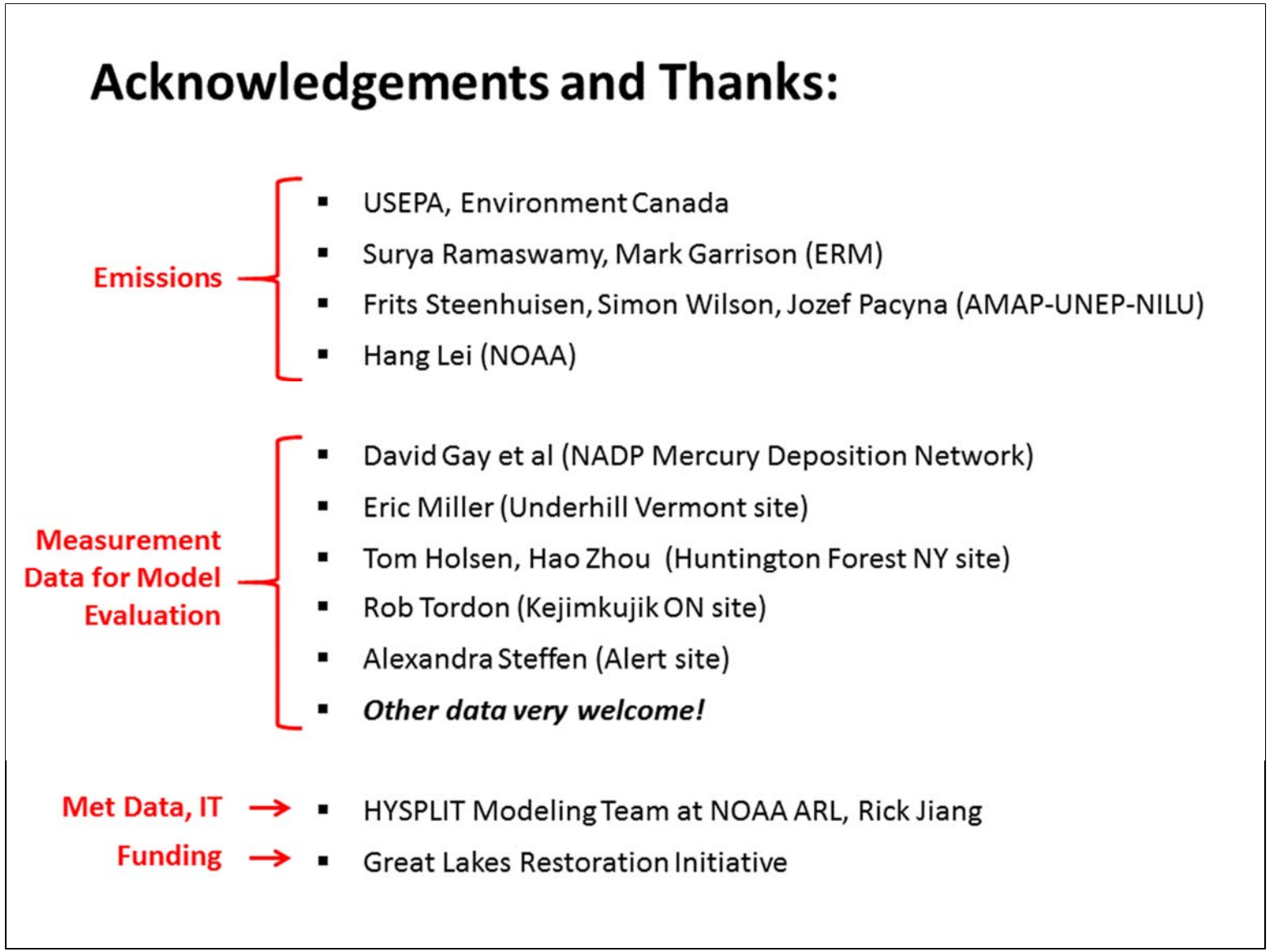

Figure 201. Slide 27

Figure 202. Slide 28